



UNIVERSIDAD
DE CÁDIZ

DOCTORAL THESIS

SURFACES AND INTERFACES CHARACTERIZATION FOR THE DEVELOPMENT OF DIAMOND POWER ELECTRONIC DEVICES

Gonzalo Alba Muñoz

Thesis committee:

D. Dietmar Leinen

Catedrático de Universidad. Dpto. de Física Aplicada – Universidad de Málaga (Spain)

D. Philippe Bergonzo

Visiting professor. Dpt. of Electronic and Electric Engineering – University College London (United Kingdom)

D^a Concepción Fernández Lorenzo

Catedrática de Universidad. Dpto. de Química Física – Universidad de Cádiz (Spain)

Surrogate thesis committee:

D. David Eon

Associate professor. Institute Néel – Université Grenoble Alpes (France)

D^a Ana María Beltrán Custodio

Profesora titular de Universidad. Dpto. de Ciencia de los Materiales – Universidad de Sevilla (Spain)

Co-directed by:

D^a. María del Pilar Villar Castro

Profesora Titular de Universidad. Dpto. de Ciencia de los Materiales e IM y QI – Universidad de Cádiz (Spain)

D. Rodrigo Alcántara Puerto

Profesor titular de Universidad. Dpto. de Química Física – Universidad de Cádiz (Spain)

Reported by:

D. Robert J. Nemanich

Professor. Dpt. of Physics – Arizona State University (United States)

D. Tokuyuki Teraji

Chief researcher. Wide Bandgap Semiconductors Group – National Institute for Materials Science (Japan)



DOCTORAL THESIS

SURFACES AND INTERFACES
CHARACTERIZATION FOR THE DEVELOPMENT
OF DIAMOND POWER ELECTRONIC DEVICES

GONZALO ALBA MUÑOZ

CO-DIRECTED BY

Dr. RODRIGO ALCÁNTARA PUERTO

Dra. M. PILAR VILLAR CASTRO



**UNIVERSIDAD
DE CÁDIZ**

DEPARTAMENTO DE CIENCIA DE LOS MATERIALES E IM Y QI

& DEPARTAMENTO DE QUÍMICA FÍSICA

PUERTO REAL, MAYO 2022

A mi familia, por acompañarme en este camino.

A Rocío, por su amor, comprensión y paciencia.

A mi hija Leire, mi pequeña gran ilusión.



UNIVERSIDAD
DE CÁDIZ

DEPARTAMENTO DE CIENCIA DE LOS MATERIALES E IM Y QI

& DEPARTAMENTO DE QUÍMICA FÍSICA

Thesis co-directed by:

D^a. María del Pilar Villar Castro

*Profesora Titular de Universidad. Dpto. de Ciencia de los Materiales e IM y QI –
Universidad de Cádiz (Spain)*

D. Rodrigo Alcántara Puerto

Profesor titular de Universidad. Dpto. de Química Física – Universidad de Cádiz (Spain)

Reported by:

D. Robert J. Nemanich

Professor. Dpt. of Physics – Arizona State University (United States)

D. Tokuyuki Teraji

*Chief researcher. Wide Bandgap Semiconductors Group – National Institute for
Materials Science (Japan)*

Thesis committee:

D. Dietmar Leinen

Catedrático de Universidad. Dpto. de Física Aplicada – Universidad de Málaga (Spain)

D. Philippe Bergonzo

*Visiting professor. Dpt. of Electronic and Electric Engineering – University College
London (United Kingdom)*

D^a Concepción Fernández

Catedrática de Universidad. Dpto. de Química Física – Universidad de Cádiz (Spain)

Surrogate thesis committee:

D. David Eon

Associate professor. Insitute Néel – Université Grenoble Alpes (France)

D^a Ana María Beltrán

*Profesora titular de Universidad. Dpto. de Ciencia de los Materiales – Universidad de
Sevilla (Spain)*

Doctoral Student and thesis data				
Ph.D. Student name and surname	Gonzalo Alba Muñoz			
Title of the Thesis	Surface and Interfaces Characterization for the Development of Diamond Power Electronic Devices			
Expert/examiner data				
Name and Surname:	Robert J. Nemanich			
Category:	Professor			
University/Research Center:	Arizona State University, Department of Physics			
Address and Country:	Tempe, Arizona USA 85287-1504			
Thesis Assessment				
	Very Good	Good	Pass	Fail
<i>Originality</i>	x			
<i>Aims</i>	x			
<i>Methodology</i>	x			
<i>Results relevance/significance</i>	x			
<i>Bibliography</i>	x			
<i>Discussion and conclusions</i>	x			
Free Format Report				
<p>This dissertation presents a detailed and careful experimental study of diamond surfaces with a focus on hydrogen or oxygen terminated diamond and diamond interfaces with a focus on tungsten carbide – diamond interfaces.</p> <p>Understanding the hydrogen and oxygen terminated surface is crucial to advancing diamond power electronics. The hydrogen terminated diamond surface enables a hole accumulation layer that is integral to the fabrication of field effect transistors. The oxygen terminated surface is employed with metal layers to enable electrical contacts.</p> <p>Understanding the interface of tungsten carbide on diamond is crucial for Schottky barrier structures that are stable for high temperature operation.</p> <p>The major originality of the research is the application of angle dependent x-ray photoemission spectroscopy (ARXPS) to profile diamond surfaces and interfaces. Traditional x-ray photoemission spectroscopy, which is employed at normal incidence, is an important method to characterize diamond surfaces and interfaces, but the technique cannot determine the specific location of the different surface components. The angle dependent measurements are much more sensitive to the surface layers, and measurements at different angles can be analyzed to determine the location of the specific layers.</p> <p>The aims of the project were focused on two important aspects related to diamond electronics: 1) the properties of hydrogen terminated, air exposed diamond compared to oxygen terminated diamond, and 2) the properties of tungsten-carbide contacts on diamond. The hydrogen terminated, air exposed diamond surface results in a surface</p>				

conducting layer that is attributed to a hole accumulation layer. This layer has a high charge density which has been studied for various field effect transistor designs. The oxygen terminated surface is often used for metal contacts and Schottky barriers. The tungsten-carbide contacts show stability at high temperature which is important for many applications.

The methodology of the project is carefully organized to fully support the conclusions and impact of the research. The first chapter provides a very complete summary of the technology and the state of knowledge of the field – including the important issues that are to be addressed. The second chapter provides necessary detail on the angle dependent x-ray photoemission spectroscopy and on the sample synthesis and fabrication. The third chapter extensively addresses the hydrogen terminated, air exposed surfaces and the oxygen terminated surfaces. The research on the hydrogen terminated surface considered several different possibilities to understand the origin of the surface conducting layer. The research on the oxygen terminated diamond (100) surface provided important insight into the presence of sp² bonded carbon within the surface layer. The fourth chapter addressed the interface of tungsten carbide combining both high resolution electron microscopy and angle dependent XPS. The research is very complete and carefully supports the conclusions which are summarized in the fifth chapter.

The results relevance and significance is evident in each chapter. There is still controversy on the origin to the surface conducting layer for air exposed, hydrogen terminated diamond. The results presented here consider two models, the more commonly accepted surface transfer doping model and the surface acceptor model. The new results add insight and point to the possibility that the surface acceptor model may be relevant, but more research is necessary to consider the surface conducting layer that forms after oxide deposition. The evidence of sp² bonded carbon within the surface of oxygen terminated diamond is very helpful in understanding the contacts that form on the surface. The research on tungsten-carbide – diamond interface showed a very complex interaction of this technologically relevant surface.

The bibliography presents the relevant research results that describe the state of the understanding of the surfaces and interfaces addressed in this research. It is both complete and concise. The most relevant papers are carefully summarized and carefully cited to describe the impact to this work.

The discussion and conclusions are fully supported in this dissertation. Chapters 3 and 4 discuss the relevance of the research and how the results impact the current understanding. The last chapters brings together all of the results and conclusions and also points out areas where additional research is necessary.

Suitable

No Suitable

Date: 11/ 26/ 2021

Signature:



Ph.D. THESIS ASSESMENT (International Mention)

Doctoral Student and thesis data				
Ph.D. Student name and surname	Gonzalo Alba Muñoz			
Title of the Thesis	Surface and Interfaces Characterization for the Development of Diamond Power Electronic Devices			
Expert/examiner data				
Name and Surname:	Tokuyuki Teraji			
Category:	Chief Researcher at Wide Bandgap Semiconductors Group, Research Center for Functional Materials			
University/Research Center:	National Institute for Materials Science			
Address and Country:	305-0044 1-1 Namiki, Tsukuba, Ibaraki, Japan			
Thesis Assessment				
	Very Good	Good	Pass	Fail
<i>Originality</i>	x			
<i>Aims</i>	x			
<i>Methodology</i>	x			
<i>Results relevance/significance</i>	x			
<i>Bibliography</i>		x		
<i>Discussion and conclusions</i>	x			
Free Format Report				
<p>Understanding the band bending structure is very important when designing diamond-based electronic devices. This thesis describes in detail how to quantitatively analyze XPS data to extract band bending structures, and the research purpose is important and clear. Then, by applying this method, the band bending structure is explained for hydrogen-terminated and oxygen-terminated surfaces, which are typical surface terminations of diamond.</p> <p>It is also unique in that it visualizes the band bending. Finally, the analysis method for estimating band bending using XPS is extended to the band bending measurement at the interface of the Schottky diode, which is directly linked to the device characteristics. This thesis containing these contents can be judged to be of high value.</p> <p>If I make comments to this thesis, it was a pity that the band bending diagram obtained analytically in this study was not drawn in this thesis, but only in the text. If the comparison between the band diagram obtained in this study and the previously reported band diagram is discussed while describing the band diagram, it can be said that the thesis has a greater impact.</p>				

 Suitable No Suitable

Date: Nov. 3, 2021

Signature:

Acknowledgements

There are many people who have been part of this PhD and who to a greater or lesser extent have accompanied me on this journey. I want to thank all of them for the support and company that they have offered me over the years. In a special way I would like to thank to:

Dr. Daniel Araujo Gay, leader of the diamond research line in the research group TEP120 (Materials Science and Engineering), for giving me this opportunity and introducing me to the world of research for the first time. His support and willingness have been key.

Dr. M^a del Pilar Villar Castro, my PhD director, who has also given me the opportunity to be part of the diamond group and has guided me throughout this trip. Her expertise in electron microscopy, crystallography and chemistry have been essential for the achievement of this PhD.

Dr. Rodrigo Alcántara Puerto, my PhD supervisor, for accepting the direction of my PhD, for allowing me to use the Department of Chemistry-Physics facilities for numerous experiments, for his advice and kind availability.

Dr. Javier Navas Pineda, my supervisor's office mate, for introducing me to X-ray spectroscopy and helping me in the analysis and interpretation of the results with very productive discussions.

Dr. Rafael García Roja, main leader of the TEP120 group, for accepting me as a member and easing my continuity during the PhD.

Dr. Julien Pernot, Dr. David Eon and Dr. Gauthier Chicot, for hosting me during my stays in Grenoble (France) both at the Institut Néel and at DiamFab to carry out surface studies in diamond, and to introduce me to the process of diamond synthesis and the manufacture of devices.

Dr. Satoshi Koizumi and Dr. Tokuyuki Teraji, for giving me the opportunity to collaborate in their research group during my stay at NIMS in Tsukuba (Japan), showing me the manufacturing process of diamond-based devices and passing on their experience on electrical characterization.

Dr. Dietmar Leinen, from the University of Málaga, for his great contribution to the XPS experiments, analysis and results interpretation. His expertise in this analysis technique has been fundamental.

The group and office colleagues with whom I have shared many moments on a day-to-day basis and who have allowed me to work in an environment of great companionship, ideal for developing my ideas: Jesús Cañas Fernández, Beatriz Soto Puerto, Dr. María de la Paz Alegre Salguero, Josué Millán Barba, Dr. Fernando Lloret Vieira, Dr. Marina Gutiérrez Peinado,

Dr. José Carlos Piñero Charlo, Dr. Daniel Fernández de los Reyes, Dr. Jesús Hernández Saz, Dr. Verónica Braza Blanco and the newcomers Lucía Nieto and Dr. Mariko Suzuki.

I would also like to mention other people and institutions that have been important to the achievement of this PhD:

- Dr. Rocío Romero Pareja, from the “Centro de Bioinnovación” (Universidad de Málaga), for transmitting her experience in the management of FIB and the manufacture of lamellae.
- Servicios Centrales de Ciencia y Tecnología (Universidad de Cádiz), especially to José María Geraldía Sánchez (TEM) and Juan José Pérez Sagasti (XPS).
- Centro de Investigación, Tecnología e Innovación (Universidad de Sevilla).
- Instituto Universitario de Investigación en Microscopia Electrónica y Materiales (Universidad de Cádiz), especially to Dr. Francisco Miguel Morales Sánchez and Manuel Figueroa Regio.
- Dr. Manolo Domínguez de la Vega and Dr. Hicham Bakkali, from the Condensed Matter Physics department (Universidad de Cádiz), collaborating with AFM experiments.
- Coordination of the Doctorate Programme in Nanoscience and Material Technologies (Universidad de Cádiz).

This research was funded by:

- Spanish Ministry of Economy and Competitiveness under Grant No. 392 TEC2017-86347-C2-1-R, by the DiamMOS project; and also under Grant No. ESP2017 91820 EXP, by the DiamAIR project.
- European H2020 Program under Grant No. SEP-210184415, GreenDiamond Project.

Resumen

La gestión de la energía eléctrica es uno de los retos más importantes de una humanidad con demandas energéticas crecientes. Actualmente, los elementos de alta potencia de la red eléctrica, como los rectificadores, están basados en el silicio. El diseño de nuevas arquitecturas ha mantenido a los dispositivos basados en silicio en la cima del mercado de dispositivos de alta potencia. Sin embargo, las limitaciones inherentes de este material han llevado a los investigadores a explorar otros candidatos semiconductores.

Las superiores propiedades electrónicas y térmicas del diamante respecto a otros semiconductores más habituales como el Si o GaAs, lo convierten en un candidato prometedor para su aplicación en regímenes de alta potencia y alta frecuencia. Los nuevos métodos de fabricación de diamante sintético han fomentado y abierto la investigación hacia esta nueva tecnología. Como semiconductor de banda ancha, la naturaleza aislante del diamante hace que su aplicación electrónica dependa mucho de aspectos científicos y tecnológicos como el dopaje, los fenómenos de superficie e interfaz, así como otras implicaciones del proceso de fabricación de dispositivos. El éxito en la definición del comportamiento final de los dispositivos electrónicos de diamante requiere un examen exhaustivo de los aspectos electrónicos más relevantes de los mismos, a fin de comprender sus orígenes y tomar el control sobre sus efectos.

Esta tesis se enmarca en los aspectos de superficie e interfaz del diamante (100) para su aplicación en dispositivos electrónicos. En primer lugar, se centra en uno de los conceptos más aceptados de la electrónica de diamante: la relevancia de las terminaciones de superficie de diamante para la definición del comportamiento del dispositivo. En este sentido, el uso de la espectroscopía de fotoelectrones de rayos X de ángulo resuelto (ARXPS) ha permitido reinterpretar las contribuciones electrónicas cerca de la superficie y continuar la discusión sobre el origen de la conducción tipo p de la superficie hidrogenada. Respecto a la terminación de oxígeno, los resultados de ARXPS han servido como plataforma de partida para nuevos modelos de reconstrucción de superficies que pasan por considerar la presencia de hibridaciones de carbono sp^2 , rompiendo con la concepción ideal y fuertemente arraigada de una reconstrucción de superficie completamente formada por hibridaciones sp^3 .

Por otro lado, los aspectos de la intercara se analizan en el marco de las uniones metal-diamante, estructura base para los contactos óhmicos y Schottky. La reacción metal-diamante se ha relacionado con la baja estabilidad térmica del contacto y el deterioro de su comportamiento electrónico. Para evitar esta reacción, algunos investigadores han elegido un carburo preformado de carácter metálico como el WC, que muestra una alta estabilidad térmica y un comportamiento Schottky cercano al ideal. La caracterización nanoscópica ha permitido poner en perspectiva la fenomenología de intercara de estas estructuras Schottky.

Los resultados de esta tesis ayudarán a comprender mejor y continuar el debate sobre algunos de los aspectos científicos fundamentales de los dispositivos electrónicos basados en diamantes.

Abstract

The management of electric energy is one of the more important challenges of humanity with increasing energy demands. High power elements in the electric grid such as rectifiers are currently based on silicon. Design of new architectures has kept silicon-based devices on top of the high-power devices market. However, the inherent limitations of silicon have lead researchers to explore other semiconductor candidates.

Diamond superior electronic and thermal properties make it a promising candidate for its application in high-power and high-frequency regime. For this reason, diamond has generated great interest to researchers in the last decades. The new methods of diamond synthesis fostered and opened research towards this new technology. As a wide band-gap semiconductor, diamond insulating nature makes its electronic application very dependent on scientific and technologic aspects such as doping, surface and interface phenomena as well as other device manufacturing process implications. Therefore, success in defining the ultimate performance of diamond electronic devices will require a thorough examination of the most relevant electronic aspects in them, in order to understand their origins and take control over the consequences.

This thesis is framed on the surface and interface aspects of (100) diamond for its application in electronic devices. It is first focused on one of the most accepted concepts on diamond electronics: the relevance of diamond surface terminations for the definition of the device performance. The use of the angle-resolved X-ray photoelectron spectroscopy (ARXPS) mode has prompted the reinterpretation of the electronic contributions near the surface and has allowed opening the discussion on the origin of surface p-type conduction of the hydrogenated surface. Regarding oxygen termination, the ARXPS results have served as a starting platform for new models of surface reconstruction that go through the consideration of sp^2 hybridizations, breaking with the strongly rooted conception of ideal full- sp^3 surface reconstruction.

On the other hand, interface aspects are discussed in the frame of metal-diamond junctions, which is the base structure for ohmic and Schottky contacts. The metal-diamond reaction has been linked to the low thermal stability of the contact and the deterioration of its electronic behaviour. To avoid this reaction, some researchers have chosen a preformed carbide with a metallic character such as WC, showing high thermal stability and a close to ideal Schottky behaviour. The comprehensive interface nanoscopic characterization allows this thesis to put into perspective its phenomenology in such Schottky structures with that of other options.

The results of this thesis will help to better understand and continue the debate on some of the fundamental scientific aspects of diamond-based electronic devices.

Acronyms

AFM – Atomic Force Microscopy

ARXPS – Angle-Resolved XPS

BB – Band bending

BB(E) – Band bending XPS peak shape

BDD – boron-doped diamond

BE – Binding Energy

BFOM – Baliga's FOM

BHFOM – Baliga's FOM for High Frequency

CL - Cathodoluminescence

CVD – Chemical Vapour Deposition

DBB – Downward band bending

DBB/SA – Downward band bending due to shallow acceptors

EDX – Energy-Dispersive X-ray spectroscopy

EELS – Electron Energy Loss Spectroscopy

FET – Field Effect Transistor

FIB – Focus Ion Beam

FOM - Figure of Merit

HPHT – High-Pressure High-Temperature

HREELS - High-resolution electron energy loss spectroscopy

HRTEM – High-Resolution TEM

H-terminated – Hydrogen terminated

KE – Kinetic Energy

MES – MEtal-Semiconductor

ML - Monolayer

MOS – Metal-Oxide-Semiconductor

NEA – Negative electron affinity

NEXAFS - Near Edge X-ray Absorption Fine Structure

NiD – non-intentionally doped

NIRIM - National Institute for Research in Inorganic Materials

O-terminated – Oxygen terminated

PEA – Positive electron affinity

RT – Room temperature

SA – Shallow acceptor

S_a – Surface arithmetic average roughness

SBD – Schottky Barrier Diode

SBH – Schottky Barrier Height

SCL – Surface Conductive Layer

SEM – Scanning Electron Microscopy

S_q – Surface root mean square roughness

SS – Surface States

STD – Surface Transfer Doping

STEM – Scanning Transmission Electron Microscopy

TEM – Transmission Electron Microscopy

TPD – Temperature programmed desorption

UBB – Upward band bending

UHV – ultra-high vacuum

UV – Ultraviolet

VUV – Vacuum ultraviolet

XPS – X-ray Photoelectron Spectroscopy

XRD – X-ray diffraction

Contents

Acknowledgements	i
Resumen	v
Abstract	vii
Acronyms	viii
Contents	xi
General introduction: Motivation, goals and thesis structure	1
Introducción general: Motivación, objetivos y estructura de la tesis	5
Chapter 1: Introduction to single-crystal diamond electronic devices	9
1.1. Diamond properties	10
1.2. Diamond synthesis	12
1.2.1. High-pressure and High-temperature methods	12
1.2.2. Chemical vapour deposition method	14
1.3. Diamond surfaces	19
1.3.1. Ideal unreconstructed (100) and (111) diamond surfaces	20
1.3.2. The (100) diamond surface reconstructions	21
1.3.3. Real surfaces: Defects, misorientation, and roughness	23
1.4. Unipolar (100) diamond electronic devices	30
1.4.1. Metal-diamond contacts	30
1.4.2. Unipolar rectifying diamond architectures	36
1.4.3. Diamond device fabrication overview.....	37
Chapter 2: Materials and methods	41
2.1. Experimental techniques and procedures	42
2.1.1. Atomic Force Microscopy (AFM).....	42
2.1.2. X-ray photoelectron spectroscopy (XPS).....	43
2.1.3. Transmission electron microscopy (TEM).....	50
2.1.4. TEM samples preparation by Focus Ion Beam (FIB).....	52
2.1.5. Experimental procedures by section.....	52
2.2. Sample description	53
2.2.1. Samples for surface characterization	53
2.2.2. Samples for interface characterization	54
Chapter 3: XPS studies of (100) diamond surface terminations	57
3.1. ARXPS study of the (100)-H-terminated surface	58
3.1.1. The (100)-H-terminated diamond.....	58
3.1.2. Surface conductive layer in (100)-H-terminated surface	60

3.1.3. Previous XPS results in the H-terminated surface.....	65
3.1.4. A new method to evaluate band bending from XPS peak shapes	67
3.1.5. The (100)-H-terminated ARXPS spectra: Results.....	80
3.1.6. The (100)-H-terminated ARXPS spectra: Discussion.....	85
3.1.7. Summary of the section	93
3.2. ARXPS study of the (100)-O-terminated surface.....	95
3.2.1. The (100)-O-terminated surface	95
3.2.2. Previous XPS results in the (100)-O-terminated surface.....	99
3.2.3. The (100) O-terminated ARXPS spectra: Results	102
3.2.4. The (100)-O-terminated ARXPS spectra: Discussion.....	111
3.2.5. Final comments	116
3.2.5. Summary of the section.....	117
Chapter 4: Tungsten-carbide/diamond interfaces for Schottky barrier diodes ...	121
4.1. Introduction to WC/diamond junctions for Schottky barrier diodes	122
4.2. The WC/O-terminated diamond interface: Results.....	124
4.2.1. TEM/STEM analysis	124
4.2.2. XPS depth profiling analysis	127
4.2.3. Summary of the results	133
4.3. The WC/O-terminated diamond interface: Discussion	134
4.3.1. Interface WC formation.....	134
4.3.2. Interface oxygen due to O-termination.....	136
4.3.3. Schottky barrier height discussion.....	137
4.3.4. WC/diamond interface mechanism formation during annealing.....	139
4.3.5. Ideal band setting of WC/O-terminated and WC/H-terminated diamond	140
4.4. Final comments	141
4.5. Summary of the section.....	142
Chapter 5: Global conclusions and perspectives	145
Conclusiones generales y perspectivas.....	149
References	153

General introduction: Motivation, goals and thesis structure

The properties of diamond are optimal for application in electronic diamond devices. For decades, the new possibility of synthesis of diamond and boron-doped diamond (BDD) by chemical vapour deposition (CVD) has opened the door to this new technology. However, there are still some factors that do not allow the manufacture of this type of device with true control over its properties and, therefore, with high reproducibility.

Among other reasons, it is noteworthy that diamond devices have so far shown a great dependence and sensitivity towards aspects related to diamond synthesis (doping, generation of defects...), diamond surface (polishing, surface defects, chemical finishes...), or phenomena related to the interface with other materials such as metals or oxides. All these aspects have been covered in some extent by researchers since their understanding is crucial to control the properties of the device and its terminals. Many of these relevant aspects with proven relevance either remain controversial or the number of results is still insufficient. This need must be addressed and provide undoubtedly fundamental feedback for the development of diamond electronic devices.

Given the above motivation, the general objective of this thesis is to precisely **respond to some fundamental scientific aspects of the electronic phenomenology of diamond electronic devices based on the characterization of the microstructure, chemistry, and/or electronic structure of diamond surfaces and interfaces**. The search for the origins of the various adverse effects observed in their electrical behaviour is essential to advance in the control of the manufacturing processes and the properties of the devices, as well as to improve their reproducibility. For this, this work has focused on collaborating with the study of the following relevant aspects:

- **Characterization of aspects related to the diamond surface:** A better understanding of the surfaces and their effects on the electronics of the devices is sought to have greater control over them. Without this base, it is difficult to advance, for example, in the simulation of structures and devices, in the understanding of energy band diagrams in metal-diamond or oxide-diamond structures or their differences when they are based on one or another surface chemical termination. In this sense, these studies focus on two highly controversial aspects:
 - o **P-type conductivity of the hydrogen(H)-terminated diamond surface.** This surface phenomenon is unique among semiconductor materials and, although its origin is still under discussion, it has great potential for application in many devices such as Field-effect Transistors (FETs).

- **The role of the oxygen(O)-terminated diamond surface for the formation of Schottky contacts.** The diamond oxygen termination is widely used for the formation of Schottky contacts for its increasing effect on the Schottky barrier and the stabilization of the electrical behaviour. The origin of this phenomenon also does not escape from some controversy. The understanding of the reconstruction of the O-terminated surface and associated chemical groups is not as consensual as in the hydrogen termination. This is due, among other reasons, to the greater heterogeneity of oxygenation treatments and their results, which make it difficult to form general conclusions.
- **Characterization of aspects related to the interface of diamond-based structures:** Diamond interfaces with other materials are the base structure of the terminals of the device, so their presence in the devices is almost unavoidable. Understanding the structural and/or chemical changes in the interface regions of these structures is crucial for greater control of device properties. The interface phenomena have been pointed out in the literature, on numerous occasions, to hypothetically explain some phenomena of the devices such as the formation of improved ohmic behaviour through the reaction of Ti with diamond forming TiC, the stabilization of the Schottky behaviour in Zr/diamond structures through the formation of interface oxides, the independence of the Schottky barrier from the metal work function with the existence of interface states that fix the Fermi level (Fermi level pinning), or the dependence of the band offset between oxides (eg. Al₂O₃) and diamond, with the existence or not of an adjustment between their crystalline lattices.

This thesis intends to answer the interface phenomena in the specific case of Schottky contacts with a WC/diamond structure. The concept of deposition of a preformed carbide was motivated to avoid the reaction of the deposited metal and the diamond that, in turn, was related to the deterioration of Schottky behaviour. It should be noted that the study of these structures is very close to the reality of the final device in terms of its microstructure, chemistry, and composition. The same cannot be said, for example, of surface studies that may undergo modifications during the subsequent formation of an interface.

The structure of the thesis is designed to meet these objectives. In this way, the thesis is divided into 5 chapters:

- Chapter 1: An introduction to the fundamental aspects of the single-crystal diamond, its potential for the manufacture of high-power electronic devices, and the state of the art.

- Chapter 2: The materials and methods that have been necessary for the preparation of the experiments and the data analysis are here summarized.

- Chapter 3: It contains the studies related to the surface aspects. These studies are based on the characterization of the surface using X-ray photoelectron spectroscopy in angle-resolved mode. This technique has rarely been used on the diamond surface. The interpretation of this novel information has required the development of own analysis methods. Comparison with the results in the literature has allowed the clarification of the surface electronic contributions in both surface terminations and the discussion of their fundamental aspects. It is divided into two sections:
 - Section 3.1: Hydrogen termination as the origin of p-type surface conduction.
 - Section 3.2: Oxygen termination and its reconstruction.

- Chapter 4: It focuses on the general interface aspects of Schottky barrier diodes (SBD) (metal-diamond reaction, oxygen in the interface, or Schottky barrier height (SBH)) but is framed in the specific case of the WC / diamond contacts.

- Chapter 5: The most important global conclusions of the thesis are summarized.

This structure is necessary to get an approach to the interface and surface phenomena that rule the diamond electronic devices such as SBDs and MOSFETs. This will help researchers to explain the electronic behaviour of diamond devices.

Introducción general: Motivación, objetivos y estructura de la tesis

Las propiedades del diamante son óptimas para su aplicación en dispositivos electrónicos de diamante. Desde hace décadas, la nueva posibilidad de síntesis de diamante y diamante dopado por deposición química de vapor ha abierto la puerta a esta nueva tecnología. Sin embargo, existe todavía una serie de factores que no permite la fabricación este tipo de dispositivos con un verdadero control sobre sus propiedades y, por tanto, con una alta reproducibilidad.

Entre otras razones es destacable que los dispositivos de diamante han mostrado hasta ahora una gran dependencia y sensibilidad hacia aspectos relacionados con la síntesis de diamante (dopaje, generación de defectos...), la superficie de diamante (pulido, defectos superficiales, terminaciones químicas...), o los fenómenos de intercara con otros materiales como metales u óxidos. Todos estos aspectos han sido en mayor o menor medida cubiertos por los investigadores ya que su comprensión es crucial para controlar las propiedades de los terminales de los dispositivos. Sin embargo, muchos de estos aspectos con una relevancia demostrada como las terminaciones superficiales o los fenómenos de intercara, o bien siguen estando bajo controversia o bien el número de resultados es insuficiente. Esta necesidad debe ser cubierta y proporcionar una retroalimentación sin duda fundamental para el desarrollo de dispositivos electrónicos de diamante.

*Dada la motivación anterior, el objetivo general de esta tesis es precisamente **responder a algunos aspectos científicos fundamentales de la fenomenología electrónica de los dispositivos electrónicos de diamante basándose en la caracterización de la microestructura, química y/o estructura electrónica de las superficies e intercaras de diamante.** La búsqueda de los orígenes de los diversos efectos adversos observados en su comportamiento eléctrico resulta imprescindible para avanzar en el control de los procesos de fabricación y las propiedades de los dispositivos, así como mejorar su reproducibilidad. Para ello se ha enfocado el presente trabajo a colaborar con el estudio de dos aspectos relevantes:*

- ***Caracterización de aspectos relacionados con la superficie del diamante:*** *Se busca una mayor comprensión de las superficies y sus efectos en la electrónica de los dispositivos con el fin de tener un mayor control sobre los mismos. Sin esta base es difícil avanzar, por ejemplo, en la simulación de estructuras y dispositivos, en la comprensión de los diagramas de banda energética en las estructuras de metal-diamante u óxidos-diamante o de sus diferencias cuando están basadas en una u otra*

terminación superficial. En este sentido estos estudios se enfocan a aspectos de gran controversia como:

- **Conductividad tipo p de la superficie de diamante terminada en hidrógeno.** Este fenómeno de superficie es único entre los materiales semiconductores y, pese a que su origen sigue bajo discusión, tiene un gran potencial de aplicación en los dispositivos como los FET.
- **El rol de la superficie de diamante terminada en oxígeno para la formación de contactos Schottky.** La terminación de oxígeno de diamante es ampliamente utilizada para la formación de contactos Schottky por su efecto aumentador de la barrera de Schottky y por la estabilización del comportamiento. El origen de este fenómeno tampoco escapa de cierta controversia. La comprensión de la reconstrucción de la superficie terminada en oxígeno y los grupos químicos asociados no está tan consensuada como en la terminación de hidrógeno. Esto es debido entre otras razones a que existe una mayor heterogeneidad de tratamientos de oxigenación y sus resultados, que hacen difícil la formulación de conclusiones generales.
- **Caracterización de aspectos relacionados con la intercalación de estructuras basadas en diamante:** Las intercalaciones de diamante con otros materiales son la estructura base de los terminales por lo que su presencia en los dispositivos es casi ineludible. El entendimiento de los cambios estructurales y/o químicos en las regiones de intercalación de estas estructuras es crucial para un mayor control de las propiedades de los dispositivos. Los fenómenos de intercalación han sido señalados en la literatura en numerosas ocasiones para explicar, hipotéticamente, algunos fenómenos de los dispositivos como la formación de comportamiento óhmico mejorado por medio de la reacción de Ti con diamante formando TiC, la estabilización del comportamiento Schottky en estructuras Zr/diamante por medio de la formación de óxidos de intercalación, la independencia de la barrera de Schottky de la función de trabajo del metal con la existencia de estados de intercalación que fijan el nivel de Fermi (Fermi level pinning), o la dependencia del band-offset entre los óxidos (e.g. Al₂O₃) y el diamante, con la existencia o no de un ajuste entre sus redes cristalinas.

En esta tesis se pretende dar respuesta a los fenómenos de intercalación en el caso concreto de los contactos Schottky de estructura WC/diamante. El concepto de deposición de un carburo preformado fue motivado para evitar la reacción del metal depositado con el diamante que estaba relacionada con un deterioro del comportamiento Schottky. Debe notarse que el estudio de estas estructuras está muy cerca de la realidad del dispositivo final en cuanto a su microestructura, química y

composición. No se puede decir lo mismo, por ejemplo, de los estudios superficiales que pueden sufrir modificaciones durante la posterior formación de una intercara.

La estructura de la tesis está planteada para ajustarse a dichos objetivos. De esta forma, la tesis queda dividida en 5 capítulos:

- *Capítulo 1: Una introducción a los aspectos fundamentales del diamante mono-cristalino, su potencial para la fabricación de dispositivos electrónico de alta potencia y el estado del arte.*
- *Capítulo 2: Se resumen aquí los materiales y métodos que han sido necesarios para la elaboración de la tesis.*
- *Capítulo 3: Contiene los estudios relacionados con los aspectos de la superficie. Estos estudios se basan en la caracterización de la superficie por medio de la espectroscopia de fotoelectrones de rayos X en el modo de ángulo resuelto. Esta técnica ha sido rara vez empleada en diamante. La interpretación de esta novedosa información ha requerido el desarrollo de métodos de análisis propios. La comparación con los resultados en la literatura ha permitido la clarificación de las contribuciones electrónicas de superficie en ambas terminaciones superficiales y la discusión aspectos fundamentales de las mismas. Está dividido en dos grandes secciones:
 - o *Sección 3.1: La terminación de hidrógeno como origen de la conducción de superficie tipo p.*
 - o *Sección 3.2: La terminación de oxígeno y su reconstrucción.**
- *Capítulo 4: Se centra en los aspectos de intercara generales de los diodos Schottky (la reacción metal-diamante, el oxígeno en la intercara o la altura de la barrera de Schottky) pero se enmarca en el caso concreto de los contactos WC/diamante.*
- *Capítulo 5: Se resumen las conclusiones globales más importantes de la tesis.*

La estructura planteada es la necesaria para llegar a entender los fenómenos de intercara que dominan el comportamiento de los dispositivos electrónicos tales como los diodos de barrera de Schottky o los transistores metal-óxido-semiconductor de efecto campo.

Chapter 1:

Introduction to single-crystal diamond electronic devices

Diamond properties, diamond synthesis, diamond surfaces, and unipolar diamond-based devices are introduced to motivate the current subject of the thesis. The advantages of this material, the state of the art of technology and devices, as well as the challenges to face, are pointed out in this first chapter.

The chapter is divided into next sections:

- 1.1. Diamond properties
- 1.2. Diamond synthesis
- 1.3. Diamond surfaces
- 1.4. Unipolar (100) diamond electronic devices

1.1. Diamond properties

Diamond is a metastable allotrope of carbon with a face-centered cubic structure where four tetrahedral interstitial sites are occupied by a carbon atom. This structure is known as diamond structure (see Figure 1.1) and other common semiconductors such as silicon or germanium are also based on it. Diamond lattice parameter is 0.3567 nm and the distance between two bonded carbon atoms is 0.154 nm. This structure results in a high atomic packing factor of 0.34, an atomic density of $1.76 \times 10^{23} \text{ cm}^{-3}$, and a density of $\sim 3.5 \text{ g}\cdot\text{cm}^{-3}$ which are related to an exceptional rigidity and one of the highest hardness of all materials in the world (7000 $\text{kg}\cdot\text{mm}^{-2}$, Knoop hardness). Among other mechanical properties, diamond presents a low friction coefficient, low thermal expansion, and high chemical resistivity. All these properties make diamond an outstanding material for mechanical applications such as cutting tools or wear components coatings. Moreover, its high thermal conductivity ($22 \text{ W}\cdot\text{cm}^{-1}\cdot\text{K}^{-1}$) and intrinsic electrical insulator character also make it suitable for heat dissipation applications, such as integrated circuit substrates or for hybrid circuit packages.

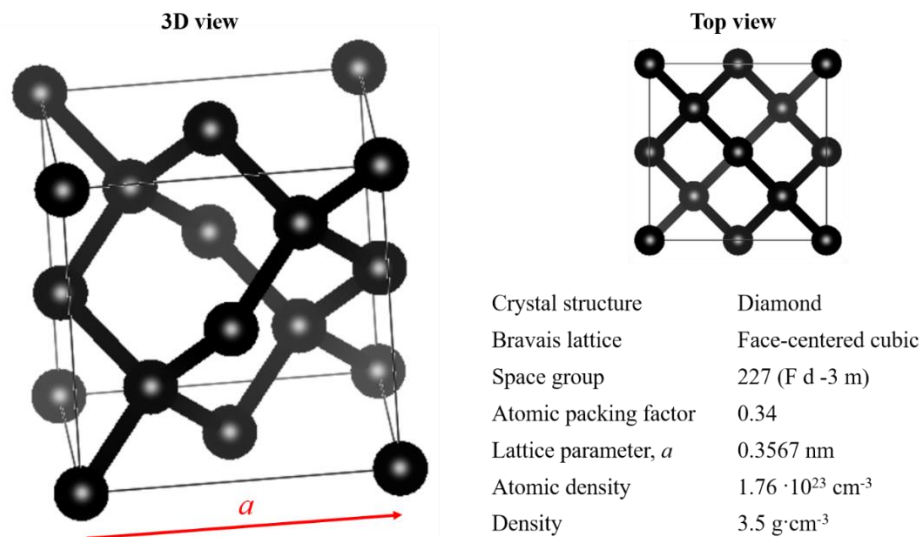


Figure 1.1: Diamond structure unity cell 3D view (left) and top view (right). Some crystal parameters are included.

On the other hand, other interesting properties make it also a promising material for electronic devices working in high-power, high-voltage, high-temperature, and high-frequency modes ((Wort & Balmer, 2008) and references therein):

1. **Bandgap:** The conductivity of intrinsic semiconductors is strongly dependent on the bandgap since the only available charge carriers for conduction are those having enough thermal energy to be excited across the bandgap. In this sense, diamond is considered as a wide-bandgap semiconductor, which has been estimated as $\sim 5.47 \text{ eV}$

at 300 K. This high value yields an extremely low level of the intrinsic carrier concentration and makes diamond-based electronics very sensitive to impurities and defects presence.

2. **Carrier mobility, μ :** The net movement of charge due to an electric field is called drift. The net drift of charge gives rise to a drift current. The mobility, μ , of a certain carrier (hole or electron) is the proportionality factor of the drift velocity (charge displacement velocity), v_d , to the applied electric field, \mathcal{E} , i.e. $v_d = \mu\mathcal{E}$. Thus, it defines how well a carrier will move through a semiconductor material. Diamond presents high mobility of electrons and holes ($4500 \text{ cm}^2/(\text{s}\cdot\text{V})$ and $3800 \text{ cm}^2/(\text{s}\cdot\text{V})$ respectively at 300 K) in comparison to other commonly used semiconductors (see Table 1.1). The mobility is dependent on different scattering processes such as those related to phonon or ionized impurities which, in turn, are dependent on the temperature. Generally, higher temperature and higher impurities concentration are related to mobility reduction.
3. **Saturation drift velocity:** At low electric fields, the mobility is considered constant which is also called low-field mobility. There is however an electric field threshold from which charge carriers cannot move any faster. The corresponding drift velocity is known as its “saturation velocity”. At this point, the velocity of charge carriers is saturated by the generation of optical phonons in the crystal lattice. This can be advantageous for field-effect transistors (FET) applications. Most experimental diamond values stand in the ranges of $v_s = 0.85\text{-}1.2 \times 10^7 \text{ cm}\cdot\text{s}^{-1}$ and $v_s = 1.5\text{-}2.7 \times 10^7 \text{ cm}\cdot\text{s}^{-1}$ for holes and electrons, respectively.
4. **Breakdown field:** The breakdown field is a characteristic property of an insulator material that defines the maximum electric field that can be applied across the material before it conducts. The higher the breakdown field the lower the size of the device and, hence, the faster switching. For this reason, it is desirable a semiconductor material with a high electric breakdown field for many devices. Since it is an intrinsic property, once the semiconductor material in the device is chosen, the breakdown field is defined by the device sizing. Diamond exhibits the highest predicted breakdown field of any semiconductor with values in the range $5\text{-}10 \text{ MV}\cdot\text{cm}^{-1}$.
5. **Carrier lifetime:** The carrier lifetime is defined as the average time it takes, for a minority carrier, to recombine. It is very important for bipolar devices but less for unipolar devices. For the latter, however, the carrier lifetime is an indicator of the quality of the crystal. Synthetic diamond presents carrier lifetimes higher than $2 \mu\text{s}$ (Isberg et al., 2002).
6. **Thermal properties:** Again, the outstanding thermal properties such as thermal conductivity and low thermal expansion allow diamond to dissipate the heat produced

as a result of the device operation. Diamond thermal conductivity is much higher than main semiconductor competitors (see Table 1.1), which makes it a promising candidate for high-power applications.

Another way of evaluating the potential of a given material for application in electronic devices is through the use of Figures of Merit (FOMs). It is useful as an indicator of the margin of improvement of electronic devices that are based on a certain material. Different FOMs have been used in the literature, but perhaps the most repeated are those proposed by Baliga: Baliga's FOM (BFOM) and Baliga's FOM for High Frequency (BHFOM). Table 1.1 summarizes the main electronic properties and values of both merit figures for diamond and other wide-bandgap semiconductor materials (Umezawa, 2018).

Table 1.1: Comparison of electronic properties and Baliga's Figures of Merit of wide bandgap semiconductors.

		4H-SiC	GaN	Diamond	Application benefit
Bandgap [eV]		3.2	3.45	5.47	High temperature
Saturation drift velocity [$\times 10^7$ cm·s⁻¹]	<i>e</i> ⁻	1.9	2.5	0.8	High frequency
	<i>h</i>	1.2	-		
Carrier mobility, μ [cm²·V⁻¹·s⁻¹]	<i>e</i> ⁻	1000	1500	4500	
	<i>h</i>	120	200	3800	
Thermal conductivity λ [W·cm⁻¹·K⁻¹]		4.9	1.3	22	High power
Breakdown field \mathcal{E}_{max} [MV·cm⁻¹]		2.8	5	10-22	High electric field
BFOM $\epsilon_r \mu \mathcal{E}_{max}^3$		440	2950	473078	Unipolar performance
BHFOM $\mu \mathcal{E}_{max}^2$		58	237	12510	Unipolar High-Frequency performance

1.2. Diamond synthesis

The consideration of diamond as a semiconductor material and its potential for electronic devices would not have been developed without the advancement of diamond synthesis techniques. The first industrial use of diamond began with the first synthesis in 1955 based on the High-Pressure High-Temperature (HPHT) method (Bundy et al., 1955). From this date, a wide variety of manufacturing methods have been developed to allow the fabrication of diamonds including the control of impurities and defects level, among which CVD methods are highlighted.

1.2.1. High-pressure and High-temperature methods

The HPHT methods were first implemented in the 1950s and used by companies such as General Electrics. Due to its reduced manufacturing cost, it is currently the most widely used method for manufacturing substrates. It is based on the use of similar conditions than necessary for the natural diamond formation. The most used HPHT methods are Belt-Press, Cubic-Press, and Split-Sphere Press, being the latter the most energy-efficient.

Belt presses are the oldest systems but are still used today by several manufacturers at a much larger scale than the original designs. A schematic of the Belt press system is shown in Figure 1.2. All these processes required a carbon source, a diamond seed, a pressure chamber able to work above 5 GPa, a heating system that allows reaching temperatures around 1500 °C, and the presence of a molten metal, which serves as a solvent and transport medium of the carbon source to the seed. The most effective catalyst materials are metals of group VIII, such as iron, nickel, cobalt, and their alloys that are carbon solvents. Other elements can be included for other purposes such as aluminum to avoid the nitrogen impurities incorporation that gives the crystal a yellowish colour.

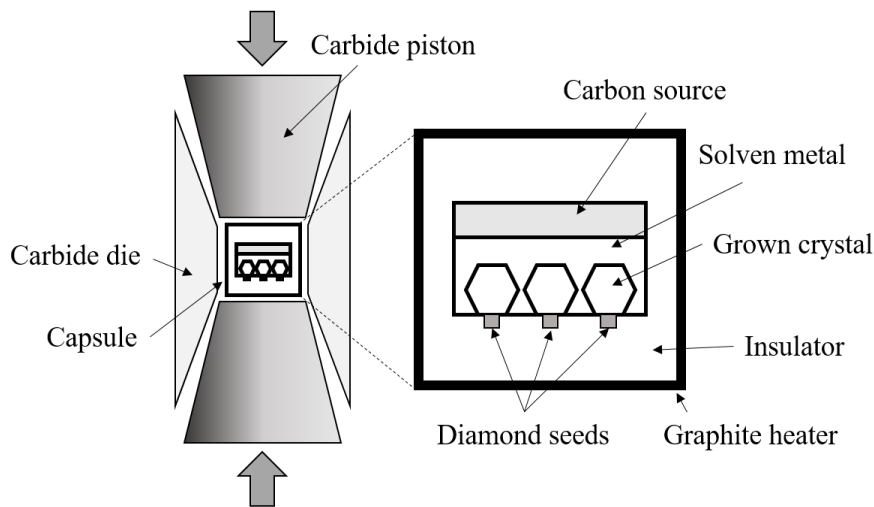


Figure 1.2: Schematic example of a Belt type HPHT press. Diamond seeds are placed at the bottom of the press. The internal part of the press is heated by a tubular, graphite heater. This generates temperatures above 1500°C and melts the solvent metal. The molten metal dissolves the high purity carbon source, which is then transported to the diamond seeds and precipitates.

The growth occurs from the seed to multiple crystallographic directions at the same time but some faces ($\{100\}$, $\{110\}$, $\{111\}$ and $\{113\}$) are more stable than others. The growth and impurities incorporation rates depend on the crystalline direction. For example, nitrogen impurities concentrations for the main growth sectors directions are related by $[N]_{\{111\}} > [N]_{\{100\}} > [N]_{\{113\}} > [N]_{\{110\}}$. The resultant synthetic diamond must be then cut in slices maximizing the desired surface orientation. In Figure 1.3 the cut for a (100) oriented substrate is schematized. Once the cut is done, different growth sectors can be visually distinguished based on the nitrogen concentration from the top view. The three primary planes to consider for the diamond crystal are the (111), (100), and (110) planes. The cutting and polishing process difficulty differs from one surface orientation to another. The lower hardness is found in the (110) orientation while the hardest is the (111) and, thus, it is directly related to its polishing difficulty. The polishing direction must be also optimized to increase mechanical efficiency.

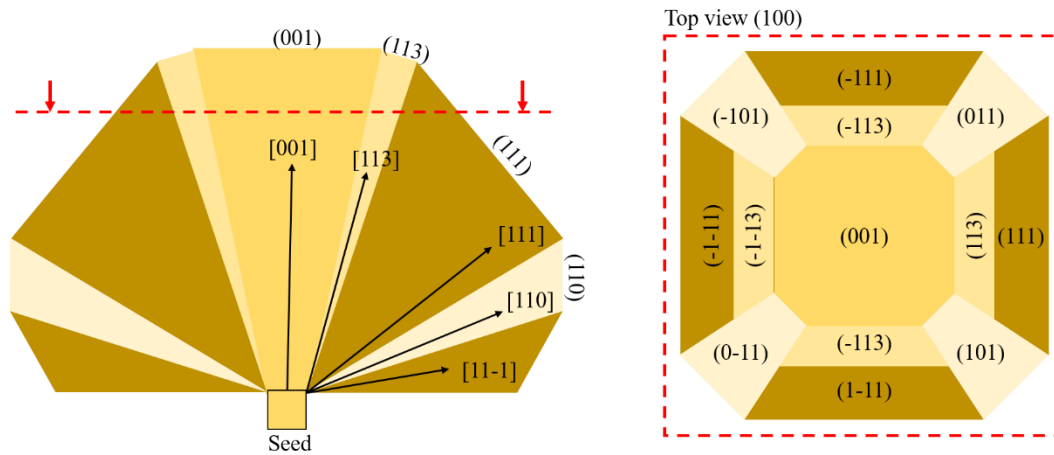


Figure 1.3: (Left) Cross-section schematic of a diamond crystal synthesized by the HPHT method. The growth starts from a diamond seed and occurs in multiple directions with different growth and impurities incorporation rates. The vertical axis corresponds to the [001] direction. The crystal is cut in the horizontal plane (001). (Right) Top view (001) of the diamond crystal sliced by the red dashed line. An index is used to label the origin growth direction of the growth sector.

1.2.2. Chemical vapour deposition method

The techniques subscribed under CVD allow the deposition of different types of carbon materials, from amorphous to poly- and monocrystalline diamond. One of the great strengths of the CVD method which put diamond on the shuttle for electronic applications is the fabrication of high-quality homoepitaxial diamond layers with a low density of defects and controlled impurities incorporation. Thus, undesirable electronic phenomena related to defects are reduced and the synthesis of diamond with controlled impurities density.

The CVD methods have been studied since the early 1980s for different worldwide research groups. Researchers from the National Institute for Research in Inorganic Materials (NIRIM) (currently National Institute for Material Research (NIMS), Japan), first published a remarkable series of papers in which different CVD methods were described (Kamo et al., 1983; S. Matsumoto et al., 1982). These methods involve the chemical reaction in a gas-phase and the deposition on a substrate surface. A schematic of the process procedure is shown in Figure 1.4, including the adjustable parameters such as the different usable gases or the energy sources required for the activation of the chemical process.

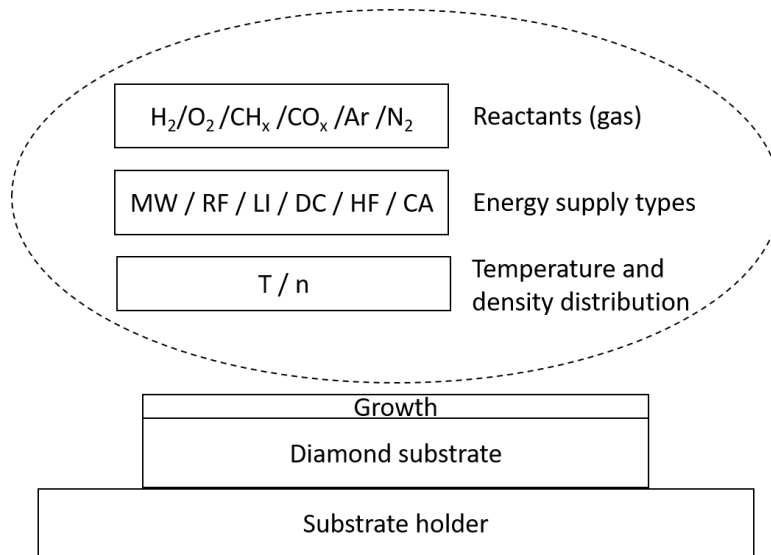


Figure 1.4: Schematic diagram of the mechanism from Chemical Vapour Deposition (CVD) processes for diamond growth.

The mixture of hydrogen and methane is the most frequently gas used for diamond growth. The presence of atomic hydrogen or oxygen is the most critical component in the gas mixture while methane and its conversion to other hydrocarbon molecules such as acetylene are necessary as a carbon source. The hydrogen main function is the saturation of the dangling bonds of the outermost diamond layers, removing the non-diamond carbon phases and allowing other reactive radicals such as CH_2 to be generated. On the other hand, the use of small oxygen amounts has been related to the growth rate and quality enhancement, the lowering of the substrate temperature, or reduced incorporation of boron (Omnès et al., 2011).

The substrate material, which can be either diamond or another material, is very decisive. The first case is normally used for homoepitaxial growth, while, for the second case, polycrystalline films are usually expected. The deposition of diamond on a non-diamond substrate requires additional nucleation steps. These steps provide the necessary diamond seeds to the non-diamond substrate to grow three-dimensionally, forming a continuous polycrystalline film. Silicon is frequently chosen as a substrate material for polycrystalline diamond growth. Homoepitaxial diamond growth requires a careful diamond substrate selection process. This is because the quality of diamond substrates and surface morphology is directly related to the quality of the diamond growth layer. Indeed, dislocations can propagate from the substrate through the interface to the homoepitaxial layer. As a peculiar and novel approach, large area monocrystalline diamond layers have been recently obtained on Si using an Ir layer as a buffer (Schreck et al., 2001). However, the quality of the obtained diamond layer is relatively poor with a dislocation density around 10^8 cm^{-3} . Among others, cathodoluminescence (CL) and X-ray topography are the main non-destructive methods to evaluate the presence of these defects to optimize the quality of the growth. The surface defects and polishing issues are discussed in Section 1.3.3.

Concerning energy sources a wide range of methods have been applied in the literature: microwave (MW), radio frequency (RF), laser-induced (LI), direct current (DC), hot-filament (HF), and chemical activation (CA), among other. It must be noted that different energy supplies can generate different mole fractions and temperature distributions under the same other experimental conditions. The detailed description or comparison of the different CVD methods and tuning parameters are out of the scope of this thesis.

1.2.2.1. Doped diamond growth

The very large bandgap of diamond (~ 5.47 eV) makes intrinsic carrier generation very low. As a metaphor, for a diamond the size of the earth, the carrier generation and recombination dynamic results in only ~ 1 electron-hole pair at 300 K. This absence of carriers in an intrinsic diamond makes the doping a must for its electronic purposes applicability. Moreover, dopants in such a wide bandgap semiconductor tend to have higher ionization energies what results in a low activation at room temperature (RT). The short atomic distances in the diamond crystal make the incorporation of impurities more difficult and most doping elements lead to severe distortions of the unit cell. Although other methods such as ion implantation or HPHT have been successfully carried out for impurities incorporation, electronic devices require higher control on the

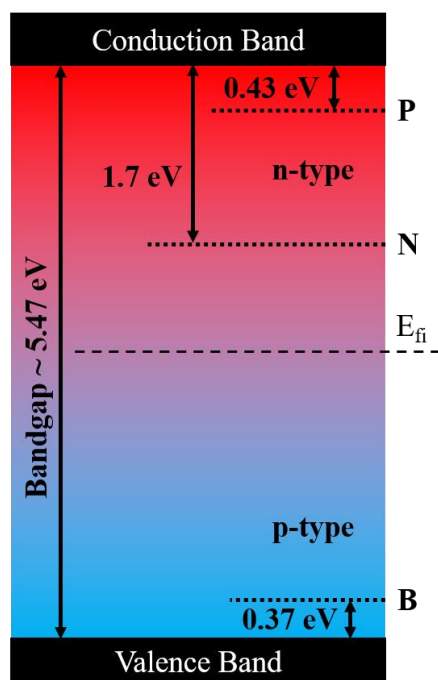


Figure 1.5: Schematic band diagram showing the main dopants of diamond, its types and ionization energies.

fabrication process with special caution in doping level, defect generation, or architecture sizing. This makes CVD the most relevant technique for the fabrication of controlled diamond doped layers. The most common dopants in diamond are nitrogen, boron, and phosphorus. A summary of its types and ionization energy is shown in Figure 1.5.

Nitrogen is the most common impurity and is known to influence most physical properties of diamond. In small aggregates or substitutional sites of the diamond lattice, nitrogen has a direct effect on the growth habit and in the electrical resistivity of diamond. Most of the synthetic diamonds are, to a lesser or greater extent, doped with nitrogen, and also result in the distortion of the diamond lattice. Nitrogen generates a deep donor level below the conduction band (n-type dopant). The

determination of the ionization energy of N as diamond dopant requires the understanding of the complexes and their singular ionization energies. For its substitutional form, the ionization energy

has been determined to be at 1.7 eV below the conduction band (Kajihara et al., 1993). This ionization energy is very high, even compared to other semiconductors' bandgap (e.g. Silicon bandgap is 1.14 eV). Therefore, the ionization of these dopants requires very high temperatures, which makes nitrogen unsuitable as an effective n-type dopant for electronic devices.

Another n-type dopant with lower ionization energy and, hence, with a promising application for electronic devices is phosphorus. The discovery dates from the 1990s (Koizumi et al., 1997) making it the latest dopant found among the top three. From this date, several works have been published concerning the growth aspects of n-type doped diamond which further allows designs and fabrication of the first bipolar device (Koizumi et al., 2001). The growth of controlled phosphorus-doped layers is mostly based on Plasma-Enhanced CVD technology using phosphine (PH_3) or tertiary-butyl phosphine ($\text{C}_4\text{H}_{11}\text{P}$) as phosphorus sources. The success of this recipe is based on the elimination of hydrogen co-incorporation which is responsible for the passivation of P atoms. Because of the larger atomic radius of P, the growth of P-doped films leads to a negative effect on grown crystal quality. Its crystallographic substitutional incorporation is eased by using the {111} growth direction but can be also achieved in the {100} or {113} directions (Makino et al., 2005) reaching lower doping concentration. The ionization energy is still under discussion since some spread of values in the range from 0.43 to 0.63 eV is found in the literature (see (Stenger et al., 2013)).

Boron is the most studied diamond dopant up to date. The early stages of diamond electronics were directly linked to the development of the CVD growth technology of BDD layers. This p-type dopant can be incorporated with high reproducibility and has lower ionization energy among effective diamond dopants (0.37 eV (Lagrange et al., 1998)). Because of this, huge efforts have focused on the development of p-type unipolar devices such as SBDs or Metal-Oxide-Semiconductor Field-effect transistors (MOSFETs). The BDD growth for diamond electronic devices is mostly carried out in a CVD system and boron is introduced through the incorporation of diborane (B_2H_6) or trimethylboron ($\text{B}(\text{CH}_3)_3$) into the gas mixture. While the control of the doping level is in an advanced state, the appearance of defects is still not overcome. A relationship between the boron doping level and the defect density has been published (Alegre et al., 2014), and growth rates to avoid dislocation generation have been established. Other milestones in the diamond growth-related techniques are the delta-doped layers (Chicot et al., 2012), or the lateral growth (Lloret, 2017). The latter is still not in an advanced technology stage but the near future will allow new devices architectures and the rethinking of the fabrication process.

Other dopants such as sulphur or oxygen have been also considered in the literature. The effect of oxygen in the CVD diamond growth is has been used in the literature (Fiori, 2012; Harris & Weiner, 1990; Omnès et al., 2011). The incorporation of O during diamond growth has been

discarded (Harris & Weiner, 1990). Another way to incorporate O is the ion implantation which leads to n-type layers when followed by low-temperature annealing (Prins, 2000). The activation energy of such O⁻ donor states tends to be even lower than that of boron acceptors at approximately 0.32 eV below the conduction band. Concerning sulfur, the activation energy of the conductivity in sulfur-ion-implanted diamond is 0.19–0.33 eV (Hasegawa et al., 1999) and only a few results on such n-type conductivity have been reported (Y. Wang & Yin, 2014)(Nakazawa et al., 2003). However, the donor level seems to be shallower than that of boron and high conductivity can probably be obtained. This is supported by theoretical calculations in which donor levels for substitutional sulfur or some complexes of sulfur are placed in the range of 0.15–1.63 eV below the conduction band (Saada et al., 2000).

Among the characterization techniques, CL is the most frequently used either for the quantification of doping level (Barjon et al., 2007) or on the defects characterization (Robins et al., 1989). Moreover, it is a non-destructive technique that makes it ideal to quickly check the quality of the layer and the growth conditions and, in case of the fabrication of a diamond heterostructure, the resumption of the next layer growth process. Destructive techniques for doping level determination include Secondary Ion Mass Spectroscopy (SIMS) or Transmission Electron Microscopy (Araujo et al., 2013).

1.2.2.2. Diamond classification

The diamond type classification system divides diamonds into categories based on the presence or absence of nitrogen and boron impurities and how they are arranged in the lattice (see Figure 1.6). Type I diamonds are defined as containing sufficient N to be measurable by infrared (IR) absorption spectroscopy, whereas type II diamonds do not contain enough N to be detected by the IR spectrometer. This concentration limit is established around 5 ppm. These general categories are then subdivided, based on the nature of the impurities, into “a” and “b” types (some authors also include a third type “c” not related to nitrogen nature (Zaitsev, 2001)).

Type I diamonds are divided into type Ia and type Ib. Both subgroups contain nitrogen, but the nitrogen atoms are arranged differently in each group. In type Ib diamonds, single nitrogen atoms that have replaced carbon atoms in the lattice, are isolated. In contrast, type Ia diamonds contain N atoms that are near each other in one or two spectroscopically detectable configurations. The most common configuration for type Ia diamond involves two adjacent N atoms in the lattice. Although these two atoms occupy neighbouring sites, each pair is isolated from other N atoms in the lattice. These N impurities are commonly referred to as A aggregates, and the diamonds that contain them are termed type IaA. The other configuration involves four N atoms that symmetrically surround a vacancy. This complex grouping is formed when two combined A

aggregates. These N impurity groupings are called B aggregates, and the associated diamonds label is type IaB.

Type II diamonds are divided into types IIa and IIb. Type IIa diamonds contain neither easily measurable N nor boron impurities. Natural type IIb diamonds likewise contain no IR-measurable N impurities but contain boron impurities that are thought to be isolated single atoms that replace carbon in the diamond lattice. Characteristic properties of type IIb diamonds, such as electrical conductivity or bluish colour, are a direct result of the boron impurities.

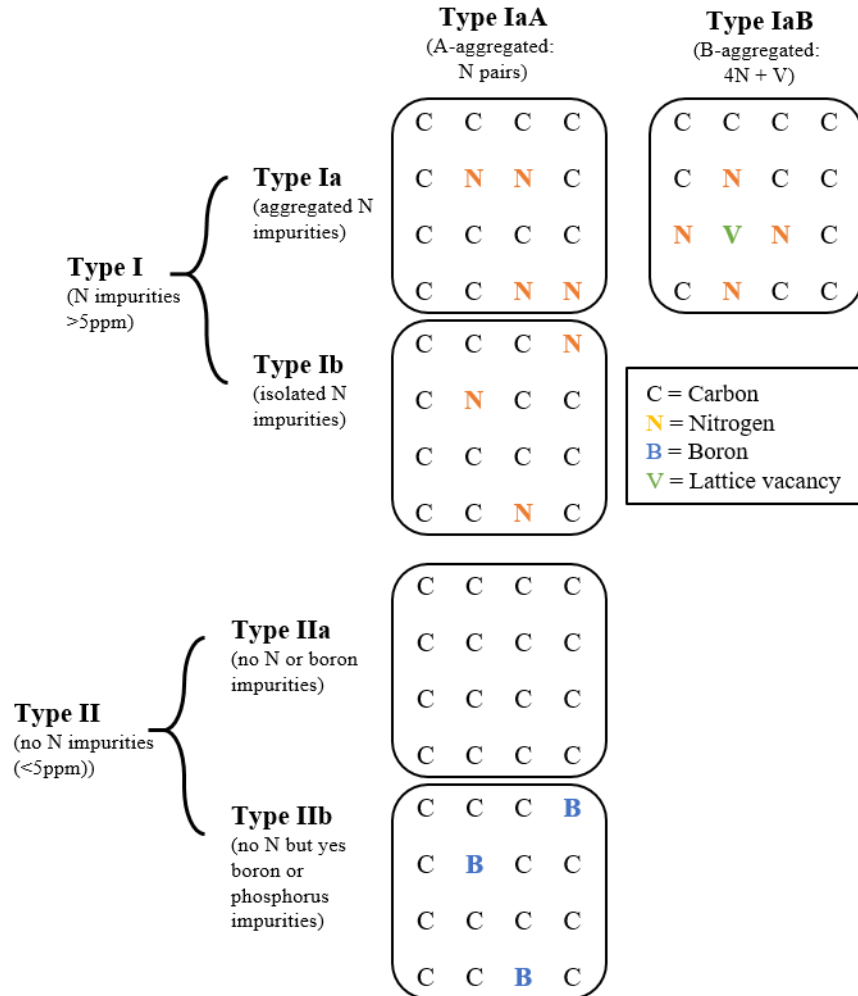


Figure 1.6: Diamond type classification based on the presence or absence of nitrogen and boron impurities and their configurations in the diamond lattice.

1.3. Diamond surfaces

Diamond surfaces and the understanding and control of their properties is a decisive task in the way to the development of diamond electronic devices. During the manufacturing process of diamond electronic devices, it is necessary, at least once, to define a diamond surface that will, directly or indirectly, influence the performance of the final device. Despite the great advances

and numerous published results, diamond surfaces continue to lead researchers to discuss the origin of complex issues of great controversy.

In this subsection, the diamond surface general concepts and problematics are introduced as well as some relevant results in the topic.

1.3.1. Ideal unreconstructed (100) and (111) diamond surfaces

A surface is a disruption in the material periodicity, which induces changes in the electronic structure and leads to the appearance of new properties different from the bulk. In the outermost layers of an ideal crystal, the surrounding forces of the atoms are altered and the equilibrium positions for these atoms should be modified from that of the bulk. Furthermore, the bond breaking on one side due to the surface is expected to have a more dramatic effect on the atomic configuration at the surface of a semiconductor and further on the energy-band diagram.

The ideal unreconstructed surface is referred to the surface atoms structure just after the

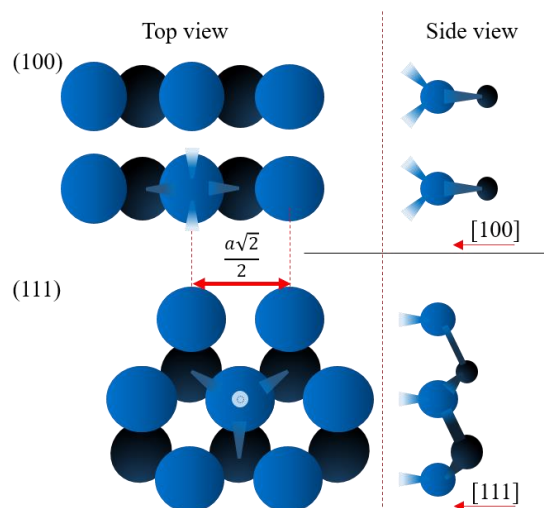


Figure 1.7: Schematic top view and side view of the two outermost layers of carbon atoms in the ideal unreconstructed (100) and (111) diamond surface. The second layer from the surface is darker than the top layer. The four bonds of a top atom are also represented in the top view. Two dangling bonds exist on the (100) surface and only a single dangling bond on the (111).

surface creation instant, i.e. keeping the bulk interatomic distances and with the appearance of a certain number of dangling bonds per outermost surface atom that depends on the surface orientation. This way, the ideal unreconstructed (100) and (111) surfaces in the diamond lattice are common for all materials with this structure, such as Ge or Si, except for the lattice parameter, which is noticeably smaller for diamond. In Figure 1.7, the (100) and (111) diamond surfaces are represented. Some representative parameters of those surfaces are summarized in Table 1.2.

Table 1.2: Representative parameters of the ideal unreconstructed (100) and (111) diamond surfaces where a is the diamond lattice parameter.

Surface orientation→	(100)		(111)	
Surface density ($\times 10^{15} \text{ cm}^{-2}$)	$2/a^2$	1.57	$4/a^2\sqrt{3}$	1.82
Interplanar distance (nm)	$a/4$	0.089	$a/\sqrt{3}$	0.206
Volume density ($\times 10^{23} \text{ cm}^{-3}$)	$8/a^3$	1.76	$8/a^3$	1.76
Number of broken bonds	2		1	
Number of remaining bonds	2		3	
Surface energy (J/m^2) (Lüth, 2010)	5.71		4.06	

It is known that for crystalline materials, most surface properties depend on the orientation. In particular, the number of bonds that have to be broken to create a piece of surface is defined by the surface orientation. The surface energy or surface reactivity is directly related to this concept and can be deduced that reactivity of the (100) surface, with 2 broken bonds, is in principle higher than that of the (111) surface with 1 broken bond. Although unreconstructed models can be useful to predict some of these properties from one to another orientation, diamond unreconstructed surfaces are unstable and surface atoms and dangling bonds should rearrange, forming new surface atomic configuration. At this point, two different phenomena can be identified: relaxation and reconstruction. Relaxation refers to the displacement normal to the surface of the outermost atomic plane or planes, while reconstruction involves more dramatic changes in the position of atoms that move parallel to the surface plane and lose the in-plane periodicity and interatomic distances of the bulk.

In the next subsection, a summary of the (100) diamond surface reconstructions is exposed.

1.3.2. The (100) diamond surface reconstructions

The (100) diamond surface orientation is the most used for diamond electronic devices because of its greater ease and lower cost of manufacture, higher boron incorporation rate, and more advanced state of growth technology, among other reasons. Reconstruction of the (100) diamond surface is highly dependent on the chemical termination and treatments. In this sense, hydrogen and oxygen are the most frequently used chemical terminations to date for the design of diamond-based electronic devices. Other chemical terminations such as nitrogen have also been investigated (Chandran et al., 2015; Stacey et al., 2015) but are out of the scope of the thesis. Researchers have made a great effort over the past decades to find out the most stable surface configurations for the different chemical terminations and clarify the origin of the different properties. However, the surface chemical and structural changes due to surface termination treatments are still controversial despite the numerous results in this topic.

Reconstructions related to the (100) surface when it is subjected to different treatments have been investigated in the literature using electron diffraction techniques (Hamza et al., 1990; R. E. Thomas et al., 1992). A general idea of the (100) surfaces reconstructions is given by *Thomas et al.* (1992). Thus, when a (100) surface is under ultra-high vacuum (UHV) conditions and is annealed at a sufficient temperature for the total desorption of adsorbates (over 900-1000 °C), the outermost carbon atoms tend to form double bonds, creating a 2×1 configuration (the unit cell of surface atoms has a size of 2×1 the unit cell of bulk). This reconstruction is known as bare (or clean) 2×1 (100) surface. This appears to be the stable configuration under these conditions, which is supported by the literature (Futera et al., 2014; Sque et al., 2006). As expected, if the surface is submitted to other ambient conditions at lower temperatures, the bare configuration is not stable and the reconstruction depends on the environmental chemistry and physical conditions. Thus, if the surface is immersed in a hot acid mixture (typically used as a cleaning step as well as an oxygenation treatment) the reconstruction becomes a 1×1 and oxygenated groups are present on the surface. This reconstruction is commonly denoted as $1\times 1:\text{O}$ (see discussion and schematic atomic configuration in Section 3.2.4.). On the other hand, if it is exposed to molecular hydrogen, the 2×1 pattern is maintained, with double-bonded surface carbon atoms forming dimer rows, but this time with the additional presence of surface hydrogenated groups. The latter is known as a $2\times 1:\text{H}$ reconstruction and is stable in the air (Kawarada, 1996). Moreover, these reconstruction changes are reversible, that is, once the $1\times 1:\text{O}$ reconstruction has been obtained by some oxygenation treatment, the sample can be annealed to obtain the bare 2×1 pattern. In the same way, the sample can be directly subjected to a hydrogenation treatment and a $2\times 1:\text{H}$ is obtained. The successive hydrogenation and annealing cycles (from bare 2×1 to $2\times 1:\text{H}$) seem not to lead so much to the deterioration of the surface morphology compared to what occurs in the oxygenation and annealing cycles (change from 2×1 to $1\times 1:\text{O}$), in which the roughness significantly increases. This is explained because, during the annealing of a $1\times 1:\text{O}$ surface, CO and CO₂ groups are desorbed, detaching atoms from the carbon structure, while during the annealing of the $2\times 1:\text{H}$ only molecular hydrogen is released without the deterioration of the carbon structure. The existence of oxygenated or hydrogenated groups, respectively, as well as their desorption characteristic, has been evidenced by techniques such as temperature-programmed desorption (TPD) or X-ray Photoelectron Spectroscopy (XPS), among others.

Several oxygenation treatments are possible (acid treatment, exposure to O₂ atmosphere, vacuum ultraviolet(VUV)/ozone treatment...) making it difficult to get consensus on resulting atomic configuration, i.e. to a $1\times 1:\text{O}$ reconstruction as well as on oxygenated groups are involved in this reconstruction. . Strong dependencies on the particular oxygenation treatment seems to influence the final results. In contrast, for hydrogenation treatments, H₂ plasma is by far the most commonly used and there is a high consensus on the chemical groups involved. This surface

treatment is highly reproducible. The main chemical groups associated with each diamond surface termination are discussed in Chapter 3.

1.3.3. Real surfaces: Defects, misorientation, and roughness

In addition to reconstructions and relaxation effects, real surfaces show additional characteristics such as roughness, misorientation, and multiple defects whose implications in the development and performance of a diamond electronic device are of relevant consideration. During the device manufacturing process, there can be numerous processes (cleaning, polishing, growth, metal depositions, etching processes...) with implications in modifying diamond surface morphology and/or in surface defects generation. In turn, the fabrication processes' performance can be more or less affected by the starting surface characteristics as well. Thus, understanding diamond real surfaces and how it is related to the electronic device requires a complex analysis of the surface properties, the fabrication processes, and its dependencies. Some of them have been pointed out by researchers, such as the increasing roughness and electron affinity of acid-treated surfaces when compared to the hydrogenated samples surfaces; the CVD diamond growth process, in which the starting diamond surface morphology, impurities, and defects are known to be directly related to the CVD layer quality (Takeuchi et al., 1999; Tallaire et al., 2008); the metal depositions processes implication on the modification of the diamond surface electron affinity (Baumann & Nemanich, 1998a); the reactive ion etching processes, in which the quality of the resultant surfaces depends on the micro-masking mechanisms and the defects of the starting diamond surface (Toros et al., 2020); or the surface and subsurface defects generation during mechanical polishing (Tallaire et al., 2008). Also, some dependencies between morphology and electronic effects have been reported (Wade et al., 2017) making the analysis more complex.

The following subsections describe the different elements that are part of a real surface as well as some results in this regard.

1.3.3.1. Defects

In general, surface defects vary from the simplest, such as the addition or absence of a single atom (adatoms and vacancies, respectively), to the more complex, such as pyramidal hillocks. The different defects that can be found on the surface of the diamond are defined by the following:

1. **Adatom/Adparticle:** An adatom is an atom adsorbed on a material surface. For molecules, ions, and clusters the word “adparticle” can be used.
2. **Vacancy:** A vacancy is a point defect into the periodic lattice structure consisting of the absence of an atom. It is a “bath” defect that can be, in some cases, located at the surface.

3. **Adsorbates:** This is the general term to refer to adatoms and adparticles that are adhered from a gas, liquid, or dissolved solid to a surface. By this process, a film of the adsorbate on the surface of the adsorbent is generated. Adsorbates can be placed in substitutional positions (where, ideally, there would be a carbon atom in the diamond structure) or interstitial (other positions). In diamond, elemental adsorbates such as hydrogen and oxygen play a fundamental role in surface reconstructions.
4. **Terraces/Steps:** It is known as a step, the line of atoms that make up the delimitation between two surface regions of the same orientation and structure that are at different heights to their normal. These steps can be one or more atomic layers high and can span macroscopic distances longitudinally. The surfaces delimited by steps are known as terraces or domains. The atomic configurations of the steps mainly depend on the orientation and reconstruction of the terraces. The number of steps per unit area is related to the miscut or misorientation of the surface (see Section 1.3.3.2). For the 2×1 reconstruction in diamond (100) two different types of steps are observed, labelled S_A and S_B , where S_A steps have dimer rows parallel to the step edge, and S_B steps have dimer rows perpendicular to the step edge. Double S_A and S_B steps are called D_A and D_B steps, respectively (Stallcup & Perez, 2001). The presence of surface steps has been related to the dislocations formation on (100) diamond CVD layers (Araujo et al., 2010; Martineau et al., 2009) and has been related to having strong implications on the growth process (Harris & Goodwin, 1993; Lee & Badzian, 1997).
5. **Hillocks:** Hillocks consist of the overgrowth of material over the surface. On the diamond surface, pyramidal hillocks present four-fold symmetry defects with (111) oriented lateral facets with a quadrilateral basis. Flat Hillocks consist of a truncated pyramidal hillock. One possible origin of such flat and pyramidal hillocks generation during HPCVD growth is a bunch of dislocations formed at the interface between the diamond substrate and the layer created at dark inclusions containing impurities (Tallaire et al., 2008).
6. **Unepitaxial crystallites:** Unepitaxial crystallites are small diamond crystals, in the order of hundreds of nanometers, which are normally found isolated at the top of pyramidal hillocks (Takeuchi et al., 1999) with a random orientation at the diamond surface, usually embedded in the CVD layer (Sawada et al., 2001a, 2001b; Tallaire et al., 2008).
7. **Solid contaminant particles:** These solid particles frequently appear in HPHT substrates and are probably related to mechanical polishing diamond residues. The shape is normally rounded and is much smaller than hillocks. It can hardly be

completely removed by ultrasound bath or hot acid treatment-based methods. H_2 plasma is an effective process to etch and eliminate these particles.

8. **Etch pits:** Etch pits are surface depressions formed as a consequence of the preferential etching on lattice defects such as vacancies, dislocations, or impurities. It has been shown that the formation of etch pits on the diamond surface occurs for a wide variety of treatments, mainly using H_2 (Ichikawa et al., 2016; Ivanov et al., 2015; John & Stoikou, 2011; Ri et al., 2006) or H_2/O_2 (Naamoun et al., 2012; Tsubouchi et al., 2016) plasma for a more controlled process. Etching on dislocations produces pits of reasonable depth and marked geometry, which allows its detection and density estimation.
9. **Metallic inclusions:** HPHT synthetic diamonds often contain metal flux inclusions that appear black and opaque in transmitted light and can even allow distinguishing natural from synthetic HPHT diamond (Feral, 2012). Its origin is the HPHT growth process in which some metals such as iron, nickel, and cobalt, are used as catalysts and can sometimes enter the diamond crystal and eventually be discovered on diamond surface. Surface metallic inclusions have been identified as the origin of CVD layers defects (Tallaire et al., 2008).
10. **HPHT growth sectors and boundaries:** Except for the mono-sectorial, most HPHT substrates present different growth sectors, i.e. regions in which the growth has occurred in different orientations. In the case of diamond containing nitrogen, growth sectors can even be identified on the surface by colour contrast. This is because nitrogen incorporation during HPHT growth process varies with the crystal growth orientation and is then different in each directional growth sector (see Figure 1.3). Thus, the lattice constant of diamond increases with increasing nitrogen content. This lattice parameter difference is accommodated between sectors by elastic strain only, with no compensation by misfit dislocations (Burns et al., 2009). At the surface growth sector boundaries multiple defects are expected to appear. Strained surface periodicity or a surface reconstruction discontinuity is also expected.

1.3.3.2. Surface misorientation

Surfaces generated by polishing processes will hardly be oriented to a perfect desired major crystallographic direction. Thus, real surfaces will always include an angular misorientation (also known as miscut angle) (see Figure 1.8) with respect to a surface major crystallographic direction. Although the fabrication process is well controlled, the precision errors are commonly between 0.5° and 3° for most HPHT suppliers.

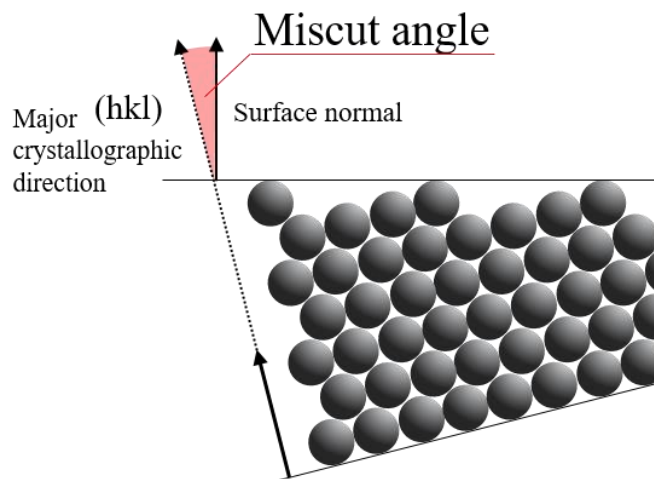


Figure 1.8: Miscut angle definition scheme. It is defined as the angle between the real surface normal direction and the most approached major crystallographic direction.

As a consequence, the diamond surface will be covered by terraces of the major crystallographic surface orientation and steps, whose density is expected to increase almost proportionally with miscut. Surface defects such as steps at the starting surface play an important role in the generation of dislocations which normally start in the first instant of CVD growth (Araujo et al., 2010; Ri et al., 2002; Tallaire et al., 2008). Therefore, the misorientation angle becomes an important parameter for the improvement of the CVD growth crystal quality. In this sense, the step-flow CVD growth process on the (100) surface is based on the steps as preferential growth regions and occurs under the conditions of low and CH_4/H_2 gas flow ratio (Takeuchi et al., 1999). This method allows the generation of atomically flat surfaces in order to get them ready for a high-quality crystal with a higher growth rate process. Another approximation is the use of misorientation angles of 10° or above along the $\langle 110 \rangle$ direction, which allows to etch surface defects by H_2/O_2 plasma without impacting on the roughness parameters (Naamoun et al., 2012). On the other hand, the misorientation angle has been directly related to the CVD growth and boron incorporation rates at constant precursors flow in the (100) surface (Ogura et al., 2011).

1.3.3.3. Roughness

Surface roughness is a component of surface texture that is quantified by the deviations in the normal surface direction, i.e. heights, of a real surface from its ideal form. Note that the normal surface direction does not have to correspond to a major crystallographic direction. The presence of surface defects such as atomic steps is behind the modification of the heights function which can belong to macroscopic surface texture and patterns such as polishing stripes. Multiple parameters of roughness can be defined on a unique trace (denoted R_a, R_q, \dots) or on a whole surface (denoted S_a, S_q, \dots). Surface height parameters depend on the surface area A and the heights function $Z(x,y)$ and are defined in the ISO-2178. Among the most frequently used parameters are:

- **Arithmetic average roughness, S_a :** S_a is one of the most effective surface roughness parameters commonly adopted in general scientific practice. It gives a general description of the height variations in the surface. It is defined as:

$$S_a = \frac{1}{A} \iint_A |Z(x, y)| dx dy \quad (1.1)$$

- **Root Mean Square roughness, S_q :** The Root Mean Square (RMS) roughness (S_q) is the root mean square average of the roughness profile area.

$$S_q = \sqrt{\frac{1}{A} \iint_A |Z^2(x, y)| dx dy} \quad (1.2)$$

The discrete or digital definition of these parameters is included in Section 2.1.1. Other common height parameters are the Skewness, S_{sk} , or the Kurtosis, S_{ku} . Also, spacing or counting, roughness parameters are useful to describe repetitive roughness profiles.

Roughness parameter has been commonly used to evaluate the surface quality and the morphologic effect of different treatments on diamond surfaces such as growth (Ri et al., 2002), termination treatments (Shpilman et al., 2008), reactive etching (Toros et al., 2020), among others. Also, it has been directly related to electrical properties such as surface conductivity on H-terminated diamond (Crawford et al., 2018; Tranvouez et al., 2009; Wade et al., 2017), which has been tentatively linked to the removal of surface defects as part of a more aggressive hydrogen-termination process (Crawford et al., 2018). In this sense, roughness scattering is an important effect in electronic devices that contain thin layers, such as FETs, and has been also tentatively related to the surface conduction phenomenon (Wade et al., 2017).

1.3.3.4. Surface chemical termination

The electronic affinity of diamond is highly dependent on its chemical termination and, for the (100) surface, it can vary from negative values of ~ -1.3 eV for hydrogen termination (Diederich et al., 1996; Krainisky & Asnin, 1998; Takeuchi et al., 2005) to positive values of up to +1.7 eV for oxygen termination (Maier, Ristein, et al., 2001) or even higher for other terminations such as nitrogen or fluorine. For diamond electronic devices, it can have strong implications on the definition of electronic performance. For instance, as will be described in the next section, the electron affinity is directly dependent on the SBH, which is a key concept for the metal-diamond contacts. Indeed, one of the most accepted ideas on diamond electronic devices is that surface termination has a crucial role in device performance. For example, an Au/diamond contact manufactured in analogous conditions can show a linear I/V behaviour (ohmic) or a

rectifying behaviour (Schottky) if a hydrogenation or oxygenation treatment is respectively used just before the metallic deposition (Teraji et al., 2014).

Remarkably, hydrogenated surfaces are also related to a unique phenomenon among semiconductors consisting of the appearance of a surface p-type conductivity (Landstrass & Ravi, 1989a, 1989b). This fact supposes the presence of additional p-type carriers on the surface and the consequent modification of the energy-band diagram of the devices. The p-type conductivity phenomena must be considered in the design of the device since, for example, it would mean an electrical connection between terminals manufactured on the same diamond surface. To eliminate this effect of surface conduction, the surface is usually subjected to an oxygenation treatment.

Given the importance of diamond surface chemical terminations in devices, Sections 3.1 and 3.2 are dedicated to the state of the art and the controversial topics of hydrogen and oxygen terminations, respectively.

1.3.3.5. Diamond surface polishing process

Polishing the diamond surface is one of the most important technological processes for defining the morphology of a real surface. Mainly, this process is related to the crystalline quality of the diamond in CVD processes so that the initial morphology of the HPHT substrate is related to the quality of the CVD layer (Fiori, 2012). In this sense, not only the surface morphology but also the presence of subsurface defects generated during the polishing process, are known to be responsible for the defects inside the epilayer.

Polishing is a complex and, in some cases, expensive process (the price of polishing one diamond substrate surface side can be similar to that of the substrate) so its application must be sufficiently justified. In this sense, HPHT substrates manufacturers include a polishing process to the final surfaces. However, the quality of the surface morphology, either in terms of the roughness or the density of surface and subsurface defects generated, may not be adequate to address certain growth processes or when it is intended to obtain a controlled interface, metal-diamond or from heterojunctions, free from defects. The quality of the surfaces is evaluated through techniques such as Atomic Force Microscopy (AFM), Scanning electron microscopy (SEM), or phase-shifting interferometry (optical profilometry), among others.

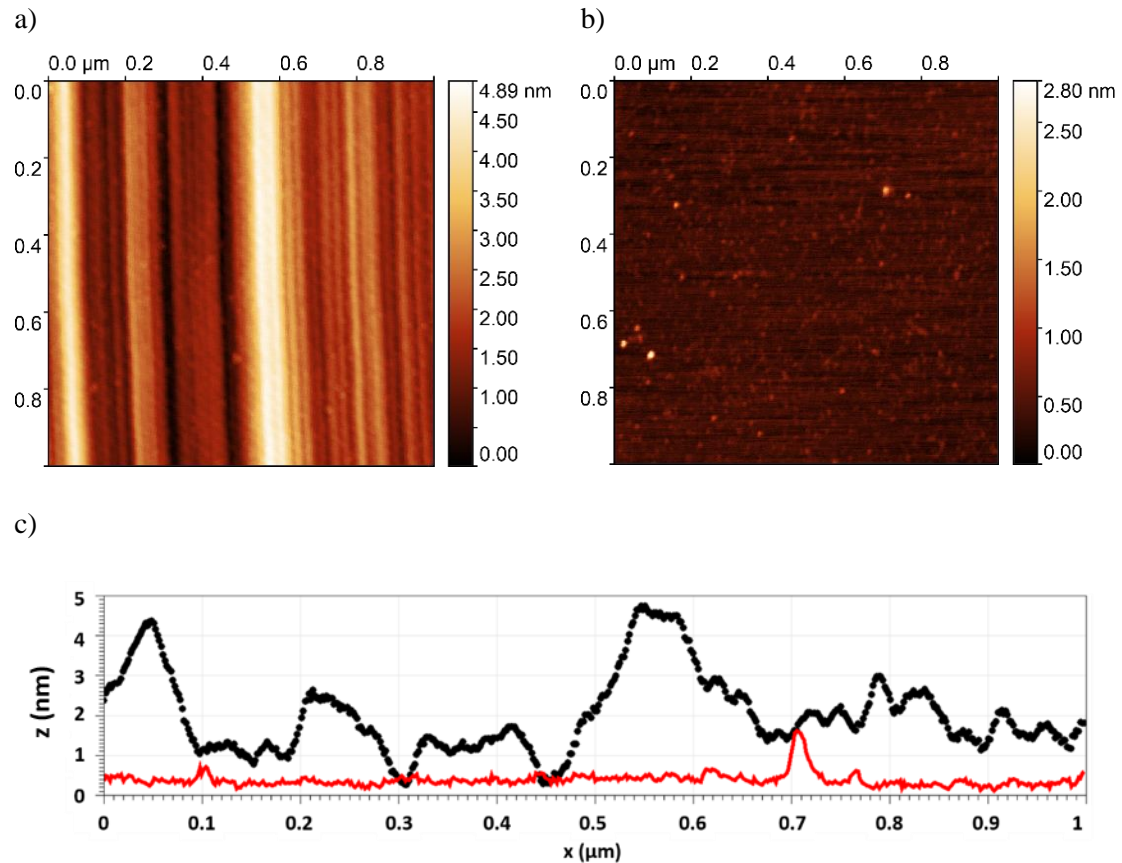


Figure 1.9: $1 \times 1 \mu\text{m}^2$ AFM measurements on (100)-oriented HPHT diamond surface: **a)** As received: polishing patterns are visible as well as some contaminant particles. Root mean square roughness (S_q) value is ~ 1 nm, **b)** After specialized company polishing process: increased homogeneity and lowered roughness values are evidenced ($S_q \sim 0.1$ nm). Some particles can still be found. In **c)** profiles corresponding to image **a)** (black dotted) and **b)** (red line) have been extracted for comparison.

Polishing processes can vary from manufacturer to manufacturer. That is why many researchers choose to derive these processes to specialized companies that guarantee a superior polishing quality or even develop their polishing methods. There are several approaches to diamond polishing and their difficulty and results can vary from one surface orientation to another. Purely mechanical methods are the most widely used for their simplicity. For this, dispersed diamond grains are normally used as the main abrasive material, although grains of other materials such as SiC can also be added. The main drawback of this type of process is the production of a greater degree of superficial and subsurface damage such as dislocations or deformation of the network. Therefore, to improve these processes and reduce damage, other authors opt for approaches through the use of chemical agents (E. L. H. Thomas et al., 2014) or UV irradiation (Watanabe et al., 2013) among others. There is no consensus between which methods are the most appropriate for growth, although quality criteria are usually linked to roughness parameters and the type and density of defects. In this sense, specialized companies often save their polishing recipes for obvious reasons. To illustrate the change in morphology when applying a polishing process, we show in Figure 1.9 the AFM study of the morphology of

a diamond (100) HPHT substrate surface as received after purchase (Figure 1.9(a)) and after the polishing process carried out by a specialized company (Figure 1.9(b)).

It can be seen how the polishing process of the manufacturing company is mainly based on mechanical methods since the polishing lines and direction are clearly visible. It must be said that the polishing direction is of vital importance for efficient polishing. However, this results in a relatively high roughness when compared to the result of the specialized company whose roughness S_q is of the order of hundreds of picometers.

1.4. Unipolar (100) diamond electronic devices

Since BDD growth is the most advanced diamond doping technology, most researchers have based their designs on p-type unipolar architectures, i.e. using holes as majority carriers. This fact has mainly restricted the possibilities to the (100) diamond orientation. The development of unipolar devices is normally simpler than that of bipolar, and therefore the number of factors that must be controlled and evaluated during the manufacture and the device performance results are reduced.

1.4.1. Metal-diamond contacts

Despite being one of the simplest structures for electronic devices in terms of their manufacture, metal-diamond contacts have been one of the first technological challenges in diamond electronics. Its importance lies in its applicability either as an ohmic or as a Schottky contact for electronic devices such as diodes or transistors. The difference between these two types of contacts relies on their electronic behaviour. The thermal-equilibrium energy-band diagram of the metal-semiconductor contact is a key concept to understand the Schottky-to-ohmic electrical behaviour difference.

1.4.1.1. The ideal thermal-equilibrium energy-band diagram: The Schottky Barrier Height

In the energy band diagram of a metal-semiconductor contact before making contact, on one hand, the metal level is defined by its work function, ϕ_M , and on the other hand, the semiconductor, in this case, diamond, is defined by its electronic affinity, χ_S , and its bandgap, E_G . Consider the case in which, before the Metal-semiconductor junction is made, the Fermi level of the semiconductor is below that of the metal (see Figure 1.10 for the p-type diamond example). When the junction is made and thermal equilibrium is reached, the Fermi level of both materials must be aligned. For this to occur, holes from the semiconductor flow into the upper energy states in the metal (Figure 1.10(b)). Then, negatively charged acceptor atoms remain in the semiconductor, creating a space charge region. Depending on the ϕ_M , χ_S , and E_G values, it induces

an energy barrier which is known as Schottky barrier. Thus, in the ideal case, the SBH for p-type devices is defined by the Schottky-Mott rule:

$$SBH = \chi_S + E_G - \phi_M \quad (1.3)$$

Because diamond is a wide band-gap semiconductor ($E_G \sim 5.47$ eV at 300 K) most metals will have a ϕ_M value lower than E_G (only reached by some metals such as platinum). For this reason, in the ideal case and for positive electron affinity (PEA) ($\chi_S > 0$), it is expected the existence of a Schottky barrier for holes for most metals-diamond contacts. For negative electron affinity ($\chi_S < 0$), lower SBH values are expected.

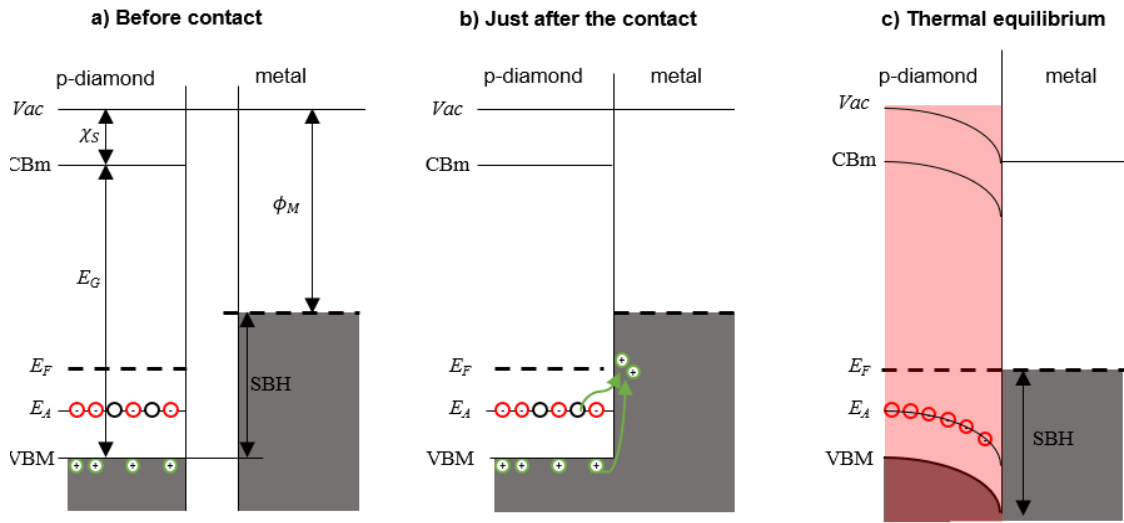


Figure 1.10: Band diagram for the metal/p-type diamond junction Fermi level (E_F) alignment and Schottky barrier formation showing a) before the contact is made: the fermi level of diamond is under that of the metal. Red, black and green circles are ionized acceptors, non-ionized acceptors, and holes in the diamond valence band, respectively. The ideal Schottky barrier height (SBH) can be predicted by putting surface electron affinity (χ_S), diamond bandgap (E_G), and the metal workfunction (ϕ_M) parameters into equation (1.3); b) just after the contact is made: holes from the acceptor level (E_A) and the valence band in diamond migrates towards higher energy position in the metal; and c) in thermal equilibrium: an effective negative charge due to ionized acceptors exists in the diamond interface region generating a space charge region with downward band bending.

1.4.1.2. Ohmic contacts

The ohmic contact is the first challenge to be reached when trying to manufacture electronic devices in a new semiconductor material. This task may not be easy for wide-bandgap semiconductors. From the point of view of the band diagram of the metal-diamond junction, the aim is to eliminate the effect of the Schottky barrier to make the carriers flow completely linear in both polarizations of the contact. Thus, the I/V characteristic of an ohmic contact is described by Ohm's law.

The simpler strategy to overcome this issue passes through the reduction of the SBH. This can ideally be reached by proper choice of the metal (to set the metal work function) and the

control of diamond surface electron affinity. In this case, the lower electron affinity (negative values are preferred) and the higher metal work function are desired.

$$SBH \leq 0 \rightarrow \phi_M - \chi_S \geq E_G \quad (1.4)$$

Thus, once the work function is set, only negative electron affinities will allow to reach or overpass the E_G value getting an SBH equal or lower than 0. In this sense, hydrogen termination has been related to a negative electron affinity (NEA) of ~ 1.3 eV (Diederich et al., 1996; Krainisky & Asnin, 1998; Takeuchi et al., 2005). This fact would ideally give a chance to metals having work functions around or higher than 4.15 eV (e.g. Ag, Al, Au, Cr, Mo, Ni, Pd, Pt, Ti, or W) to eliminate the SBH effect and getting an ohmic behaviour. Unfortunately, the Schottky-Mott rule did not predict correctly the interface behaviour due to other uncontrolled factors. Mainly, the presence of interface defects can fix the Fermi level of the junction (Fermi level pinning) making the SBH independent of the metal work function (F. N. Li et al., 2018) and it is dependent on the diamond surface termination. On the other hand, although the electron affinity has a direct relation to the SBH, it has been observed the modification of the electron affinity during metal deposition (Baumann & Nemanich, 1998a) from hydrogen termination (lower SBH) to fluorine termination (higher SBHs) (F. N. Li et al., 2018). It has been related to the metallization process affecting the pristine surface configuration.

The most used methods of manufacturing ohmic contacts on diamond are based on the narrowing of the Schottky barrier by using heavily BDD layers ($[B] \sim 10^{21} \text{ cm}^{-3}$) in close contact with the metal (Figure 1.11). The main approaches to get it are the boron ion implantation and the CVD growth, being this latter the best option to get better control of the doping and defects formation. It is based on the fact that the space charge width in a rectifying metal-semiconductor contact is inversely proportional to the square root of the semiconductor doping. The width of the depletion region decreases as the doping concentration in the semiconductor increases. Therefore, the higher the doping concentration the higher the probability of tunneling through the barrier is. It means that over a certain doping level, the effective energy barrier for carriers would disappear and an ohmic behaviour is observed.

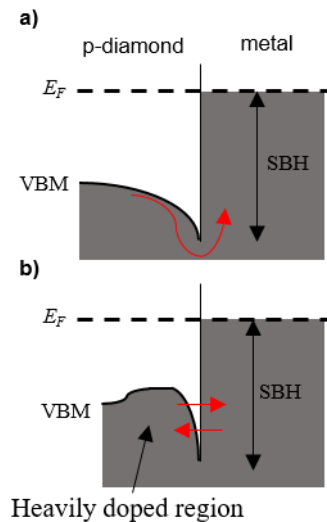


Figure 1.11: Band diagram for the metal/p-type diamond ohmic contact formation by heavily doped layer. a) Schottky contact: the thermionic emission is the dominant current mechanism, i.e. carrier pass over the potential barrier. b) Ohmic contact: a heavily doped layer reduces the Fermi level to valence band distance at the interface region. Then, the Schottky barrier gets narrowed and tunnel emission probability increased. It allows the carriers to pass through the barrier.

Following this principle, the method that has been established as the best option for researchers for ohmic contact fabrication is the one based on a Ti deposition on a heavily BDD layer (Y. G. Chen et al., 2005). This kind of contact presents very low contact resistances, greater stability, reproducibility, and a simple fabrication method. The Ti contact is already ohmic right after its deposition, but after proper annealing, the Ti reacts with the diamond forming a TiC layer that has been associated with greater stability and reduced contact resistance. As already discussed, the hydrogen termination is more suitable for ohmic contacts fabrication not only because it can reduce the electronic affinity to negative values (and thus the ideal SBH) but also because it is expected to generate additional holes on the near-surface region with the consequent effect on the barrier narrowing, analogous to that of boron doping.

1.4.1.3. Schottky contacts

If, for ohmic contact, the approach consists on mitigate the effect of SBH through increased doping, hydrogen termination, or the reaction between metal and diamond; for Schottky contacts, the opposite is sought. Thus, the rectifying character of the contact is desired, i.e. an effective barrier for carriers is necessary. For this reason, the fabrication of Schottky contacts on diamond is normally based on the next concepts:

- **Metals with a low work function:** Ideally lower work functions are related to higher SBH in p-type devices by the Schottky-Mott rule.
- **Metal-diamond reaction avoidance:** The reaction of metals with diamond and the formation of interface metallic carbides has been related to the rise of an ohmic behaviour or the deterioration of the Schottky performance. Thus, refractory metals such as Ti are

not preferred for this application. To avoid this effect, the choice of inert metals, such as gold or platinum; or the deposition of preformed carbides (Liao et al., 2005) are used.

- **Surface termination:** The electronic affinity of diamond is highly dependent on its chemical termination and, for the surface (100), varying from negative values of ~ -1.3 eV for the hydrogen termination (Diederich et al., 1996; Krainisky & Asnin, 1998; Takeuchi et al., 2005) to positive values of up to $+1.7$ eV for oxygen termination (Maier, Ristein, et al., 2001). Since the SBH is ideally dependent on electronic affinity it is inferred that surface termination related to PEA is preferred for Schottky contacts.
- **Doping level:** In the case of Schottky contact, the doping level cannot be so high as to overcome an ohmic behaviour. Thus, normally the doping level is set around 5 or more orders of magnitude lower than for ohmic contacts. This doping level can be obtained when no boron-related gases are introduced during growth. If the growth is performed in a reactor dedicated to p-doping, residual boron in the reactor led to slightly doped layers. This is known as non-intentional doping (NiD). Some Schottky diode architectures can even be based on intrinsic or n-type layers for the Schottky contact (see Section 1.4.2.1), when grown on boron-free reactors.

Even though numerous metals have been tested as Schottky contacts, the results show low reproducibility of the contacts, even for the same manufacturing process and systems. Those critical factors of the process are difficult to monitor since they can have multiple origins making it difficult to identify them separately. Among others, some main factors have been identified by researchers to affect the performance of diamond Schottky contacts:

- **Diamond growth defects:** Generation of defects such as dislocations in the diamond crystal during the CVD growth process is still not perfectly controlled. Thus, defects such as dislocations are normally present on most devices. This is related to negative effects on the behaviour of the device since it implies more favourable energy pathways causing leakage and ineffective Schottky barriers in metal-diamond contacts. This can also hinder the lithography step of the device fabrication.
- **Interface states/Fermi level pinning:** the presence of defects in the interface can generate a density of states in this region that can set the Fermi level of the junction at the defect-related level. This effect is known as Fermi Level pinning and it would explain that the SBH is independent of the metal work function in the diamond contacts.
- **Thermal stability:** The thermal evolution of the contact performance is another key factor since it is expected that they can operate stably at high temperatures. However, it is commonly reported in the literature that the early annealing steps usually improve the performance of the device. Then, above a critical annealing temperature, device

properties degrades. The origin of such behaviour is still controversial and depends on each case. Some authors point to the desorption of oxygen from the diamond surface and to the metal – diamond reaction as possible reasons for this deterioration.

- **Schottky barrier inhomogeneities:** This term is referred to the existence of regions with different SBH in the same contact. It can simply occur as a consequence of different interface defects density, doping, or the presence of diamond bulk defects, among other factors, which are not distributed homogeneously throughout the whole contact region. Remarkably, the presence of defects in some interface regions can be critical and make the effective Schottky barrier of the contact to become considerably lower. This is because these defective regions imply more energetically favourable current paths. This way, the effective SBH of the contact will appear lower by I/V characterization.
- **Schottky barrier lowering:** This is a well-known effect of metal-semiconductor contacts. It consists of the reduction of the effective barrier height as a consequence of the image charges potential generated during carrier transport phenomena. This barrier lowering only occurs when a carrier approaches the interface and therefore will not be noticeable in a capacitance-voltage measurement. Since the barrier height and the barrier lowering will appear in exponential terms in the current-voltage relationship a small change in the SBH can thus have a significant effect on the I/V characteristic.

1.4.1.3.1. Current/Voltage relationship: the ideality factor n

The current transport in a metal-p-diamond junction is mainly due to majority carriers, i.e. holes. The thermionic emission theory describes the transport of holes over the potential barrier. This theory is derived by assuming that the SBH is much larger than kT (where k is the Boltzmann constant and T is the temperature). The forward current density J is a function of the concentration of holes that have velocities high enough to overcome the barrier. According to this model, the forward current density can be described as:

$$J = A^* \cdot T^2 \cdot \exp\left(\frac{-e \cdot SBH}{k \cdot T}\right) \cdot \left[\exp\left(\frac{e \cdot V}{n \cdot k \cdot T}\right) - 1 \right] \quad (1.5)$$

where n , T , e , k , and A^* are the ideality factor, absolute temperature, electron charge, Boltzmann constant, and Richardson constant, respectively. The Richardson constant, A^* , is widely taken as $90 \text{ A} \cdot \text{cm}^{-2} \cdot \text{K}^{-2}$ in the literature (Fiori et al., 2014a; Piñero et al., 2017; Teraji et al., 2014). The ideality factor is a measure of how closely the current fits the ideal current model. In practice, there can be second-order effects so that the current does not follow this equation. Thus, the ideality factor provides a way of detecting these mechanisms. An ideality factor equal to 1 means a perfect fit to the thermionic emission current model while higher values should be identified as other current mechanisms taking place.

1.4.2. Unipolar rectifying diamond architectures

In this subsection, it is intended to globally illustrate the different architecture options that have been explored by researchers and the technologies and strategies on which are based to get unipolar rectifying diamond-based devices. Notice that most architectures include ohmic, Schottky, or metal-insulator-semiconductor (MIS) structures as well as can be based on the hydrogen termination p-type conductivity concept.

1.4.2.1. Diodes

Concerning unipolar diodes, they consist of two terminals devices: ohmic contact and Schottky contact. The ohmic contact is normally based on a Ti contact on a heavily BDD layer. Among the possible architectures it includes:

- **Schottky barrier diode (SBD)** (e.g. (Traore, 2014)): Although the term SBD is the general term for all Schottky diodes architectures, it is also used to refer to those diamond SBD in which a NiD diamond layer ($[B] \sim 10^{16} \text{ cm}^{-3}$) is in contact to the Schottky metal.

Main SBD architectures can be classified based on the relative position of the different terminals as lateral, pseudo-vertical, and vertical (see Figure 1.12). Vertical architectures are the target of many researchers (Umezawa et al., 2013), as it takes better advantage of the properties of diamond for devices. However, it requires high quality and size substrates which, in turn, depends on novel CVD methods normally limited by a very short growth rate. In meanwhile, pseudo-vertical architectures are the most used for research because high crystal quality is obtained from CVD methods and low-cost insulating substrates can be utilized. Lateral architectures, due to their greater simplicity, are interesting to check fundamental aspects of devices and terminal structures (ohmic, Schottky...), but they have no real application potential on power electronics.

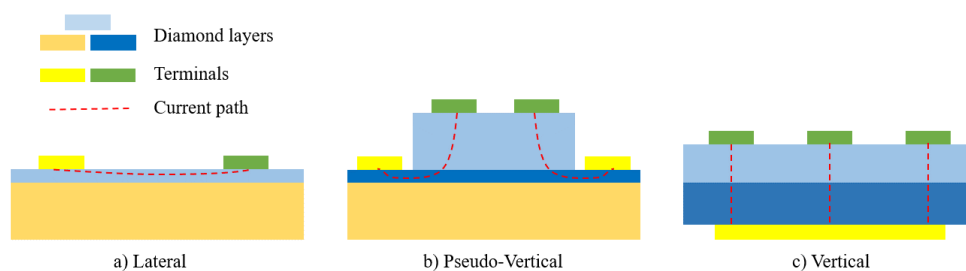


Figure 1.12: Sample device architectures: a) Lateral, b) Pseudo-vertical, and c) Vertical

- **Metal-intrinsic-P-type diode (MiPD)** (Brezeanu, 2007): The MiPD is the same architecture as an SBD but has a much lightly doped layer (ideally intrinsic) in contact with the Schottky metal. This allows the system to take advantage of the extremely high

hole mobility of intrinsic diamond, compensating for the lack of carriers (which come from the heavily doped layer of the ohmic contact) and getting an acceptable conductivity.

- **Schottky PN diode (SPND)** (Makino et al., 2009; T. Matsumoto et al., 2017): The SPND is composed of a lightly doped n-type layer placed in contact with the Schottky metal. The key structure of the SPND is the fully depleted n-type active layer. The concept is similar to the M-i-P diode but an n-type diamond layer is used as intrinsic material instead of p-type.

1.4.2.2. Field-effect transistors

Concerning FETs, it consists of a three-terminal device: drain, source, and gate. The gate gets control of the conduction between the other two terminals by the application of an electric field. P-type FETs can be classified based on the gate terminal structure as:

- **MESFET** (Metal–semiconductor FET), (see (Umezawa, 2018) and references therein): is a FET in which the gate consists of a Schottky junction.
- **MISFET** (This term includes MOSFET): In this case, the gate of the FET consists of a MIS capacitance. The insulator layer is usually an oxide with a high dielectric constant such as Al_2O_3 , or intrinsic/n-type diamond.

Other architectures classification refers to the channel type, although they are normally based on MES or MIS structures as a gate terminal. The main types of channels are:

- **Boron doped channels:** this type of channel includes any FET architecture in which a BDD is required. It includes the next specific case:
 - **δ -channel:** The delta doping concept consists of a very thin layer of heavily BDD ($[\text{B}] \sim 10^{20} \text{ cm}^{-3}$) placed between two undoped layers. Thus, the conduction due to holes of the δ -layer is expected to mostly occur through the undoped layers. This architecture has high potential but requires great control on the CVD growth process so it has still not been materialized. The FET based on this concept is known as δ -FET.
- **Surface channel (SC):** When the diamond surface is terminated by hydrogen, a p-type surface conduction appears. The high hole concentration and the low activation energy make it proper as a channel for FET architectures. These architectures are known as SC-FET or H-FET.

1.4.3. Diamond device fabrication overview

Diamond electronic device architectures typically include most of the following fabrication steps:

1. **Manufacture/choice of the substrate:** Although the manufacture of the HPHT substrate is usually carried out by a specialized company, there is usually a selection process by the device manufacturer, which chooses those substrates that best suit its design, mainly evaluating the presence and level of defects and impurities.

2. **Diamond surface polishing** (see Section 1.3.3.5): This step is mostly recommended when the selected bulk substrate does not offer an acceptable surface morphology. It can also be used for the fabrication of vertical devices. The chosen polishing method is important as it decides the final level of surface and subsurface defects, as well as the roughness of the surface.

3. **Cleaning:** The cleaning process is of vital importance to avoid the presence of contamination on the surface, which can modify the quality of the CVD growth stages or the depositions of other materials. They usually involve at least a cleaning process in a hot mixture of acids, an ultrasound bath process in acetone, ethanol, and/or isopropanol, or a drying process with inert gases under pressure, typically Ar.

4. **Growth:** CVD growth is one of the most important processes in device manufacturing. During this process, many of the properties of the device are decided. The density of defects and the level of doping are the main parameters to evaluate their quality.

5. **Etching:** It is usually necessary when there are terminals in the device linked to different layers of diamond. Since selective growth is still a technological challenge to be solved (Lloret et al., 2021), this type of process is necessary to reveal previous growth layers where terminals can be then manufactured. These processes are performed with the aid of masks to select etching regions and again lead to a modification of the surface morphology that is not very controllable (Toros et al., 2020).

6. **Surface termination treatments:** Surface termination treatments are important for modulating the electronic properties of surfaces in favour of a specific application. For example, the hydrogen termination generates surface conductivity while the oxygen termination is related to the passivation of the surface. Among the hydrogenation treatments, the H₂ plasma stands out, and the VUV/ozone treatment or the hot acid treatment for oxygenation treatment.

7. **Depositions:** Deposition of other materials on diamond is one of the last steps in the manufacturing process. Metal deposition is necessary to make ohmic or Schottky contacts, either on the diamond itself or on other insulating materials previously deposited on it, e.g. oxides. For the deposition of metals, various sputtering methods are mainly used and masks are used to define the shape and position of the contacts. On the other

hand, for the deposition of oxides and nitrides, the atomic layer deposition technique is usually used due to its ease and low cost.

The need for each of these steps and their sequence during manufacturing depends on the design of the device, its architecture, and the methodologies to be applied in each step. Thus, some of the steps such as depositions are usually repeated in the same manufacturing process. Of course, there are interdependencies between the various manufacturing processes that affect the quality of the subsequent steps and, consequently, the quality of the final device. For example, if the HPHT substrate has a high density of dislocations, a proper polishing process is not applied, or a satisfactory cleaning is not performed, the overgrown CVD layer will surely be adversely affected.

Chapter 2:

Materials and methods

Samples preparation descriptions and definitions, as well as main experimental techniques and procedures, are described in this second chapter. Special attention is focused on certain aspects of photoelectron spectroscopy and its related modes as it is the core characterization technique of the thesis.

The chapter is divided into the next sections:

2.1. Experimental techniques and procedures

2.2. Samples description

2.1. Experimental techniques and procedures

2.1.1. Atomic Force Microscopy (AFM)

Atomic force microscopy consists of a cantilever with a very sharp tip at its end that is used to scan a sample surface. When the tip is close enough to the surface, the forces between tip and sample cause the deflection of the cantilever according to Hooke's law. This deflection can be measured by different methods depending on the working mode. The AFM can be operated in many modes, depending on the application. In general, possible imaging modes are divided into static or contact modes and a variety of dynamic (non-contact or "tapping") modes. An AFM system diagram is shown in Figure 2.1.

The tapping mode is a non-contact AFM mode with application in measuring soft samples. By this mode, the cantilever is driven to oscillate up and down at either its resonant frequency (frequency modulation) or just above (amplitude modulation) where the amplitude of oscillation is typically a few nanometers (<10 nm) down to a few picometers. Van der Waals forces, dipole-dipole interactions, electrostatic forces, etc., act to change the resonance frequency of the cantilever. This change in resonant frequency, combined with the feedback loop system, maintains a constant oscillation amplitude or frequency by adjusting the average tip-to-sample distance. Measuring the tip-to-sample distance at each data point allows the scanning software to build a topographic image of the sample surface. The most common method for cantilever-deflection measurements is the beam-deflection method. In this method, a laser beam light from a solid-state diode is reflected off the back of the cantilever and collected by a position-sensitive detector (PSD), consisting of two closely spaced photodiodes, whose output signal is collected by a differential amplifier. The angular displacement of the cantilever results in one photodiode collecting more light than the other photodiode, producing an output signal (the difference between the photodiode signals normalized by their sum), which is proportional to the deflection of the cantilever.

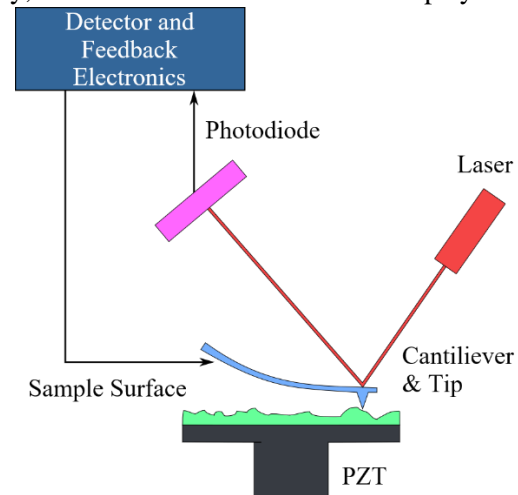


Figure 2.1: AFM set-up scheme

Both lateral and vertical resolution must be considered. The former is highly dependent on the quality of the tip and its radius of curvature and the latter is typically below 1 nm. One of the main disadvantages of this technique is that the measurement areas are small when compared to other techniques such as SEM. However, its sensitivity and reliability, in addition to its

simplicity, is remarkable. Good optimization of the configuration parameters is necessary even more when diamond surfaces are expected to have a very low roughness.

Using this technique, the roughness parameter or the presence of surface defects can be analysed. This analysis is made by the open-source software Gwyddion (Nečas & Klapetek, 2012). The digital roughness parameters considered to characterize the surfaces are mainly the following:

- Arithmetic average roughness, S_a : S_a is one of the most effective surface roughness measures commonly adopted in general scientific practice. It gives a good general description of the height variations in the surface. It is defined as:

$$S_a = \frac{1}{N} \sum_{k=0}^{N-1} |z_k - \bar{z}| \quad (2.1)$$

where z is the height of the k -th point, \bar{z} is the z mean value and N is the number of data points.

- Root Mean Square roughness, S_q : The Root Mean Square (RMS) roughness (S_q) is the root mean square average of the roughness profile ordinates.

$$S_q = \sqrt{\frac{1}{N} \sum_{k=0}^{N-1} (z_k - \bar{z})^2} \quad (2.2)$$

2.1.2. X-ray photoelectron spectroscopy (XPS)

X-ray photoelectron spectroscopy is a powerful technique for chemistry and compositional characterization as well as for the analysis of electronic phenomena such as the estimation of surface band bending, SBH of a metal-semiconductor contact (Kono et al., 2015; F. N. Li et al., 2016), or the heterojunctions band-offset (Cañas et al., 2020).

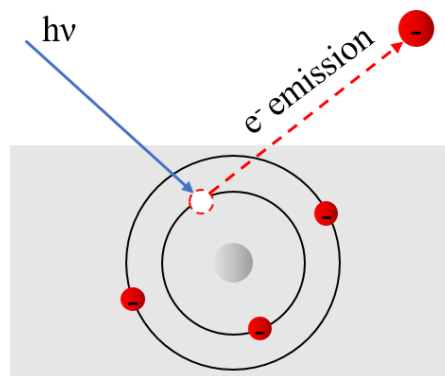


Figure 2.2: Schematic of the principle of XPS technique: the photoelectric effect. Electrons of sample atoms are emitted as a consequence of an incident X-ray excitation.

This technique is based on the photoelectric effect and consists on the excitation by an X-ray beam of the electrons in the sample under study (see Figure 2.2). During the XPS experiment, the KE of the extracted electrons is measured. The energy conservation equation of the process can be expressed as:

$$h\nu = BE + \varphi_{spectrometer} + KE + eV_{charge} + eV_{bias} \quad (2.3)$$

where h is the Planck constant, ν is the frequency of the photon, BE is the binding energy relative to the Fermi level of the system, KE is the kinetic energy measured in the spectrometer, $\varphi_{spectrometer}$ is the work function of the spectrometer, V_{charge} is the charge potential that can occur at the measured surface if the secondary electron current is not compensated and V_{bias} is a potential that can be used between the sample and the spectrometer (also called pass energy) and serves to filter electrons in a specific energy range. In the ideal case, in which other effects are negligible, the values of $\varphi_{spectrometer}$, V_{charge} , and V_{bias} are known or negligible and thus, the KE measured becomes accurate. Since the energy of the source is known (e.g. Al- $\kappa\alpha$: $h\nu = 1486.6$ eV) the measured KE values can be converted to BE values by

$$BE = h\nu - KE \quad (2.4)$$

X-rays are generated by bombarding a metallic anode with high-energy electrons. The energy of the emitted X-rays depends on the anode material, while beam intensity depends on the electron current to the anode. X-rays emitted from the anode are intercepted by a quartz crystal. A monochromatic beam of X-rays is then focused onto the sample. The most used source radiations in the laboratory are Al- $\kappa\alpha$ and Mg- $\kappa\alpha$ with 1486.6 eV and 1253.6 eV photon energy, respectively. The range of photon energies allows the analysis of elements core-levels as well as valence band contributions. However, for the analysis of the latter, lower photon energies in the range of UV are recommended. Other electron transitions such as Auger effect also results in the emission of electrons. The lighter the element the higher the probability of Auger transition to occur is. For this reason, this kind of contribution is always detected in diamond samples. The KE of Auger electron emissions is independent of the source energy what can be useful to discern it from core-level contributions. The analysis of these contributions is framed within the Auger electron spectroscopy what is out of the scope of this text.

2.1.2.1. Depth sensitivity

The depth sensitivity of XPS is mainly limited by the inelastic mean free path of electrons λ , which defines the average distance an electron can travel through a solid before losing energy. This parameter is dependent on the KE of the escaping electron and the material through which the photoelectrons are traveling. The diamond inelastic mean free path has been estimated

theoretically (Shinotsuka et al., 2015). However, the theoretical values tend to underestimate the experimental values. For an Al- $k\alpha$ energy source and the C 1s core-level electrons, the λ value has been estimated as 2.4 nm (Kono et al., 2009) while the theoretical value is in the range of 1.76-1.9 nm.

Thus, the electron escape probability $P(z)$ is ruled by the Beer-Lambert Law as:

$$P(z) = e^{\frac{-z}{\lambda \cdot \cos\theta}} \quad (2.5)$$

where θ is the electron escape angle with respect to the surface normal (polar angle), λ is the inelastic mean free path of electrons and z is the distance to the sample surface. The sensitivity depth in the photoelectron spectroscopy can be mainly modified by three approaches:

- 1) By using different source energies because it would modify the KE of escaping electrons and, in turn, the λ value;
- 2) by analysing different core-levels of the same element. The escaping electrons have different KE and thus, are related to different depth positions; and
- 3) by modifying the polar angle value θ .

The first approach is possible in tuneable energy sources such as synchrotron X-ray sources or multi-anode sources. The second approach is not possible in diamond since only C 1s core-level is detected in carbon-based materials but can be used to analyse other elements such as aluminum or tungsten. The third approach is known as angle-resolved XPS (ARXPS) and can be applied in those systems that allow tilting of the sample holder or the detector column angle. This approach is detailed in Section 2.1.2.6.

2.1.2.2. Peak intensity and relative intensity

Notwithstanding, other factors must be considered in a real XPS experiment. Thus, an XPS signal intensity differential can be described theoretically as:

$$dI_{XPS} = S \cdot F \cdot T(KE) \cdot N_1 \cdot \sigma \cdot P(z) \cdot dz \quad (2.6)$$

where S is the analysed region area, F the photon flux, T is the analyzer transmission as a function of KE , N_1 is the density of atoms per volume unity, σ is the photoionization cross-section, z is the depth measured from the surface, S is the analysed region area, and the term $P(z)$ corresponds to equation (2.5).

In this line, there are peak intensity estimation methods that require knowledge of the multiple common and specific factors of XPS systems. Without controlling for all these factors, it is possible to assess the relative intensity of various contributions. This is because all the factors that are assumed to be common to all contributions (S , F ...) would be nullified from the

expressions of relative intensity. Based on this principle, multilayer surface models can be applied, which have been frequently used to estimate the thickness of surface layers such as metallic oxides (Bernstein & Grepstad, 1989). In Section 3.2.3 this principle has been applied for the quantification and calculation of the thickness of layers on the diamond surface.

2.1.2.3. Peak position

The energetic position of a given contribution depends on the energy level that the electron occupies before escaping. Several factors can modify the energetic position of electrons. First of all, in solids, the energy levels of electrons are affected by their interaction with those of their environment, which defines what is known as its chemical environment. It depends mainly on the structure and composition of the solid. In this way, for example, it is intuitive to think that the energy level of the electrons in the C1s orbital will be different in diamond and graphite. This is so because the chemical environment of the carbon atoms in both materials is different, producing different shields in the electrons of the C1s orbital, which is reflected in the spectrum as an energetic distance between the two contributions. Estimating this energy distance can be a complex calculation. However, in simple cases, it can be intuited whether one contribution will have a higher or lower *BE* than another. To do this, the concept of electronegativity is very useful. If an isolated atom of a specific element combines with another more electronegative, this element will attract more the surrounded electrons, reducing the shielding suffered by the C1s level of the carbon atom, and, therefore, raising this energy level. Based on this reasoning, it can be intuited that the contributions of C1s from the Si-C, W-C, C-C, C-N, C-O, and C-F molecules will be distributed on the *BE* axis in the same order, from lowest to highest, which agrees with the experimental results. Since carbon electronegativity depends on its hybridization as $\chi(\text{sp}) > \chi(\text{sp}^2) > \chi(\text{sp}^3)$, it can be deduced that C-C (sp^2) contributions will appear at lower *BE* than C-C (sp^3). This can be extrapolated to graphite and diamond contributions, respectively.

On the other hand, because this energy level is estimated relatively through the *KE* of the electron when it reaches the detector, any variation of *KE* in its escape path would change the perceived energy position. In insulators materials, the sample surface normally tends to acquire a positive potential and the *KEs* of the escaping electrons are decreased by the same amount. To correct it, charge compensation methods (neutralizers) such as electron flux are often used.

The band bending is another effect to consider. Whatever its origin, it causes all the energy levels of the band bending region to be distributed in the *BE* axis accordingly. This effect is developed as a necessary part of the analysis of the H-terminated surface (Section 3.1.4.).

2.1.2.4. XPS spectra analysis overview

The analysis of an XPS spectrum is normally divided into the next steps:

- Analysis of the Survey spectrum:
 - Identification of the main peaks by using the Survey spectrum.
 - Survey spectrum background subtraction
 - Preliminary quantification of elements.
- Analysis of the relevant core-level spectra (C1s, O1s, and the valence band for diamond).
 - Identification of the main components in each core-level spectrum.
 - Background subtraction: mainly used the Shirley (Shirley, 1972) or the Tougaard (Tougaard, S.; Simund, 1982) models.
 - Peak deconvolution: For the peak deconvolution, the Voigt distribution for fixed energy level is normally used. It is defined as the convolution of a mixed Gaussian–Lorentzian distribution where the Lorentzian component is related to the lifetime broadening of electrons (Graupner et al., 1998).
 - Surface model application and quantification: this step depends on the sample geometry, composition, and microstructure.

2.1.2.5. Energy references

When measuring electronic effects such as changes in *BE* (chemical shifts) and changes in photoelectron shape due to chemical-compound formation or band bending effects as well as the determination of metal-semiconductor SBH or heterojunction band offsets, it is necessary an energy reference for a more precise analysis. This reference can be, among others, any core-level, the fermi level, or the valence band maximum as long as it is known to remain constant during the experiment. For those samples in which no fixed energy levels are expected, an external metallic reference such as a gold deposition in electric contact to the system (Kraut et al., 1983) is normally used.

2.1.2.6. Angle-resolved XPS (ARXPS)

Angle-resolved XPS is based on the possibility of tuning the polar angle θ of an XPS experiment. Normally, the θ value is selected by tilting the sample holder with respect to the photoelectron detector column (see Figure 2.3). Thus, the photoelectrons escaping at other polar angles than normal to the surface can be aligned to the detection column direction. The angle between the incident X-ray beam and the photoelectron detection column remains fixed.

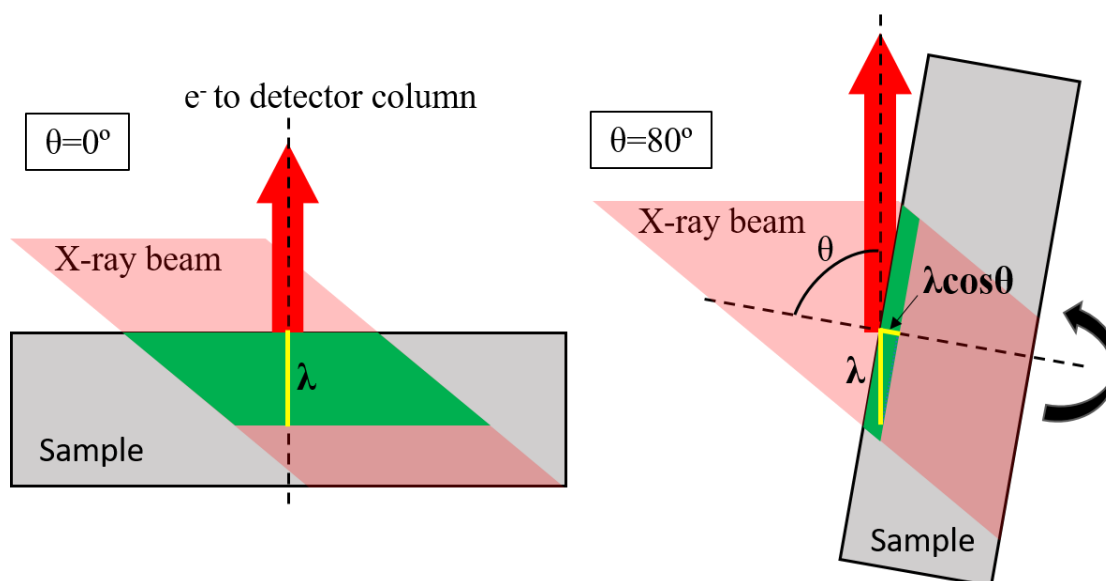


Figure 2.3: ARXPS set-up scheme as proceeded in Chapter 3 for samples #H and #O (See Section 2.2.1). The angle between the X-ray beam and the detection column is constant. Polar angle θ is the angle between the sample normal and detector column is obtained by tilting the sample stage. An electron that can escape from the sample by traveling an average distance λ in the detector column direction can ideally come from the same depth λ as maximum for $\theta = 0^\circ$. For different θ values, the same electron will escape from a reduced maximum depth equal to $\lambda \cos\theta$. The region from which electrons can escape by traveling a distance λ to the detection column is green.

Figure 2.4 represents the variation of the probability of escape of electrons with angle as well as the 99%, the 50%, and the $\lambda \cos\theta$ probability curves. The λ of diamond has been set to 2.4 nm (Kono et al., 2009) and the refraction effect has been taken into account (see next subsection for details). It can be observed that for $\theta = 0^\circ$ photoelectrons can escape from a depth as high as 10 nm ($P < 99\%$), while for $\theta = 80^\circ$ this depth is reduced to 2 nm. Therefore, the higher the polar angle the lower the depth sensitivity. The $P(z) < 50\%$ curve represents the depth from which half of the photoelectrons escape. Since $P(z)$ follows an exponential curve, the $P < 50\%$ is much closer to the surface than the $P(z) < 99\%$. On the other hand, the $\lambda \cos\theta$ probability curve is commonly used in the literature for easy estimation of depth sensitivity. However, interpreting the escape probability as a fixed depth value is still a simplification. In this sense, note that the $P(z) < 50\%$ curve is very close to the $\lambda \cos\theta$ curve.

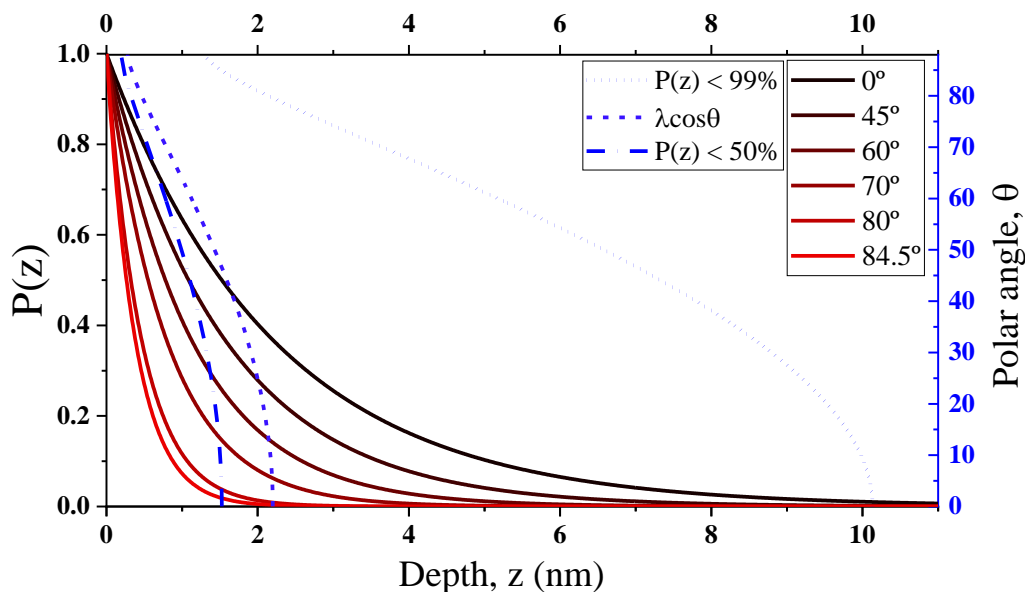


Figure 2.4: Depth sensitivity estimation of ARXPS measurements in diamond for the present work conditions. The graph shows the electron escape probability $P(z)$ of C1s photoelectrons (left Y-axis) versus depth for different polar angles (solid lines) and the $P(z) < 99\%$, $P(z) < 50\%$, and $\lambda \cos\theta$ depth curves (discontinued lines) versus polar angles (right Y-axis). $P(z) < 99\%$ is an estimation of the maximum depth sensitivity while $P(z) < 50\%$ represents the depth from which half of the total signal is generated. The $\lambda \cos\theta$ value is useful to extract a rapid approximation of the depth sensitivity. The refraction effect is taken into account which becomes not negligible when the polar angle increases.

2.1.2.6.1. The refraction effect

The photoelectron refraction effect must be also taken into account, as it can be significant at higher polar angles. This effect makes detected photoelectrons come from lower angles of escape than the angle defined here as polar angle, reducing the depth sensitivity. An angular correction is included in the algorithm based on equation (2.7) (Fadley, 1984) where θ' is the angle inside the sample, V_i is the inner potential that has been estimated to be ~ 18 eV elsewhere (Kono et al., 2009) and KE is the kinetic energy of photoelectrons inside the sample.

$$\tan(90 - \theta) = \frac{\sqrt{\sin^2(90 - \theta') - V_i/KE}}{\cos(90 - \theta')} \quad (2.7)$$

2.1.2.7. XPS depth profiling

XPS depth profiling is used to refer to the use of an ion beam to etch layers of the surface or surface contamination on a given XPS experiment, revealing subsurface information. The combination of ion gun etch cycles with XPS analyses provides quantified information on a depth profile. The sequence of etching and spectrum acquisition is repeated until profiling has proceeded to the required depth. An XPS depth profile procedure scheme is given in Figure 2.5. Some key parameters must be considered by researchers in such experiments:

- Surface roughness: The surface roughness of the original sample will affect the depth resolution and it will remain similar during the whole experiment.
- Beam energy: High energy ion is preferred for speed while low energy gives a better depth resolution.
- Incident angle: Grazing angles are preferred for smooth samples.
- Ion mass: At a given energy, the larger the ion the shorter its depth range within the sample, which will result in improved depth resolution.
- Azimuthal rotation (Zalar rotation (Zalar, 1985)): the sputtering process can cause topography or roughness to appear during a profile and degrade the depth resolution. This effect is overcome by rotating the sample (azimuthal rotation) during the sputtering steps.
- Sputtered area and analysis area: Analysis area must be small compared with crater size and well centered within the crater.
- The sputter yield: determines the rate at which material is removed from the sample during a depth profile expressed as a (number of atoms removed/number of incident ions). It depends on the following factors: material, ion energy, incidence angle and mass, and nature of the primary ion.
- Redeposition/reabsorption: Some removed material could be redeposited or reabsorbed during the recording steps what would modify the real sample data.

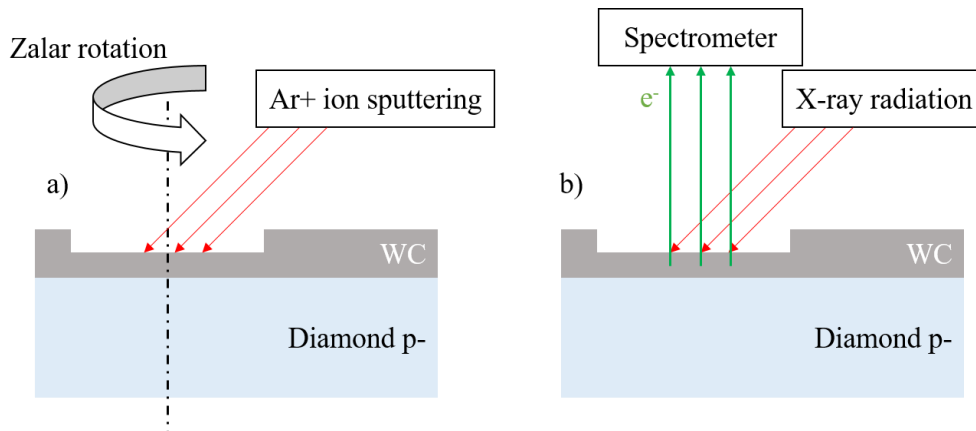


Figure 2.5: XPS depth profile set-up scheme as proceeded in Chapter 4 for sample #WC (see Section 2.2.2): a) the sample is bombarded by Ar⁺ ion gun. During this step, Zalar rotation is activated. b) the sample is then irradiated with an X-ray beam. Some excited electrons can escape from the sample towards the spectrometer to be detected.

2.1.3. Transmission electron microscopy (TEM)

In Transmission electron microscopy (TEM) a beam of electrons is transmitted through an ultra-thin specimen, interacting with the specimen as it passes through the solid matter. An image is formed from the interaction of the electrons transmitted through the specimen; the image

is magnified and focused onto an imaging device. The main TEM techniques used during this thesis were:

- (i) **Bright-field (BF) and High-Resolution TEM (HRTEM):** BF forms the contrast in the image directly by the occlusion and absorption of electrons in the sample. Its name comes from the fact that regions with no sample in the beam path appear bright while regions with a high atomic number will appear dark. When magnification is very high and the crystal orientation such as a proper zone axis is parallel to the optical axis, it is possible to see atomic columns and high resolution is obtained. For this, interferometry of transmitted and diffracted beams is required.
- (ii) **Scanning transmission electron microscopy (STEM):** The images are formed by scanning the surface of the samples by a probe, that is, the image is formed point by point as the probe sweeps the surface of the sample. In this image, each pixel is formed from the transmitted or diffracted electrons that are generated by striking the electron beam on an area of the surface that is being scanned. The output signal can be collected by many different detectors. Thus, depending on the type of detector used for this, various methodologies are defined.
 - a. **High-Angle Annular Dark-Field (HAADF) STEM:** One of the main advantages of a STEM microscope is that various analysis techniques can be used together. Among them, the so-called HAADF or "Z contrast", uses a detector with an annular geometry that collects the scattered electrons at high angles; generates an image that is directly related to the atomic number Z, specifically, its intensity is considered proportional to the square of the atomic number of the elements present in the analyzed material
 - b. **Energy-dispersive X-ray spectroscopy (EDX):** is an analytical technique used for the elemental analysis or chemical characterization of a sample based on STEM mode. The incident beam (electron beam in a TEM system) may excite an electron in an inner shell, ejecting it from the shell while creating an electron-hole pair where the electron was. An electron from an outer, higher-energy shell then fills the hole, and the difference in energy between the higher-energy shell and the lower energy shell may be released in the form of an X-ray. The number and energy of the X-rays emitted from a specimen can be measured by an energy-dispersive spectrometer. As the energies of the X-rays are characteristic of the difference in energy between the two shells and of the atomic structure of the emitting element, EDX allows the elemental composition of the specimen to be measured.

2.1.4. TEM samples preparation by Focus Ion Beam (FIB)

To carry out the characterization of the diamond-based structures through TEM-based techniques, it is necessary to obtain a representative fraction of them. For this, it is required to use thinning techniques that allow the thickness to be reduced to electron transparency. Due to the highest known hardness of diamond, conventionally known techniques cannot be applied in most cases and Focused Ion Beam dual-beam SEM (FIB-SEM) is required to obtain electron-transparent diamond including samples. The protocol for lamella fabrication is described elsewhere (Piñero, 2016).

2.1.5. Experimental procedures by section

Following, the experimental procedures in this thesis are described:

- Chapter 3: XPS studies of (100) diamond surface terminations
 - Samples: The samples for Chapter 3 are described in Section 2.2.1.
 - ARXPS experiments: These experiments were carried out in a Kratos Axis Ultra DLD spectrometer (Kratos Analytical, Manchester, UK) at UHV and RT with an Al- α radiation source (1486.6 eV) with an accuracy of 0.1 eV and an energy pass of 20 eV. This equipment is located at the “Servicios Centrales de Investigación Científica y Tecnológica” (SC-ICyT) of the University of Cadiz. In this system, the stage needs to be tilted to achieve the required polar angle. The angle between the X-ray beam and the detection column remains constant. A charge neutralizer based on a flood gun of low-energy electrons was used to avoid charge effects. Spectra were recorded for different electron polar angles ranging from $\theta = 0^\circ$ to 84.6° . A charge neutralizer based on a flood gun of low-energy electrons was used to avoid the charge effect. The background was subtracted using the Tougaard model. Peak deconvolution was carried out in MATLAB R2018b software (The MathWorks, Inc., Natick, MA, USA) and/or OriginPro software (version 8, OriginLab Corporation, Northampton, MA, USA). The spectra were calibrated versus the Au4f7/2 peak located at 84.0 eV.
- Chapter 4: Tungsten carbide/diamond interfaces for Schottky barrier diodes
 - TEM/STEM analysis: TEM lamellas were prepared by FIB lift-off method to get electron-transparent specimens using an FEI-FESEM-FIB Helios Nanolab 650 located at the Universidad de Málaga. HRTEM experiments were carried out in an FEI-Titan 3 Themis at 300 kV at the SC-ICyT of the University of Cadiz (FEI-(Field Electron and Ion Company, 5350 NE Dawson Creek Dr, Hillsboro, OR 97124, U.S.A))

- XPS depth profile: It was carried out on a PHI VersaProbe II system in UHV conditions. This system is located at the University of Malaga. The sample was irradiated using a monochromatic Al-K α radiation source ($h\nu = 1486.68$ eV) on a window of 50 μm diameter. The sample corresponds to #WC and is described in Section 2.2.2. It was mounted on an XPS holder by using metal adhesive plates. The sample surface was also connected to the holder through the lateral sides of the substrate to avoid charging effects during XPS measurements. Pass energy was set up to 23.5 eV. Charge neutralization was carried out by a dual-beam of low-energy electrons and low-energy ions. For the Ar $^+$ ion sputtering, the energy of 0.5 kV was used. Ar $^+$ ion direction was set to 30 $^\circ$ with respect to the surface normal covering a 500x500 μm region. Zalar rotation with axis normal to the surface was activated. The atomic concentrations were calculated from the photoelectron peak areas using Tougaard background subtraction and sensitivity factors provided by the spectrometer manufacturer PHI (Physical Electronics, 6509 Flying Cloud Drive, Eden Prairie, MN 55344, U.S.A.).

2.2. Sample description

Samples have been classified corresponding to the main topics in the thesis. Thus, two samples labeled as #H and #O, are used for the surface characterization, and another one, labeled as #WC, is related to interface characterization. The sample fabrication procedures are given below.

2.2.1. Samples for surface characterization

For both #H and #O samples, the same 3x3 mm 2 diamond (100)-oriented type IIa substrate from the New Diamond Technology (NDT) (Saint Petersburg, Russia) company was used. Diamond supplier commonly applies a polishing step that results in a surface roughness too high to be considered for the XPS experiment. To get a flatter and more homogeneous surface, as received substrate was submitted to an extra polishing step made by Syntek company (Yokohama, Japan). Surface morphology was then evaluated by AFM in an AFM-VEECO-NSIV system working in tapping mode. This system is located at the Insitut Néel (Grenoble, France). Several measurements were carried out in a central region of the sample by using a 5x5 μm window each time. *Gwyddion* software has been used for data analysis (Nečas & Klapetek, 2012). From the combined analysis of all recorded measurements, surface roughness parameters $S_q = 0.2$ nm and $S_a = 0.13$ nm were deduced.

Table 2.1: Summary of the #H and #O samples fabrication description.

Sample label	Related Section	Substrate	Size (mm ²)	Extra polishing	Cleaning	Surface treatment 1	Surface treatment 2
#H	Section 3.1	NDT (IIa) (100)	3x3	Syntek polishing	Hot acid mixture + acetone, ethanol, isopropanol ultrasound bath + Ar gas flow dry	H ₂ plasma	X
#O	Section 3.2						Hot acid mixture

The cleaning process was as follows: first, was immersed in a hot acid mixture HClO₄:H₂SO₄:HNO₃ (1:3:4) for 2 hours. The temperature of the heating platform was adjusted to 450° C. Then it was consecutively submitted to acetone, ethanol, and isopropanol ultrasound bath for 5 min each. Finally, the substrate was dried by Ar gas flow and stored in room conditions.

H₂ plasma was performed in a NIRIM type reactor at the Institute Néel (Grenoble, France) using a microwave power of 260 W, at a pressure of 30 Torr, a gas H₂ flow of 200 sccm, and a temperature of ~800 °C for 2 hours. The surface was analogously again evaluated by AFM after H₂ plasma showing a final $S_q \sim 0.12$ nm and $S_a \sim 0.09$ nm.

Finally, the H-terminated sample was submitted again to a final hot acid mixture to obtain the O-terminated diamond surface. AFM measurements showed an increasing roughness from $S_q \sim 0.12$ nm and $S_a \sim 0.09$ nm (after the H₂ plasma) to $S_q \sim 0.3$ nm and $S_a \sim 0.12$ nm (after acid treatment).

2.2.2. Samples for interface characterization

Table 2.2: Summary of the #WC sample fabrication description.

Sample label	Related Section	Substrate	Size (mm ²)	Polishing	CVD Growth	Ohmic contacts	Surface treatment	Schottky contacts
#WC	Chapter 4	Sumitomo (Ib) (100)	3x3	Syntek 3° miscut along [110]	3 μm thickness [B] ~ 10 ¹⁵ cm ⁻³	Ti/Au Ø ~ 500 μm e-beam + Annealing 800 K 1h	VUV/Ozone 30 min RT	WC 1:1 Ø ~ 400 μm Magnetron Sputtering

The fabrication of WC/O-terminated diamond SBD was carried out at NIMS (Tsukuba, Japan) (Figure 2.6). First, a diamond BDD NiD epilayer of $3\ \mu\text{m}$ ($[B] \sim 10^{15}\ \text{cm}^{-3}$) was grown in a microwave plasma-enhanced CVD reactor on a $3 \times 3\ \text{mm}^2$ diamond (100)-oriented Ib-type substrate with a 3° miscut angle along [110] direction. Circular contacts of $500\ \mu\text{m}$ diameter that consist of a stack of $20\ \text{nm}$ Au over $20\ \text{nm}$ Ti were deposited at the four corners of the p- layer surface by e-beam and annealed under vacuum at $\sim 800\ \text{K}$ for 1 h. Afterward, the surface was oxidized for 30 min by a VUV/ozone treatment at RT. Finally, $1:1$ stoichiometric $50\ \text{nm}$ WC contacts were deposited through a metallic shadow mask by conventional magnetron sputtering with a base pressure under $10^{-6}\ \text{Pa}$. The thickness of this layer was confirmed by TEM. The ohmic behaviour of Au/Ti/diamond contacts was proved by I/V measurements. WC contacts electronic performance was also characterized after each annealing step based on temperature increasing sequence under vacuum to prove the thermal stability of the contact performance. A Schottky behaviour was evidenced and improved by the annealing process up to $600\ \text{K}$. The results of the electrical characterization were previously published elsewhere (Fiori et al., 2014a).

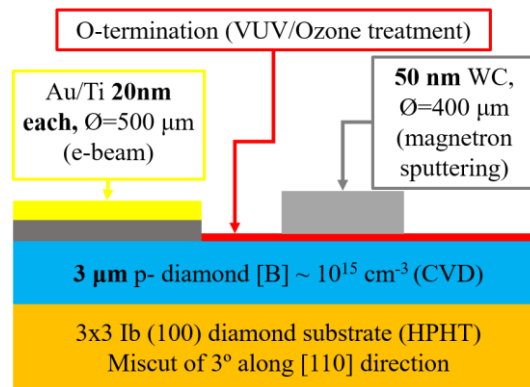


Figure 2.6: Schematic cross-section view of the WC/O-terminated diamond SBD architecture.

Chapter 3:

XPS studies of (100) diamond surface terminations

In this chapter, the two main chemical terminations applied to the fabrication of diamond-based electronic devices under discussion are discussed. (100)-oriented O-terminated and H-terminated diamond surfaces are analysed by ARXPS to revise some of the most relevant diamond surface topics: the surface conductive layer (SCL) in H-terminated and the chemistry and reconstruction of the O-terminated surface.

The chapter is divided into the next sections:

- 3.1. ARXPS study of the (100)-H-terminated surface
- 3.2. ARXPS study of the (100)-O-terminated surface

3.1. ARXPS study of the (100)-H-terminated surface

In this section, an overview of the (100)-H-terminated diamond main results are presented in Section 3.1.1. One of the most particular phenomena on the diamond surface, the p-type surface conduction, is addressed in Section 3.1.2. A summary of the XPS results on the H-terminated diamond is shown in Section 3.1.3, focusing on the recently proposed surface downward band bending (DBB) phenomenon. A novel approach to the detection of band bending shapes is proposed in Section 3.1.4. By using this novel approach, DBB contributions are characterized and discussed in Section 3.1.5.

The sample used in this section corresponds to #H, which is described in Section 2.2.1. The experimental procedure details for the ARXPS experiment are summarized in Section 2.1.5.

3.1.1. The (100)-H-terminated diamond

Hydrogen is one of the most used terminations in diamond. Among the methods to obtain H-terminated surfaces, H₂ plasma is surely the most frequently used. This is because, in turn, this treatment is used as a key step during the diamond CVD growth process. Its importance relies on the saturation of dangling bonds to avoid the formation of sp² carbon phases at the surface but also is used as a cleaning step and because of its roughness lowering effect (Crawford et al., 2018; Koslowski et al., 1998). In the case of the (100)-diamond surface, a 2×1:H reconstruction is up to now the most accepted model in the literature (Thoms & Butler, 1995) (see Figure 3.1). In this reconstruction, carbon atoms on the top layer are forming dimer rows and a hydrogen atom is bonded to each of the top layer atoms. However, some authors point out that hydrogen termination would be composed of a combination of monohydride, dihydride, and trihydride structures (Kawarada, 1996). In any case, ideally, all carbon atoms in the mentioned structures should remain in the sp³ hybridization. The 2×1:H model is supported by several experimental and theoretical results. The *Tomas et al.* studies must be highlighted. In it, diamond clean surfaces are repeatedly submitted to dosed H₂ and thermal treatments (R. E. Thomas et al., 1992). Low-energy electron diffraction (LEED) and TPD experiments evidenced that clean and H-terminated diamond surfaces present a 2×1:H pattern when surfaces are exposed to a very wide range of H₂ doses. Results of TPD experiments showed that the primary desorption product is molecular hydrogen. The desorption starts from approximately 720° C and has a maximum desorption rate at 900°C, which is related to the destruction of the 2×1:H reconstruction. It is worth notice that these experiments are carried out under vacuum. Thus, this very high stability cannot be fully extrapolated to samples on ambient conditions where oxygen and other chemical agents can affect the termination properties.

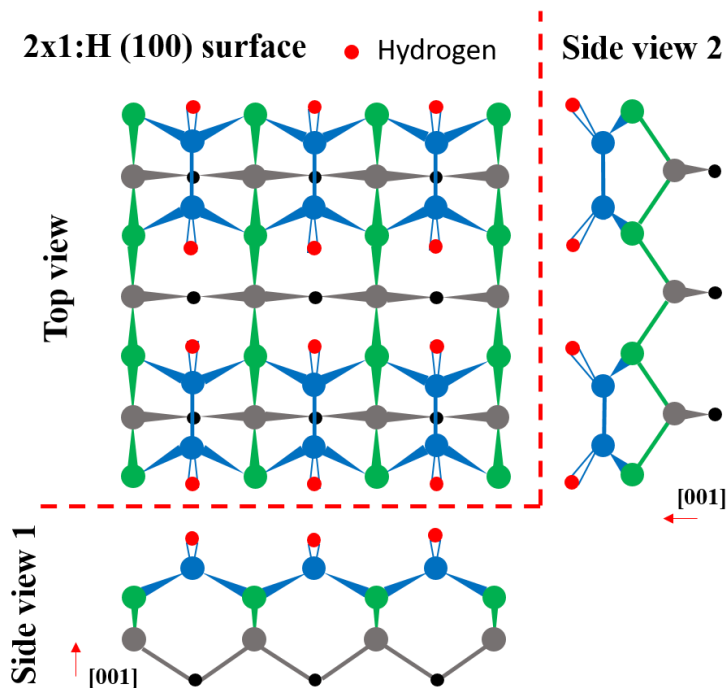


Figure 3.1: Schematic of the 2×1:H surface reconstruction of (100)-oriented diamond showing the four topmost carbon layers. One hydrogen atom (red circle) is bonded to each topmost carbon layer (blue atoms).

Similar LEED results were found for H₂ plasma-treated samples with similar sample preparation to the present work (Thoms & Butler, 1995). The authors pointed out that H₂ plasma on diamond leads to atomically flat terraces on the diamond surface. Additionally, the H-terminated surface was stable in air and free of contaminants and sp² carbon. Surface vibrational spectra were obtained for this sample by High-resolution electron energy loss spectroscopy (HREELS). C-H stretching vibration contributions were attributed to monohydride structures. It led to conclude that no other hydride or oxygenated structures were present for the used conditions. For similar sample preparation, scanning tunnel microscopy experiments were carried out (Bobrov et al., 2003; Koslowski et al., 2001). These authors observed the formation of dimer rows in agreement with a 2×1:H reconstruction and the presence of surface domains or terraces separated by steps. Thus, every terrace dimer rows can run in different orthogonal directions. Some relevant theoretical results about the stability of the (100)-H-terminated diamond surface for different reconstructions and coverages are summarized in (Hong & Chou, 1997).

On the other hand, the presence of C-H bonds surface dipoles, with a positive component towards the surface, has been related to the consequent reduction of the electron affinity and ionization energy as compared to the clean and oxygenated surfaces. An NEA of approximately 1.3 eV is found on (100)-H-terminated diamond surface (Diederich et al., 1996; Krainisky & Asnin, 1998; Takeuchi et al., 2005). It means that the vacuum level will fall below the conduction band and, since the diamond bandgap is ~5.5 eV, an ionization energy of ~4.2 eV is expected.

This property is interesting to achieve high-quality field emitters or for the optimization of surface electronic devices based on diamond.

One of the most relevant and discussed H-terminated properties is the appearance of a p-type surface conductive layer (SCL). This phenomenon is widely addressed in the next section.

3.1.2. Surface conductive layer in (100)-H-terminated surface

As-grown doped and undoped CVD diamond surfaces, as well as those treated by H₂ plasma, expose a unique and interesting property among semiconductors: a p-type SCL (Landstrass & Ravi, 1989a, 1989b). This property has been exploited for the fabrication of diamond electronic devices such as MOSFETs (Maréchal et al., 2017; Verona et al., 2015) in which a hole accumulation in the subsurface region is originated by the interaction with the 2D hole gas formed below the H-terminated surface. Thus, the SCL is used as an active channel in FET devices. Concerning metal/diamond junctions, other results show that some metals form ohmic contacts when deposited on an H-terminated diamond while exhibiting Schottky behaviour on O-terminated (Teraji et al., 2008), which is related to the contrasting electronic configuration from H- to O- terminated diamond. However, despite its wide applications, the origin of the SCL is still very controversial.

There is broad agreement that hydrogen plays a fundamental role in the appearance of this superficial unique phenomenon. Surface conductivity is found in boron-doped and undoped CVD diamond as well as in type IIa diamond. In natural type IIa diamond, an abrupt resistivity change from $\sim 10^{15} \Omega \cdot \text{cm}$ to $\sim 10^5 \Omega \cdot \text{cm}$ after hydrogen treatment is found. A post-annealing process at $\sim 780 \text{ }^\circ\text{C}$ leads to a resistivity increase back to $\sim 10^{14} \Omega \cdot \text{cm}$ (Landstrass & Ravi, 1989a). Analogous behaviour was found in CVD undoped and doped films (Landstrass & Ravi, 1989b). As-grown samples showed a $\sim 10^6 \Omega \cdot \text{cm}$ resistivity and annealing step is found to be very significant with the resistivity of the diamond increasing by up to six orders of magnitude ($\sim 10^{13} \Omega \cdot \text{cm}$). It means that the hole transport phenomenon is not related to carriers coming from boron acceptors. The authors postulate that the resistivity of the hydrogenated crystals and films is governed by shallow acceptor (SA) levels, whereas removal of the hydrogen by annealing electrically activates deep donors, pinning the Fermi level and giving rise to the observed high resistivity. In this sense, samples of type Ib (with a high N concentration) showed a high resistivity even after hydrogenation treatment, what has been linked to the presence of substitutional nitrogen which acts as a compensating donor for the SAs, suppressing hole accumulation (Maier, Riedel, et al., 2001). Other authors found that the carrier concentration in BDD CVD films was found one decade or higher than the amount of doped boron, which once again has been related to the presence of additional acceptor levels due to hydrogenation treatment (Shiomi et al., 1991).

The areal density of the p-type carriers responsible for SCL is in the order of $\sim 10^{13} \text{ cm}^{-2}$ in CVD diamond, slightly higher for undoped films. It is mostly independent of the temperature in boron-doped and undoped diamond films in the range of 150 to 400 K (Hayashi et al., 1996). A slight increasing charge density for boron-doped films with temperature can be noted while undoped films do not show this tendency. In this sense, three acceptor levels with ionization energy from 20 to 250 meV at 200 K have been characterized (Maki et al., 1992). The activation energy of the p-type conduction is very shallow in comparison to that of boron acceptors in diamond (370 meV) and, thus, were related to hydrogenation-induced acceptors.

On the other hand, CVD samples that are exposed to air showed four orders of magnitude resistivity reduction which was related to air acid components (Gi et al., 1995). In that work, the authors proposed for the first time a model for the surface conduction layer generation. The model is based on the surface transfer doping (STD) phenomena in which electrons from the diamond valence band can be transferred to surface adsorbates or defects related to energy levels (see Figure 3.2). This and analogous mechanisms are up today the most accepted explanation (W. Chen et al., 2009; Gi et al., 1995; Maier et al., 2000; Ristein, 2006a, 2006b).

In the STD model, the Fermi level of the surface-related energy levels lies deeper than that of the bulk diamond. An Upward Band Bending (UBB) and, hence, a hole accumulation layer is created at thermal equilibrium, explaining the generation of a 2D-hole gas (2DHG). It is generally accepted that the appearance of high surface conductivity is very dependent on the presence of atmospheric adsorbates. In several experiments, it has been demonstrated that exposure to different gaseous species varies the SCL by many orders of magnitude (Kubovic & Kasu, 2010; Sato & Kasu, 2013). While N_2 , O_2 , and Ar exposure have a negligible effect on the SCL, NO_2 and O_3 are related to an improvement of the surface conductivity (Kubovic & Kasu, 2010; Riedel et al., 2004). Oppositely, when samples are placed into vacuum the conductivity lies after a certain time. Additionally, if the annealing step or other surface modifications has been carried out, destroying the SCL, could be restored by re-hydrogenation treatment (Koslowski et al., 2001).

In (Riedel et al., 2004), the hydrogenated surface was sequentially annealed in vacuum and exposed to different gaseous ambient. The authors observed that below 190 °C annealing, the SCL can be fully recovered to the original conductivity values. Over 750 °C annealing, the SCL is irretrievably lost. Both results are compatible with the STD model in which the interaction of an H-terminated surface and external adsorbates is necessary. Thus, over 750 °C annealing will promote hydrogen desorption and the consequent loss of the NEA surface. This result is in agreement with TPD experiments (R. E. Thomas et al., 1992) and establish the maximum hydrogen desorption rate at 900 °C. Furthermore, intermediate annealing temperatures

(250 °C- 700°C) lead to a partial loss of the SCL which, in turn, can be recovered by UV illumination. This phenomenon has been related to the presence of ozone and agrees with other observations (Bobrov et al., 2003; Kubovic & Kasu, 2010). The observations at intermediate annealing temperatures are not fully compatible with the STD model, since the H-terminated surface and SCL is expected to remain stable for the same atmosphere exposition at this temperature range. Other experimental results that cannot be explained by the STD model have been summarized (Kono et al., 2010). The existence of experimental evidence that is not fully compatible with the STD model together with the fact that this UBB was not empirically observed has led some researchers to explore other mechanisms that fit all the observations and proposed other possibilities based on the evidence.

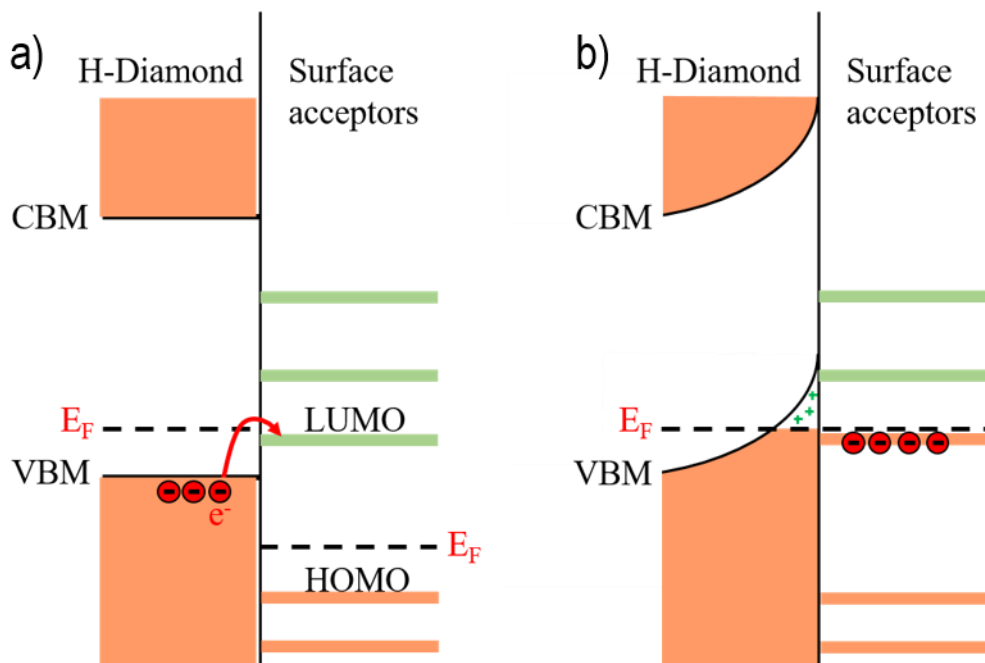


Figure 3.2: Schematic energy diagram to illustrate the origin of SCL from the p-type surface transfer doping (STD) mechanism in H-terminated diamond. a) Neutral diamond and neutral surface acceptors before the charge exchange. Red lines and green lines refer to occupied and unoccupied molecular orbitals, respectively. b) The band diagram at equilibrium. Note that the alignment of energy levels intimately at the surface is unchanged. The charge exchange between surface acceptors and the semiconductor is accompanied by a band bending that finally equalizes the Fermi levels.

At this point, it is necessary to classify surface states (SS) into two types: a) Intrinsic SS which are related to the existence of a perfect surface, including the states arising due to relaxation and reconstruction; and b) extrinsic SS that exist as a result of perturbations to the ideal surface, what can be related to defects or being produced by the adsorbed atoms. The latter SS cause changes in the chemical bonds near the surface, thus affecting the distribution of intrinsic SS. Besides, new electronic states are formed by the bonding and antibonding orbitals between the chemisorbed atom or molecule and the surface. Therefore, STD models refer to the perturbation

of the ideal SS by the presence of adsorbates. However, the depicted diagram used for the STD model (Figure 3.2) is, in turn, a simplification in which no intrinsic SS and its interaction with extrinsic SS remains uncertain.

Previously to the STD model, *Kawarada et al.* proposed the existence of intrinsic SS due to the hydrogen termination to explain the surface conductivity in undoped diamond (Kawarada, 1996) (see Figure 3.3). If an intrinsic acceptor SS is placed near the valence band, those states below the Fermi level will be filled by electrons resulting in a negative charge. For the charge neutrality condition to be fulfilled, the same but positive charge in the diamond bulk is necessary to compensate the negative charge in SS, resulting in a UBB. The higher the density of filled SS the more negative charge at the surface and the more abrupt the UBB. It must be noticed that, if all SS are fulfilled, an alleged shift of position of the SS towards deeper energies will not change the band bending because the SS are already fulfilled and the total negative charge would remain constant. From the latter, it is deduced that, for a 2DHG to occur in undoped diamond films, the position of the SS is not as important as the density of SS.

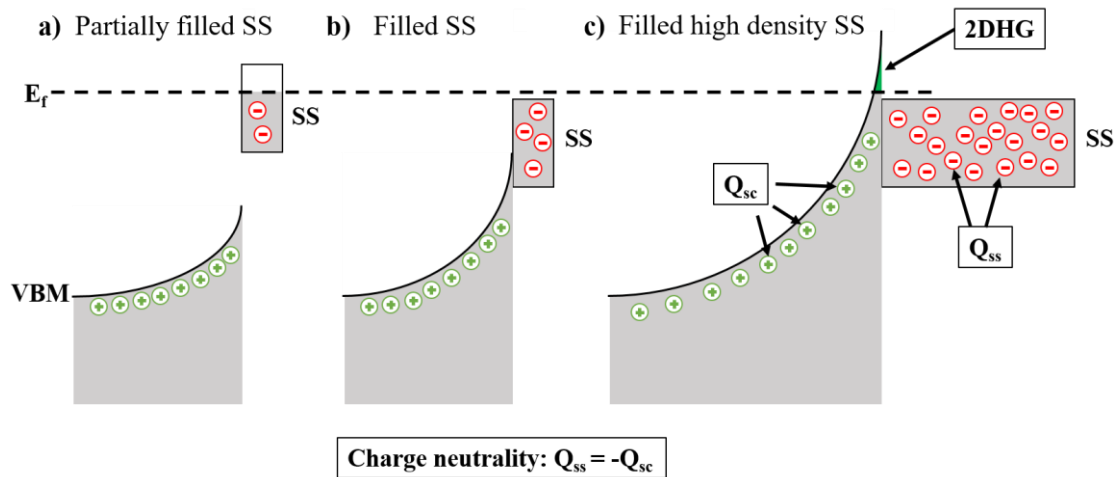


Figure 3.3: Schematic band diagram for an undoped diamond with the presence of intrinsic acceptor surface states (SS) (based on Kawarada model). When the SS is positioned below the Fermi level E_f , electrons will fill these states. The occupied acceptor SS represents a negative charge Q_{ss} that needs to be compensated to get the charge neutrality condition. Thus, the same but positive charge Q_{sc} appears on the bulk generating an UBB. Partially filled SS in a) will represent a lower negative charge than in b), where SS is already fulfilled. Thus, the band bending in a) is higher than in b). It must be noticed here that, even if the position of the SS in b) is placed deeper, the band bending will not change because the SS is already fulfilled and the total negative charge will remain constant. However, an increase in the density of states will allow a higher negative charge to exist at the surface and hence a higher UBB (c). If the UBB is strong enough to overcome the Fermi level, a 2D hole gas (2DHG) will be created.

The proposed model is analogous to the STD model but does not require extrinsic SS for the SCL to occur. Thus, it could explain the case of SCL in undoped diamond surfaces. A high density of unoccupied states above the Fermi level in the diamond bandgap has been found by STM which was attributed to intrinsic SS of the H-terminated surface (Bobrov et al., 2003). Analogous results were found by angle-resolved photoelectron spectroscopy which related the

2×1 hydrogenated reconstruction to a density of SS extended in a ~ 1.5 eV range over the valence band maximum (VBM) (Hamza et al., 1990). In this line, other authors estimated that the Fermi level would be at 0.24-0.52 eV above the VBM for different samples (Kono et al., 2007). Thus, these results would support the Kawarada model. However, the effect of the interaction of the intrinsic and extrinsic SS is not addressed and the reasons why the conductivity should increase under the presence of different environments remains unanswered in such a model.

Recently, a DBB at the very near surface of (100)-H-terminated diamond has been proved (Kono et al., 2005, 2010, 2019). The phenomenon has been linked to the presence of SAs which, in turn, were potentially related to the presence of subsurface hydrogen, contributing to the SCL. The related mechanism was called Downward Band Bending due to SA (DBB/SA). In this model, two band bending effects coexist: UBB due to extrinsic and/or intrinsic SS (as expected for STD and Kawarada models, respectively) which are pinning the Fermi level at the surface; and DBB very near the surface due to the presence of the SA (Figure 3.4). As a starting point to illustrate the phenomenon, a UBB due to the presence of SS as described in any of the preceded models is considered (Figure 3.4(a)). Then, the presence of acceptors with very low ionization energy in the subsurface region will ionize promoting holes to the valence band (Figure 3.4(b)). However, as a consequence of the ionization of SA, a negative space charge is generated within the subsurface region. This negative space charge density generates a downwards electric potential modifying the band curvature (Figure 3.4(c)). Under this band configuration, free holes are accumulated at the very near surface.

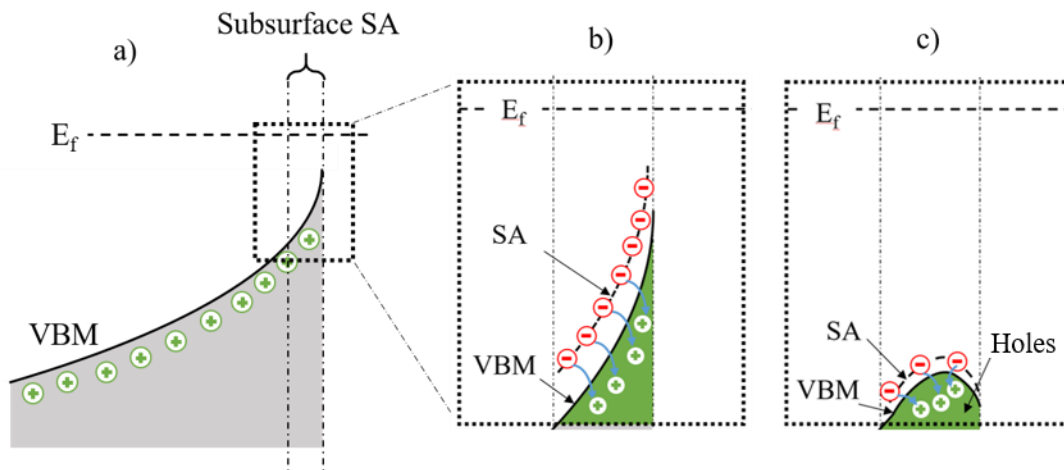


Figure 3.4: Schematic band diagram to illustrate the downward band bending due to shallow acceptors (DBB/SA) phenomenon. a) An upwards band bending exists as a consequence of the presence of SS near the valence band maximum (VBM) as described for STD and Kawarada models. Differently, shallow acceptors (SA) with very low ionization energy are present in the subsurface region. b) SA just during the ionization process. The ionization of the SA will generate a negative space charge density in the subsurface region. Free holes could accumulate in this band configuration. c) The negative space charge region created by ionized SA results in a downwards electric potential very near the surface modifying the band curvature. Free holes are accumulated very near the surface. Remarkably, the VBM does not need to overcome the Fermi Level to generate the hole accumulation layer because of the SA presence.

Note that due to the presence of SA, it is not required that VBM overcome the Fermi level to get a hole accumulation layer as in Figure 3.3(c). Thus, it is not required a very strong UBB for this to occur, tentatively explaining the conductivity in samples that are not exposed to air. The model, as the preceded one, could also explain the conduction of undoped diamond films since carriers are provided by the hydrogenation treatment-induced carriers. Indeed, it is compatible in combination with the STD model since an additional UBB could be defined by the presence of extrinsic SS coming from external molecules, therefore explaining the higher conductivity in samples exposed to air. The DBB/SA mechanism is supported by other previous results such as the observation of hydrogen subsurface contributions of a few monolayers (ML) (Bobrov et al., 2003; Chevallier et al., 1998; Hamza et al., 1990; Maier et al., 2000). TPD observations suggest that much of the desorbed hydrogen originates in the bulk and near-surface. Hydrogen concentrations on the order of 10 ML (for 1 ML = 2 hydrogen atoms per surface carbon) were evidenced for high atomic hydrogen exposure (Hamza et al., 1990). Another example: the interaction of hydrogen and boron acceptors has also been evidenced (Chevallier et al., 1998). Indeed, the authors found a direct relation between boron concentration and hydrogen diffusivity, which was related to the formation of (B-H) pairs (Fernández-Lorenzo et al., 2010). Thus, boron acceptors become negatively charged under hydrogen incorporation. In this sense, when samples are lightly doped, the interaction between the hydrogen and some native defects would determine the hydrogen diffusivity limit. In this line, some theoretical results point to the stability of hydrogen in C-C bond center sites of the diamond lattice which can result in SS close to the VBM (Kanai et al., 2002, 2003). In this sense, an exhaustive theoretical approach to the role of hydrogen in diamond can be found in (J. P. Goss et al., 2002; Jonathan P Goss, 2003).

In summary, the STD model, based on extrinsic SS, is the main model for the SCL but cannot explain all related phenomena. Kawarada model (intrinsic SS) would explain the undoped diamond case but the interaction of intrinsic and extrinsic SS remains unexplained. The DBB/SA model has been recently proposed to explain some experimental phenomena and is compatible with the preceded models. Among other results, the DBB/SA model is supported on the detection of a DBB in the very-near H-terminated surface by ARXPS. This topic is addressed in the next section.

3.1.3. Previous XPS results in the H-terminated surface

XPS is a very useful technique for the study of surfaces and has been widely employed for studying diamond chemical terminations in the literature (David et al., 2013; Kono et al., 2003; Kozak et al., 2009; Maier et al., 1999; Navas et al., 2018; Speranza et al., 2011). It must be noticed that XPS results mostly agree with the position of the main C 1s peak for (100)-H-terminated diamond and, thus, the results show a high reproducibility even for doped and undoped samples

(Bobrov et al., 2003; Kono et al., 2019; Kubovic & Kasu, 2010; Navas et al., 2018). The energy distance between the C 1s maximum peak and the valence band maximum has been estimated to be 284.01 ± 0.12 eV (Kono et al., 2014) in as-grown CVD diamond and 283.9 ± 0.1 eV for hydrogenated diamond (Maier, Ristein, et al., 2001).

For the study of diamond SS (surface bonding groups C-O, C-H...) as well as those phenomena at the very surface, e.g. surface band bending, conventional XPS measurements could not be sensitive enough. This is because, as shown in Section 2.2.2.1, the depth sensitivity is ~ 10 nm in diamond for Al- $K\alpha$ source ($h\nu = 1486.6$ eV) and these very near surface contributions will represent a small portion of the total signal. To overcome this limitation two main approaches can be applied: a) filtrate the electrons that escape from deeper in the sample by varying the sample-to-detector angle and b) tune the incident photons energy. The technique associated with the first approach is called ARXPS (or generally ARPES) which indeed is a very powerful near-surface characterization tool for the generation of sample depth profiles and the study of SS (Baxter et al., 2008; Fadley, 2010). However, its application in the diamond surface is today rarely found in the literature. Among others, it must be highlighted the work of *Kono et al.* in which a DBB in the (100)-H-terminated surface was detected and characterized by this technique (Kono et al., 2010). This result was linked to the presence of SA (DBB/SA model, see Section 3.1.2), and became a step towards the understanding of the SCL. In their analysis, the presence of a SA layer along with the first ~ 1 nm and with an acceptor concentration of $\sim 1.7 \times 10^{13} \text{ cm}^{-2}$ was assumed. A few years later, an exhaustive review of ARXPS results for O- and H- diamond surface termination in the (111) and (100) orientation was also reported by the same author (Kono et al., 2019). This work focused on reaching a consensus on the literature XPS results. Some conclusions can be extracted from the (100)-H-terminated diamond spectra: a) A surface contribution towards higher *BE* is normally present in the C 1s spectrum for different samples. This contribution becomes clearer as the surface sensitivity increase, that is, for the higher polar angles spectra and b) A shift towards higher *BE* of the main C 1s peak was linked to a surface DBB. Moreover, the more the sheet resistivity of the SCL, the higher the C 1s maximum peak shift towards higher *BE*. The observation in b) was supported by the intensity of the surface contribution in a), which far exceeds the feasible 1 ML coverage of C-H bonds. Thus, the shift should not be motivated by the increasing intensity of the surface contribution but by another component related to the band bending effect at the near-surface.

The characterization of the H-terminated diamond DBB was then made by using ARXPS spectra. To do this, the positions of maximum C 1s peak for different polar angles were tracked and used to estimate the surface band bending. The method, while widely used in the literature, has some limitations which depend on the definition of the limits of the band bending to the maximum depth sensitivity of the ARXPS measurement. Namely, if the space charge width d ,

within which the band bending occur, far exceeds the XPS maximum depth sensitivity (as in a Schottky junction), then a shift of the core-level will reasonably occur when increasing the polar angle (reducing the depth probe) in correspondence with the band bending. However, when d is lower than the XPS sensitivity depth as in the present discussion of the DBB/SA model, the problem is not straightforward. As will be proved in the next section, in such a case the band bending must be deconvoluted as an additional peak. The position and intensity of this peak and its variation with the polar angle require a definition of the energy curvature. Therefore, a novel approach to the characterization of band bending contributions by XPS is proposed. The method is based on the description of the XPS peak shapes that can be deduced from the definition of an electric potential. The description of XPS band bending shapes is hardly addressed or used in the literature but gives some advantages such as the estimation of the space charge width or the simulation of peak shifts due to the presence of an electric potential.

Thus, this work is in agreement with the presence of a DBB in the very near surface as stated by *Kono et al.* However, disagreement is found in the DBB characterization method used there. In the next section, the description of a novel characterization method is addressed. This method is applied for the deconvolution of H-terminated diamond ARXPS spectra in the next sections.

3.1.4. A new method to evaluate band bending from XPS peak shapes

As detailed in the experimental section, XPS spectra represent the intensity in electron counts recorded at each energy level. It exhibits peaks of intensity at defined energy levels. To describe mathematically the XPS peak contribution, a Voigt distribution is commonly used. It is defined as the convolution of a mixed Gaussian-Lorentzian distribution where the Lorentzian component is related to the lifetime broadening of electrons (Graupner et al., 1998). However, when a band bending exists and hence all energy levels bend accordingly, the contribution should be different from a Voigt distribution. In this section, a theoretical approach is obtained for the generation of surface band bending contributions in XPS. The result is applied to the ARXPS C 1s core-level spectra of the (100)-H-terminated diamond for the characterization of a surface DBB in the next sections. The proposed idea can serve as a guide for other authors to evaluate electric potentials from photoelectron spectroscopic techniques.

3.1.4.1. XPS intensity and the probability of escape of electrons, $P(z)$

The recorded XPS intensity generated by a certain photoelectron contribution is dependent on several factors. Under certain assumptions and experimental conditions, most of

these factors can be reduced. In the following paragraphs, perfectly flat samples with homogeneous composition are assumed.

The depth-related contribution, to a specific XPS peak intensity, can be expressed from the surface ($z=0$) to a depth d ($z=d$) as:

$$I_1(z) = \underbrace{S \cdot F \cdot T \cdot N_1 \cdot \sigma}_K \int_0^d \underbrace{e^{-z/\lambda \cdot \cos\theta}}_{P(z)} dz \quad (3.1)$$

where S is the analysed sample area, F is the photon flux, T is the analyser transmission, N_1 is the density of atoms per volume unity, σ is the photoionization cross-section, z is the depth measured from the surface, λ is the attenuation length or the inelastic mean free path and θ is the polar angle to the surface normal,. The exponential term $P(z)$ inside the integral is the Beer-Lambert law describing the inelastic electron escape probability. K is defined as the product of all the terms outside the integral term.

Since the sample has a homogeneous composition, the terms T , N_1 , σ , and λ can be considered as constant within the sample depth for a specific core-level (e.g. C 1s in diamond). The value of F and S are assumed to remain constant at a certain polar angle. Hence, if two different contributions are considered, with respective intensities I_1 , for $z \in [0, d]$, and I_2 , for $z \in [d, \infty)$, then the intensity ratio is calculated as:

$$\frac{I_1(z)}{I_2(z)} = \frac{K \cdot \int_0^d e^{-z/\lambda \cdot \cos\theta}}{K \cdot \int_d^\infty e^{-z/\lambda \cdot \cos\theta}} = \frac{\int_0^d e^{-z/\lambda \cdot \cos\theta} dz}{\int_d^\infty e^{-z/\lambda \cdot \cos\theta} dz} \quad (3.2)$$

Therefore, the intensity ratio between two contributions is independent of K and only depends on z ranges. In consequence, the intensity ratios are defined by the probability of electron escape $P(z)$ by setting the corresponding z ranges to each contribution. Since λ and θ are known, the thickness d of the first contribution can be estimated from equation (3.2). For this purpose, the correct modeling of the sample is necessary. Indeed, this idea is commonly applied for the estimation of the thickness of oxidized metal layers (Bernstein & Grepstad, 1989).

3.1.4.2. 1D surface potential approximation, $V(z)$

The electric potential versus space charge density is described by Poisson's equation. Assuming that charge distribution is invariable in the x and y directions, i.e. in the plane parallel to the surface, then the electric potential, $V(z)$, for a one-dimensional analysis is determined from Poisson's equation

$$\frac{d^2V(z)}{dz^2} = -\frac{d\mathcal{E}(z)}{dz} = -\frac{\rho(z)}{\epsilon_0\epsilon} \quad (3.3)$$

where $\rho(z)$ is the space charge density along the z -axis, ϵ_0 is the vacuum permittivity and ϵ is the relative permittivity of the material under study, $\mathcal{E}(z)$ is the electric field, $V(z)$ is the electric potential. The solution depends on the space charge density along with the sample, $\rho(z)$. Under the absence of scientific evidence about the space charge density, it is necessary to get an approximation by using some simple mathematic solutions for the space charge density ρ . In the following, some particular cases are discussed:

- a) **Constant space charge density:** The assumption of a constant space charge density lead to a solution of Poisson's equation, known as Schottky approximation.

Assuming that a homogeneously distributed negative charge within the z range $(0, d)$, then

$$\rho_1(z) = -eN \quad 0 \leq z \leq d \quad (3.4)$$

where N is the charge density and e is the electron charge. A sample $\rho_1(z)$ curve is represented in Figure 3.5(a). Poisson's equation becomes:

$$\frac{d^2V}{dz^2} = -\frac{eN}{\epsilon_0\epsilon} \quad (3.5)$$

For a positive charge, the sign of the second term must be adjusted consequently. The electric field in this region is found by integration. Then:

$$\mathcal{E}_1(z) = \int \frac{\rho(z)}{\epsilon_0\epsilon} dz = \int \frac{eN}{\epsilon_0\epsilon} dz = -\frac{eN}{\epsilon_0\epsilon} z + C_1 \quad (3.6)$$

where C_1 is a constant of integration. The electric field is assumed to be zero in the neutral out of the negative space charge region for $z \geq d$. Thus, the constant of integration is determined by setting $\mathcal{E}(d) = 0$,

$$\mathcal{E}_1(d) = -\frac{eN}{\epsilon_0\epsilon} d + C_1 = 0 \Rightarrow C_1 = \frac{eN}{\epsilon_0\epsilon} d \quad (3.7)$$

The electric field in the space charge region is then given by:

$$\mathcal{E}_1(z) = -\frac{eN}{\epsilon_0\epsilon} (z - d) \quad 0 \leq z \leq d \quad (3.8)$$

The potential in this region is found by integrating the electric field. Therefore,

$$V_1(z) = -\int \mathcal{E}_1(z) = \frac{eN}{\epsilon_0\epsilon} z \left(\frac{z}{2} - d \right) + C_2 \quad (3.9)$$

where C_2 is again a constant of integration. The potential is a continuous function, so the potential must be equal to a certain value V_0 , called here as bulk potential, at the space charge region edge d in the semiconductor, so the constant of integration can be found as:

$$V_1(d) = \frac{eN}{\epsilon_0\epsilon} d \left(\frac{d}{2} - d \right) + C_2 = V_0 \Rightarrow C_2 = V_0 + \frac{eN}{2\epsilon_0\epsilon} d^2 \quad (3.10)$$

The potential in the space charge region can thus be written as:

$$V_1(z) = V_0 + \frac{eN}{2\epsilon_0\epsilon} (z - d)^2 \quad 0 \leq z \leq d \quad (3.11)$$

The potential at the surface with respect to the potential at the bulk is obtained by using the $V(0)$ expression:

$$V_{bb} = V(0) - V_0 = \frac{eN}{2\epsilon_0\epsilon} d^2 \Rightarrow \frac{eN}{2\epsilon_0\epsilon} = \frac{V_{bb}}{d^2} \quad (3.12)$$

Then, $V_1(z)$ can be written as a function of V_{bb} :

$$V_1(z) = V_0 + \frac{V_{bb}}{d^2} (z - d)^2 \quad 0 \leq z \leq d \quad (3.13)$$

The electric potential due to a surface band bending is then defined by the bulk potential V_0 , the surface potential V_{bb} , and the space charge width, d .

The solving process, can be summarized in four steps: 1) definition of the space charge density, 2) double integration of the Poisson's equation to obtain $V(z)$, 3) application of the boundary conditions $E(d) = 0$ and $V(d) = V_0$ to obtain the integration constants and, optionally, 4) transformation of the $V(z)$ expression to a function of the surface potential, by using $V_{bb} = V(0) - V_0$.

b) Linear space charge density. In this case, the space charge density is a decaying linear distribution. Thus, the charge density at the surface ($z = 0$) is eN and 0 at $z = d$, then

$$\rho_2(z) = -eN \left(1 - \frac{z}{d} \right) \quad 0 \leq z \leq d \quad (3.14)$$

A sample $\rho_2(z)$ curve is represented in Figure 3.5(a). Poisson's equation is

$$\frac{d^2V}{dz^2} = -\frac{eN}{\epsilon_0\epsilon} \left(1 - \frac{z}{d} \right) \quad (3.15)$$

By double integration and after obtaining the integration constants by $E(d) = 0$ and $V(d) = V_0$, the electric potential is obtained as

$$V_2(z) = \frac{eN}{6\epsilon_0\epsilon} \left(\frac{(d - z)^3}{d} \right) + V_0 \quad 0 \leq z \leq d \quad (3.16)$$

and finally, $V_2(z)$ can be transformed into an equivalent equation as a function of V_{bb} using the change

$$\frac{eN}{6\epsilon_0\epsilon} = \frac{V_{bb}}{d^2} \quad (3.17)$$

c) Exponential approximation. Again the charge density at the surface ($z = 0$) is eN and 0 at $z = d$. The space charge density is defined as:

$$\rho_3(z) = eN \left(e^{-kz} - \frac{e^{-kd}}{d} z \right) \quad 0 \leq z \leq d \quad (3.18)$$

where k is an exponential form factor. It must be noticed that for $k = 0$, a linear space charge density as described in a) is obtained. Sample $\rho_3(z)$ curves for $k = 2$ and $k = 4$ are represented in Figure 3.5(a). Poisson's equation is:

$$\frac{\partial^2 V}{\partial z^2} = \frac{eN}{\epsilon_0\epsilon} \left(e^{-kz} - \frac{e^{-kd}}{d} z \right) \quad (3.19)$$

by double integration and applying the boundary conditions:

$$V_3(z) = \frac{eN}{\epsilon_0\epsilon} \left[\frac{e^{-kz}}{k^2} + e^{-kd} \left(-\frac{1}{6d} z^3 + \left(\frac{d}{2} + \frac{1}{k} \right) z - \left(\frac{d}{k} + \frac{1}{k^2} + \frac{d^2}{3} \right) \right) \right] + V_0 \quad (3.20)$$

in the z range $[0, d]$. Finally, $V(z)$ can be transformed into an equivalent equation as a function of V_{bb} using the change:

$$\frac{eN}{\epsilon_0\epsilon} = \frac{V_{bb}}{\frac{1}{k^2} - e^{-kd} \left(\frac{d}{k} + \frac{1}{k^2} + \frac{d^2}{3} \right)} \quad 0 \leq z \leq d \quad (3.21)$$

Following, the three space charge densities cases described in this section $\rho_1(z)$, $\rho_2(z)$, and $\rho_3(z)$; and its corresponding generated electric potential $V_1(z)$, $V_2(z)$ and $V_3(z)$, are compared in Figure 3.5(b) for the case in which the same surface potential V_{bb} is obtained and for the same space charge width d . For the exponential approximation, the $k = 2$ and $k = 4$ results are represented. The bulk potential V_0 is set to 0 and thus, $V(0)$ directly corresponds to V_{bb} .

Under the present condition, a high similarity among $V_1(z)$ and $V_2(z)$ functions is found. Concerning $V_3(z)$, the lower the values of k in the exponential approximation, the closer $V_3(z)$ approaches $V_2(z)$ and, in turn, to $V_1(z)$. Additionally, at a fixed k value, the lower the d value the better the $V_3(z)$ approximates $V_2(z)$ and hence, the step function. In this sense, the use of the step function is a good approximation choice when the space charge width is expected to be very small as in the case of a surface band bending. However, it must be noticed that to reach the same V_{bb} value, the charge density N must be modified consequently in every case. For the same space charge width, it can be proved by using equations (3.12), (3.17) and (3.21) that the charge density

necessary to reach the surface potential V_{bb} are related by $N_3(k=4) \sim 9.86N_1 > N_3(k=2) \sim 4.83N_1 > N_2 = 3N_1$. Therefore, a constant space charge density requires less charge density than the other approximations. The higher the k value the higher the charge density is needed.

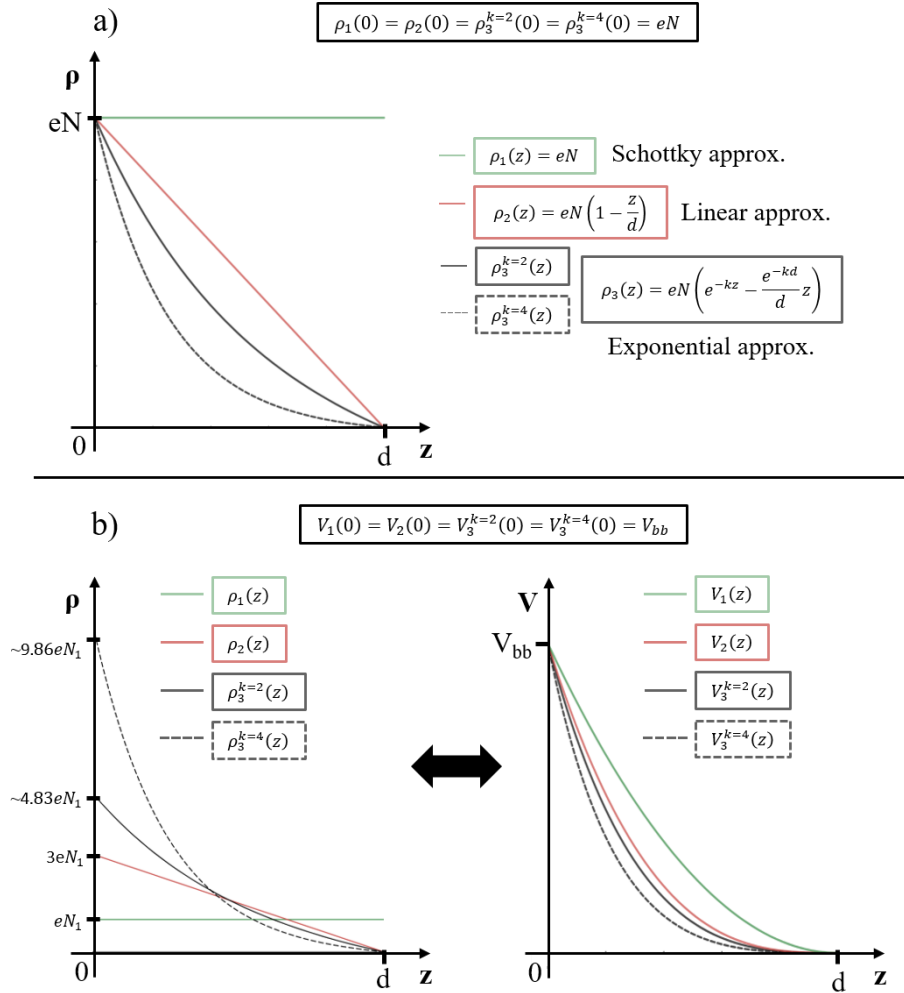


Figure 3.5: Representation of the charge density and the respective induced potential for different cases: a) Surface charge density $\rho(z)$ fixed at eN and b) Surface potential $V(z)$ fixed at V_{bb} . Subscripts indicate which space charge density solutions are related, being 1 for the constant, 2 for the linear, and 3 for the exponential approximation. The latter is evaluated for $k=2$ and $k=4$. The bulk potential V_0 was set to 0. For the same space charge width, it can be proved by using equations (3.12), (3.17) and (3.21) that the density necessary to reach the same surface potential V_{bb} are related by $N_3(k=4) \sim 9.86N_1 > N_3(k=2) \sim 4.83N_1 > N_2 = 3N_1$. Therefore, a constant space charge density requires less charge density than the other solutions. The higher the k value, the higher the charge density is required.

3.1.4.3. The probability of escape of electrons as a function of its energy, $P(V)$

In sections 3.1.4.1. the probability of escape of electrons $P(z)$ given by the Beer-Lambert law has been directly related to the XPS intensity when using intensity ratios. The electric potential $V(z)$ expression for the surface has been obtained for different space charge density

functions. Since both are functions of the depth z , the probability of escape of electrons could be described as a function of their electric potential. a) Under the consideration of the constant space charge density in the region $0 \leq z \leq d$, the generated electric potential $V_1(z)$ can be obtained using equation (3.13). By substituting the value of z in $V_1(z)$ into the electron probability of escape function $P(z)$:

$$V_1 = V_0 + \frac{V_{bb}}{d^2} (z - d)^2 \rightarrow z = d \left(1 - \sqrt{\frac{V - V_0}{V_{bb}}} \right) \rightarrow$$

$$\rightarrow P_1(V) = e^{\frac{-d \left(1 - \sqrt{\frac{V - V_0}{V_{bb}}} \right)}{\lambda \cos \theta}} \quad 0 < V < V_{bb} \quad (3.22)$$

where $P_1(V)$ is the probability of escape of electrons as a function of its electric potential, d is the space charge width, V_0 is the bulk potential at $z \geq d$, V_{bb} is the surface potential, λ is the inelastic mean free path or the attenuation length of electrons and θ is the polar angle respect to the surface normal.

b) In the same way, for the linear solution $V_2(z)$ (equation (3.16)) the probability of scape as a function of the potential, $P_2(V)$, is obtained:

$$V_2 = \frac{6V_{bb}}{d^2} \left(\frac{(d - z)^3}{6d} \right) + V_0 \rightarrow z = d \left(1 - \sqrt[3]{\frac{V - V_0}{V_{bb}}} \right) \rightarrow$$

$$\rightarrow P_2(V) = e^{\frac{-d \left(1 - \sqrt[3]{\frac{V - V_0}{V_{bb}}} \right)}{\lambda \cos \theta}} \quad 0 < V < V_{bb} \quad (3.23)$$

For other complex solutions such as the exponential approximation $V_3(z)$ (equation (3.20)), this step is not straightforward and would require the use of numerical approximations.

As an example and for comparison purposes, the shapes of $P_1(V)$ and $P_2(V)$ are shown in Figure 3.6. For fixed space charge width d (Figure 3.6(a)), the lower the polar angle the closer the $P_1(V)$ and $P_2(V)$ functions are, tending to $P(V) = 1$. Samely, as it approximates to the $\theta = 90^\circ$ value, $P_1(V)$ and $P_2(V)$ get close again. It is explained by the modification of the detection limit effect of the polar angle variation. When the polar angle is $\theta = 0^\circ$ the technique is sensitive to $\sim 5\lambda$ and the space charge region-related signal represents a short portion of the detected signal. Thus, $P_1(V)$ and $P_2(V)$ appear very similar. Contrary, at higher polar angles, the maximum sensitivity is reduced by the factor $\cos \theta$ and the measurement starts to be sensitive to the space charge region contribution partially. Therefore, the probability of escape of those electrons, deeper than the detection limit (or with lower electric potential), becomes lower. Analogous discussion can be

done for a fixed polar angle θ (Figure 3.6(b)). The lower the d the more the space charge region represents a portion of the total detected signal. And again, for very large d values, the space charge region is defined beyond the detection limits and is only partially detected.

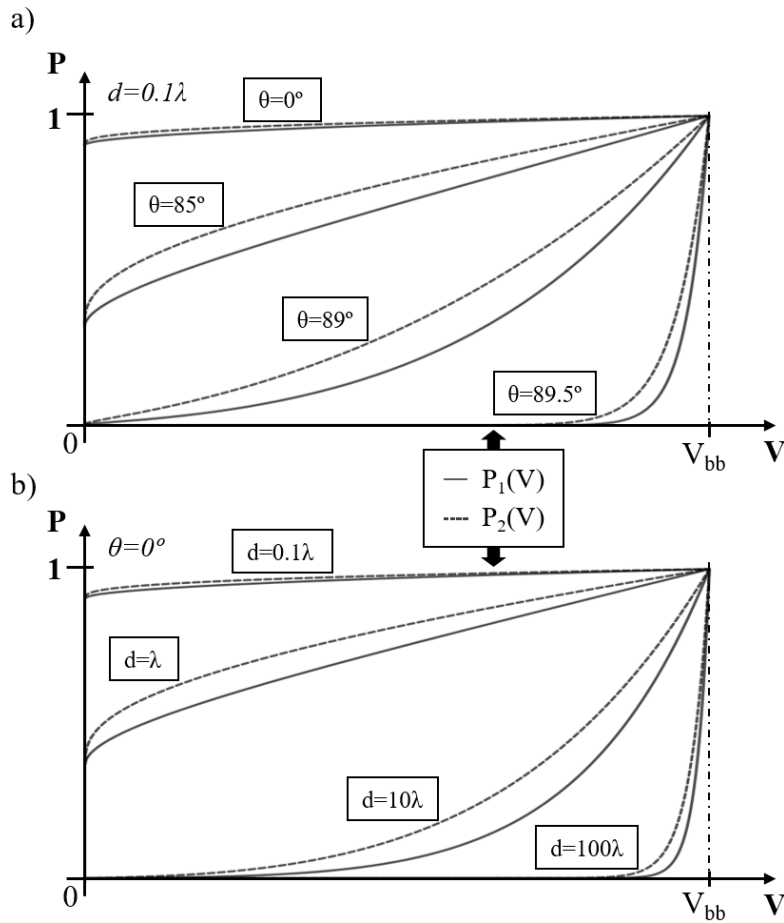


Figure 3.6: $P_1(V)$ and $P_2(V)$ functions comparison showing the effect of using a) different space charge width d for fixed polar angle $\theta = 0$, and b) different polar angles for fixed space charge width $d = 0.1\lambda$. $P_1(V)$ and $P_2(V)$ are obtained from the constant (solid line) and the linear (dashed line) space charge density solutions in Section 3.1.4.2, respectively. The related electric potential was set to reach the same surface potential V_{bb} .

Concluding, generally, very short space charge width will lead to very similar $P(V)$ expressions for different space charge density definitions. The same is achieved for a very large space charge width and high polar angles. Intermediate space charge width and polar angle values must be analysed individually.

3.1.4.4. XPS band bending shapes, $BB(E)$

The description of the XPS peak shapes generated by a space charge region is rarely found in the literature. In this section, a solution to this problem is addressed. The band bending shape generation and the functions involved in the process are summarized. A more detailed description of the involved functions can be found in the immediately preceding sections.

To start, the main idea is to transform the expression of the probability of escape of electrons P , commonly described as a function of the depth, $P(z)$, to a function of the electric potential, $P(V)$. To do this, first, it is necessary to obtain an expression of the electric potential as a function of depth $V(z)$ by using a solution of Poisson's equation. This solution will depend on the space charge density definition. Then, the electrical potential value at each depth z must be obtained. For simple solutions, it can be solved analytically while more complex solutions require the use of numeric approximations. Once it is done, the $P(z)$ expression can be transformed into the $P(V)$ form as well as to a function of energy, $P(E)$, by proper unit change. In this sense we define band bending energy as $E_{bb}=eV_{bb}$.

On the other hand, it is widely accepted that the XPS peak shape of a fixed energy level can be estimated as a Voigt distribution. Hence, every depth differential dz will correspond to a differential XPS intensity, which is described as a Voigt distribution with area dI . In a fixed energy level all these dI areas contribute to the same energy position resulting in a Voigt shape with the same form parameters but with an accumulated area. Under an electric potential, the dI terms are distributed along the energy axis. Under the assumptions in Sections 3.1.4.1, 3.1.4.2, and after the transformation $P(z) \rightarrow P(E)$, each dI can be attributed to a certain energy level dE . Then, it is reasonable to compute the resulting shape as the sum of scaled and shifted dI . This is exactly what the operation of convolution accomplishes. Therefore, the expression describing the generated shape $BB(E)$ is given by the convolution of a Voigt distribution $Voigt(E)$ over the $P(E)$ expression:

$$BB(E) = Voigt(E) * P(E) \quad (3.24)$$

where $Voigt(E)$ can be defined as a function of its Gaussian and Lorentzian width parameters. The choice of these two parameters will depend on the experimental setup conditions. It can be estimated from a reference sample or leave as a parameter for the analysis fitting process. An overview of the $BB(E)$, $P(z)$, $E(z)$, and $P(E)$ functions for a constant charge distribution in the range $0 \leq z < d$ are represented in Figure 3.7. The showed solutions are given for the polar angles $\theta = 0, 45, 70$, and 80° . The represented space charge width d is shorter than the detection limit for all polar angles and, thus, only the $P(z)$ values related to the space charge region are represented. $BB(E)$ is approximated by the discrete convolution $BB'(E)$. Accordingly, the higher the number of points of the discrete signals the better the XPS band bending shape is approximated.

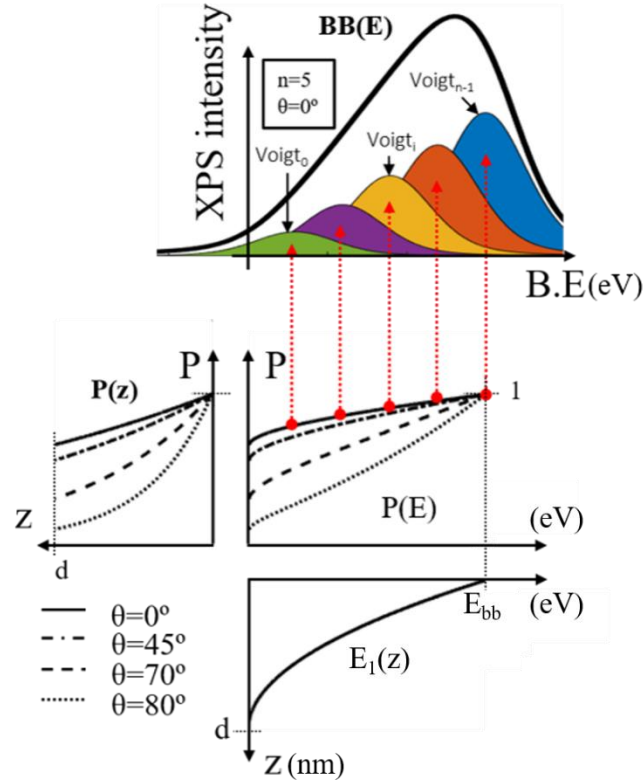


Figure 3.7: Summary of the required functions for the generation of a band bending shape contribution: $P(z)$ is the inelastic electron escape probability ruled by the Beer-Lambert law (see equation (3.1)). $E_1(z)$ is the band bending function obtained from Poisson's equation solution in equation (3.13) and proper unit change. The band bending $E_{bb} = eV_{bb}$ is defined within the space charge width d . $P(E)$ is the probability of escape of electrons as a function of its energy (see equation (3.22)). It is obtained by substitution of z in $E_1(z)$ into $P(z)$. The probability functions are represented for polar angles $\theta = 0, 45, 70,$ and 80° . Finally, the generation of the XPS band bending shape $BB(E)$ is calculated as the convolution of a Voigt distribution over the $P(E)$ curve. The example $BB(E)$ for $\theta = 0^\circ$ is approximated by the discrete convolution.

To illustrate the variability of XPS band bending shapes, some peculiar cases are presented:

1. The space charge width d is shorter than the XPS depth sensitivity for any polar angle (Figure 3.8).
2. The space charge width d is larger than the XPS depth sensitivity for any polar angle. (Figure 3.9).
3. The space charge width d is similar to the XPS depth sensitivity at 0° polar angle. (Figure 3.10).

These three sets of results are given for three band bending functions $E(z)$ generated by a constant space charge density (Equation (3.13)) and defined by its band bending E_{bb} , and the space charge width, d . For each result, $E(z)$, $P(E)$, and $BB(E)$ at the polar angles $\theta = 0, 70, 85^\circ$ are evaluated. The area under $BB(E)$ peaks has been normalized for comparison purposes. The percentage difference, $Diff$, between E_{bb} and the position of the $BB(E)$ maximum is shown for

each $BB(E)$ graph. The Gaussian and Lorentzian width parameters necessary for the Voigt definition were $w_G = 0.6$ and $w_L = 0.2$.

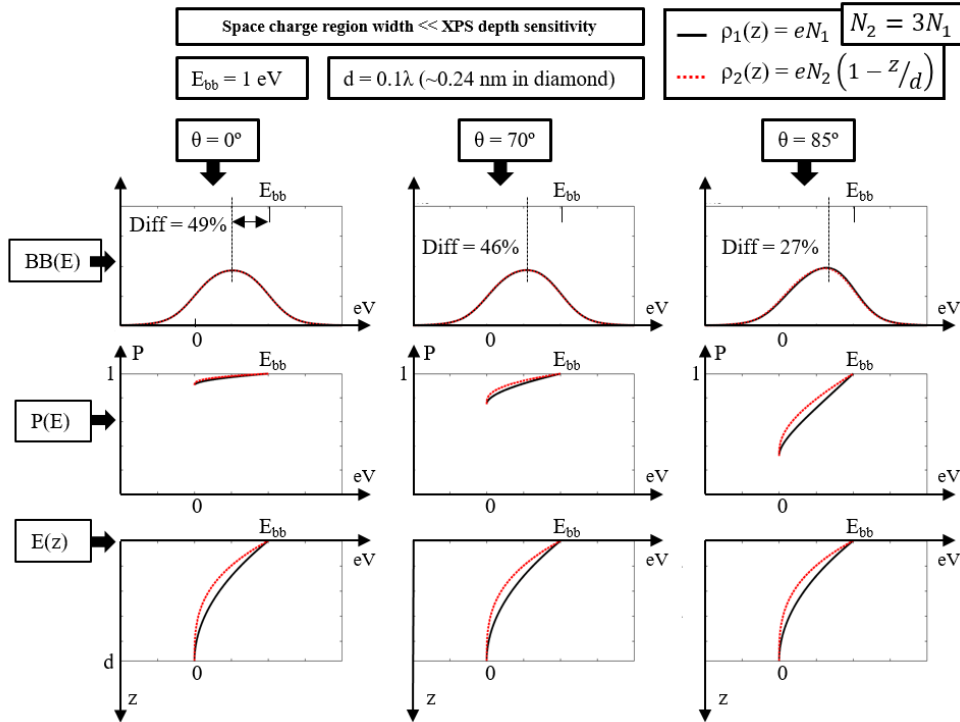


Figure 3.8: Simulated XPS band bending shapes for the case in which the space charge width is shorter than the depth sensitivity at every polar angle. $BB(E)$, $P(z)$, and $E(z)$ are the band bending shape, the probability of scape of electrons, and the electric potential, respectively. The constant and the linear space charge densities results are compared ($\rho_1(z)$ (black lined) and $\rho_2(z)$ (red dotted), respectively) defined to reach the same band bending $E_{bb} = 3$ eV. All the functions are evaluated for $\theta = 0, 70$, and 85° . The parameter *Diff* is related to the $\rho_1(z)$ solution (black lined) and is defined as the percentage difference between the maximum $BB(E)$ and E_{bb} .

1. The first set of simulated shapes (Figure 3.8) shows the case in which the space charge width is shorter than the depth sensitivity at every polar angle. It is for example the case of a very near-surface band bending. The peak is characterized by an increased width which strongly depends on the band bending. Moreover, as the sensitivity depth ($\sim 5\lambda\cos\theta$) approaches the space charge width d , that is, for higher polar angles, the shape becomes more asymmetric. The position of the maximum peak poorly approximates the real E_{bb} ($Diff = 27\%$ at $\theta = 85^\circ$). The differences between $BB(E)$ for the two space charge density solutions are reduced at lower polar angles. Additionally, it must be noticed that since d is lower than the detection limit, at least two contributions should be expected from such experiment, one for the space charge region, $z \in (0, d)$, and other for the bulk region just below it, $z \in (d, \sim 5\lambda\cos\theta)$.

2. The second set of measurements (Figure 3.9) is related to the case in which the space charge width clearly exceeds the depth sensitivity range at each polar angle. That is the case, for example, of a Schottky junction in which a potential barrier is generated between a metal and a semiconductor material. In that case, the space charge width is in the order of μm . Note that the

width of the $BB(E)$ peaks is clearly lower than that of the first case. This occurs because the measurement is now only sensitive to the highest range of the potential curvature. The asymmetric peak shape is not detectable, even less for higher polar angles. The peak shift for $d = 50\lambda$ (~ 120 nm in diamond) is still notable. However, it is deduced that the higher the d value, the more the peak shift will be reduced. For example, if the space charge width is $1\ \mu\text{m}$ in diamond then the shift between the $\theta = 0^\circ$ and $\theta = 85^\circ$ spectra for an $E_{bb} = 3$ eV is 0.012 eV. It means that for a great space charge width, the band bending phenomenon could remain undetectable even by changing the polar angle. Positively, the estimation of the E_{bb} through the maximum $BB(E)$ peak position is very reliable ($Diff = 3\%$ at $\theta = 85^\circ$). The differences between $BB(E)$ for the two space charge density solutions are higher at lower polar angles.

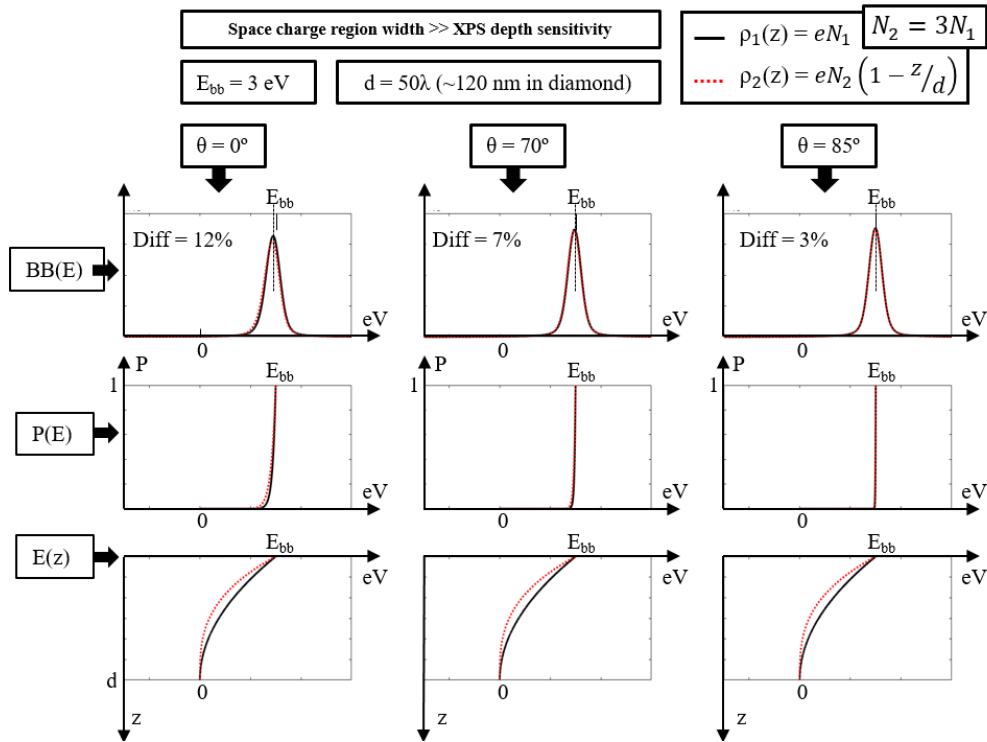


Figure 3.9: Simulated XPS band bending shapes for the case in which the space charge width well exceeds the depth sensitivity range at each polar angle. $BB(E)$, $P(z)$, and $V(z)$ are the band bending shape, the probability of escape of electrons, and the electric potential, respectively. The constant and the linear space charge densities results are compared ($\rho_1(z)$ (black lined) and $\rho_2(z)$ (red dotted), respectively) defined to reach the same band bending $E_{bb} = 3$ eV. All the functions are evaluated for $\theta = 0, 70$, and 85° . The parameter $Diff$ is related to the $\rho_1(z)$ solution (black lined) and is defined as the percentage difference between the $BB(E)$ maximum and E_{bb} .

3. The third set (Figure 3.10) is representing the case in which the space charge width is similar to the sensitivity depth at $\theta = 0^\circ$. Then, a very asymmetric peak shape is observed at $\theta = 0^\circ$. The peak shape will recover the symmetry as the polar angle increase. The shift of the $BB(E)$ maximum is also noticeable and the estimation of E_{bb} is similar to the second case ($Diff = 3\%$ at $\theta = 85^\circ$). The differences between $BB(E)$ for the two space charge density solutions are lower at higher polar angles.

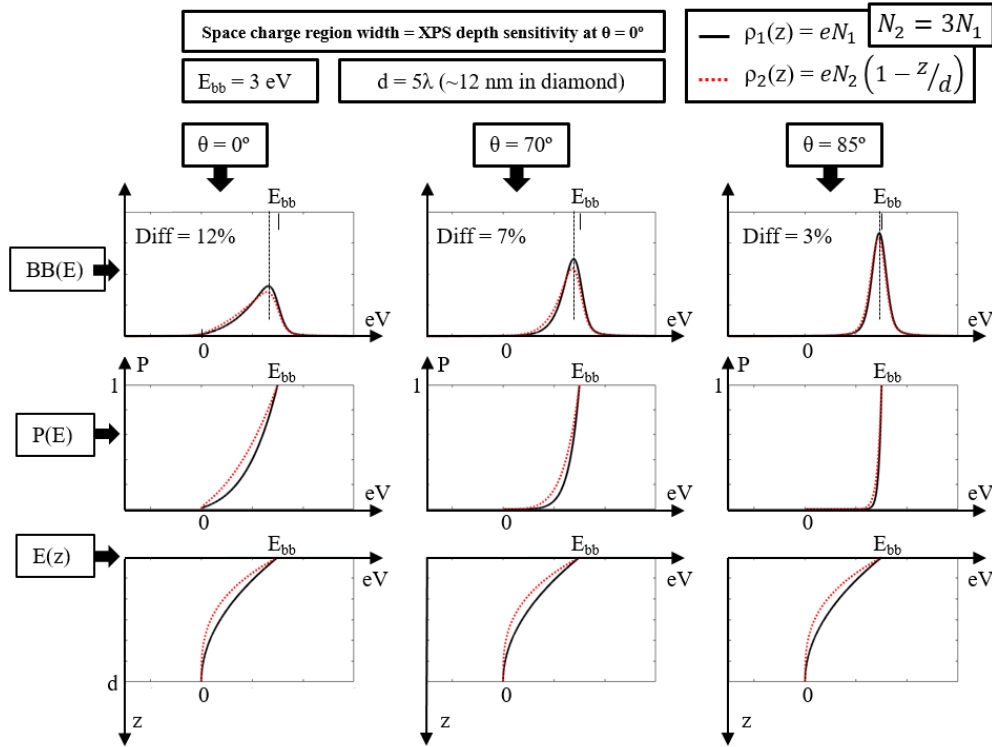


Figure 3.10: Simulated XPS band bending shapes for the case in which the space charge width d is close to the depth sensitivity at $\theta = 0^\circ$ ($d = 5\lambda$). $BB(E)$, $P(z)$, and $V(z)$ are the band bending shape, the probability of scape of electrons, and the electric potential, respectively. The constant and the linear space charge densities results are compared ($\rho_1(z)$ (black lined) and $\rho_2(z)$ (red dotted), respectively) defined to reach the same band bending $E_{bb} = 3 \text{ eV}$. All the functions are evaluated for $\theta = 0, 70$, and 85° . The parameter Diff is related to the $\rho_1(z)$ solution (black lined) and is defined as the percentage difference between the $BB(E)$ maximum and E_{bb}

Some general considerations about band bending shapes are highlighted:

- The more the space charge width d approaches to the depth sensitivity ($\sim 5\lambda \cos\theta$), the more asymmetric the peak shape will appear.
- The higher the polar angle the better the peak maximum position estimates the band bending E_{bb} .
- Analogously, the higher the space charge width d , the better the peak maximum position represents the band bending E_{bb} .
- The more the $P(E)$ expressions for different space charge densities approach each other the more similar its band bending shapes are. The discussion of the cases in which $P(E)$ expressions become similar, was given in Section 3.1.4.3.

An isolated $BB(E)$ shape will be indistinguishable from a fixed energy level shape when neither energy shifts nor asymmetry peaks under polar angle variation as well as no peaks with increased width can be observed. It will happen for 1) very low E_{bb} because the energy levels contributions will approach one each other and, hence, $BB(E)$ will tend to appear as a fixed energy level shape and, 2) large space charge width since the peak shift between polar angle

measurements becomes negligible. Reasonably, the problem will become more complex when other overlapping contributions come into play. Indeed, when the space charge width d is lower than the detection limit, at least two contributions should be expected from such experiment, one for the space charge region, $z \in (0, d)$, and other for the bulk region just below it, $z \in (d, \sim 5\lambda\cos\theta)$. This is the case in the next section analysis of a surface DBB.

3.1.5. The (100)-H-terminated ARXPS spectra: Results

3.1.5.1. Preliminary discussion and peak attributions

In this section, the chemistry and electronic phenomena on the (100)-H-terminated diamond are analysed by ARXPS experiments. The attribution of the XPS contributions is discussed and the possible presence of a surface band bending is considered. The recorded (100)-H-terminated diamond ARXPS C 1s spectra for $\theta = 0^\circ, 45^\circ, 70^\circ$, and 80° are shown in Figure 3.11. A detailed analysis of the corresponding depth sensitivity of these measurements is shown in Section 2.1.2.6.

The position of diamond bulk contribution is better estimated as the position of the maximum peak of the C 1s spectrum at $\theta = 0^\circ$, in which most of the signal comes from the bulk C 1s level. Since the UBB described by STD is defined far beyond the limits of the XPS depth sensitivity, it is expected to be detected as a shifted energy peak. Thus, diamond C 1s bulk contribution is found at 284.05 eV, which is very similar to previous results (Kono et al., 2015; Kubovic & Kasu, 2010). On the other hand, the C 1s XPS peak at $\theta = 0^\circ$ is asymmetric with a small tail towards higher BE . As θ increases, this tail becomes higher with increasing intensity with respect to the bulk contribution. This indicates the surface nature of this second contribution. The position of maximum C 1s peak lightly moves towards higher BE for increasing θ values. Very similar behaviour has been previously observed (Kono et al., 2019).

In order to find the origin of the surface contribution, a preliminary deconvolution of the C 1s spectra into two contributions, related to bulk and surface components, was made using a similar procedure to the previous works. For the deconvolution, the peak width necessary for the surface contribution fit was higher than that of the bulk contribution. All spectra were decomposed by considering the same bulk to surface energy width relation. After the deconvolution, the corresponding depth thickness of the surface contribution was estimated by using the intensity ratio of both contributions using equation (3.2). The estimation gave a ~ 10 ML thickness of the surface contribution (1 ML = 0.089 nm for (100)-diamond). Additionally, the surface contribution shifted towards higher BE with increasing θ while the bulk peak remains energy fixed.

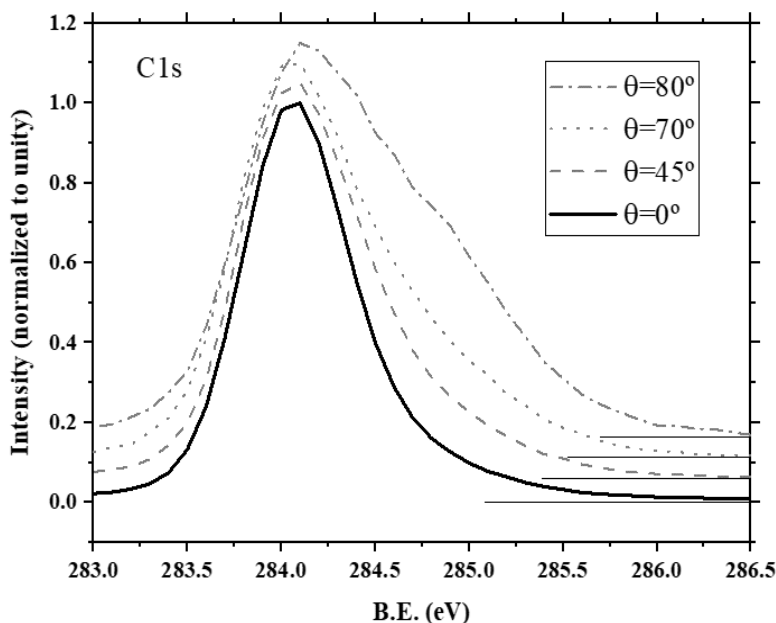


Figure 3.11: Normalized intensity ARXPS C 1s spectra of a (100)-H-terminated diamond for $\theta = 0, 45, 70,$ and 80° after background subtraction.

The attribution of the surface contribution is not straightforward and will be discussed. First, it must be noticed that ~ 10 ML is a very high value in comparison to the feasible ideal 1 ML hydrogen covering of the (100)-H-terminated diamond model. Thus, while the presence of C-H bonds is mandatory, another contribution should be considered. On the other hand, the high similarity of sp^3 C-C and C-H bonds polarity makes the topmost carbon atoms of H-terminated diamond have soft different polarities. For this reason, and in the absence of surface band bending, C-H contributions are expected at higher BE than the bulk but lower BE than the C-O contributions, this latter at $\sim +1$ eV from bulk. In any case, candidates in that energy range are scarce. The presence of defects and contamination is a very recursive candidate. However, the high reproducibility of this peak, even for different methodologies, raises the doubt about the attribution to surface contamination or defects. Indeed, other authors discarded the presence of contamination or damaged layers as-prepared *ex-situ* H-terminated samples (Bobrov et al., 2003; Tranvouez et al., 2009). In this sense, (100)-H-terminated diamond ARXPS C 1s spectra in (Kono et al., 2019) are very similar to that of Figure 3.11. Also, conventional XPS experiments on diamond show the presence of a tail towards higher BE which has been routinely attributed to C-H (Bobrov et al., 2003; Navas et al., 2018). It supports again the idea of the high reproducibility and repeatability of the energy position of this XPS contribution.

Among other explanation candidates for the surface contributions, one can assume that the bulk peak position is the consequence of a UBB as described in the STD model. Then the position of the surface contributions such as C-O will vary consequently towards lower BE ,

keeping constant its relative distances. Even in that case, C-O contributions are expected at ~ 285 eV which will not explain the spectra in Figure 3.11 because most of the surface contributions are closer to the bulk position. The chemical adsorbates related to the STD mechanism are discarded since most of them are not based on carbon, such as the water overlayer proposed in (Maier et al., 2000). The attribution of a similar peak to subsurface hydrogen in *Brovob et al.* was also discarded since it showed a clear shift that makes no sense for energy-fixed levels. In this sense, the fact that the surface contribution is shifted towards higher BE with respect to the bulk contribution at higher polar angles cannot be attributed to a fixed energy level candidate such as the ones discussed here.

At this point, the presence of a surface band bending XPS contribution as described in Section 3.1.4.4 is under discussion. First, note that the intensity of any XPS contribution depends on the depth range in which it is defined. Thus, if a band bending is defined from a fixed depth position, the higher the space charge width the greater its XPS contribution intensity is. Therefore, it can explain the detected ~ 10 ML signal. On the other hand, since the electric potential must be continuous, the energy positions of a surface band bending contribution are necessarily defined from the bulk energy towards the potential at the surface. If it is a DBB, then the related contributions will appear towards higher BE (and so the opposite for a UBB). It is in agreement with the energy position of the fitted surface contribution. Finally, the shape of a surface band bending XPS contribution will show an increased peak width as well as a shift towards higher BE when the polar angle is increased. This shift and width will depend on the definition of the space charge density. In any case, it explains the observed shift of the fitted surface contribution.

This attribution is in agreement with the observation in previous results (Kono et al., 2010, 2019). One of the arguments to justify the presence of DBB was literally that “(...) amounts of surface components well exceed the physically feasible amount of ~ 1 ML”. This observation is in agreement with the present results. However, in that case, the surface DBB characterization was made by tracking the C 1s maximum peak variation. Given the results in Section 3.1.4.4, it is reasonably applicable cases where the space charge width exceeds the XPS maximum sensitivity. Even in that case, a non-negligible error should be assumed. However, in the present case, the space charge width of the DBB region is expected to be much lower than the XPS sensitivity and, thus, it should be treated as an additional peak during the fitting process. Using the proposed method, the band bending curvature can be characterized not only in terms of the potential at the surface but also in terms of its width. In Section 3.1.4.4, we show that for a very short space charge width, the maximum peak position of a band bending contribution can hardly represent the real potential at the surface. As the polar angle increases and depending on the distance between bulk and surface peaks, the shift of the maximum C 1s peak is indirectly originated by the shift of the band bending peak as well as by the bulk-to-surface peaks intensity

ratio variation. It is then concluded that the measurement of the potential variation through the shift of the maximum C 1s peak is not very reliable in the present case. This fact will be demonstrated with an example in the next sections.

3.1.5.2. Sample model and peak deconvolution

Based on the previous discussion, the existence of a surface DBB contribution is assumed. The use of a constant space charge density as a good and reliable approximation for the characterization of a band bending shape when defined within a very short space charge width (below the XPS depth sensitivity at any polar angle) has been demonstrated (see Section 3.1.4.4).

At this point, the recorded spectra have been decomposed based on a model consisting of a diamond bulk region ($\text{Peak}_{\text{bulk}}$), a diamond with a DBB region (Peak_{bb}), and 1 ML of C-H (Peak_{CH}) XPS contribution (Figure 3.12). The relative intensities of the three peaks are obtained as in equation (3.2). The position of C-H_x contributions has been widely reported to be at $\sim +0.5$ eV from bulk contribution, however, the existence of a band bending near the surface will make the C-H_x contribution to be relative to the band bending E_{bb} . Thus, C-H bonds position was set to $+0.5 \pm 0.2$ eV from E_{bb} . The shapes of both $\text{Peak}_{\text{bulk}}$ and Peak_{CH} are Voigt distributions determined by their corresponding Lorentzian and Gaussian widths $wL = 0.2$ and $wG = 0.6$, respectively, and their intensities. The value of the Lorentzian width is taken from the previous report for a graphite sample (C. T. Chen & Sette, 1990) and is expected to be similar in this case. For wG the value was estimated from $\theta = 0^\circ$ spectrum as used in the preliminary deconvolution. For the $\text{Peak}_{\text{bulk}}$, it is considered that, even under the existence of a UBB due to the STD phenomenon, it is defined deep enough into the sample to be approximated as an energy-fixed level. This idea is supported by previous simulations in which the STD band bending effect should lie deeper into the surface in the order of hundreds of nanometers (Kono et al., 2010). The shape of Peak_{bb} is generated as described in Section 3.1.4.4 using the same wL and wG parameters.

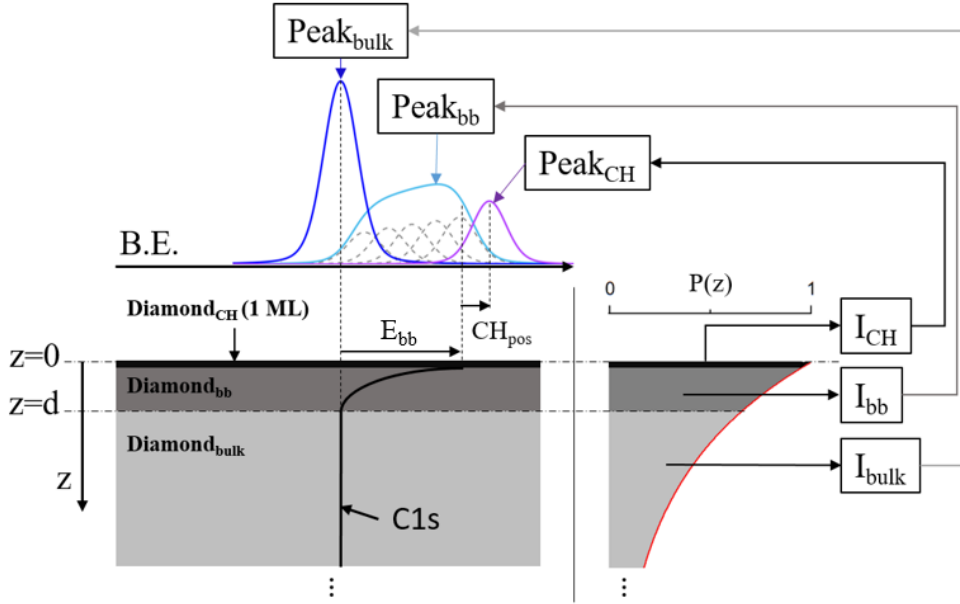


Figure 3.12: Schematic of the XPS model used for C 1s peak analysis. The sample is divided into three regions: diamond bulk ($Diamond_{bulk}$) for $z \in [d, \infty)$, diamond with band bending ($Diamond_{bb}$) for $z \in [1 \text{ ML}, d]$, and diamond surface C-H_x ($Diamond_{CH}$) for $z \in [0, 1 \text{ ML}]$. The relative intensities I_{bulk} , I_{bb} , and I_{CH} of the respective XPS peaks $Peak_{bulk}$, $Peak_{bb}$, and $Peak_{CH}$ are obtained as in equation (3.2). $Peak_{bulk}$ and $Peak_{CH}$ follow Voigt distributions while $Peak_{bb}$ is obtained from equation (3.24) (see Section 3.1.4.4) and is defined by its band bending width (d) and band bending (E_{bb}). The latter is set to the $Peak_{bulk}$ position. The $Peak_{CH}$ position (CH_{pos}) is defined relative to E_{bb} and is set within the range $+0.5 \pm 0.2 \text{ eV}$.

The photoelectron refraction effect was also taken into account, as it can be significant at higher polar angles. This effect makes detected photoelectrons come from lower angles of escape than the angle defined here as polar angle, reducing the depth sensitivity. An angular correction is included in the algorithm based on equation (2.3) (Fadley, 1984)(see Section 2.1.2.6.1).

The fitting process was carried out in MATLAB R2018b software. The algorithm search for the band bending parameters d and E_{bb} as well as the position of C-H peak (CH_{pos}) to get an optimal solution reducing the accumulated error of the four angles spectra. This solution is finally found for $d = 0.5 \text{ nm}$ and $E_{bb} = 0.67 \text{ eV}$. CH_{pos} was established at $E_{bb} + 0.37 \text{ eV} = 1.04 \text{ eV}$ from $Peak_{bulk}$. The resulting spectra deconvolution is shown in Figure 3.13. The fitted peaks have been normalized to the maximum. It is observed that the 1 ML signal corresponding to $Peak_{CH}$ is almost undetectable at low polar angles and only becomes noticeable from $\theta = 70^\circ$. The shift of the band bending peak is almost negligible but occurs mostly as a consequence of a more asymmetric peak. At $\theta = 80^\circ$, the bulk signal intensity becomes even lower than the band bending contribution.

The difference between measured and fitted curves can be originated from multiple reasons such as background subtraction process, polar angle positioning accuracy, roughness effect, or the discrepancy to the used space charge density simplification in equation (3.13).

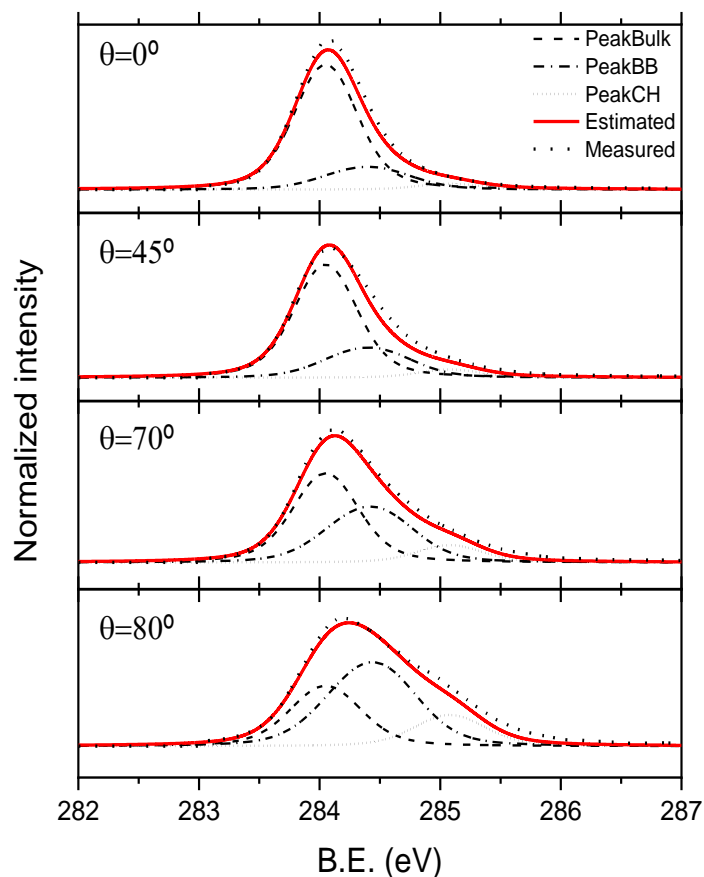


Figure 3.13: ARXPS C 1s measured spectra (black dotted) and accumulated deconvolution (red line). The deconvoluted spectra are composed of three peaks each: $Peak_{bulk}$ (dashed), $Peak_{bb}$ (dashed-dot), and $Peak_{CH}$ (short-dotted) corresponding to diamond bulk region, diamond space charge region and 1 ML of surface C-H, respectively. For the generation of the $Peak_{bb}$, band bending width, d , and band bending, E_{bb} , were found to be 0.5 nm and 0.67 eV, respectively. CH_{pos} was found at +1.04 eV $Peak_{bulk}$ position.

3.1.6. The (100)-H-terminated ARXPS spectra: Discussion

3.1.6.1. Maximum C 1s peak shifts reinterpretation

The interpretation of the band bending contribution through the observation of XPS peak shifts leads to contradictory conclusions than the present method based on band bending peak shapes. The shorter the bulk-to-surface peak energy distance the higher the shift of the maximum C 1s peak with polar angle increase will be. This is because the lower bulk-to-surface peak distance makes the increasing intensity of the surface peak more strongly influence the shift of the bulk peak.

In this work, with respect to the $\theta = 0^\circ$ fitting spectrum, the maximum of the simulated C 1s spectra for $\theta = 45, 70$ and 80° shows a shift of +0.01, +0.04, and +0.11 eV, respectively. Similar shifts were found in CVD sample “C(001)-H_Ra0.2”, being +0.01, +0.01, +0.04 eV for $\theta = 60, 72.5,$ and 85° , respectively in analogous experimental conditions (Kono et al., 2019). With respect to the latter, the bulk-to-surface peak distance is slightly higher than that of the present work. It is claimed here that the lower shift values found for the “C(001)-H_Ra0.2” sample are a

consequence of the higher bulk-to-surface peak distance. Additionally, higher surface roughness sample in the same work (“C(001)-H_Ra0.5”) show a lower bulk-to-surface peak distance, as well as increased maximum C 1s peak shifts: +0.06, +0.07, +0.08 eV for $\theta = 60, 72.5,$ and 85° , respectively, supporting this reasoning.

Table 3.1: Surface DBB values for different hydrogenated samples as obtained by three different methods: maximum C 1s peak shifts, band bending shapes, and bulk-to-surface peak distance. No data for band bending shapes simulations is available for external samples. Thus, an estimation is obtained by simulating band bending shapes with $d = 0.5$ nm whose position at $\theta = 72.5^\circ$ is equal to the bulk-to-surface energy distance at the same angle.

	S. Kono et al.		This work
Sample label	“C(001)-H_Ra0.2”***	“C(001)-H_Ra0.5”***	#H
Maximum C 1s peak shifts	0.06 eV	0.21 eV	0.16 eV
Band bending shapes	0.67-1.2* eV	0.67-0.8* eV	0.67 eV
Bulk-to-surface peak distance	0.84 eV ($\theta=72.5^\circ$)	0.56 eV ($\theta=72.5^\circ$)	0.54 eV ($\theta=70^\circ$)
* values ranges are estimated using the present result and simulated band bending shapes for $d = 0.5$ nm for its position to be equal to the bulk-to-surface energy distance, both at $\theta = 72.5^\circ$. These shapes will overestimate E_{bb} . ** (Kono et al., 2019)			

Namely, using the band bending peak shapes method, the bulk-to-surface peak distance is interpreted as a higher DBB. Oppositely, under the interpretation of maximum C 1s peak shifts, more separated peaks lead to lower maximum C 1s peak shifts and hence a lower DBB potential is interpreted. Therefore, the method based on peak shifts estimates an $E_{bb} \sim 0.12$ eV for the present work, which is far from the $E_{bb} \sim 0.67$ eV by the proposed method. For the “C(001)-H_Ra0.2” sample an $E_{bb} \sim 0.06$ eV was estimated but, at this point, it was expected E_{bb} higher than the present work ($E_{bb} > \sim 0.67$ eV) because of the higher bulk-to-surface peak energy distance. Analogously, for the “C(001)-H_Ra0.5” sample, values are expected to be similar to the present work because the spectra peaks show similar energy distances.

Indeed, the bulk-to-surface peak distance will be a better estimator of the band bending than the maximum C 1s peak shift as shown in Table 3.1. Estimations made by the three different methods are there summarized for the samples revised. The results show a great contrast between the method based on maximum C 1s peak shifts and the proposed ones. It is concluded that the observed maximum C 1s peak shifts variation from one sample to another is a consequence of a reduction of the DBB and the consequent lower bulk-to-surface peak distance. This demonstrated the poor reliability of the surface band bending characterization method based on peak shifts when the space charge width is defined within the XPS depth sensitivity.

3.1.6.2. The bulk peak position as an upward band bending consequence

Previous work showed that the loss of the hydrogenated surface leads to a shift of the main C 1s bulk peak by thermal annealing. This shift was found as $\sim+0.5$ eV by thermal annealing at 950°C (Bobrov et al., 2003) and $\sim+0.6$ eV when annealed at $1030\text{-}1050^\circ\text{C}$ (Kono et al., 2009). It can be explained as a consequence of the loss of the UBB effect (described in the Kawarada model (see Section 3.1.2)) since it coincides with the dehydrogenation temperature founded by TPD experiments. This dehydrogenation supposes the loss of intrinsic SS effect. Since the mentioned experiments are carried out into UHV and the desorption of external molecules is expected to occur at lower temperatures, the STD model cannot explain this abrupt modification of the C 1s bulk peak. The vision of the H-terminated C 1s bulk peak position as a consequence of a UBB has been supported by other authors (Bobrov et al., 2003; Kubovic & Kasu, 2010). *Bobrov et al.* showed that the C 1s bulk peak shifted towards lower *BE* when the depth sensitivity was reduced and it was explained as a UBB effect. The UBB could even be higher than reported values since the bare diamond C 1s peak position is used as an energy reference and it could also be linked to a certain UBB.

As shown in this work, if the space charge width well exceeds the XPS depth sensitivity limit (~ 12 nm in diamond), then the band bending will appear as a shifted bulk peak of the main core-level. This shift is almost undetectable for H-terminated samples, indicating the very large space charge width of the UBB. By the simulation of isolated diamond XPS band bending shapes for $E_{bb} = 0.5$ eV (energy distance observed between H-terminated and clean diamond surfaces) with $wG = 0.5$ and $wL = 0.2$, it is found that space charge widths over around 200 nm will lead to undetectable UBB energy shifts (<0.01 eV) between 0 and 80° ARXPS spectra.

For the charge neutrality condition to be fulfilled the charge on the SS must be equal to that generated in the diamond bulk. Thus, the density of occupied SS, N_{ss} , necessary for the generation of this UBB condition, can be estimated assuming the Schottky approximation (constant space charge density) resulting in $N_{ss}=1.52\times 10^{10}$ cm^{-2} . This result shows the high sensitivity of diamond to the presence of a relatively low density of SS. Of course, a 0.5 eV UBB defined in a shorter space charge width would lead to a higher N_{ss} value. The present calculation is also in agreement with previous simulations showing that the UBB effect should lie deeper into the surface in the order of hundreds of nanometers (Kono et al., 2010). This is because the screen length in a wide bandgap semiconductor is high in comparison to narrow semiconductors. In summary, it is concluded that the $\sim+0.5\text{-}0.6$ eV shift of the main C 1s bulk peak from hydrogenated to bare (100) diamond is due to the presence of the UBB generated by intrinsic SS. This idea is in agreement with the Kawarada model.

3.1.6.3. Annealing effect reinterpretation based on downward band bending

Intermediate annealing steps, before the H-terminated reconstruction is lost, lead to a reduction of the surface-related photoelectron contributions (Bobrov et al., 2003; Graupner et al., 1998; Kono et al., 2010) as well as a higher insulate surface behaviour. *Bobrov et al.* suggested that the surface peak is related to the presence of subsurface hydrogen-related acceptors because it was found a direct relationship between the intensity of the surface peak and the electric transport deterioration. For this reason, the authors conclude that the amount of holes in the subsurface layer is linked to the amount of subsurface hydrogen, which is desorbed as an annealing consequence at intermediate temperatures. Moreover, *Graupner et al.* demonstrated a direct relationship between the intensity of the C 1s surface peak and the H₂ plasma temperature but no electrical measurements were carried out in that case to confirm its relationship with SA. This way, *Graupner et al.* considered that the surface component is due to adsorbed hydrocarbons such as methyl radicals.

Both observations are very similar and can be summarized as follows: 1) as-prepared samples show a surface peak analogous to that shown in this work. Its intensity seems to depend on the plasma conditions (Graupner et al., 1998); 2) Upon annealing at temperatures up to 750 °C the surface component is reduced till it becomes almost negligible. The loss of the surface peak intensity was related to the deterioration of the electric transport (Bobrov et al., 2003); 3) after annealing above this temperature bounded hydrogen desorbs and the bare 2×1 reconstructed diamond surface is formed, which is characterized by a new surface component towards lower *BE* related to the surface dimers and the bulk peak shift towards higher *BE* as discussed in the previous subsection.

Under the present work considerations, the loss of the surface peak should be understood as a reduction of the DBB generated by subsurface SA. Thus, the presence of subsurface hydrogen would be detected through the potential generated as a consequence of its ionization as a SA. To prove this, it must be noticed that, through the subsurface hydrogen desorption, the negative space charge density due to ionized SA will be reduced and surely also the space charge width. Thus, two effects must be noted in XPS under such a desorption process: 1) reduced intensity because of the space charge width reduction and 2) a shift towards lower *BE* as a result of the electric potential reduction. Remarkably, it was noted that these two phenomena are observed in (Bobrov et al., 2003). In that study, the surface peak decreased its intensity and is shifted towards lower *BE* with increasing temperature, as expected for a DBB contribution. These results support its relation to the presence of DBB due to SA. Unfortunately, not intermediate temperatures C 1s spectra were published in (Graupner et al., 1998) to confirm this claim.

It must be reminded here that the position of the C-H bonds XPS contributions must be placed at higher BE than the DBB contribution as it will shift accordingly to the potential at the surface. Thus, a shift in the DBB contribution results in a shift of the peak related to the C-H bonds. The intensity of this peak is expected to be under 1 ML as simulated in the present work.

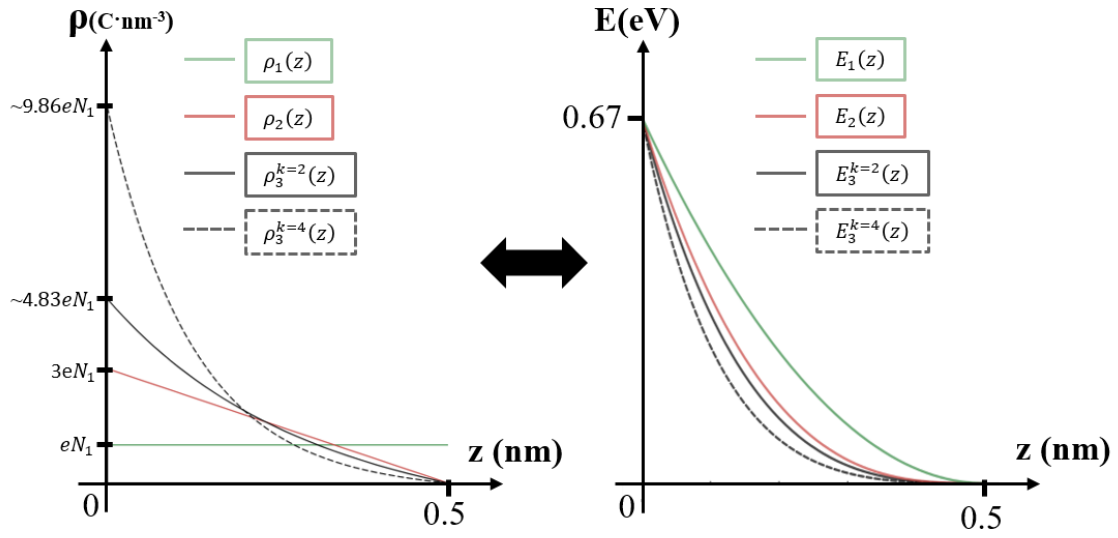
In conclusion, the fact that the surface DBB peak disappears before the H-terminated reconstruction is lost (surface C-H bonds desorption and bare 2×1 reconstruction), its relation to a deterioration of the electrical transport, and its behaviour upon intermediate annealing support the presence of DBB due to SA as stated by *Kono et al.* (2010).

3.1.6.4. Charge density estimation

As it has already been discussed, when a band bending contribution is defined within a very short space charge width, very similar XPS shapes are expected even for different space charge densities making it not possible to directly deduced it from spectra deconvolution. Therefore, the charge density deduced from the present XPS results (Figure 3.14.) will depend on the assumption of a specific space charge density which can be obtained from equations (3.12), (3.17), (3.21) and other analogous results. The band bending parameters can describe multiple band bending curvatures (Figure 3.14 (Right)), generated by charge density distributions showed in Figure 3.14 (Left), all of them compatible with the present XPS results. For the calculations, a dielectric constant of 5.5 was considered for diamond.

These results are compatible with previous experiments. Namely, a SA density of $\sim 10^{13} \text{ cm}^{-2}$ was estimated by using the Schottky approximation for the space charge density, that is, a constant charge distribution (*Kono et al.*, 2010). Comparing it with the present result for the constant space charge density ($8.15 \times 10^{12} \text{ cm}^{-2}$) it is found a good agreement. In another previous result, a hydrogen density of $\sim 10^{13} \text{ cm}^{-2}$ with an exponential decay space density over the first 1.5 nm depth was found (*Kimura et al.*, 2001). Considering that each hydrogen atom only produces a SA, it is also in agreement with the present results. In this sense, the density of SA can be higher than that of subsurface hydrogen. Subsurface deuterium of $1.7 \times 10^{15} \text{ cm}^{-2}$ at the diamond surface and decreasing trend within the first 0.5 nm was found for deuterated CVD surface (*Bergmaier et al.*, 2001). For the latter, a background of hydrogen and deuterium in the order of $\sim 10^{12} \text{ cm}^{-2}$ is claimed as common evidence in diamond. This experimental data points up to the possible relation of subsurface hydrogen, the XPS surface contribution, and DBB. However, the confirmation or not of this claim still requires the realisation of new complementary experiments. Note that samples in the present experiment are under UHV condition and, thus, the STD mechanism cannot be activated while other mechanisms such as intrinsic SS due to hydrogen bonds are possible, as proposed by *Kawarada et al.* (1996) Thus, the estimated charge density is independent of the STD mechanism here. The characterized DBB is originated in other

mechanisms such as SA as proposed by *Kono et al.* The origin of this DBB and the charge distribution related to it requires additional and focused experiments before being clarified.



Space charge density approximation, $\rho(z)$	Surface charge density [$\text{C}\cdot\text{cm}^{-2}$]
Constant (ρ_1)	8.15×10^{12}
Linear (ρ_2)	2.45×10^{13}
Exponential approx. ($k = 2$) ($\rho_3^{k=2}$)	3.93×10^{13}
Exponential approx. ($k = 4$) ($\rho_3^{k=4}$)	8.03×10^{13}

Figure 3.14: Surface charge density estimation from ARXPS band bending deconvolution results. Band bending curves ($E_1, E_2 \dots$) (Right side) obtained for different space charge densities ($\rho_1, \rho_2 \dots$) by solving the Poisson equation (Left side) as obtained to be compatible with the ARXPS result: band bending of 0.67 eV and space charge width of 0.5 nm. The surface charge density in second column is calculated by using equation (3.12), (3.17) and (3.21), according to each space charge density approximation, and using the estimated band bending parameters. For this calculation, diamond dielectric constant was set to 5.5.

3.1.6.5. Surface band bending, roughness, and sheet resistance correlation

For the samples analysed by *S. Kono* (2019), it was also found a correlation between measured roughness, sheet resistance, and the DBB (See Table 3.2). The lower the roughness, the lower the sheet resistance, and the higher the band bending observed in XPS. The effect of increased roughness on the widening of XPS peaks is discarded since it follows the opposite trend.

Table 3.2: Arithmetic average roughness (S_a), sheet resistance, and E_{bb} for two samples (Kono et al., 2019). The E_{bb} is estimated by using the bulk-to-surface peak distance what tends to overestimate its value but has been shown as a good approximation in Section 3.1.6.1.

	S_a (nm)	Sheet resistance ($K\Omega/sq$)	E_{bb} (eV)
“C(001)-H_Ra0.2”	0.2	11	0.84
“C(001)-H_Ra0.3”	0.3	24	(not published XPS data)
“C(001)-H_Ra0.5”	0.5	40	0.56

First, it is worth noting that the sheet resistance at a given temperature is expected to be inversely proportional to the hole mobility and the carrier density. Additionally, the hole mobility is dependent on the ionized acceptor scattering, among other effects. On one hand, a high density of ionized SA would harm the hole mobility as a result of Coulomb interactions between carriers and the ionized impurities. On the other hand, the higher the density of ionized SA also means the higher carrier density.

From the results in Table 3.2, a higher band bending means a higher concentration of ionized SAs (reducing hole mobility) and also a higher carrier density. Assuming constant hole mobility, Kono *et al.* (2019) deduced a reduction of the carrier density that agrees with the presented DBB trend. Without considering the roughness effect, the observed relation is compatible with a reduction of the sheet resistance under the assumption of the carrier density effect is dominant over the hole mobility reduction in modifying the sheet resistance. In this sense, a direct relationship between increased hole density and reduced hole mobility has been consistently reported for H-terminated diamond SCL ((Wade et al., 2017) and references therein) which is in agreement with the present discussion.

Concerning the roughness effect, the discussion becomes even more complex since the mechanism for roughness to modify the conductivity remains uncertain. In this sense, increased surface conductivity with increased surface roughness was observed in previous reports (Crawford et al., 2018; Wade et al., 2017) These results are contradictory to those analysed by Kono *et al.* (2019) in which the sheet resistance increases with sample roughness what can be related to the different ambient conditions during measurements. Wade *et al.* (2017) attributed the decreasing sheet resistivity at higher roughness to an increase in “surface activation sites” which in turn led to an increase in carrier density by the STD model. However, Crawford *et al.* (2018) found that the carrier density remains the same and, thus, a hole mobility enhancement would be involved in the sheet resistance reduction. For the latter, increasing power plasma was used to obtain increased surface roughness. Thus, the hole mobility enhancement was attributed to the “removal of surface defects as part of a more aggressive hydrogen-termination process”

(Crawford et al., 2018). At this point, the analysis of such a complex phenomenon requires new experimental results to analyze the correlations between DBB, surface roughness, and sheet resistance (carrier mobility and carrier density).

3.1.6.6. Final comments

From the present discussion, a reinterpretation of the H-terminated C 1s photoelectron spectra is given as follows: The C 1s spectra are composed of three contributions: bulk, surface DBB, and C-H bonds. The position of the bulk contribution is the result of a UBB due to the presence of SS close to the VBM. Thus, SCL models based on fermi level pinning due to intrinsic SS support this bulk peak attribution. Secondly, a DBB occurs at the very near surface with high reproducibility. The related peak is attributed to the presence of SA as supported by DBB/SA model. Finally, the C-H bonds peak will appear relative to the surface potential that, in turn, is modified by the surface band bending.

Based on all the obtained results, the STD-based model explains the presence of modifiable UBB under the presence of different ambient conditions, as widely reported. However, this UBB is also induced by the presence of unoccupied intrinsic SS that are inherent to the presence of C-H bonds (Bobrov et al., 2003; Kawarada, 1996). The detection of surface DBB deduced in this work supports the hypothesis that ionized acceptors exist at the subsurface region, although its origin remains uncertain. The combination of these intrinsic SS with the presence of SA is enough to explain the superficial conduction in undoped diamond, without the need for a large UBB curvature (high density of SS). On the other hand, it is necessary to understand how the intrinsic SS interacts under the presence of extrinsic ones to explain the carrier conductivity variations when the surface is subjected to different environments. If this effect induces an increase of SS acceptors density, then a greater upward band curvature occurs, modifying the conductivity of the accumulated holes and, thus, explaining the STD observations.

3.1.7. Summary of the section

The SCL generated by the hydrogenation of diamond surface is still a very controversial topic. Various models have been proposed to explain this unique phenomenon. The STD, intrinsic SS, and DBB due to SAs are the most highlighted mechanisms that explains the SCL.

The presence of DBB has been recently reported and its characterization was mainly based on ARXPS technique. The present work exhibits a discrepancy with the methodology used for this previous characterization which motivate the development of a new method of band bending characterization for photoelectron spectroscopy. The method considers that a band bending region must be seen as an isolated contribution whose shape is defined as the deconvolution of a Voigt distribution and the probability of escape of electrons as a function of its energy. To obtain this, first, an expression of the electric potential is deduced by solving Poisson's equation. The description of a band bending shape is exhaustively shown and its dependence on the definition of main parameters discussed.

Based on this method a DBB of 0.67 eV along the first 0.5 nm has been estimated. Previously published methods lead to a 0.1 eV DBB and do not any information about the space charge width. Therefore the present work demonstrates that previous method based on C 1s maximum peak is not reliable when the band bending is defined with the XPS maximum depth sensitivity.

The findings are in wide agreement with the DBB model. Indeed, this model is compatible with those based on the presence of SS which generates a UBB. Band bending is linked to the presence of SAs that has been tentatively related to subsurface hydrogen presence. Finally, the combined effect of SS (extrinsic and/or intrinsic) and the presence of SAs very near the surface can explain most of the experimental phenomena of the H-terminated diamond SCL.

Resumen de la sección

La conducción superficial generada por la hidrogenación de la superficie del diamante sigue siendo un tema de gran controversia. En la literatura se han propuesto varios modelos para explicar este fenómeno único. La transferencia superficial de carga, la presencia estados de superficie intrínsecos y la flexión de bandas hacia abajo debido a los aceptadores superficiales son los mecanismos más prometedores utilizados para explicar esta conducción superficial.

Recientemente la presencia de una flexión de bandas descendente ha sido caracterizada principalmente basándose en la espectroscopia de fotoelectrones de rayos X en el modo de ángulo resuelto. Una discrepancia con la metodología utilizada previamente para esta caracterización, ha motivado aquí el desarrollo de un nuevo método de caracterización de flexión de banda para la espectroscopia de fotoelectrones. El método considera que una región de flexión de banda debe verse como una contribución aislada cuya forma se define como la convolución de una distribución de Voigt sobre una expresión de la probabilidad de escape de electrones en función de su energía. Para obtener esto, primero se obtiene una expresión del potencial eléctrico resolviendo la ecuación de Poisson. La descripción de la forma de un pico de XPS generado por una región de flexión de banda es discutida en base a sus parámetros de generación.

Basándose en este método, se ha estimado una flexión de banda hacia abajo de 0.67 eV a lo largo de los primeros 0.5 nm. Desde los métodos anteriores, se habría deducido una flexión 0.1 eV para el mismo experimento sin aportar información sobre la profundidad en la que estaría definido. En este sentido, demostramos que el método anterior basado en los desplazamientos del pico máximo de C1s no es aplicable cuando la flexión de la banda se define dentro de la sensibilidad máxima del experimento XPS.

Los hallazgos concuerdan con el modelo de flexión de banda descendente debido a aceptores superficiales. De hecho, este modelo es compatible con aquellos basados en la presencia de estados de superficie que generan una flexión de banda ascendente. La flexión de banda está vinculada a la presencia de aceptores poco profundos, lo cual se ha relacionado tentativamente con la presencia de hidrógeno bajo la superficie. Finalmente, el efecto combinado de los estados superficiales (extrínsecos y/o intrínsecos) y la presencia de aceptores poco profundos muy cerca de la superficie pueden explicar la mayoría de los fenómenos experimentales de la capa conductora de la superficie del diamante hidrogenado.

3.2. ARXPS study of the (100)-O-terminated surface

In this section, an overview of the (100)-O-terminated main results are first presented in Section 3.2.1. A summary of the previous XPS results on the O-terminated diamond is shown in Section 3.2.2, focusing on the frequent detection of a non-diamond contribution. ARXPS results are here used to characterize the transition from H- to O- terminated in Section 3.2.3.1. The deconvolution of the C 1s spectra of the (100)-O-terminated surface, as well as its quantitative analysis, is carried out in Sections 3.2.3.2 and Section 3.2.3.3, respectively. The ARXPS results and the attribution of the non-diamond C 1s contribution are discussed in comparison to previously published studies in Section 3.2.4. Finally, novel 1×1:O reconstruction models for the (100)-O-terminated diamond are proposed to explain the non-diamond surface contribution in Section 3.2.4.1.

The sample used in this Section corresponds to #O, which is described in Section 2.2.1. The experimental procedure details for the ARXPS experiment are summarized in Section 2.1.5.

3.2.1. The (100)-O-terminated surface

Oxygen termination is one of the most studied diamond chemical terminations. The oxygenation of the (100) diamond surface leads to very different surface properties in comparison to the H-terminated surface (Section 3.1.). Moreover, the range of surface oxygenation methods is wider than those used for hydrogenation what makes O-termination to involve many possible experimental setups, hindering the results analysis and drawing conclusions process. Fortunately, some results are compatible with most of the oxygenation treatments which point up to similar mechanisms occurring during the oxygenation process.

Concerning the surface reconstruction, a characteristic 1×1 pattern has been widely described using electron diffraction techniques for the oxygenated surface, in contrast to the 2×1 found on the hydrogenated and bare diamond surfaces (Baumann & Nemanich, 1998b; Hamza et al., 1990; Kono et al., 2019; Skokov et al., 1994; R. E. Thomas et al., 1992; Y. M. Wang et al., 2000; Zheng et al., 2001). As a matter of example, one of the most accepted 1×1:O reconstruction models is presented in Figure 3.15 (Left side)). This 1×1 pattern is observed either in acid-treated diamond surfaces (Baumann & Nemanich, 1998b; R. E. Thomas et al., 1992), oxygen exposed surfaces (R. E. Thomas et al., 1992; Zheng et al., 2001) as well as those treated by O-plasma, or VUV/ozone treatment (Teraji et al., 2014). The 1×1 pattern seems to be independent of the oxygenation treatment.

Oxygenation identification of the diamond surface was demonstrated by TPD experiments, among other techniques. These experiments show that the main desorbed species are CO₂ and CO with a very low-temperature difference. In this sense, CO is the major desorption

product seen in the (100) face, while small quantities of CO₂ are also observed (R. E. Thomas et al., 1992). Oxygen desorption in diamond surface occurs in a broad range of temperatures starting from ~400 °C with a maximum desorption rate at ~600 °C (Ando et al., 1993; R. E. Thomas et al., 1992).

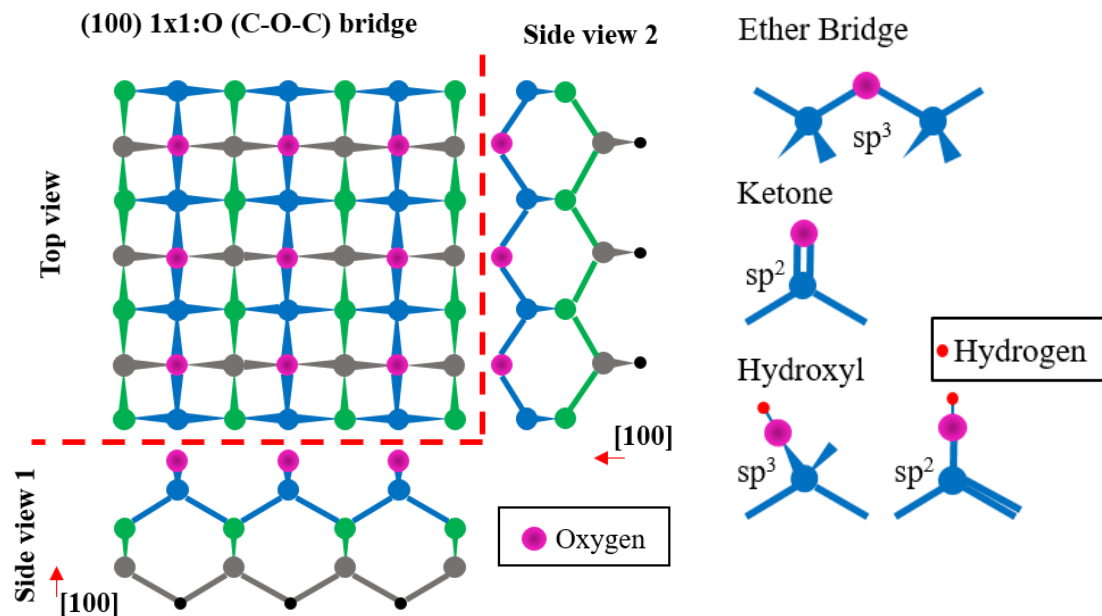


Figure 3.15: Schematic of the $1\times 1:O$ surface reconstruction of (100)-oriented diamond showing the four topmost carbon layers (Left side) and the main surface chemical group candidates (Right side). The showed $1\times 1:O$ reconstruction is based on ether-bridge oxygen configuration. Each surface oxygen atom (pink) is bonded to two carbon atoms of the first layer (blue atoms). Surface carbon atoms in this configuration are sp^3 hybridized. Other candidates are the ketone in which oxygen atom is double-bonded and hydroxyl in which carbon atoms can, in principle, exist in the sp^2 or sp^3 hybridization.

Ando *et al.* did not observe oxygen reaction occurring below 300 °C in the H-terminated diamond powder surfaces (Ando et al., 1993). In agreement with this result, Zheng *et al.* (2001) established that the $2\times 1:H$ to $1\times 1:O$ (100) reconstruction transformation occurs at 300 °C. Ando *et al.* (1993) also proposed that the oxidation of H-terminated diamond surfaces can be divided into three steps:

- (1) dehydrogenation (300-380 °C),
- (2) oxygenation (380-480 °C),
- (3) combustion (continuous oxidation with CO desorption) (> 500 °C).

Thomas *et al.* (1992) observed that the surface is etched after each CO desorption and oxygenation cycle which may lead to roughening of the surface and deterioration of the 1×1 pattern. The authors also noticed the apparent ability of atomic oxygen to break the C-C dimer bonds on the surface either of the bare 2×1 and the $2\times 1:H$ reconstructions required for the transformation to the $1\times 1:O$ reconstruction.

However, electron diffraction is not able to discern the possible bonding configurations for this 1×1 reconstruction, which remains controversial. Indeed, in principle, oxygen termination can exist in a variety of states (see Figure 3.15 (Right side)): ether-bridge (C-O-C), hydroxyl (C-OH), ketone (C=O), or a combination of all three (Fiori et al., 2014c; Laikhtman et al., 2003; Maier, Ristein, et al., 2001; Sque et al., 2006). The stability of those surface configurations is still not clear. Some theoretical results indicate that simple bonds C-O groups are the most energetically favourable for (100) diamond (Skokov et al., 1994) or even that the hydroxyl state is the most stable one (Long et al., 2008). Another study indicates that the ketone state is the most stable configuration for high surface coverage (Song & Larsson, 2015). Such disparity of surface configuration results from its dependency on oxygenation treatment. Acid and plasma treatments led to the formation of different chemical bonds forming a heterogeneous surface (hydroxyl, carbonyl, carboxyl, and ether-bridge bonds). The oxygenation methods based on UV radiation make the hydroxyl the dominant group (Boukherroub et al., 2005; Ohta et al., 2004; Torrenco et al., 2013). *Boukherroub et al.* observed an increase of the oxygen content in the H-terminated surface after UV irradiation in air for 2 h using a low-pressure mercury arc lamp, which was attributed to the formation of hydroxyl groups. The latter is in agreement with other results based on a high-pressure UV lamp in ozone enriched ambient on the (100) diamond surface (Ohta et al., 2004). Additionally, electrochemical oxidation promotes the formation of hydroxyl groups, as compared to UV enhanced methods (M. Wang et al., 2009, 2010). An exhaustive comparison of different oxygenation treatments shows that double-bonded oxygen groups only represent 5-10 % of the total oxygen signal (Klauser et al., 2010). From the quantitative point of view, UV enhanced treatments seem to yield lower coverages than other treatments (Klauser et al., 2010; Navas et al., 2018). According to the latter, studies on nanocrystalline diamond show increased oxygen concentration for acid treatments, followed by O₂ plasma and finally UV radiation in O₂ atmosphere (Speranza et al., 2011).

Whatever the oxygenation method is used, the presence of oxygen on diamond surface has a significant influence on its chemical reactivity (Foord et al., 2001), wettability (Kaibara et al., 2003), electrical conductivity, field emission (Koinkar et al., 2003; May et al., 1998; Tian, 1999), and SBH (F. Li et al., 2016, 2017). Moreover, oxygen termination is related to the appearance of a PEA, in contrast to the NEA of the bare and hydrogenated surface. This behaviour has been attributed to the C-O dipoles generated at the diamond surface. The NEA to PEA surface transformation must be understood as a function of the hydrogen and oxygen coverage. The PEA is expected to be very sensitive to the oxygenated chemical groups and some theoretical results point that higher PEA (~2.7 eV) should be present in the ether-bridge configuration (C-O-C) while hydroxyl (C-OH) and ketones should show a lower PEA value (Sque et al., 2006). However, realistic oxygenated surfaces exposed a PEA at least as higher as ~1.7 eV

(Maier, Ristein, et al., 2001). Deposition of other materials on diamond surfaces has been eventually related to the loss of the PEA surface (Baumann & Nemanich, 1998a) which could have important implications on the performance of diamond electronic devices.

O-terminated surfaces are also characterized for the absence of the SCL (see Section 3.1.2.). Thus, the resultant oxygenated surface bonding configuration causes the passivation of the diamond surface. This phenomenon must be taken into account when manufacturing electronic devices on diamond. For instance, if metal/diamond contacts are fabricated on the same hydrogenated surface (lateral or pseudo-lateral devices), then a surface p-type channel (the SCL) connecting all contacts is expected. Therefore, oxygenation of the diamond surface is necessary to electrically isolate these contacts and nullify the SCL. In this sense, VUV/ozone treatment proposed by *Teraji et al.* has shown to be very efficient to remove the SCL condition (Teraji et al., 2014; Teraji, Garino, et al., 2009). In contrast to other UV enhanced oxygenation treatments, the VUV/ozone treatment requires a high-pressure UV lamp. The results have been related to more homogeneous SS with higher reproducibility in comparison to that of acid-treated surfaces (Teraji, Garino, et al., 2009). This treatment also leads to higher SBHs and lower leakage currents than the chemical methods very probably for the lowered reactivity of the resultant O-terminated surface. For this reason, it has been widely applied for the fabrication of diamond-based SBDs.

The true effect of the UV enhanced oxygenation treatments is not fully understood and requires further investigation and discussion. It is more likely related to chemical or structural changes. As commented in Section 3.1.2., UV light exposition (low-pressure lamp) of the H-terminated surface leads to a recovery of the SCL conductivity in the 250 °C-750 °C temperature range (Riedel et al., 2004). Since it does not occur in UHV conditions, its attribution to an electronic effect of the UV radiation was discarded. The reaction of ozone with the surface was used to explain the SCL recovery by transfer doping through oxygen-related catalytic centers, i.e. partial O-termination. On the other hand, the presence of hydroxyl groups found for similar oxygenation procedure led other authors to consider the presence of electrostatic (CH⁺)-(OH⁻) pairs as the main candidate to occur as a consequence of the UV radiation in an oxygen ambient (Torrengo et al., 2013). These kinds of pairs would justify the recovery of SCL and its volatility at low-temperature annealing. The results could be also related to the claimed hydroxyl termination of the VUV/ozone-treated surface (Ohta et al., 2004). At this point, whether the use of a low-pressure or high-pressure UV lamp has a different effect on the diamond surface, remains unknown and new evidence are still necessary before concluding the true UV enhanced oxygenation effect on diamond surface.

Another interesting characteristic observation of the O-terminated diamond is the detection of a low non-diamond carbon content which has been probed based on several

techniques. This contribution has been systematically attributed to contamination, defects, or adsorbates. Its attribution requires an extended discussion of previous results and the evaluation of some relevant aspects of this contribution. For this reason, the next section is mostly dedicated to its detection by XPS and other techniques.

3.2.2. Previous XPS results in the (100)-O-terminated surface

On the way to understanding the chemistry of the O-terminated surfaces, XPS has been one of the most widely used techniques. It has been applied not only for the analysis of diamond surface chemistry but also for surface-related electronic phenomena (Alba et al., 2020; Cañas et al., 2020; Kono et al., 2015; Kubovic & Kasu, 2010). Unfortunately, quantification details and surface coverage criteria are not yet unified, making it even more difficult to compare results, which can sometimes be reduced to qualitative factors.

Regarding the C-O bonding configuration, XPS contributions are expected to appear either in the C 1s and the O 1s spectra. In this sense, C 1s spectra are normally used to distinguish whether XPS C-O contributions are recorded at the diamond surface. These C-O contributions are located at a higher *BE* than the diamond contribution. However, photoelectron C 1s energy levels are expected to be in the same energy range for single-bonded C-O chemical groups such as hydroxyl or ether-bridge, making it difficult to discern one from another. Double bonded oxygen groups such as ketones are expected at relatively higher *BE* and can be then well distinguished. In this sense, the XPS results point up that (100)-O-terminated diamond surface is characterized by the dominant presence of single-bonded oxygen groups such as hydroxyl or ether-bridge (Klauser et al., 2010; Kono et al., 2019; Navas et al., 2018; Strobel et al., 2008; Takeuchi et al., 2009). These results are related to the widely accepted ether-bridge 1×1:O reconstruction model. However, no marked qualitative differences between the oxygenation treatments can be deduced from the XPS results and other single-bonded oxygen groups such as hydroxyl can, in principle, participate in the 1×1:O reconstruction.

Remarkably, the presence of a non-diamond C-C bonds contribution in the C 1s XPS spectrum has been widely reported in O-terminated diamond (Gao et al., 2008; Kono et al., 2019; Kubovic & Kasu, 2010; Navas et al., 2018; Stacey et al., 2010, 2019; Strobel et al., 2008; M. Wang et al., 2009). This contribution appears at ~1-1.5 eV lower *BE* than the diamond contribution. Its origin remains under discussion yet but it shows a high reproducibility even for different oxygenation treatments. *Strobel et al.* (2008) report that this sp^2 contribution after 5 min of H₂O plasma and attribute it to the starting diamond graphitization process. In this sense, the diamond graphitization process has been extensively studied (Butenko et al., 2000; Davies & Evans, 1972; Petit et al., 2011), but its relationship with the oxidation process remains unclear. It is generally known that sp^2 bonded carbon is faster oxygenated than sp^3 bonded carbon and,

indeed, some results linked the early stages of oxidation of diamond films to sp^2 bonded carbon (Joshi et al., 1990). *Klauser et al.* (2010) and *Torrenzo et al.* (2013) compared different oxygenation treatments in polycrystalline diamond. XPS C 1s spectra showed the presence of a contribution at lower *BE*. This can be attributed, at least partially, to grain boundaries, i.e. non-diamond phase of polycrystalline diamond. *Klauser et al.* (2010) also studied (100)-oriented CVD diamond and the results were also compatible with the presence of an sp^2 contribution which was attributed to surface π -bonded carbon. *Takeuchi et al.* (2009) attributed this lower *BE* contribution to the reconstruction of the surface, although no models were proposed to confirm this assumption. In fact, on the bare (100) 2×1 reconstructed surface, such sp^2 bonding configurations with C=C double bonds or delocalized π electrons are reported in the literature (Bobrov et al., 2003; Graupner et al., 1998; Stacey et al., 2010). In this sense, *Stacey et al.* (2010) show a shoulder of the diamond C 1s peak at lower *BE* at the (100) diamond surface annealed at 1000 °C, which was consistent with the expected 1 ML of sp^2 carbon surface atoms for the bare reconstructed surface. It is also highlighted that the non-diamond contribution is not detected in H-terminated diamond in which, ideally, all carbons are sp^3 hybridized. This puts even more doubts on the origin of this sp^2 -like XPS peak inherent to the O-terminated surface.

On the other hand, most diamond XPS experiments in the literature are based on normal emission which, as detailed in Section 2.2.2., can not be sensitive enough to discriminate between the different surface bonding states. In this sense, the use of the ARXPS allows extrapolating with high accuracy the different surface contributions. Unfortunately, such an approach is rarely used (Alba et al., 2020; Denisenko et al., 2011; John et al., 2003; Kono et al., 2019; Pietzka et al., 2010) and most times with a lack of quantification analysis details. As in Section 3.1.3, it must be highlighted the comprehensive work made by *S. Kono et al.* that reviews most XPS data on (100) and (111) diamond surfaces and extends the study to the ARXPS analysis of acid-treated oxygenated surfaces. The results for the (100)-O-terminated diamond are similar to those previously reported. Again, a non-diamond contribution at lower *BE* was detected and, in this case, it was attributed to extrinsic hydrocarbons molecules absorbed on the surface. The result of the quantification shows that the total coverage of the oxygenated groups and the non-diamond component amounts to 3.23 ML, corresponding to 1.5 ML to the non-diamond component. Note that this non-diamond component would hardly be detected or quantified without the use of ARXPS measurements or a different photon energy source.

The appearance of this non-diamond C-C contribution is supported by other experimental techniques observations, some of which are summarized here. Namely, by Near Edge X-ray Absorption Fine Structure (NEXAFS) experiments, O_2 -dosed (100) diamond surfaces show a characteristic spectrum that allows to clearly differentiate it from other surface configurations such as bare reconstructed surfaces, H_2O -dosed treated, or H-terminated. Thus, O_2 treatment

induces new states at the surface, and, remarkably, a contribution at an analogous position to the characteristic C=C attributed to bare (100)-2×1 reconstructed diamond at ~284 eV is identified. This peak is not detected for H-terminated surfaces and has been attributed to defects (Shpilman et al., 2014; Stacey et al., 2010, 2019). By Raman spectroscopy, the observation of a broad contribution in the 1550-1580 cm⁻¹ range on acid-treated diamond surfaces indicates the presence of non-diamond sp² carbon presence (Joshi et al., 1990; Koinkar et al., 2003). This contribution is primarily reduced under acid treatment which has been related to the oxidation process starting in defective sites. By HREELS, a small feature is observed on oxygenated samples and was attributed to small amounts of surface graphitic carbon. The observation of these features coincided with the 2×1 to 1×1 LEED pattern transition and was attributed to the formation of C=C dimers because of its similarity to the bare (100)-2×1 surface. HREELS features at similar energy positions seem to be inherent in the oxidized surface (Pehrsson et al., 2002). Note that the latter results are in wide agreement with NEXAFS experiments. Thermogravimetry analysis (600-800 °C) exhibited a high initial diamond oxidation rate representative of sp² carbon, attributed to a relatively thin diamond-like carbon (sp²) layer (Joshi et al., 1990). Other indirect evidence is the increased oxidation rate of samples that are submitted to consecutive oxygenation and thermal desorption treatments which is related to the increased sp² content as a consequence of the oxygenation. Thus, the oxidation rates are directly influenced by the sp² content (Nimmagadda et al., 1990). Moreover, surfaces generated by desorption of oxygen have shown more reactivity than surfaces generated by desorption of hydrogen (Pehrsson et al., 2002; Pehrsson & Mercer, 2000). This fact can be also related to the remaining presence of sp² carbon generated during the oxidation process. Other studies pointed out that diamond oxidation is accompanied by the formation of a non-diamond carbon overlayer (Evans & Phaal, 1961) without a considerable increase in the overall oxygen content (M. Wang et al., 2009). Thus, by oxygen exposition of diamond surface, the graphitization was observed at temperatures much lower than those required for “true” graphitization and was claimed to result from surface oxidation (Davies & Evans, 1972; Pehrsson et al., 2002). It has been also found that surface sp² content plays an important role in the enhancement of field emission characteristics of CVD diamond films (Kang et al., 1997).

From all these results, a strong relationship between the diamond oxygenation process and the appearance of a non-diamond surface component is deduced. However, it was also found a lack of exhaustive characterization concerning its quantification, reproducibility, or comparative discussion focused on its attribution. For this reason, new experiments are required before providing new perspectives about their attribution. For this purpose, the (100)-O-terminated diamond surface XPS contributions are examined in the next sections.

3.2.3. The (100) O-terminated ARXPS spectra: Results

An understanding of the chemical and structural changes occurring during the oxygenation of the diamond surface is required to get control of diamond surface and interface properties for its application in power devices. The transition from H- to O-terminated diamond normally occurs in most experimental procedures for diamond electronic device fabrication. For this reason, the same (100)-H-terminated diamond surface, analysed in Section 3.1., was oxygenated. Therefore, the analysis is here focused on this transition as well as on the quantification of surface contributions and its comparison of the O-terminated diamond spectra with previous XPS results. First, the two chemical termination spectra are compared in Section 3.2.3.1. Then, the C 1s spectra of the (100)-O-terminated surface are deconvoluted in Section 3.2.3.2. Finally, the surface contributions are quantified by using a sample model in Section 3.2.3.3. The results are discussed in Section 3.2.4.

3.2.3.1. From H- to O-terminated (100) diamond surface

The ARXPS C 1s spectra for the H-terminated and the O-terminated (100)-diamond surface are compared in Figure 3.16. The H-terminated spectra correspond to that studied in Section 3.1.

Diamond bulk peak position and width are estimated from the 0° spectrum. At this polar angle, most of the XPS signal comes from the bulk region (up to ~ 10 nm depth as estimated in Section 2.2.2.), and thus, diamond bulk must be the main contribution. Diamond sp^3 carbon peaks for H-terminated and O-terminated diamond are located at ~ 284.05 eV and ~ 284.45 eV, respectively. This energy difference of ~ 0.4 eV, or even higher, between H- and O-terminated diamond has been widely reported in previous works but the reasons for this effect remain under discussion. In (Kubovic & Kasu, 2010) this C 1s maximum peak shift was related either to an upward band bending in H-terminated diamond related to the SCL phenomenon (see Section 3.1.2.) and to a DBB in O-terminated diamond. Indeed, it has been discussed in Section 3.1.6.3. how the position of the bulk contribution would be related to a band bending regarding the peak shift observations in H-terminated and bare (100) surfaces. This attribution is supported by other authors (Speranza et al., 2010). In any case, the band bending is expected to be defined deeper than the XPS depth sensitivity. This is because if the band bending would be defined within the XPS depth sensitivity, it will rather appear as another peak than a peak shift (see Section 3.1.4.4).

Moreover, the position of the diamond sp^3 peak is very reproducible even using different experimental setups and procedures. In this sense, most of the conventional XPS experiments (0° polar angle) in the literature were compared. Another very reproducible XPS feature is that the 0° C 1s spectrum appears asymmetric. This tail is defined towards higher *BE* (Figure 3.16, arrow A) in (100)-H-terminated diamond (Kono et al., 2019) and oppositely, towards lower *BE* (Figure

3.16, arrow B), in (100)-O-terminated diamond XPS studies, independent on the oxygenation treatment. The reason for these tails is, in fact, the presence of surface contributions. Thus, at 0° polar angle, these surface contributions have a very low intensity in comparison to the bulk contribution, which is only intense enough to transform the bulk peak into an apparent asymmetric shape.

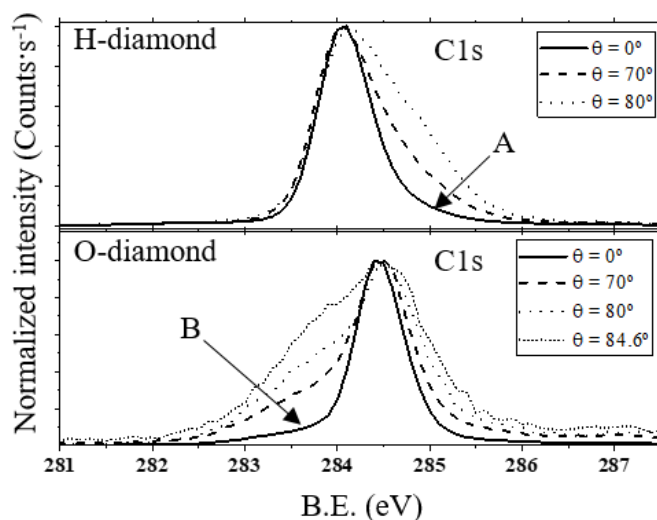


Figure 3.16: Normalized ARXPS C 1s spectra for H-terminated (top) and O-terminated (bottom) (100) diamond surface at different polar angles. The position of the maximum C 1s peak is shifted ~ 0.4 eV as widely reported in the literature. Surface contributions at higher BE are observable for higher polar angles in H-terminated diamond. Differently, O-terminated diamond shows surface contributions at both sides of the main peak. The contribution at lower BE is related to non-diamond C-C contributions. This component is not present in H-terminated diamond.

Surface contributions are clarified by the observation of higher polar angle XPS spectra (Figure 3.16). The increasing intensity of contributions along the tail energy positions (Arrows A and B) is observed. These new contributions are necessarily related to additional superficial contributions than the diamond sp^3 bulk. The evolution of these surface-related contributions is very different between H-terminated diamond and O-terminated diamond, which evidences a contrasting surface bonding configuration. All surface components are placed towards higher BE in the H-terminated surface which were attributed to surface DBB and C-H bonds in Section 3.1.5. Concerning the O-terminated one, it shows a big contribution towards lower BE and a smaller one at higher BE. For the latter, C-O contributions are the main candidates based on peak positions. The contribution at lower BE than diamond sp^3 carbon is related to non-diamond carbons with different chemical environments that can be compatible with defects or sp^2 hybridizations, contamination, and surface band bending, based on its energy position. The attribution of this peak is finally discussed in Section 3.2.4.

Regarding O 1s spectra, it must be noticed again that most of the oxygen quantification in the literature has been made by using the 0° polar angle XPS spectrum. At this polar angle, the

C 1s XPS signal comes from the first ~10 nm and most of the signal is related to diamond sp^3 contribution. Surface contributions are relatively very weak and, thus, atomic % O estimated from 0° polar angle (according to equation (3.25)) is not very accurate and does not give any representative information on the real oxygen coverage. It can be useful for comparison purposes but not for an accurate surface coverage determination. Using different polar angles (or different photon energy sources), variations of the different peaks can be observed, as performed in the C 1s spectra, and information from the surface-related contributions can be deduced. Moreover, the higher the polar angles (or the lower the photon energy source) the lower the depth sensitivity is and, thus, the estimated at. % O at high polar angles is more accurate and representative of the surface coverage.

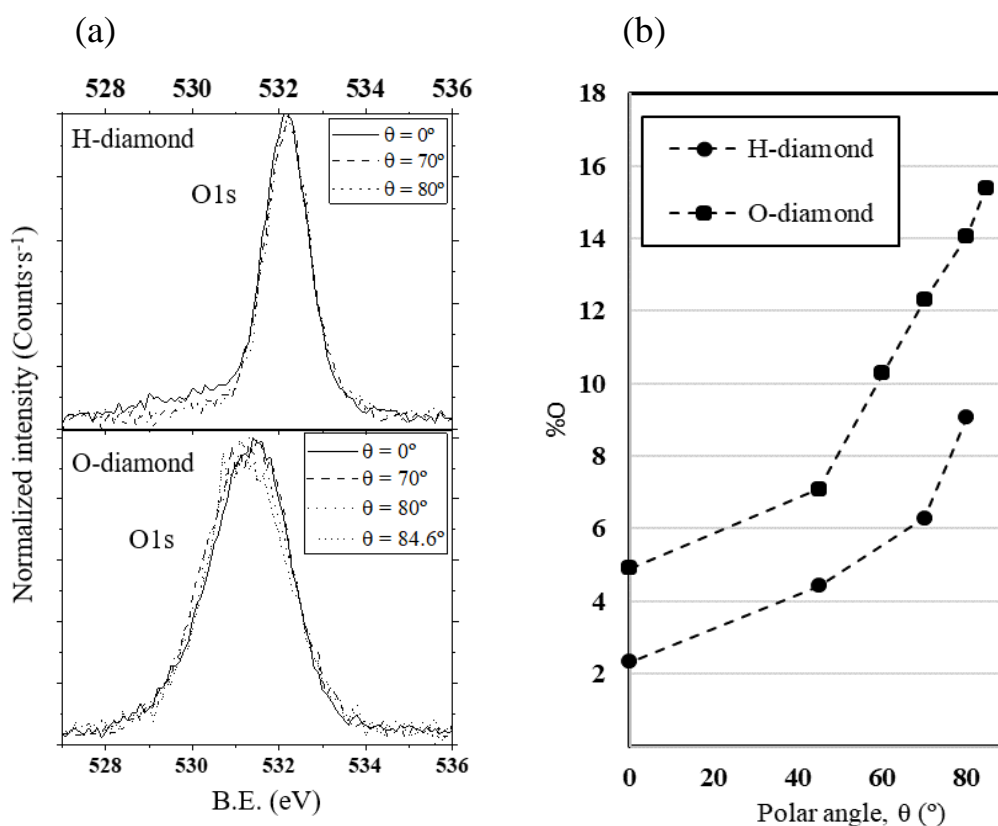


Figure 3.17: ARXPS oxygen data comparison for H- and O-terminated diamond showing: (a) Normalized O 1s ARXPS spectra: no qualitative variations are observed along with the sample depth. O-terminated diamond spectra show a wider O 1s peak shifted towards lower BE; and (b) Atomic % O obtained from equation (3.25): The O 1s contribution is higher for O-terminated diamond at every polar angle. The higher O 1s width and intensity in O-terminated diamond is related to the formation of surface C-O and C=O groups.

Normalized ARXPS O 1s spectra at different polar angles for H- and O-terminated diamond are represented in Figure 3.17(a). In both cases, the O 1s peak shapes remain mostly invariable for different polar angles which means that there are no qualitative variations along with the sample depth. It is worth noting that the width of the O 1s peak in H-terminated diamond

is nearly half that of O-terminated diamond. Moreover, the appearance of this new XPS contribution also causes the O 1s peak to shift towards lower *BE*. This enlargement of the O 1s peak could be in principle attributed to the formation of non-diamond carbon structures at the surface in O-terminated diamond and the consequent formation of C-O bonds. As commented in Section 3.2.2, it has been observed that the early stages of oxidation of diamond films are related to sp^2 bonded carbon (Joshi et al., 1990) and that surfaces generated by desorption of oxygen show increased reactivity (Pehrsson et al., 2002; Pehrsson & Mercer, 2000) related to the remaining presence of sp^2 carbon generated during the oxidation process. Moreover, the position and width of the O 1s peak in the present experiment is very similar to that previously reported for O-terminated diamond (Kono et al., 2019).

To quantitatively compare the oxygen contents of H- and O-terminated diamond, the atomic % O at each polar angle was deduced using:

$$\%O = \frac{I_{O1s}/RSF_{O1s}}{I_{C1s}/RSF_{C1s} + I_{O1s}/RSF_{O1s}} \cdot 100 \quad (3.25)$$

where I_{C1s} and I_{O1s} are the peak intensities for C 1s and O 1s spectra, respectively; and RSF_{C1s} and RSF_{O1s} are the relative sensitivity factors provided by the XPS manufacturer for C 1s and O 1s, respectively. The results are summarized in Figure 3.17(b). It must be noticed that, based on equation (3.25), a total coverage is related to a certain at. % O value which is, indeed, depends on the specification of a sample surface model. In any case, higher at. % O for all the polar angles is observed on the O-terminated diamond in comparison to H-terminated diamond, as expected. The value deduced for $\theta = 80^\circ$, related to the first 2 nm of the sample, is the most surface representative and, in that region, the at. % O for O-terminated diamond is 1.55 times that of H-terminated diamond. However, some caution must be put when comparing oxygen contents since these coverages can include partially adsorbed water molecules (Bobrov et al., 2003; de Theije et al., 2001). Thereby, previous XPS experiments show that oxygen coverage decreases after several days in vacuum which is attributed to the desorption of water molecules (Kono et al., 2019). In such a case, the water contribution can hardly be resolved from that of oxygen atoms chemically bonded on the diamond surface by observing the O 1s spectrum. Thus, only the observation of C 1s can give some information about the real presence of C-O contributions. From H-terminated diamond C 1s spectra (see Figure 3.16), the absence of C-O contributions according to the attributions made in Section 3.1., even at high polar angles led to think that most of the oxygen detected in H-terminated diamond is not chemically bonded to carbon. This idea is in agreement with the water overlayer model used to explain the STD model proposed in (Maier et al., 2000) and other observations (Kono et al., 2019). Oppositely, these C-O contributions can be clearly detected in the C 1s spectra for O-terminated diamond and, as will be shown in Section 3.2.3.2.,

their intensities are in good agreement with the O 1s intensity. For this reason, it is concluded that, while a partial water contribution cannot be discarded, most of the detected oxygen in the O-terminated diamond is chemically bonded to carbon atoms.

3.2.3.2. C 1s spectra peak deconvolution

The C 1s spectra deconvolution of the O-terminated diamond surface and their evolution with angle is shown in Figure 3.18. The deconvolution of the H-terminated diamond C 1s spectra was already discussed in Section 3.1.5. According to the previous section, four peaks have been used for the spectra deconvolution: sp^3 carbon (diamond); non-diamond carbon (related to sp^2 and defects); C-O simple bonds such as C-O-C bridges or hydroxyl (C-OH) groups and C=O double bonds such as ketones. The position of the oxygenated groups is expected around 285.5-286.5 eV for C-O groups and over 286.5-287 eV for C=O based on previous results (Klauser et al., 2010; Kono et al., 2019; Loh et al., 2002; Navas et al., 2018; Torrenco et al., 2013). The position of the non-diamond carbon bond is expected at 283-283.5 eV as discussed in Section 3.2.2.

Regarding XPS peak shapes, Voigt distributions were used. The Lorentzian width was fixed to 0.2 eV based on graphite lifetime broadening result (Sette et al., 1990), and the Gaussian width is dependent on spectrometer energy resolution and, in turn, on the polar angle. The dispersive monochromatic Al $k\alpha$ radiation is incident on the sample and the electron-lens system takes photoelectrons from the different size area of the sample depending on the polar angle. This makes energy resolution change and hence the Gaussian width of contributions is expected to increase with polar angle. In this sense, it was set for each polar angle using the Au $4f_{7/2}$ peak as a reference. The Gaussian width value for $\theta = 0^\circ$ for the diamond peak was set to 0.5. For the non-diamond carbon peak, the Gaussian width is higher than that of diamond contribution what, in principle, could be related to the presence of several carbon chemical environments. Thus, all these contributions are here integrated under the same “non-diamond” label. For this peak, the Gaussian width was set to follow an analogous width trend to that of the diamond peak. A summary of the main deconvolution parameters is shown in Table 3.3. The here observed energy distance between the diamond and the non-diamond contribution peak agrees well with previously published theoretical works related to sp^2 and sp^3 carbon contributions (Titantah & Lamoen, 2005).

Table 3.3: Parameters for the O-terminated diamond C 1s spectra peak deconvolution.

Peak attribution	Non-diamond C-C	Diamond C-C sp^3	C-O	C=O
Peak position (eV)	283.5±0.1	284.5±0.1	285.5±0.1	287±0.1
Gaussian width	(0.75-1.2)	(0.5-0.75)	(0.5-0.75)	(0.5-0.75)
$\theta = (0^\circ - 84.6^\circ)$				
Lorentzian width	0.2			

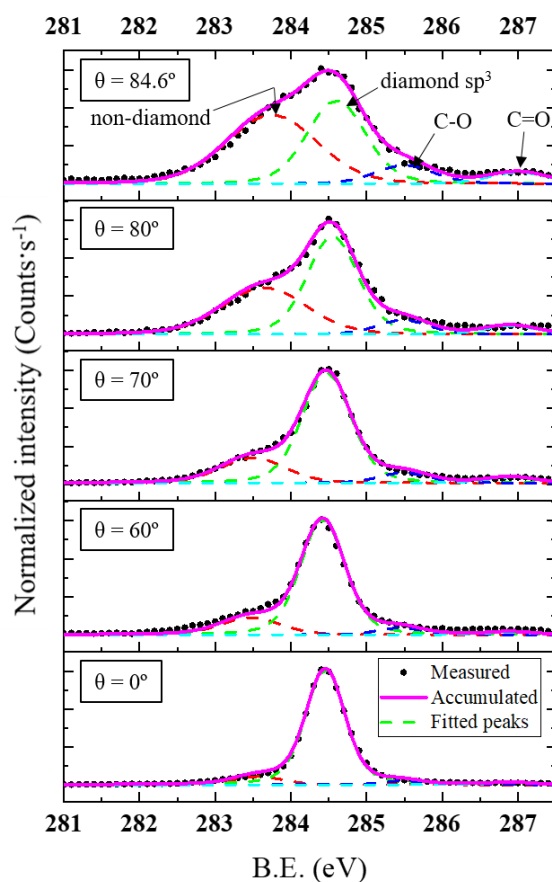


Figure 3.18: Normalized ARXPS C 1s spectra deconvolution of O-terminated diamond for different polar angles. Four peaks were considered in the deconvolution. From lower to higher BE: non-diamond C-C bonds, diamond sp^3 , C-O (simple bonds groups such as hydroxyl or C-O-C bridges), and C=O (double bonds groups such as ketone). The diamond peak is placed at 285.45 eV. The Gaussian width of the non-diamond peak is wider possibly because it is formed as the sum of various peaks related to diverse carbon chemical environments (hybridization, defects, etc...). The C-O and C=O areas matched well with the O 1s contribution.

3.2.3.3. Surface model and quantification

The XPS peak intensities are sensitive to the quantity of material emitting the XPS electrons and to the distance to the free surface. The relative intensity of each peak recorded during the XPS experiments follows this principle. In the previous section, three types of C 1s contributions were recorded: diamond sp^3 carbon atoms at ~ 284.5 eV, carbon atoms bonded to oxygen (C-O and C=O, at ~ 285.5 and ~ 287 eV, respectively), and finally, carbon atoms that are bonded to other carbon atoms but with chemical environment modified in terms of hybridization, chemical structure or presence of defects at ~ 283.5 eV.

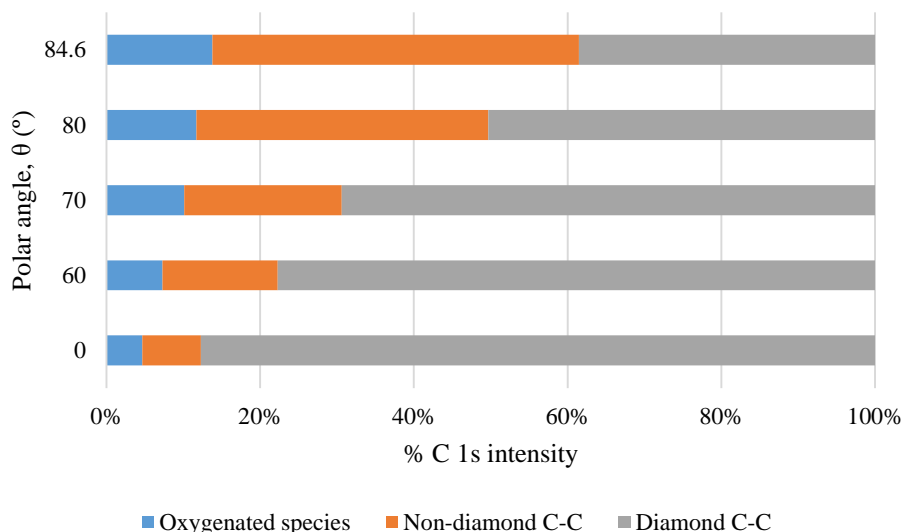


Figure 3.19: Relative C 1s peak intensity for different polar angles as obtained from ARXPS peak deconvolution, showing diamond C-C (grey), non-diamond C-C (orange), and the combination of C-O and C=O species (oxygenated species).

The relative C 1s intensity for each of these contributions at any polar angle was deduced from the deconvolution process in the previous section and is presented in Figure 3.19. The relative intensities are proportional to the number of each type of carbon chemical environment and their distance to the surface. Using these relative intensities, the resulting O-terminated diamond bonding configuration can only be deduced by the assumption of a specific sample model. From the observations pointing that oxygenation treatments modify the diamond surface in terms of low sp^2 contents, it is expected that the non-diamond and the C-O contributions are placed over the diamond one as can be deduced from the ARXPS C 1s relative intensity evolution in Figure 3.19.

For this reason, it was proposed, as a first approximation for quantification, to consider three homogeneous layers: (i) Layer 1: a superficial C-O / C=O bonding layer, (ii) Layer 2: a sub-surface layer consisting in partial modification of the diamond sp^3 bonding resulting from the oxygenation treatment; (iii) Layer 3: the bulk diamond. Figure 3.20 gives a schematic description of the layer configuration. These layers correspond to C 1s ARXPS contributions intensities as follows: Layer 1: C-O and C=O peaks; Layer 2: non-diamond peak; and Layer 3: diamond sp^3 peak. Homogeneous and atomically flat layers neglecting surface roughness and inhomogeneity effects are assumed. The effects of electron refraction have been considered (see Section 2.2.2.). For an extensive discussion of these effects and the validity of the above assumptions see (Fadley, 1974).

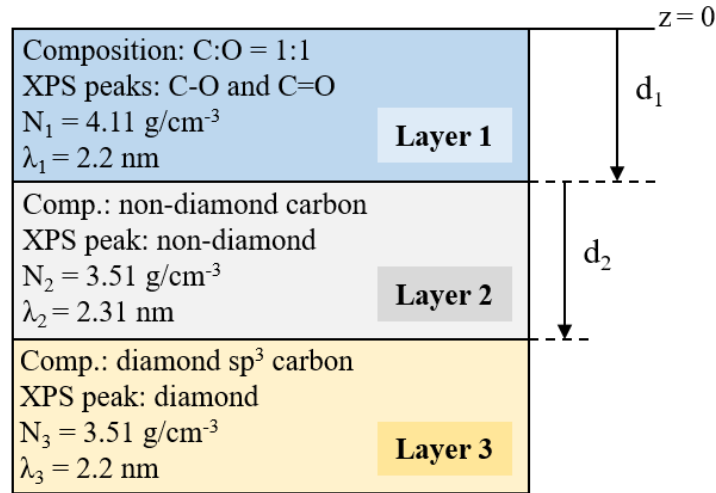


Figure 3.20: Schematic of the sample model and its representative parameters: Composition, attributed XPS peak, density, attenuation length, and thickness. The sample is divided into three layers: Layer 1: C-O bonds layer; Layer 2: non-diamond carbon-containing layer; and Layer 3: diamond bulk. The density of layer 2 and 3 were set to diamond values, $N_2 = N_3 = 3.51 \text{ g/cm}^3$. The density of Layer 1 was calculated using the atomic density of diamond, a C:O = 1:1 ratio, and the respective molar mass values for C and O. The attenuation length for Layer 2 was set to graphite value while for Layer 1 and 3 it was set to diamond value. Finally, d_1 and d_2 correspond to the thickness of Layer 1 and 2, respectively.

By considering this methodology, the thickness of Layer 1 and 2 can be estimated from any of the C 1s peak intensity ratios as widely used for metal-oxide thickness estimation (Bernstein & Grepstad, 1989). In this analysis, the peak intensities ratio I_1/I_2 and I_2/I_3 are estimated as follows:

$$\frac{I_1}{I_2} = \frac{N_1 \lambda_1}{N_2 \lambda_2} \cdot \frac{1 - \exp\left(\frac{-d_1}{\lambda_1 \cos\theta}\right)}{1 - \exp\left(\frac{-d_2}{\lambda_2 \cos\theta}\right) \cdot \exp\left(\frac{-d_1}{\lambda_1 \cos\theta}\right)} \quad (3.26)$$

$$\frac{I_2}{I_3} = \frac{N_2 \lambda_2}{N_3 \lambda_3} \cdot \frac{1 - \exp\left(\frac{-d_2}{\lambda_2 \cos\theta}\right)}{\exp\left(\frac{-d_2}{\lambda_2 \cos\theta}\right)} \quad (3.27)$$

where I , N , d , and λ refer to the XPS intensity, density, thickness, and attenuation length of a layer, respectively. The subscripts indicate the layers to which these properties are attributed. The densities for Layer 2 and Layer 3 were set to diamond values, which is $N_2 = N_3 = 3.51 \text{ g/cm}^3$. The attenuation lengths for Layer 1 and 3 were set to diamond value $\lambda_1 = \lambda_3 = 2.4 \text{ nm}$ while Layer 2 was set to graphite value $\lambda_2 = 2.5 \text{ nm}$. In this sense, the attenuation length of graphite is known to be very close to diamond despite the big density difference and has been estimated using the expression $\lambda_{\text{graphite}} = \lambda_{\text{diamond}}/0.95 = 2.5 \text{ nm}$ (Kunz et al., 2009; Shinotsuka et al., 2015). For Layer 1 the density has been obtained by considering the molar mass of oxygen and carbon and the atomic density of diamond, supposing that C-O layer composition is C:O = 1:1. A summary of the model parameters is shown in Figure 3.20.

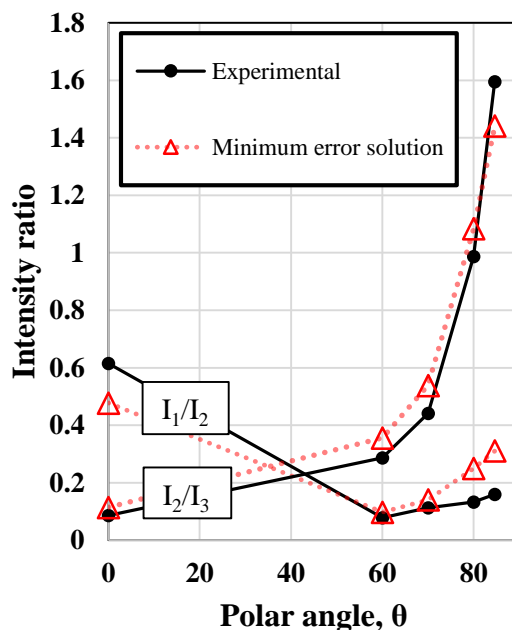


Figure 3.21: Graph showing the intensity ratios I_1/I_2 and I_2/I_3 obtained experimentally from XPS peak areas (solid line) and obtained by applying equations (3.26) and (3.27) (dotted lines) at different polar angles. The minimum error solution ($d_1 = 0.089$ nm and $d_2 = 0.237$ nm) is presented. The error is calculated as the sum of the errors of both I_1/I_2 and I_2/I_3 estimators at every polar angle.

I_1/I_2 and I_2/I_3 were then obtained experimentally from XPS peak intensities. Then, the value of d_1 and d_2 were optimized to reduce the sum of the errors of the estimators in equations (3.26) and (3.27) at every polar angle. The optimal solution occurs for the thickness values $d_1 = 0.089$ nm and $d_2 = 0.237$ nm. The experimental and theoretical values for I_1/I_2 and I_2/I_3 are presented in Figure 3.21. The value of d_1 corresponds to 1 ML what can be understood as full coverage of C-O and C=O bonds.

As can be seen, the proposed three-layer model fits well the experimental result. In this sense, the mixing of non-diamond and diamond carbon contributions intensities into Layer 2 was also considered but the solutions were not optimal. Also, the model of a contamination overlayer (non-diamond contribution is placed over C-O bonds) was considered resulting in higher error estimations.

On the other hand, the total area of oxygen peaks contributions in the C 1s spectra (C-O, C=O,...) has been compared to that of the O 1s peak area. By using the relative sensitivity factors, the total area of oxygen contributions in the C 1s spectra matches well to the corresponding area estimated from O 1s spectra. Thus, it means that all detected oxygen can be attributed to diamond surface C-O and C=O bonds.

3.2.4. The (100)-O-terminated ARXPS spectra: Discussion

Based on the present results, it is concluded that the transition from H- to O- terminated diamond as observed in XPS is mostly defined by:

- a. A C 1s peak maximum energy shift of +0.4 eV (this work) or higher (other works). Possibly related to upward (H-terminated) and DBB (O-terminated) defined beyond the XPS detection limit.
- b. New C 1s C-O/C=O contributions at higher *BE* than diamond peak, with dominant C-O contribution. The coverage has been quantified as ~1 ML.
- c. New O 1s component, deduced from the increased peak width and chemical shift towards lower *BE*. It is mostly attributed to C-O bonds due to its intensity well correspondence to C 1s C-O/C=O bonds.
- d. New C 1s non-diamond C-C contribution at lower *BE* than the diamond peak. This contribution corresponds to ~2.67 ML and is placed deeper than the oxygenated species. Thus, the non-diamond C 1s peak should be directly related to new oxygenated species. It is deduced from the better fitting of the proposed sample model to the experimental XPS results.

It must be noticed that these conclusions are compatible with previous XPS reports described in Section 3.2.2., since O-terminated diamond spectra show a high reproducibility. Unfortunately, not many surface-sensitive XPS studies on O-terminated diamond are available for surface contributions analysis and data comparison. In this sense, an ARXPS experiment carried out on acid-treated boron-doped (100)-diamond surface was recently reported (Kono et al., 2019). In that work, C 1s spectra exhibit the same four contributions described here. Even more, the reported O 1s spectra match well in position and width with that observed in this work. Concerning oxygenated groups, the present results are in agreement with the bonding configuration generally accepted in the literature for the O-terminated surface in which single-bonded oxygen groups are dominant.

The attribution of the non-diamond peak requires further discussion. As summarized in Section 3.2.2, most authors attributed it to surface defects (C=C), adsorbed hydrocarbons, or contamination, and only *Takeuchi et al.* (2009) linked it to the 1×1:O reconstruction of the (100)-O-terminated diamond, analogously to the widely accepted attribution of similar contribution found in the bare (100) 2×1 surfaces (Bobrov et al., 2003; Graupner et al., 1998). Following, it is here analysed if the possible attributions considered in the literature (defects, contamination, adsorbed hydrocarbon overlayer, and reconstruction) can correspond to our experimental results.

First, the present results show that the oxygenated surface fits well with a non-diamond subsurface layer model (C-O over non-diamond) rather than a contaminated overlayer (non-diamond over C-O). Thus, the ARXPS results are in principle incompatible with any overlayer attribution. It has been also shown here how this non-diamond peak is absent for the H-terminated diamond fabricated on the same substrate *ex-situ*, i.e. with analogous exposition to air than the O-terminated diamond. It leads to thinking about why should contamination or adsorbates be preferentially present on O-terminated diamond and not in H-terminated diamond. Even if the systematic contamination of oxygenated samples can occur in *ex-situ* oxygenation experiments, *in-situ* oxygenation of H-terminated or bare reconstructed surfaces points up to the appearance of non-diamond content which, in that case, cannot be explained by contamination or adsorbed species, e.g. (Shpilman et al., 2014).

Another crucial argument is that non-diamond peak is detected with high reproducibility. Indeed, most XPS results of (100)-O-terminated diamond in the literature show a characteristic tail towards lower *BE* at 0° C 1s spectra which has been here related to a surface non-diamond contribution by ARXPS. Thus, high reproducibility of this peak observation even using different experimental procedures, e.g. VUV/ozon treatment or acid treatment (Navas et al., 2018) or the use of CVD (Kono et al., 2019) or HPHT (this work) diamond surfaces lead to think that this contribution exists as a consequence of the oxygenation process. Note that the reproducibility is not only qualitative but also quantitative since the tail is normally showing similar relative intensities with respect to diamond contribution. For instance, the present results find the total surface contributions amounts are similar in two ARXPS studies: 3.23 ML (Kono et al., 2019) and 3.67 ML (this work). Additionally, the energy distance of the non-diamond to the diamond C 1s contributions is also highly reproducible. This fact is an indication of an electronic connection between both contributions which cannot exist between diamond and a contaminated layer.

All these results are also supported by other techniques observation summarized in Section 3.2.2, which definitively, leads to conclude that the diamond oxygenation process is mostly linked to the formation of non-diamond carbon structures at the subsurface region. For this reason, it is fully discarded that this contribution totally comes from external sources such as contamination or adsorbates. The low contents of non-diamond contributions, its high reproducibility together with the fact that the oxygenated surface is commonly characterized by a 1×1 reconstruction pattern evidence that the non-diamond contribution occurs homogeneously along the (100) surface, regardless of oxygenation treatment. For all these reasons, we proposed here that the non-diamond contribution must be, at least partially, attributed to the inherent 1×1:O reconstruction, as claimed by *Takeuchi et al.* (2009), in the same way, that it has been reasonably done for the bare 2×1 reconstructed surface.

In this respect, most of the proposed 1×1:O reconstruction models up today are based on fully sp^3 hybridized carbon configurations. These reconstruction models have been mostly supported by the evidence of oxygen bonding configurations (C-O-C, C-OH, C=O) widely detected by several experimental techniques. Also by the theoretical calculations concerning the stability of different oxygenated groups which in turn were based on these fully diamond sp^3 hybridized models. The appearance of non-diamond carbon has been systematically ignored when considering reconstruction candidates. This way, the 1×1:O models based on fully sp^3 hybridized carbon are not representing realistic O-terminated diamond surfaces because they are omitting the evident non-diamond carbon presence.

3.2.4.1. Towards new 1×1:O reconstruction models

The optimal solution, as deduced in Section 3.2.3.3., supports that the carbon atoms just below the oxygenated carbon layer are in a different chemical environment than that of the diamond as discussed previously. Furthermore, from the previous section discussion, it is concluded that the non-diamond contribution is inherent to the oxygenated surface reconstruction that should include the presence of carbon atoms in a non-diamond chemical environment. In this sense, most of the proposed (100) 1×1:O reconstructions models in the literature are based on a full sp^3 hybridized carbons structure.

One of the most accepted 1×1:O models is based on C-O-C bridges (Pehrsson et al., 2002; Zheng et al., 2001) (see Figure 3.22 (Top-Left side)). However, as well as other possible reconstructions based on sp^3 carbon (Nakamura & Ito, 2005) it is not compatible with the experimental evidence of non-diamond carbon contributions. In this sense, another possible reconstruction, based on ketone groups, in which the top layer atoms are sp^2 hybridized, is here not considered. This reconstruction is discarded because of the dominant single-bonds oxygenated species widely reported. Ketone groups can be easily detected in XPS and are known to represent less than 10 % of the oxygenated species. Therefore, the presence of non-diamond carbon subsurface contribution cannot be fully justified by ketone groups.

We propose a different reconstruction model that explains the presence of the subsurface non-diamond carbon layer and is compatible with previous experimental results. In Figure 3.22 (Top-Right and Bottom side), a schematic of the proposed (100) 1×1:O “C-on-top” and “C-on-top_2” models are represented. In both reconstructions, the carbon atoms of the first and second layers are sp^2 hybridized. The carbon atoms of the first layer are placed just on top of the atoms of the second layer and are bonded to them. The carbon atoms of the third layer are sp^3 hybridized but are bonded to two sp^2 carbons of the second layer and two sp^3 carbons of the fourth layer. Therefore, the atoms of the second and third layers have different chemical environments than in a pure diamond structure due to the presence of sp^2 carbons. Thus, the contributions in

C 1s XPS spectra are located at lower *BE* than diamond and will lead to two different peaks (see Section 2.2.2.). This behaviours support the presence of the non-diamond carbon XPS contribution and its higher peak width. Additionally, the carbon atoms of the first layer correspond to the C-O XPS contribution at ~ 285.5 eV. The correspondence of the layers used in the quantification model with the atomic layers of the reconstruction model is shown in Figure 3.22.

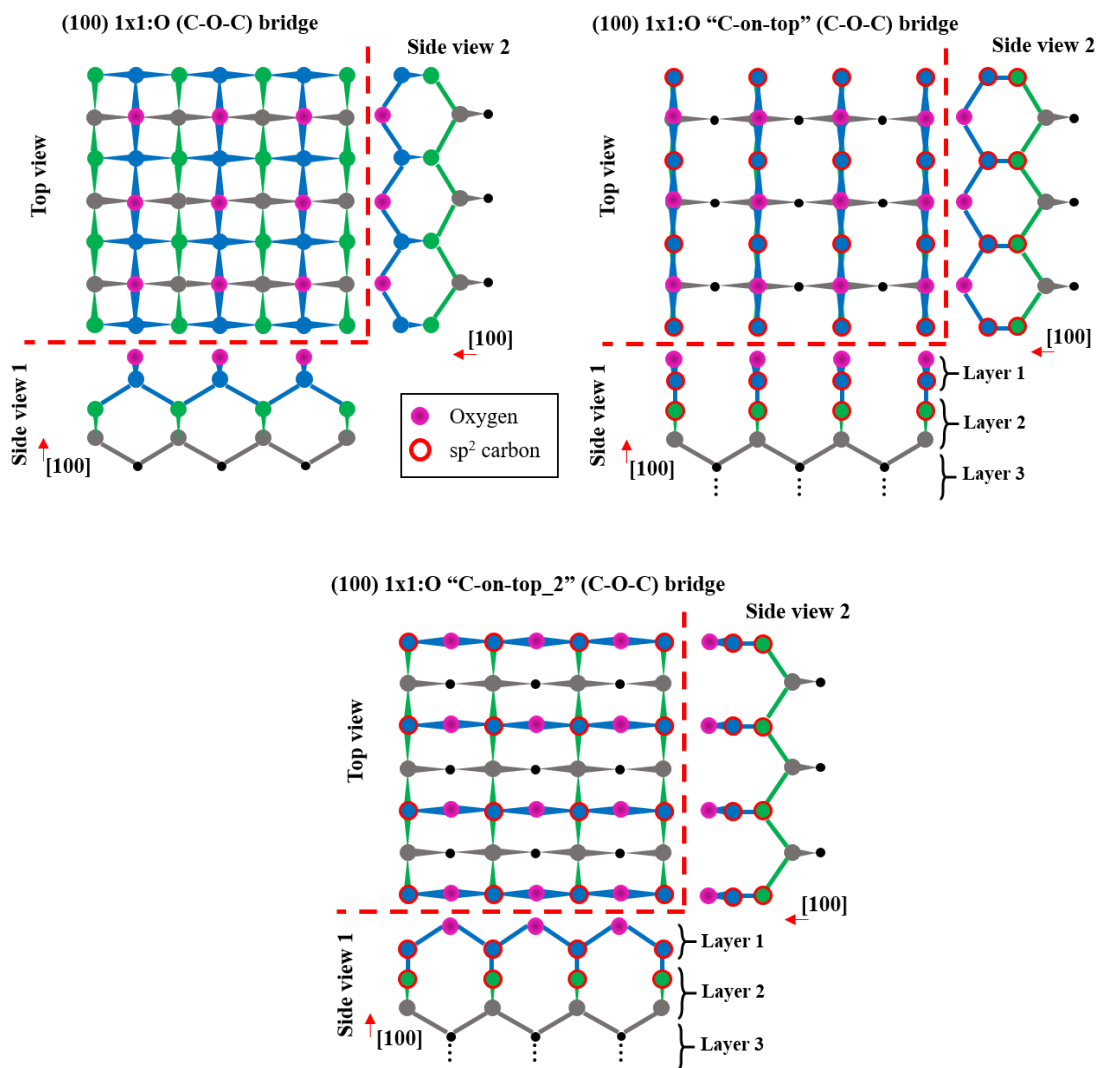


Figure 3.22: Schematic image (top and side views) of the four topmost layers of carbon atoms and the surface oxygen atom layer of the (100) diamond surface. The oxygen atoms are coloured in purple and the sp^2 carbon is marked by red circumference. Top-Left side: the (100) $1\times 1:O$ (C-O-C) bridge reconstructed surface is based on full sp^3 hybridized carbon. The carbon atoms of the first layer are bonded to two surface oxygen atoms and two carbon atoms in the second layer. Top-Right and Bottom-Left side: the (100) $1\times 1:O$ "C-on-top" and "C-on-top_2" reconstructions, respectively, are proposed in this work. In both cases, the carbon atoms of the first layer are bonded to two surface oxygen atoms and one carbon layer of the second layer and are positioned just on top of them. Thus, the first and second carbon atoms layers are sp^2 hybridized.

On the other hand, the partial coverage by ketone groups is also compatible with the present XPS result. In ketone groups, the carbon atoms bonded to oxygen are related to the contribution at 287 eV and also contribute to Layer 1. These carbon atoms are sp^2 hybridized and,

for this reason, the carbon atoms of the second layer are in a different chemical environment than in diamond and should be related to lower BE peaks. The contribution of the second atomic layer in the ketone-based reconstruction is also integrated into the non-diamond XPS peak, and therefore, is related to Layer 2 of the quantification model.

Additionally, the parameters used in the quantification model should not differ from those of the proposed reconstruction model. As already commented, the attenuation length values for diamond and graphite are very similar (2.2 and 2.31 nm, respectively). Thus, the presence of sp^2 carbon hardly changes the attenuation length of Layer 2, and, therefore, neither would the estimated result. Concerning the density values, it must be noticed that the areal atomic densities of the topmost atomic layers in the proposed reconstruction are the same as in the ideal diamond structure since it can be virtually obtained by an in-plane lateral shift of the complete first atomic layer. Thus, only the volumetric density modification is expected as a result of the different bonding structures which would change the distance between (100) atomic planes of the topmost layers.

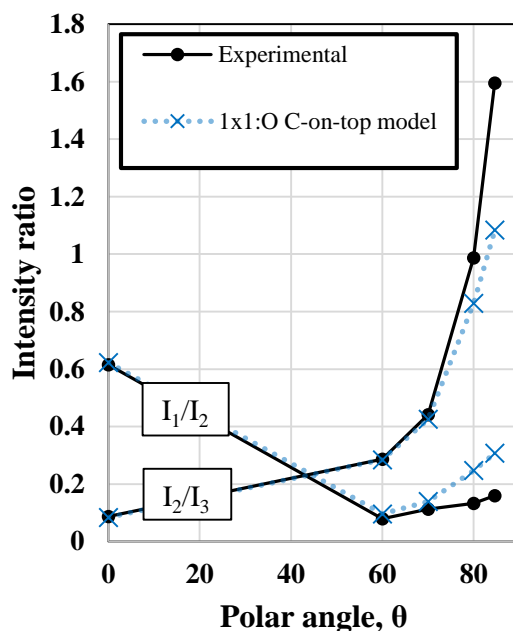


Figure 3.23: Graph showing the intensity ratios I_1/I_2 and I_2/I_3 obtained experimentally from XPS peak areas (solid line) and obtained by applying equation (3.26) and (3.27) (dotted lines) at different polar angles for the ideal (100) 1x1:O “C-on-top” model ($d_1 = 0.089$ nm and $d_2 = 0.178$ nm) as proposed in this work.

The theoretical estimations of the two versions of the (100) 1x1:O “C-on-top” reconstruction to the XPS results are the same and have been included in Figure 3.23. It must be noticed that these models are considering the partial covering of ketone groups. The thickness of Layer 1 and 2 was fixed to 1 ML and 2 ML, respectively. Due to the different carbon bonding structure in Layer 2, the (100) interplanar distance should differ from the ideal 2 ML of diamond

structure. As noticed, the models fit well the experimental values. The error increases for higher polar angle data, what can be related to other surface phenomena whose effects were not considered here such as roughness.

3.2.5. Final comments

In this section, it has been carried out a comprehensive study and discussion on the surface contributions of the (100)-O-terminated diamond surface. For first time, special attention is paid into the non-diamond contribution widely detected in the literature but systematically ignored by researchers. The use of ARXPS allowed accurate quantification and the verification of a surface model in which this non-diamond contribution is forming a sublayer just below oxygenated species. After extended discussion, it is concluded that the oxygenation of the diamond surface and the formation of this non-diamond carbon sublayer are linked. Thus, according to other authors, it is observed the $1\times 1:O$ reconstruction of the (100) O-terminated diamond is the most reasonable explanation for this contribution. The reproducibility, homogeneity (1×1 pattern), and the low contents of a few MLs are the most important arguments supporting this claim. Moreover, some of the previous attributions to this component (contamination, defects, or adsorbed hydrocarbons) are not supported by any evidence or cannot explain its high reproducibility and the observation of a 1×1 pattern.

This result implies the reconsideration of the (100) $1\times 1:O$ reconstructions models reported in the literature. This is because the current most accepted models support that the top surface carbon layer remains in the diamond carbon sp^3 configuration and, this way, the non-diamond contribution remains unexplained. Novel $1\times 1:O$ models are proposed here to fit with the detection of non-diamond contribution and are demonstrated to fit well with our ARXPS results.

However, some more steps are still necessary to reach a complete understanding of the (100)-O-terminated diamond surface. It is of great interest the studies focused on checking the conditions of the different oxygenation methods that lead to a defined 1×1 pattern and which simultaneously allows the quantification of the surface components. For this quantification, it would be advisable to proceed in an analogous way to this work, thus unifying criteria. *In-situ* oxygenation is also relevant to reduce the possible contamination effects. These type of studies will help to answer, for example, if the 1×1 patterns observed for different treatments respond to the same reconstruction or, on the contrary, several 1×1 reconstructions depending on oxygenation treatment are possible, which will explain the different properties already claimed by researchers, for example, between the use of VUV/Ozone treatment or acid-treatment.

3.2.5. Summary of the section

The chemistry of the (100)-O-terminated diamond surface is analysed by ARXPS and compared to H-terminated diamond showing the chemical changes occurring during the oxygenation. The appearance of a dominant single-bonded C-O contribution, the shift of the maximum C 1s peak towards higher *BE*, and the appearance of a non-diamond carbon contribution, define the transition from H- to O-terminated diamond surface and agrees with previous results. From O 1s, the atomic % O is found to be higher for O-terminated diamond as expected and differently from H-terminated diamond, most of the O 1s contribution comes from oxygen bonded to carbon, confirming the oxygenation of the surface.

Importantly, the results lead to conclude that the effect of the oxygenation on the H-terminated diamond is linked to the formation of a subsurface non-diamond carbon layer. A three-layer sample model has been used for the (100)-O-terminated diamond surface contributions quantification. Oxygen coverage of 1 ML and a subsurface non-diamond carbon layer of 2.67 ML is estimated. After an extended discussion and comparison to previous results, the described reconstruction model of the (100)-O-terminated diamond is shown to be the best explanation for the non-diamond contribution. Based on this result, a novel (100) 1×1:O reconstruction model is proposed. In contrast to most of the previous models, this model includes non-diamond carbon structures.

Resumen de la sección

En esta sección la química de la superficie (100) de diamante oxígeno-terminado (O-terminado) es analizada basándose en la espectroscopia de fotoelectrones de ángulo resuelto y se compara con la del diamante hidrógeno-terminado (H-terminado) mostrando los cambios químicos que ocurren durante la oxigenación.

La aparición de una contribución dominante de C-O de enlace simple, el desplazamiento del pico máximo de C 1s hacia una mayor energía de enlace y la aparición de una contribución de carbono distinta del diamante define la transición de la superficie de diamante de H- a O-terminado, lo que concuerda con los resultados de la literatura. Del análisis del espectro O 1s, se encuentra que el porcentaje atómico de O es mayor para el diamante O-terminado tal y como se esperaba y que, de manera diferente al diamante H-terminado, la mayor parte de la contribución de O 1s proviene del oxígeno enlazado al carbono, lo que confirma la oxigenación de la superficie.

Es importante destacar que los resultados conducen a la conclusión de que el efecto de la oxigenación en el diamante H-terminado está relacionado con la formación de una capa de carbono subsuperficial que no sigue la estructura general del diamante. Para probarlo, se ha utilizado un modelo de superficie basado en tres capas de composición homogénea, que se ha usado para la cuantificación de las contribuciones de superficie de diamante O-terminado. De esta manera se ha estimado una cobertura de oxígeno de 1 ML así como la presencia de carbono subsuperficial (distinta del diamante) de 2.67 ML. Después de una discusión extensa y una comparación con los resultados de la literatura, se propone la reconstrucción del diamante (100)-O-terminado como la mejor explicación para la contribución de carbono subsuperficial detectado. De esta manera, se propone un nuevo modelo de reconstrucción (100) 1×1: O que, a diferencia de la mayoría de los modelos anteriores, incluye estructuras de carbono que no siguen la configuración del diamante en las capas más superficiales.

Chapter 4:

Tungsten-carbide/diamond interfaces for Schottky barrier diodes

Tungsten carbide (WC)/O-terminated diamond contacts have shown very interesting properties for their application on Schottky Barrier Diodes. In this chapter, a comprehensive microanalysis of WC/O-terminated diamond contact is carried out to complement the existing data in the literature. The analysis is focused on the estimation of the SBH as well as the microstructural, compositional, and chemical changes occurring at the interface region during annealing in which the electronic behaviour of the junction is mostly defined.

The sample used in this Section corresponds to #WC, which is described in Section 2.2.1. The experimental procedure details for experiments in this chapter are summarized in Section 2.1.5.

The chapter is divided into the next sections:

- 4.1. Introduction to WC/diamond contacts
- 4.2. The WC/O-terminated diamond interface: Results
- 4.3. The WC/O-terminated diamond interface: Discussion
- 4.4. Final comments
- 4.5. Summary of the chapter

4.1. Introduction to WC/diamond junctions for Schottky barrier diodes

The diamond-metal junction is the base structure necessary for the manufacture of diamond-based SBDs. From this type of structure two electronic behaviours can arise, the ohmic and the Schottky one. The difference between them is that the ideal rectification degree of an ohmic contact is null while for Schottky contact is infinite. As summarized in the introduction (Section 1.4.1.2), diamond ohmic contacts are primarily manufactured based on a carbide-forming refractory metal such as Ti on diamond, after a proper annealing process. Precisely, the latter seems to be one of the keys to the formation of ohmic contacts with great stability and reduced resistance. On the other hand, there is also a surface termination relationship whereby the behaviour for a given metal-diamond can change from ohmic to Schottky by using hydrogen or oxygen termination surfaces, respectively (Teraji et al., 2014). Thus, the ohmic contacts are usually based on H-terminated diamond.

By the same rule, for manufacturing of Schottky contacts, it is in principle reasonable to choose metals to not being very reactive with the diamond, such as gold, silver, or platinum, in addition to the choice of diamond terminations with more electronegative elements, such as oxygen or fluorine. However, even though these contacts have increased SBH, they are also linked to instability from certain temperatures. This instability concerns not only its electronic performance (reduction of the SBH barrier, increase of the ideality factor) but also mechanical properties such as adhesion. Regarding the instability of electronic behaviour, there is a certain consensus on the loss of the O-termination condition during annealing processes playing a fundamental role. The progressive desorption of oxygen would lead not only to the loss of the PEA condition but also to a new configuration of interface states, e.g. formation of dangling bonds, which would completely modify the properties of the contact. Given the importance of O-terminations, it has been also shown that the choice of one or another oxygenation treatment can be also very relevant for the definition of its final behaviour. In this sense, as discussed in Section 3.2., VUV/ozone treatment has proven to be the best choice to reach higher SBH and homogeneity in the performance of Schottky contacts (Fiori et al., 2014a; Traore, 2014).

In an attempt to avoid the possible formation of an ohmic contact via reaction of the metal with the diamond, several authors have opted for a preformed stoichiometric carbide deposition such as tungsten carbide (WC). In this sense, WC is known to have a conductive electronic character (Pierson, 1996) and, thus, should perform analogously to a metal. This WC/(100)-diamond contacts have been previously widely investigated (Alvarez et al., 2006; Fiori, 2012; Fiori et al., 2014c, 2014b, 2014a; Koide, 2008; Liao et al., 2005, 2006; Piñero, 2016;

Piñero et al., 2017; Teraji et al., 2012, 2014) but mostly from an electrical point of view with a lack of structural and composition analysis. The results are mostly homogeneous for those contacts fabricated on VUV/Ozone oxygenation treatment and major conclusions can be summarized as follows:

- a) High reproducibility of the electrical performance of the contact.
- b) The SBH tends to 1.5-1.6 eV for the ideal contact, i.e. ideality factor $n = 1$.
- c) Annealing steps slightly increase the SBH and, progressively reduce the ideality factor to get very close to the unit. It is related to the interface homogeneity in the as-prepared sample which can hardly be improved by annealing.
- d) The electric performance is thermally stable up to 600 K. Over this temperature the deterioration of the contact occurs, i.e. ideality factor increase and SBH is abruptly reduced. This has been mostly related to oxygen desorption during annealing.

Additionally, those contacts based on acid-treatment oxygenation seem to have less homogeneity, higher ideality factor, and quite lower SBH (Alvarez et al., 2006). The mechanism concerning the variation of SBH and ideality factors during the annealing step remains unknown. *Teraji et al.* (2014c) have described the process during annealing as the early loss of most oxygen termination and the formation of WC/diamond interfacial bonds during the WC deposition process. This way, those contacts with higher SBH might content higher oxygen amounts at the interface. During annealing, this remaining interface oxygen is dissociated and then the ideality factor is reduced. *Fiori et al.* (2014c) also point to the formation of interface bonding as the main reason for the high thermal stability. The interface WC/diamond reaction could at least partially occur, thus, lowering the SBH. The authors also suggest that the dissociation of oxygen could be related to the formation of interface oxides and the stabilization of the contact as observed in Zr/O-terminated diamond contacts (Piñero et al., 2017; Traore, 2014; Traoré et al., 2014).

However, a lack of microstructural, chemistry, and composition characterizations of these WC/O-terminated diamond contacts in the literature to clarify this interface model and annealing effect is observed. In this sense, the work by *Piñero et al.* must be highlighted, which complements the electric characterization with TEM and Electron energy loss spectroscopy (EELS) measurements (Piñero, 2016; Piñero et al., 2017). EELS analysis allowed the author to detect an interface O K-edge at 532 eV after 300 K and a 600 K annealing, showing that oxygen remains after this temperature. The authors discarded the possible stable tungsten oxide formation. From these results, it is deduced that the O-termination condition remains, at least partially, after WC deposition. Whether higher temperature annealing could be related to the dissociation of oxygen and consequently to the deterioration of the contact still remains unknown.

To continue with the characterization of these aspects, a comprehensive multi-technique characterization approach of the WC/O-terminated diamond contact is carried out in the next sections.

4.2. The WC/O-terminated diamond interface: Results

In this Section, microstructure, chemistry, composition, and SBH of WC/O-terminated diamond contact are characterized to clarify some relevant interface phenomenology aspects. Thus, the analysis is mainly focused on the near-interface region in which the final contact performance is mostly defined. Two main techniques are used for characterization: TEM/STEM related techniques (Section 4.2.1.) and XPS depth profiling (Section 4.2.2).

4.2.1. TEM/STEM analysis

The details of the experiment carried out in this subsection are described in Section 2.2.3.

4.2.1.1. High-resolution TEM analysis

The microstructure of the WC/O-terminated diamond contact was investigated by HRTEM measurements. The HRTEM micrograph of WC/O-terminated diamond contact is presented in Figure 4.1(a). The diffractogram obtained by Fast Fourier Transform (FFT) of the yellow framed region in Figure 4.1(a) is shown in Figure 4.1(b). The corresponding diamond FFT diffractogram spots show that the diamond crystal orientation is 110 zone axis. The FFT diffractogram was calibrated according to diamond interplanar distances (red circumferences). In addition to diamond spots, three spot rings are observed indicating the presence of polycrystalline material (R_1 , R_2 , and R_M in Figure 4.1(b)). The radius R_M is attributed to the presence of Moiré fringes as can be observed in Figure 4.1(a) (dashed circumferences). The Moiré fringes are produced by the overlapping of two lattices in the beam direction with a suitable mutual orientation and, hence, it is evidence of the existence of polycrystalline phase formation at the near interface region. No grain extends from the interface through the WC layer. This fact, together with the presence of a clear ring and Moiré fringes lead to conclude that the WC deposition is mostly composed of nanocrystalline material in the interface region. In this sense, it must be noted that the WC/diamond interface line shows a brighter contrast as well as some discontinuities (red arrows) that are tentatively related to the crystal nucleation on the diamond surface.

Moreover, the spots radii R_1 and R_2 are found to be compatible with the interplanar distances d_{200} and d_{111} , respectively, of the cubic γ -WC_{1-x} phase (Kurlov & Gusev, 2006, 2013) sometimes called β -WC_{1-x} (Milat et al., n.d.) or simply cubic-WC. This attribution is supported by previous X-ray diffraction (XRD) characterization for a similar sample fabrication procedure

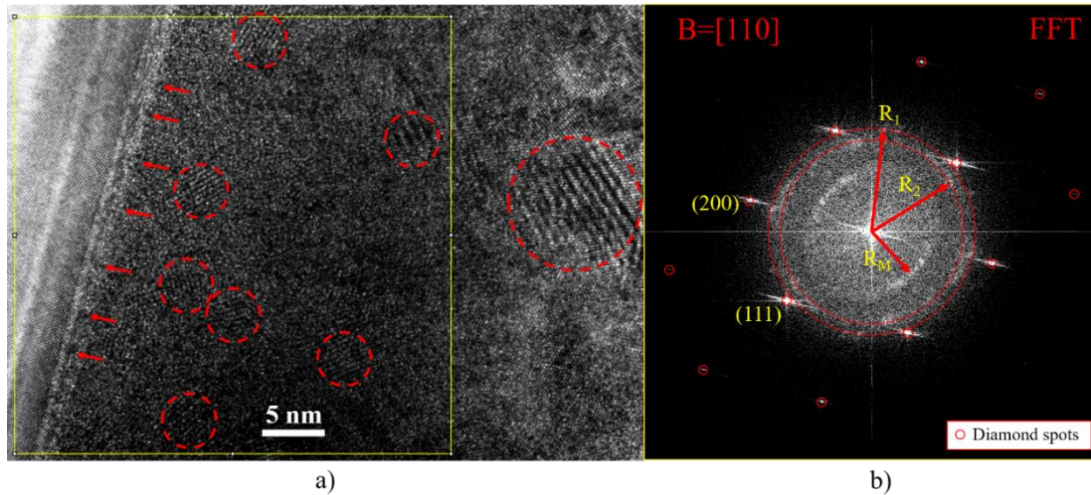


Figure 4.1: TEM analysis of WC/O-terminated diamond contact showing a) HRTEM micrographs of WC/O diamond contact interface: Moiré fringes (dashed circumferences) are related to polycrystalline material along with the whole WC layer. Smaller fringes are found near the interface. Some interface disruptions are highlighted (red arrows) possibly related to WC nucleation. b) HRTEM FFT diffractogram in the yellow framed region showing diamond spots (red circumferences) and three other spot ring radii (R_1 , R_2 , and R_M). Diamond spots are used for diffractogram calibration and beam direction deduction ($B = [110]$). The radius R_M is related to Moiré fringes as a consequence of crystal overlapping in the beam direction. Two other radii R_1 and R_2 are compatible with d_{111} and d_{200} of the cubic-WC phase. A bigger grain size radius over the interface region is deduced from the higher extension of Moiré fringes.

(Liao et al., 2006). The crystal structure of the cubic-WC phase is a face-centered cubic (FCC) with a lattice parameter ranging from 0.423 nm to 0.426 nm, which is dependent on its stoichiometry and defects density (Kurlov & Gusev, 2013). Therefore, the lower the carbon content the higher the lattice parameters would be. A summary of the interplanar distances used for cubic-WC identification is shown in Table 4.1. For comparison, the closest interplanar distances to R_1 and R_2 for two other major candidate phases, α -WC (also known as δ -WC) and α -W, are included. Note that the interplanar distances d_{110} (for α -W) and d_{100} (for α -WC) are similar to that of d_{200} and d_{111} of the cubic-WC phase, respectively. However, these two phases are incompatible with the presence of two rings at similar distances which supports the cubic-WC attribution. A lattice parameter for the cubic-WC, $a_{WC} \sim 0.423$ nm, is deduced from the present analysis what is indicative of a lowered carbon stoichiometry.

Table 4.1: Summary of the HRTEM FFT diffractogram spot identification. The corresponding theoretical interplanar distance values are compared to experimental spot radii R_1 and R_2 . The results show a good agreement of the spot radii R_1 and R_2 with the cubic-WC phase interplanar distances d_{200} and d_{111} , respectively. Interplanar distances of other low-temperature phases, α -W, and α -WC are also presented for comparison. Any of these two phases are compatible with the presence of two rings at R_1 and R_2 .

	Cubic-WC (FCC) $a_{WC} \sim 0.423\text{-}0.426$ nm (Kurlov & Gusev, 2013)		α -W (BCC) $a \sim 0.316$ nm (Lassner & Schubert, 2005)		α -WC (Hexagonal) $a \sim 0.29059$; $c \sim 0.28376$ (Kurlov & Gusev, 2013)	
Interplanar distance (nm)	d_{200}	d_{111}	d_{110}	d_{111}	d_{100}	d_{110}
Theoretical	0.211-0.213	0.243-0.246	0.223	0.182	0.252	0.145
Diffractogram radius (nm)	R_1	R_2				
Experimental	0.211	0.244				

4.2.1.2. Energy-dispersive X-ray spectroscopy

The stoichiometry of the WC deposition after annealing at 600 K is characterized by EDX experiments. The experiments were carried out on several lamella preparations corresponding to different contacts of the #WC sample. A representative sample study is shown in Figure 4.2. In the HAADF image (Figure 4.2(a)) diamond layer (dark contrast) is shown very homogeneously. WC deposition (bright contrast) can be divided into two regions: close to the interface the contrast is homogeneous while out of this regions a reduced contrast homogeneity is found. The latter could be related to compositional or structural variations such as grain formation. Concerning the WC layer composition, EDX profile shows a clear W:C ratio reduction profile towards the outermost region (Figure 4.2(b)(c)). Remarkably, most of the contacts present a clear stoichiometry W:C $\sim 1:1$ at the very near interface region which is linearly modified along with the WC deposition, showing increased W:C ratios at the WC deposition outermost region. Thus, in this region, higher W contents would, in principle, avoid the WC grain formation while metal W crystallization is reasonably to occur. This result is in agreement with HRTEM analysis by which the WC formation occurs at the interface. The α -W phase would be favoured far from the interface region where a higher W:C ratio exists. The W:C ratio at the outermost WC deposition region varies from one sample to another, in the range 1.5-4.

This observation should be related to a C diffusion towards the interface since there is no reason to think W:C atomic fraction is not constant along with the WC deposition for the as-deposited sample. It is remarkable also the high reproducibility of this phenomenon and how, despite the stoichiometry variation among contacts, the electrical performance remained quite homogeneous. It illustrates again the big importance of the interface phenomenology in the definition of the electric performance of the contact.

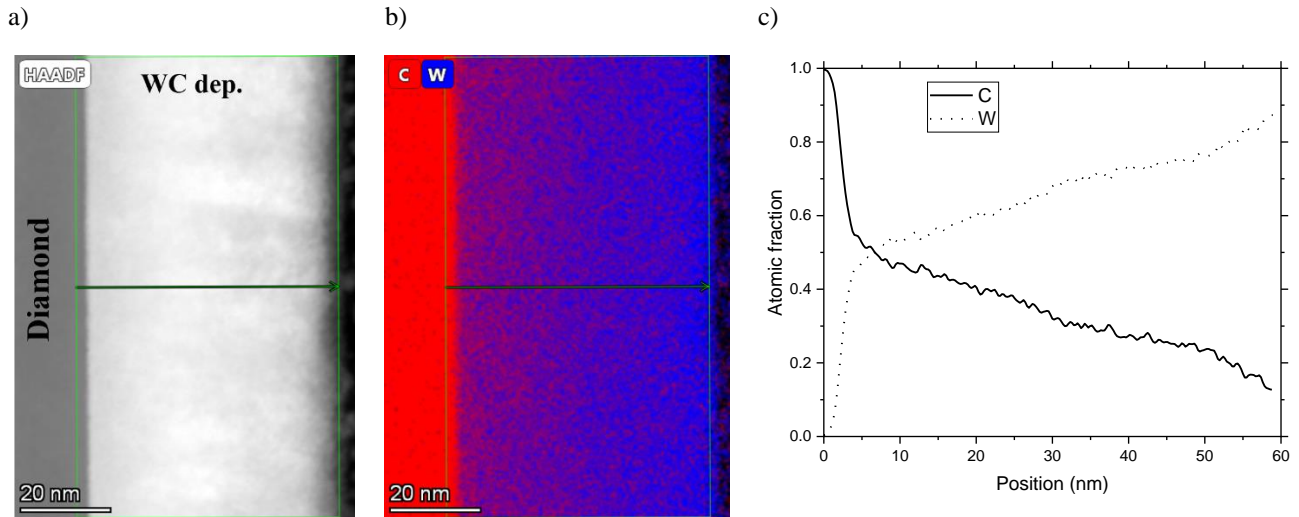


Figure 4.2: STEM EDX analysis of WC/O-terminated diamond interface: a) HAADF micrograph. From left to right: diamond, WC deposition, and platinum deposition due to FIB preparation. b) W(blue) and C (red) EDX atomic fraction map corresponding to the same region in a). The variation of the W:C atomic fraction is noticeable along the deposition direction. The arrowed rectangle in a) and b) is delimiting the integration region for the generation of W:C fraction profile showed on c). W:C is close to 1:1 near the interface region and a linear variation can be identified.

4.2.2. XPS depth profiling analysis

4.2.2.1. WC layer: Early sputtering stage analysis

Main observations from the early stage of the sputtering experiment are briefly commented on. First, increased contents of oxygen at the first 3-4 nm of the WC contact were found. This was attributed to the presence of WO_3 as a result of the natural oxidation of W and/or WC (Warren et al., 1996). It was supported by the position of the O 1s peak which matched well with previous reports for WO_3 (Nefedov et al., 1982; Wagner et al., 1979; Warren et al., 1996). Additionally, the oxygen content was linearly reduced along with the WC deposition towards the diamond interface what led to conclude that the presence of oxygen in the layer is most probably a consequence of ambient oxygen diffusion into the WC deposition during sample transport or storage.

Regarding W and C contributions, the quantitative analysis of the WC layer arose similar results that EDX. The maximum W:C ratio corresponds to the outermost region of the WC deposition in which its value is ~ 1.7 , which linearly decreases towards the diamond interface. However, from the qualitative analysis, it was found that the C 1s spectra were composed of two components related to amorphous or free-carbon, and WC formation, respectively. Although the discussion of these attributions is addressed later, from this analysis it was deduced that: a) the formation of WC bonds partially occurred through the whole WC deposition; b) the WC layer is mostly composed by a dominant W metal contribution, and c) free-carbon is present in

comparable amounts to WC formation. Although free carbon could be attributed in part to a sputtering effect, the presence of Ar⁺ ion implantation was not evidenced in this phase of the experiment. Thus, even considering that all the carbon presence is attributed to WC, almost double W metal content would exist through most of the WC layer. In this respect, the formation of W₂C was discarded since it is normally related to temperatures over 1500 K (Kurlov & Gusev, 2006).

4.2.2.2. Interface region analysis

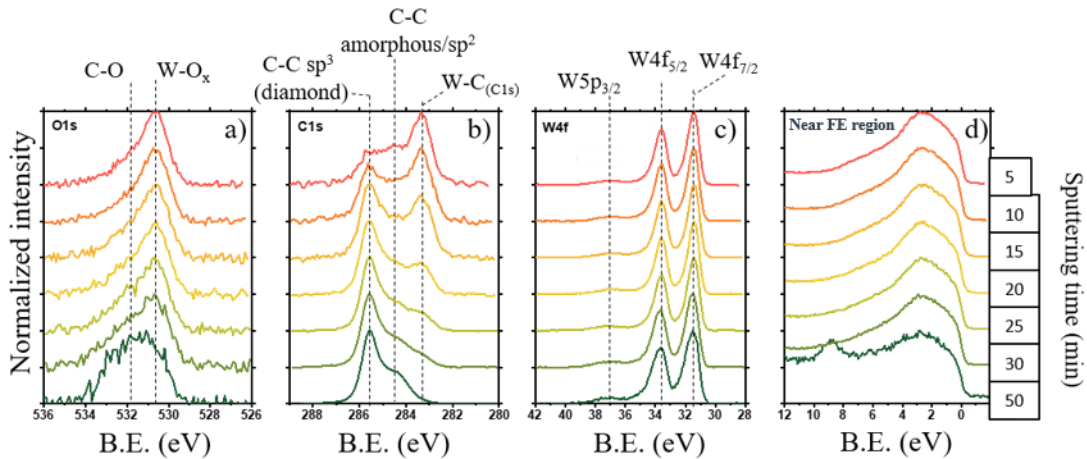


Figure 4.3: Normalized XPS depth profile spectra for WC/O-terminated diamond Schottky contact. The corresponding etching time for each spectrum, with respect to an arbitrary starting point just before reaching the interface, is indicated on the right side of the graph. (a) O 1s spectra showing the partial oxidation of W and a C-O contribution appearing towards the interface. (b) C 1s spectra showing the presence of WC formation along with the deposition. The peak related to C-C sp³ (diamond) is attributed to the higher BE peak at ~285.56 eV. Another contribution at ~284.5 eV has been attributed to amorphous/graphitized carbon due to Ar⁺ ion sputtering and free-carbon along with the WC deposition. (c) In W 4f spectra, three peaks correspond to W 4f_{7/2}, W 4f_{5/2}, and W 5p_{3/2}. W metal and carbide contributions are expected but cannot be distinguished due to short energy position distance. The position of W 4f_{7/2} maximum is ~31.4 eV. (d) The near FE region spectra are used for the Fermi level determination and the spectra calibration.

Special attention is focused on the analysis of the interface region in which the diamond contribution starts to be detected, corresponding to the last 50 min sputtering steps. The near FE region, C 1s, W 4f, and O 1s spectra of the WC/O-terminated diamond contact in this region are shown in Figure 4.3. The sputtering time for each spectrum is indicated on the right side of this figure. The spectra have been normalized for qualitative comparison purposes. The etching rate was calibrated in another contact of the sample and was estimated to ~0.25 nm/min according to the thickness information extracted from TEM measurements. The etching depth estimation, starting to count at an arbitrary in-depth point just before reaching the interface, is represented in the upper part of Figure 4.4 for a better illustration of the experiment process. As can be seen in the changing C 1s contributions in the spectra of Figure 4.3, and in the concentration changes of C(non-carbide) and W in Figure 4.4, the interface is roughly centered at 20 min sputtering depth (considering that arbitrary in-depth starting point) and has roughly 20 min sputtering width,

corresponding to about 4 nm, where one can observe the strongest concentration changes. At 5 min Ar + ion sputtering, diamond C 1s contribution can be detected (Figure 4.3(b)) what is reasonably understood since each XPS spectrum corresponds to an in-depth information of few nanometers, which depends on the photoelectron escape probability (see Section 2.1.2.). The spectra energy calibration was made by a linear fit of the Fermi edge (FE) in the near FE energy region (Figure 4.3(d)). The zero-energy position corresponds to the Fermi level of the junction since WC is known to have a metallic electronic character (Pierson, 1996).

4.2.2.2.1. Peak identification

C 1s spectra

Regarding C 1s spectra, three contributions have been considered in the C 1s spectra (Figure 4.3(b)). Diamond C-C sp³ contribution is identified with the higher *BE* peak at ~285.56 eV. This attribution is based on its increasing intensity in the final steps of the depth profile. Note that the position of the C-C sp³ peak is expected at higher *BE* than on clean diamond references as a consequence of the WC deposition. The Fermi level of both materials must be equalized at thermal equilibrium inducing a DBB on diamond. This DBB appears as a diamond peak shift towards higher *BE* in XPS which, in turn, allows estimating the SBH of the junction (see Section 4.3.).

A second C 1s contribution appears as a shoulder of the diamond peak at ~284.5 eV. This peak has been attributed to graphitized/amorphous carbon which can be related either to free-carbon along the WC layer and to the effect of Ar⁺ ion sputtering on diamond (Reinke et al., 1996) in the last sputtering steps. For the latter attribution, it was noticed that the C 1s shape at the 50 sputtering step is very similar to that found in previous works for Ar⁺ ion sputtered diamond (Fan et al., 2002; Lau et al., 1994). Unfortunately, the Ar presence in the early stages of the sputtering could not be tracked due to the overlapping Ar 2p (B. V. Crist, 1992) and W 4d_{5/2} peaks. No clear features were found either regarding Ar 2s or Ar 3p. In contrast, a new contribution at ~9 eV is found when the diamond surface is reached (Figure 4.3(d) (50 min)). This new contribution agrees with the Ar 3p core-level position (B. V. Crist, 1999).

Finally, the third C 1s contribution is attributed to the formation of WC at ~283.3 eV. This value matches with previous WC XPS experiments (Dai-Yi & Zi, 1990; Hakansson et al., 1994).

W 4f spectra

Regarding W 4f spectra (Figure 4.3(c)) three peaks can be observed corresponding to W 4f_{7/2}, W 4f_{5/2}, and W 5p_{3/2} from lower to higher *BE*, respectively. The position of the main W 4f_{7/2} is ~31.4 eV, which is in agreement with previous reports for W metal (Mcguire et al., 1973; Wagner et al., 1979; Warren et al., 1996). The presence of WC component in W 4f spectra

at higher BE than W metal contribution is expected according to the C1s spectra. However, the expected low chemical shift between W metal and WC contribution in the W 4f spectra ($\sim 0.4\text{-}0.6\text{ eV}$) (Mcguire et al., 1973; Warren et al., 1996) together with the lower WC contents make it irresolvable. Thus, WC contribution in W 4f should have little effect on W 4f peak positions and would rather appear as a slight increase in the peak width.

O 1s spectra

The O 1s spectra corresponding to the last 50 min sputtering are shown in Figure 4.3 (a). A dominant peak at $\sim 530.8\text{ eV}$ has been identified in the early stages of the experiment as the partial natural oxidation of the WC layer (Nefedov et al., 1982; Wagner et al., 1979; Warren et al., 1996). Remarkably, the O 1s spectrum evolves towards the interface showing an increasing peak width and position shift towards lower BE . This fact can reasonably be justified by the progressive appearance of a new component different from the W-O contribution, very near the diamond surface. The attribution of this second peak is discussed together with the quantitative information in Section 4.2.2.2.2.

4.2.2.2.2. Peak deconvolution and quantification

To track the formation of WC, the C 1s spectra were deconvoluted into the three peaks already commented on and highlighted in Figure 4.3(b). During the fitting process, Voigt distributions were used as peak shapes. The Lorentzian width was fixed to 0.2 eV based on graphite and WC lifetime broadening results (Hakansson et al., 1994; Sette et al., 1990). The Gaussian widths were set to 0.65, 0.8, and 1.2, respectively for diamond, WC, and amorphous carbon peaks. For W and O elements the total W 4f and O 1s intensities were used, respectively. Once the intensity for each contribution is obtained the relative sensitivity factors provided by the manufacturer are used for the quantification. The atomic percentage of W, C, and O are represented (Figure 4.4(a)). The carbon contribution is divided into WC ($C_{(WC)}$) and the rest of the total carbon ($C_{(non-carbide)}$). Thus, the latter contribution includes the diamond C-C sp^3 and the amorphous carbon contributions. Then, the WC contribution can be better visualized. Note that the contribution of amorphous carbon can be due either to the Ar⁺ ion sputtering effect on diamond and to free-carbon in the WC deposition. This is because both contributions are overlapping in BE , hindering its differentiation.

C 1s and W 4f spectra

As remarked in Section 4.2.2.1, the WC layer showed a stoichiometric excess of W metal along with the full thickness, analogously to that found in the interface region after 5 min Ar⁺ ion sputtering (Figure 3(a)). Free amorphous carbon and WC signals can be detected with comparable contributions at around 20 at. % each. Thus, the formation of WC occurs only partially in that region. The final Ar⁺ ion sputtering steps (interface region) are related to the progressive

reduction of W related contributions (metal and carbide). However, the total W contribution is more abruptly reduced than the $C_{(WC)}$ contribution. This fact is understood as an increased WC fraction in the total W contribution towards the interface. To better illustrate this W metal to WC changing character, the $C_{(WC)}/W$ ratio is represented in Figure 4.4(b). It can be seen how $C_{(WC)}/W$ increases from 30.8 % (5 min) to 58 % (30 min), what means that the carbide formation represents a higher fraction of the W signal towards the interface. Once the WC layer is mostly crossed (50 min), diamond surface is reached and the total W contribution, including the WC fraction, is drastically reduced. Note that at 50 min Ar⁺ ion sputtering must be taken with caution because the very low intensity of both the $C_{(WC)}$ and W 4f signals are very weak and a little variation in the $C_{(WC)}$ estimation (by deconvolution) would induce a great variation of the $C_{(WC)}/W$ ratio. These results lead to conclude that WC contribution increases towards the diamond layer at this interface region.

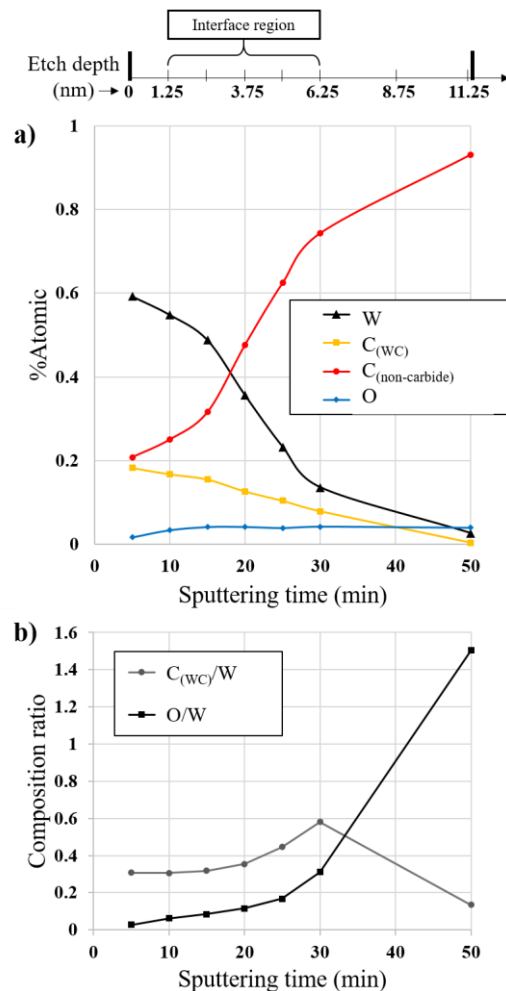


Figure 4.4: XPS composition depth profile of the WC/O-terminated diamond Schottky contact at the interface region showing a) Atomic % of W, C, and O contributions. C contribution is divided into $C_{(WC)}$ (WC contribution) and $C_{(non-carbide)}$ (rest of C contributions including diamond and amorphous/graphitized carbon); b) $C_{(WC)}/W$ and O/W atomic contribution ratio. The Ar⁺ ion sputtering time axis corresponds to that shown in Figure 4.3. An estimation of etch depth is shown in the upper part of the figure.

O 1s spectra

From the quantitative point of view, it is noticed that O contents remain almost constant (3-4 at. %) even when the presence of W is abruptly reduced at the interface (see Figure 4.4(a)). To ascertain whether the new secondary O 1s peak, appearing towards the interface, is related to the W-O bonds, the O/W ratio is represented in Figure 4.4(b). It can be seen how O/W ratio increases in this region from 2.8 % (5 min) to 30 % (30 min). At the final sputtering step (50 min), O/W ratio increases drastically up to 150%. Even though this O/W ratio is compatible with W oxide formation, no chemical shift or new peaks appears on the W 4f spectra as should be noticed under the presence of WO₂ or WO₃ (Nefedov et al., 1982; Sarma & Rao, 1980; Warren et al., 1996). For this reason, the attribution of this appearing oxygen component to W-O related bonds is discarded. The tendency of the O/W ratio along the total WC layer was, on the contrary, to decrease towards the interface. Note also that this feature is exclusively found in the interface region. If this new peak were related to free-carbon oxidation, it may have appeared also in the initial stages of the experiment in which the oxygen content was even higher but it was not the case. On the other hand, it is known that WC oxidizes more rapidly than tungsten metal but the process should start at higher temperatures over 780-790 K (Kurlov & Gusev, 2013). The formation of a W-C-O ternary phase has been also discarded since no stable phases different than carbides and oxides can occur in the W-C-O system (Worrell, 1964).

From these results, it is deduced that the oxygen presence should be related to C-O bonds rather than W-O bonds and that this oxygen contribution is uniquely located at the interface region. The low relative intensity of this new contribution makes it undetectable in the C 1s spectrum.

4.2.2.2.3. Schottky barrier height estimation

The same XPS experimental approach can be used for the estimation of the SBH of the WC/diamond contact. The present SBH estimation is based on the established Kraut's method (Kraut et al., 1983). The SBH is defined as the energy distance between the valence band maximum (*VBM*) of the semiconductor at the interface and the Fermi level of the junction and can be calculated by the following equation,

$$SBH = E_{C\ 1s_interface} - \Delta E_{diamond} \quad (4.1)$$

where $E_{C\ 1s_interface}$ is the position of diamond C-C sp³ contribution of the junction which is expected to shift towards higher *BE* as a consequence of the metal/diamond junction formation, and $\Delta E_{diamond}$ is the energy distance between the *VBM* and C 1s core-level in diamond which has been previously obtained as 284.01 ± 0.12 eV (Kono et al., 2014). A band diagram showing the energy distances necessary for the SBH estimation is shown in Figure 4.5. The Fermi level of the

junction must correspond to the Fermi level of the WC layer which was estimated by fitting the Fermi edge in the near FE spectra region. Therefore, the W 4f position should be constant along with the WC layer. However, when the WC layer is too thin (last etching steps), it could be submitted to charge effects which could modify the energy reference. To avoid this possible effect, the position of the W 4f peak in the thin WC layer (last etching steps) was compared to that of the thick WC layer (early etching steps). No energy shifts were found indicating that the Fermi level of the junction can be estimated from the thin WC layer. In this sense, it must be noted that even though the position of W 4f maximum depends on metal/carbide ratio contribution, its effect is negligible as discussed in Section 4.2.2.2.1. The effect of Ar⁺ ion sputtering on SBH estimation is also negligible since no shift or broadening of peaks is observed between consecutive etching steps. The position of C-C sp³ of the junction was estimated from the 20 min sputtering spectrum in which both, carbide and diamond contributions, are simultaneously detected. In any case, no significant variations in the C-C sp³ peak position were found among the recorded spectra. Thus, the BE of C-C sp³ bonds for WC/O-terminated diamond was estimated at 285.56±0.01 eV. Then, the SBH is calculated as SBH = 1.6 ± 0.2 eV based on equation (4.1).

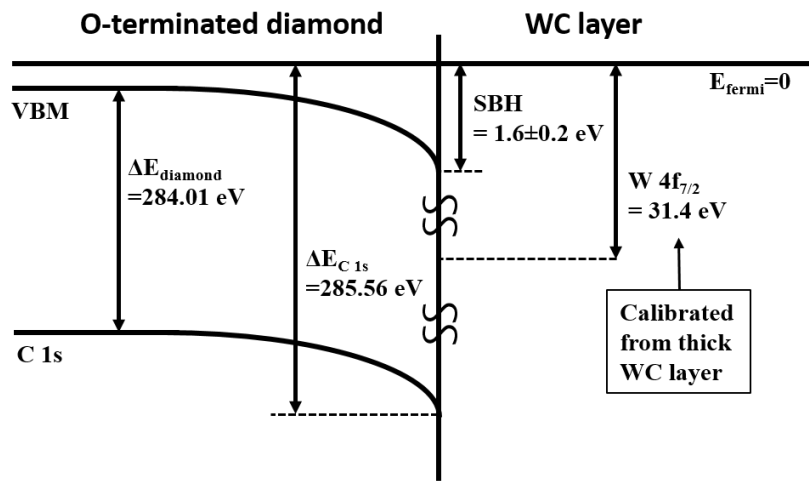


Figure 4.5: Schematic band diagram for the WC/O-terminated diamond junction showing the main energy levels necessary for the SBH estimation by XPS.

4.2.3. Summary of the results

The main observations by HRTEM, EDX, and XPS are summarized as follows:

- a) Nanocrystalline cubic-WC in the near-interface region and polycrystalline α -W (bigger grain size) in the outermost region was found compatible based on HRTEM analysis. Discontinuities at the interface line were related to the possible nucleation of WC in

- diamond. The formation of cubic-WC is supported by previous XRD analysis (Liao et al., 2006).
- b) The W:C ratio is, with high reproducibility, higher in the outermost region (1.5-4) and linearly decrease towards the interface in which the stoichiometry is closer to the ideal 1:1 WC stoichiometry. This result was supported by EDX and XPS and agrees with HRTEM observations.
 - c) WC formation occurs partially along with the whole WC deposition but it is preferentially present in the very near interface region. It was deduced by XPS by tracking the WC component in C 1s (C_{WC}) versus the total W 4f signal (Figure 4.4(b)). This result is in agreement with a) and b).
 - d) The natural oxidation of the WC deposition occurred in the outermost region on ambient conditions after a certain time. Also, low oxygen contents seem to diffuse inside of the contact and a residual W oxide contribution is found along with the whole deposition.
 - e) A new oxygen component is detected at the very near interface what has been attributed to C-O bonds. This result was deduced by quantitative and qualitative analysis of XPS O 1s spectra and agrees with previous EELS observations (Piñero et al., 2017).
 - f) An SBH = 1.6 ± 0.2 eV is deduced from XPS depth profile spectra analysis.

4.3. The WC/O-terminated diamond interface: Discussion

4.3.1. Interface WC formation

The summarized results a), b) and c) in Section 4.2.3., show a wide agreement among observations from different techniques. Results points up to the formation of nanocrystalline cubic-WC phase at the near interface region, which agrees with the increasing C_{WC}/W ratio showed in Figure 4.4(b). The identification of α -W metal phase most likely related to the external region of the WC layer is also consistent with the higher W concentration found by XPS and EDX in that region.

Cubic-WC is a metastable phase rarely found in the literature (Fujii et al., 2006; Kurlov & Gusev, 2006, 2013; Liao et al., 2006; Milat et al., n.d.; Suda et al., 2006) which has been reported since the 1960s. There is a big controversy about its temperature and composition limits. Remarkably, most stable tungsten carbides and oxides phases crystallize on a hexagonal structure. Ab initio calculations point to the low stability of cubic-WC at low temperature (Liu & Cohen, 1988), in which the hexagonal phase is energetically favourable. The phase modification under bias conditions has been also reported on the WC layer deposited on Si (100) (Tavsanoglu et al., 2013). Concerning electronic performance, cubic-WC is expected to show a marked metallic nature even higher than group V transition cubic carbides (Liu & Cohen, 1988). The work

function of WC layers grown on silicon has been estimated by Kelvin probe measurements as ~ 4.9 eV, which seems to be stable for W:C atomic ratio from ~ 2.5 to ~ 0.71 (Fujii et al., 2006). This work function value is very similar to that of polycrystalline W metal (4.50-4.56 eV (Lassner & Schubert, 2005)), so the electronic properties of the WC/diamond Schottky contact will hardly be affected by work function modifications from W to WC even in the absence of interface states (ideal contact).

The present results lead to think about the reasons why the formation of WC could be promoted by the presence of the diamond interface and why a linear W:C ratio is generated during annealing steps. In this respect, the ability for a transition metal to react with carbon increases with its number of valence electron vacancies in d- and s-orbitals (Sung & Tai, 1997). The reaction of other refractory metals such as Ti or Mo is known to form interface carbides which have been related to the formation of ohmic contacts (S. Mikhailov et al., 1995; S. N. Mikhailov et al., 1995; Tachibana & Glass, 1993). Thus, it is reasonable that W would react with diamond, and, indeed, this reaction W/diamond has been observed previously (L. J. Chen et al., 2008; Neto et al., 2012; Ukhina et al., 2017; Yeh et al., 1996). *Ukhina et al.* (2017) evidenced the WC formation as a result of the W/diamond reaction during CVD tungsten (tungsten carbonyl precursor) deposition on diamond. The authors observed that after the initial WC formation, the diffusion of carbon into W becomes weaker and W metal contributions can be found by XRD. Also, *Yeh et al.* (1996) published a comprehensive characterization of the W/diamond reaction. For this purpose, a thin W layer was sputtered on the diamond surface and submitted to different thermal treatments. The rapid diffusion of carbon into the W layer as well as the formation of an adhesive WC interface layer was evidenced using XRD and TEM observations. In the present work, the results summarized in Section 4.2.3 [a), b) and c)] supports that the W/diamond reaction and WC nucleation occurs even before the annealing steps. This reaction will preferentially take place in diamond defective sites. The finalization of the annealing temperature conditions, the low solubility of C in W at low temperatures (Goldschmidt & Brand, 1963), and the self-content of C in the WC layer would slow down the possible C diffusion processes and further reaction. The observed carbon enrichment in the near-interface region is promoted by the early nucleation of WC phases at the interface. This initial formation of WC would be also involved in halting the W/diamond reaction (Ukhina et al., 2017) and carbon diffusion (Buhsmer & Crayton, 1971) at low temperatures.

The cubic-WC is energetically favoured in these low-temperature and carbon content conditions. However, at higher temperatures, it is expected further diffusion of carbon and the consequent transformation of the low stability cubic-WC phase into other favourable phases. It may induce the generation of interface defects and the loss of this metastable interface configuration.

4.3.2. Interface oxygen due to O-termination

By the VUV/Ozone treatment used in the fabrication of sample #WC, the diamond surface is expected to show a 1×1:O reconstruction (Teraji et al., 2014) and be ideally covered by 1 ML of hydroxyl (C-OH) groups as a consequence of the reaction of ozone and C-H bonds of the original hydrogenated surface (Ohta et al., 2004). Oxygen content at the WC/diamond interface is expected to be equal or less than the ideal 1 ML as a consequence of diamond oxygenation treatment. This is because oxygen can be partially removed during the WC sputtering process. An oxygen component related to the diamond surface should be detected as a new C-O contribution, at the interface region, which will qualitatively contrast with the oxygen related to the WC deposition. The detection of this oxygen contribution is difficult and so its presence and thermal evolution are still to be solved.

Main results obtained in this work about this subject come from XPS analysis. The detection of a secondary peak in the O 1s spectrum other than the W oxide formation has been justified in Section 4.2.2.2.2. This new O 1s component has been attributed to C-O bonds existing at the interface region. The relation of this O 1s contribution to diamond O-termination is discussed here.

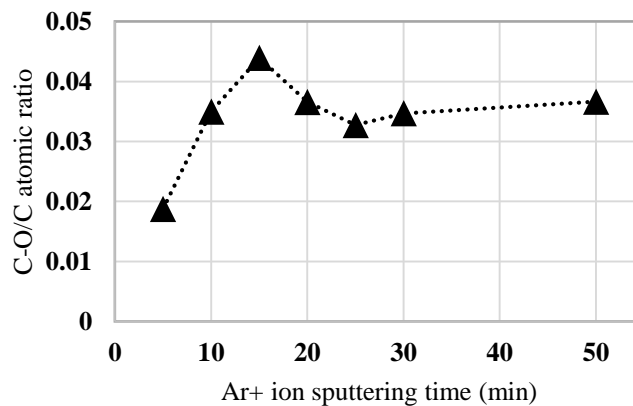


Figure 4.6: Evolution of the C-O/C atomic ratio along with the WC/O-terminated diamond interface region. The reabsorption of oxygenated species is expected to be constant during the XPS spectra recording process. A peak at 15 min Ar+ ion sputtering step contrasts with the reabsorption level of oxygenated species indicating the presence of an additional C-O contribution which is attributed to the effect of diamond surface termination.

First, it is worth note that the detected C-O contribution could be generated either by the diamond oxygenation treatment and/or by the reabsorption of oxygenated species during the spectra recording process. The spectra recording time is the same in each Ar+ ion sputtering step and, thus, the reabsorption of oxygenated species is expected to be rather constant at a certain level. The C-O/C ratio has been used to differentiate the reabsorption component (constant level) from other C-O contributions (see Figure 4.6). For this representation, deconvolution of the O 1s

spectra into two peaks, C-O at 531.7 eV and W-O at 530.8 eV, was carried out by using Voigt distributions with Lorentzian width of 0.2 eV, and Gaussian width of 2.2 eV and 1.2 eV, respectively. The appearance of a peak in the C-O/C ratio means the existence of an additional contribution of C-O bonds. This peak is centered at the 15 min Ar⁺ ion sputtering position, where the WC/diamond interface was localized (see Figure 4.4). Based on this analysis the origin of the discussed C-O contribution is partially attributed to the diamond O-termination treatment effect.

These interfacial C-O bonds have rarely been detected after a metallization process (Navas et al., 2018; Piñero et al., 2017). Its role and evolution during annealing steps have remained unknown. O-terminated diamond surfaces are mainly composed of simple C-O bonds which correspond to similar energy position to detected here (Navas et al., 2018). In this work, the C-O contribution is detected after the 600 K annealing step, which supports the hypothesis that the O-termination remains, at least partially, at this annealing temperature. The stability of oxygen at the interface could be similar to other metals used as contacts, such as Au, with low reactivity to oxygen and carbon. The oxygen desorption in Au/O-terminated diamond contacts occurs at temperatures over 800 K and has been related to the reduction of the SBH (Teraji, Koide, et al., 2009). In the present case, the initial formation of WC seems to prevent the desorption of O and the oxide formation at the interface. In this sense, the presence of O at the interface region has been previously related with the prevention of W-diamond reaction via oxide formation (Fiori et al., 2014a). This kind of process has been observed in Zr/O-terminated diamond contacts in which the redistribution of oxygen and the formation of a Zr-oxide of a few ML has been linked to the stabilization of the Schottky properties after annealing at similar temperatures (Piñero et al., 2017). This was attributed to the high oxygen affinity of Zr. The presence of W-oxides at the interface has been discarded here, refusing the interface oxide stabilization mechanism attributed to Zr contacts.

4.3.3. Schottky barrier height discussion

The estimated SBH value is in agreement with that estimated from I-V measurements in previous works (Fiori et al., 2014a; Liao et al., 2005) where the ideality factor was improved by annealing up to 600 K. After this temperature annealing, the ideality factor is close to 1, what indicates that the current transport mechanism fits well with the thermionic emission model. That is, most of the carriers pass over the barrier and other current mechanisms such as tunnel emission through interface states are negligible. Thus, interface states, if existing, should not have much effect on the current transport phenomenon. The ideality factor also indicates the spatial homogeneity of the SBH. In this sense, the present SBH estimation must be understood as the integration of the punctual SBH in the entire XPS analysed area ($\varnothing = 50 \mu\text{m}$) of the WC/diamond contact. Thus, it is expected that the XPS method overestimates the SBH in comparison to the I/V

characterization. This is because localized SBH variations could have a critical effect on the I/V performance while remaining negligible in XPS experiments. The good matching between I/V and XPS values points up to a homogeneous SBH distribution and interface. The weak dependence of the SBH on the annealing temperature (Teraji et al., 2014) evidences small chemical or structural changes occurred at the interface during the annealing steps. The process for deterioration of the contacts should not have already started at 600 K.

On the other hand, the presence of C-O bonds at the interface is discussed in Section 4.3.2., showing the O-terminated diamond key role in the improvement of the Schottky contact performance. However, the mechanism for this phenomenon is still not clear. Its possible effect as an insulating thin layer analogous to metal-insulator-semiconductor diodes is discarded since these structures are based on tunnel emission, which would have been identified with higher ideality factors. On the other hand, it is known that surface oxygenation treatments on diamond transform the electron affinity of the bare and H-terminated surfaces from negative to positive values as higher as +1.7 eV (Maier, Ristein, et al., 2001). In an ideal metal/diamond junction, higher PEA values will lead to higher SBH values since, as electron affinity increases, the *VBM* of diamond will lie deeper than the Fermi level of the metal. The ideal SBH can be deduced by applying the Schottky-Mott model for p-type semiconductor:

$$\text{SBH} = E_G + \chi - \phi_M \quad (4.2)$$

where E_G and χ are the bandgap and the electron affinity of the semiconductor, respectively, and ϕ_M is the metal work function. The application of this model is assuming that the difference between the metal work function and the electron affinity of the semiconductor does not change during WC/diamond interface formation. By using the estimated SBH ~1.6 eV, E_G ~ 5.5 eV and the WC work function (ϕ_{WC} ~ 4.5-4.9 eV (Lassner & Schubert, 2005)(Fujii et al., 2006)), a PEA of χ ~ 0.6-1 eV is deduced. The result is reasonably compatible with the partial oxygenation of diamond surface, as observed in this work, and reflects that the experimental contact at 600 K annealing could not be so far from the ideal case. Moreover, the SBH result for WC contact is reasonably similar to that of Au/O-terminated diamond contacts based on VUV/Ozone treatment. Thus, the difference between the SBH of the Au contact (~2.5 eV (Teraji et al., 2014)) and the WC contact (~1.6 eV [This work]) could be explained by their work function difference, ~5.45 eV (Sachtler et al., 1966) and ~ 4.5 eV (Lassner & Schubert, 2005) of Au and WC, respectively. This observation supports the ideality of the VUV/Ozone oxygenation treatment for the control of contact properties.

Two main mechanisms can be related to the modification of the diamond surface electron affinity of the WC/O-terminated diamond junction: metal deposition and oxygen thermal

desorption. For the first, the modification of the diamond electron affinity after the metal deposition has been previously evidenced (Baumann & Nemanich, 1998a). Certainly, during the metallisation process, it is expected some C-O bonds to be a break and the generation of multiple defects. For instance, Zr metal deposition on O-terminated diamond could even turn the diamond electron affinity from positive to negative values (Baumann & Nemanich, 1998a). In the ideal case, this effect may result in a significant SBH reduction. In practice, it is difficult to discern to what extent this electron affinity reduction is affecting the SBH due to the Fermi level pinning effect induced by defects. Secondly, the oxygen instability during thermal treatment would also lead to the loss of the PEA condition and, consequently, the reduction of the SBH. The PEA to NEA surface transformation can be understood as a function of the diamond oxygen coverage (Maier, Ristein, et al., 2001). Oxygen desorption from diamond surface is expected to occur in a wide range of temperatures with a maximum desorption rate at ~873 K (R. E. Thomas et al., 1992).

4.3.4. WC/diamond interface mechanism formation during annealing

Based on the present results and discussions, an interface formation and stabilization mechanism is proposed (Figure 4.7). After the WC contact deposition, the diamond surface shows PEA, possibly reduced by the WC sputtering process, as well as the presence of relatively low-density interface states derived from the diamond growth process or even generated during the WC sputtering. In this initial state, higher ideality factors are related to the presence of these original defects (Figure 4.7 (Left)). Subsequent annealing steps will promote the partial W-diamond reaction and the nucleation of the WC cubic phase at the interface (Figure 4.7 (Right)). The early WC formation process at the near interface region seems to be slow, and little changes should occur at the interface. The reaction process should preferentially start at defective sites. Thus, effect on the electronic performance of the original interface states will be reduced as the interface configuration is progressively stabilized. This way, the ideality factor is reduced close to 1 at ~ 600 K. Due to the homogeneity and slow kinetics of the process, the SBH can hardly be improved. The oxygen coverage is expected to remain mostly similar during annealing steps as well as having an apparent crucial role in avoiding extensive W-diamond reaction (Piñero et al., 2017). At higher temperature annealing the interface configuration can be perturbed by two main mechanisms: oxygen desorption and loss of the PEA condition, and further W-diamond reaction and increased defects density. Both phenomena could be correlated and will lead to the deterioration of the Schottky performance.

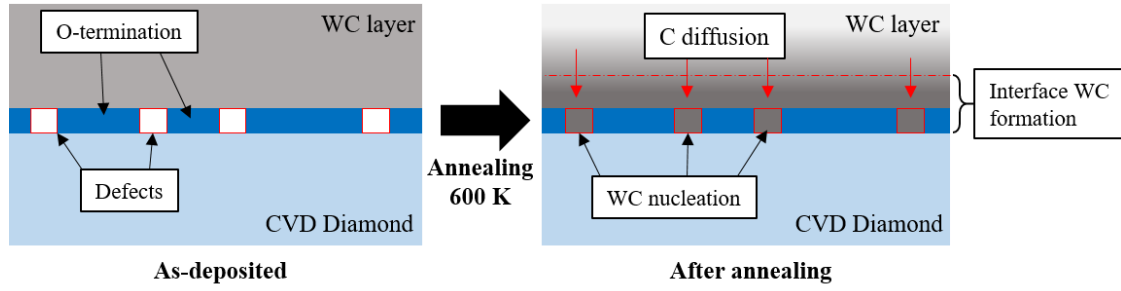


Figure 4.7: Schematic of the WC/O-terminated diamond interface modification during the annealing step. As-deposited WC contact is defined for the presence of low-density defect sites which makes the ideality factor increase as well as partial surface oxygenation (PEA surface). During annealing steps, WC nucleation preferentially occurs at interface defects. Early WC formation at the interface promotes the WC layer carbon diffusion. Higher temperature and time annealing are expected to promote further W-diamond reaction or oxygen desorption, resulting in the deterioration of the Schottky contact performance.

4.3.5. Ideal band setting of WC/O-terminated and WC/H-terminated diamond

From present results, the band setting of the ideal WC/O-terminated diamond can be represented (Figure 4.8). As has already discussed, the present results are compatible with a low density of interface states. Thus, the WC/O-terminated diamond band setting is compatible with the Schottky-Mott rule (Figure 4.8 (a)). On the other hand, if the electron affinity is modified properly from PEA of O-termination to NEA of H-termination ($\chi = -1.3$ eV has been estimated previously on H-terminated diamond (Diederich et al., 1996; Krainisky & Asnin, 1998; Takeuchi et al., 2005)) an SBH = -0.7 eV is predicted for the WC/H-terminated diamond. It means that an ohmic behaviour is expected for such a contact structure. The fabrication of WC/H-terminated diamond contacts is required to confirm this claim.

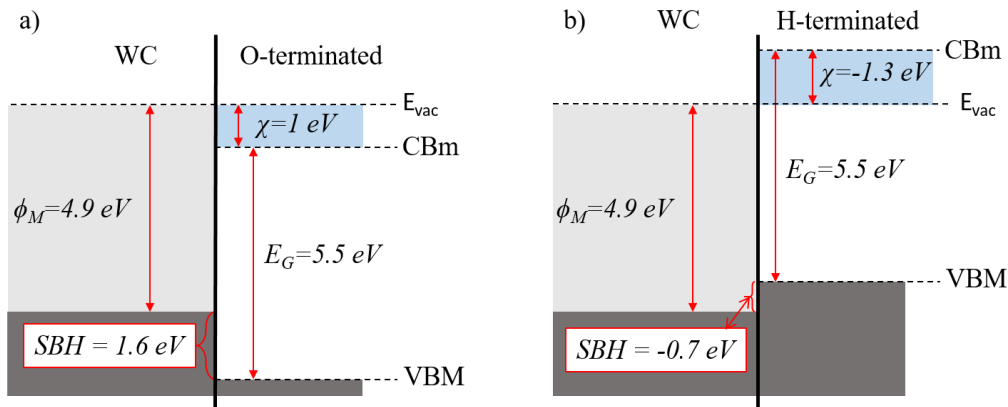


Figure 4.8: Band setting for WC/diamond contacts based on present results, electron affinity and work function data, and the application of the Schottky-Mott rule, i.e. in the ideal case (no interface states): a) a positive SBH of 1.6 eV is obtained for the O-terminated diamond and b) by using the NEA data of H-terminated diamond, a negative SBH is deduced and predicts an ohmic behaviour of the WC/H-terminated diamond contacts.

4.4. Final comments

Interface phenomenology is still a field of study of great projection for the manufacture of contacts and the control of their electronic behaviour. The main interface phenomena that determine the stability and operation of the contacts have been analyzed here for the specific case of the WC/diamond contact. The compatibility of the results with the predictions based on ideal contact suggests the effect of WC deposition in reducing interface defects. This provides superior stability during annealing which is also related to a short reaction due to the reactivity and solubility of the diamond with WC deposition.

The metal-diamond reaction is, therefore, a key factor in stabilizing the electronic behaviour of the contacts. However, it is a double-edged sword: on the one hand, this reaction is positive because it seems to cancel the interface defects but, on the other hand, an extensive and uncontrolled metal-diamond reaction can lead to the deterioration of the Schottky behaviour and, quite possibly, the appearance of an ohmic behaviour (e.g. Ti/diamond ohmic contact mechanism). Preformed carbide deposition is a way of controlling reactive processes at the metal/diamond interface. Reactivity, solubility, and crystallographic phase formation and stabilization of deposited carbides should be reviewed when seeking options for Schottky contacts. Thus, manufacturing conditions must also be found so that, at least under the operating conditions of a device, this balance is sufficient to take advantage of the positive effects of the reaction, avoiding the negative ones.

If the present results are compared with those of metal/diamond contacts where the metal is very little reactive (Au, Pt, Ag...), for the latter the desorption of oxygen will result in the generation of surface defects that can intervene negatively in the band setting of the contact, while, for the former, it is expected that these vacancies are counteracted by metal-carbon bonds, which gives the system better thermal stability. Under this prism, for example, the results found in Au/O-terminated diamond can be explained. At high temperatures, gold is not able to counteract the negative effect of dangling bonds on the diamond surface as there is no reaction with carbon. As soon as there is thermal desorption of oxygen, the electronic behaviour of the contact is affected, not only by a lower electronic affinity (lower O coverage) but also by the states induced by the defects. Therefore, the stability of this type of contact is highly dependent on oxygen desorption.

4.5. Summary of the section

In this Chapter, WC/O diamond contact after 600 K annealing, with interest for the fabrication of diamond based SBDs has been analysed by the combined analysis of XPS depth profile with low energy Ar⁺ ion sputtering and HRTEM/STEM. The studied contact shows the partial formation of a cubic-WC phase at the interface region and a dominant α -W metal phase component over the cubic-WC layer. The presence of WC is increasingly dominant as deepens, in the sample what has been related to the reaction of W and diamond and, tentatively, to the partial nucleation of WC grains at WC/diamond interface. This is supported by HRTEM analysis that allowed the identification of the cubic-WC at the interface region. Additionally, a C-O contribution at the very near interface is also evidenced by XPS and has been linked to diamond O-termination. In this sense, the formation of interface W oxides is discarded. Finally, the SBH value has been estimated through XPS measurement to be 1.6 ± 0.2 eV. This value is in agreement with that estimated by I/V measurements and is close to the maximum SBH reported for ideality factor 1 in WC/O-terminated diamond contacts. This result means that the contact is close to the ideal case (compatible with a low density of interface defects) and has a remnant partial oxidation of the surface, in agreement with the interface C-O bonds detection. A model of the interface changes occurring during the annealing process is proposed. Annealing at higher temperatures or with a longer duration is expected to induce partial desorption of oxygen, as well as promote a greater W-diamond reaction, which would lead to deterioration of the electronic Schottky behaviour of the contact.

Resumen de la sección

En este capítulo, se ha caracterizado el contacto WC/O-terminado, con interés para la fabricación de diodos Schottky, después del recocido a 600 K, mediante la combinación de estudios de perfil de profundidad XPS con pulverización catódica de iones Ar⁺ de baja energía y HRTEM. El contacto estudiado muestra la formación parcial de WC y un componente metálico dominante W a través de la capa de WC. La presencia de WC tiende a ser más dominante a medida que se profundiza en la muestra lo que se ha relacionado con la reacción de W y el diamante y, por tanto, con la nucleación parcial de los granos de WC en la intercara WC/diamante. Esto está respaldado por las mediciones de HRTEM del análisis HRTEM que permitieron identificar WC cúbico en la región de la interfaz. Además, los resultados XPS también evidencian una contribución C-O en la región de intercara que se ha vinculado a terminación de oxígeno de diamante. En este sentido, se descarta la formación de óxidos de W en la intercara. Finalmente, el valor de la SBH se ha estimado mediante la medición de XPS en 1.6 ± 0.2 eV. Este valor concuerda con el estimado por las mediciones de I/V y está cerca del SBH máximo predecible para el factor de idealidad 1 en los contactos WC/O-diamante. Este resultado significa que el contacto está cerca del caso ideal (baja densidad de defectos de la interfaz) y es compatible con la oxidación parcial de la superficie, de acuerdo con la detección de enlaces C-O de la interfaz. Se propone un modelo de los cambios que ocurren en la intercara durante el proceso de recocido. Se espera que los recocidos a mayores temperaturas o con una mayor duración induzcan la desorción parcial de oxígeno, así como promuevan una mayor reacción de W-diamante, lo que conduciría al deterioro del comportamiento electrónico Schottky del contacto.

Chapter 5:

Global conclusions and perspectives

X-ray photoelectron spectroscopy has been key to the achievement of this thesis. First, the ARXPS mode has served to elucidate the electronic contributions of the two main chemical terminations on the (100) diamond surface: hydrogen and oxygen. The achievements and results on the ARXPS analysis on this surfaces can be summarized as:

- **The development of an analysis method for photoelectron contributions that are defined in a space charge region.** The attribution of one of the XPS carbon contributions to the formation of a DBB promoted this development. In this sense, until now, the analysis of the band bending contributions has been carried out through the shifts and positions of peaks and energy levels. Here the advantages of using this method have been demonstrated and its limits explored.
- **The characterization of the surface downward band bending contribution existing at the (100) H-terminated diamond by the developed analysis method.** It allows us to find a DBB defined by $E_{bb} = 0.67$ eV along with the first 0.5 nm from the surface. The results are found to be compatible with the literature and prove the capabilities of this new method.
- **A new perspective on the origin of the XPS contributions of the (100) H-terminated diamond and its energy positions.** In this sense, the proposed XPS analysis method is key to get a more intuitive approach to the band bending origin of XPS peak shapes and positions. It allowed the reinterpretation of previous XPS results, such as the annealing effect or the origin of bulk peak positions.
- **A new perspective on the surface XPS contributions of the (100) O-terminated diamond and the transition from hydrogen to oxygen termination.** The detection of a dominant single-bonded C-O contribution, the shift of the maximum C 1s peak towards higher *BE*, and the appearance of a non-diamond carbon contribution, define the transition from H- to O-terminated diamond surface. The O 1s spectra analysis allows finding that, contrary to H-terminated, most of the O 1s contribution in O-terminated diamond comes from oxygen bonded to carbon, confirming the oxygenation mechanism of the surface.
- **The attribution of the “non-diamond” surface carbon contribution as part of the reconstruction of the O-terminated surface.** The review of previous results, the great reproducibility of this “non-diamond” C 1s contribution, the great fit of the spectra to the proposed analysis model, and the comparison to H-terminated results on the same sample, led to this conclusion.
- **A new reconstruction model for the 1×1:O surface model is proposed.** This is based on the previous conclusion and consists of the assumption that surface carbon atoms are in the sp^2 hybridization and not in the sp^3 one, as most accepted models

assume. Current models ignore this “non-diamond” contribution what makes them incompatible with experimental results.

Regarding the WC/diamond interface studies, XPS depth profiling and TEM have been key techniques to clarify the interface phenomenology of this preformed carbide contact structure. The low but existing WC-diamond reactivity is related to the higher thermal stability of its electronic behaviour. Main achievements are summarized as:

- **The nanocrystalline cubic-WC phase identification at the WC/O-diamond interface.** This finding is based on HRTEM measurements but is also supported by XPS results. It is a metastable phase rarely found in the literature and its formation is related to the WC/diamond interface.
- **The detection of remnant oxygen termination at the interface.** This kind of detection has very rarely been proved in the literature. It shows the interface oxygen thermal stability that points up to the fundamental role of oxygen in the formation of Schottky contacts.
- **The estimation of the WC/O-diamond contact Schottky barrier height by XPS.** The SBH value estimated by XPS is close to that found by I/V measurements and matches with the extrapolation for ideality factor close to 1. It leads to the conclusion that the contact band configuration is compatible with the ideal case predictions.
- **An interface thermal stabilization mechanism is proposed.** This mechanism is based on the synthesis of overall results and conclusion. It leads to conclude the potential of preformed metallic carbides for the stabilization of interface properties with high thermal stability.

In order to give a future perspective for this thesis, first, it is worth notice that the uncertainty on the origin of SCL in H-terminated diamond has not been solved yet and it is necessary to continue this path until a model to explain all the scientific evidence related to this complex phenomenon is obtained. This understanding is of great interest in device design. For future works, near-Ambient pressure XPS studies or Kelvin probe AFM can evidence the dependence of band bending changes due to different gas environment exposition, and even in operating devices. It could give a direct new perspective on the effect of surface termination on the device operation. On the other hand, the proposed XPS band bending shape generation must motivate the reinterpretation of published results, not only in the diamond electronics field but with general application. Concerning O-terminated diamond, there are still new questions as there may be several possible reconstructions that justify the present XPS results. Calculations regarding the stability and electronic configuration of these new reconstructions will help to better understand the role of oxygen on the diamond surface and its application in devices. By applying

this same method of analysis, differences could also be found between oxygenation treatments what would help to find and understand those most suitable ones for controlling the electronic behaviour of contacts. Again, the surface studies on operating devices need to be explored and will help to clarify the differences between treatments through the device operation feedback.

Concerning the WC studies, preformed carbides are potential candidates, for the manufacture of highly stable diamond Schottky contacts. These depositions must be differentiated from those of metals that form carbides because, for the latter, the formation of the carbide requires the reaction with the diamond surface that surely entails the breaking of the initial interface conditions. In preformed carbide depositions, the self-contained carbon would act as a catalyst, stopping this possible reaction and thermally stabilizing the contact behaviour and oxygen termination. A certain level of reaction seems necessary for the initial reduction of interface defects derived from the contact manufacturing processes. On the other hand, the control of diamond surface properties outside the metallic pads is key for the device operation and since surfaces could mean a possible leakage mechanism. Experiments like those already proposed in this text would help to advance in this direction.

To conclude, the studies carried out in this thesis serve to progress on the understanding of the surface and interface phenomena of diamond contacts. The issues addressed here are just a sample within the wide and complex range of scientific-technological issues and challenges that define the path towards the development of diamond-based power devices. Over time, the continued study of all these fundamental aspects will provide the answers necessary for the control and development of this desirable technology.

Conclusiones generales y perspectivas

La espectroscopia de fotoelectrones de rayos X ha sido clave para la consecución de esta tesis. Primero, el modo ARXPS ha servido para dilucidar las contribuciones electrónicas de las dos principales terminaciones químicas en la superficie del diamante (100): hidrógeno y oxígeno. Los logros y resultados del análisis ARXPS en estas superficies se resumen a continuación:

- ***El desarrollo de un método de análisis para las contribuciones de fotoelectrones que se definen en una región de carga espacial.*** La atribución de una de las contribuciones de carbono de XPS a la formación de un DBB promovió este desarrollo. En este sentido, hasta ahora, el análisis de las contribuciones a la flexión de la banda se ha realizado a través de los desplazamientos y posiciones de picos y niveles de energía. Aquí se han demostrado las ventajas de utilizar este método y se han explorado sus límites.
- ***La caracterización de la contribución de flexión de banda descendente existente en la superficie de diamante (100) H-terminado mediante el método de análisis desarrollado.*** Este método nos ha permitido caracterizar un DBB definido por $E_{bb} = 0.67$ eV en los primeros 0.5 nm desde la superficie. Los resultados son compatibles con la literatura.
- ***Una nueva perspectiva sobre el origen de las contribuciones XPS del diamante (100) H-terminado y sus posiciones energéticas.*** En este sentido, el método de análisis XPS propuesto es clave para obtener un enfoque más intuitivo del origen de la flexión de la banda y cómo estas generan las formas y las posiciones de los picos en los espectros XPS. Esto permitió la reinterpretación de resultados XPS anteriores, como el efecto de recocido o el origen de las posiciones de los picos en masa.
- ***Una nueva perspectiva sobre las contribuciones XPS de la superficie del diamante (100) O-terminado y la transición de la terminación con hidrógeno a la terminación con oxígeno.*** La detección de una contribución dominante de C-O de enlace simple, el desplazamiento del pico máximo de C 1s hacia un BE más alto y la aparición de una contribución de carbono distinta del diamante, definen la transición de la superficie del diamante terminada en H a O. El análisis de espectros de O 1s permite encontrar que, al contrario que en el diamante H-terminado, la mayor parte de la contribución de O 1s en el diamante O-terminado proviene de enlaces C-O del diamante, lo que confirma el mecanismo de oxigenación de la superficie.
- ***La atribución de la contribución de carbono superficial, distinto del diamante, como parte de la reconstrucción de la superficie O-terminada.*** La revisión de los resultados anteriores, la gran reproducibilidad de esta contribución de C 1s distinta del diamante,

el gran ajuste de los espectros al modelo de análisis propuesto y la comparación con los resultados en la misma muestra cuando estaba H-terminada, llevaron a esta conclusión.

- Se propone un nuevo modelo de reconstrucción para el modelo de superficie $1 \times 1:0$. Esto se basa en la conclusión anterior y consiste en la suposición de que los átomos de carbono de la superficie están en la hibridación sp^2 y no en la sp^3 , como asumen la mayoría de los modelos aceptados. Los modelos actuales ignoran esta contribución distinta del diamante, lo que los hace incompatibles con los resultados experimentales.

Con respecto a los estudios de la interfaz WC / diamante, la caracterización por XPS en perfil de profundidad y TEM han sido claves para aclarar la fenomenología de la interfaz de esta estructura de contacto de carburo preformado. La baja pero existente reactividad WC-diamante está relacionada con la mayor estabilidad térmica de su comportamiento electrónico. Los principales logros se resumen en:

- La identificación de fase nanocrystalina cúbica-WC en la interfaz WC / O-diamante. Este hallazgo se basa en mediciones de HRTEM, pero también está respaldado por los resultados de XPS.

- La detección de terminación de oxígeno remanente en la interfaz. Este tipo de detecciones rara vez se ha probado en la literatura. Muestra la estabilidad térmica del oxígeno de la interfaz, lo que apunta al papel fundamental del oxígeno en la formación de los contactos de Schottky.

- La estimación de la altura de la barrera de Schottky de contacto WC / O-diamante por XPS. El valor SBH es cercano al encontrado por las mediciones de I/V y coincide con la extrapolación para el factor de idealidad cercano a 1. Lleva a la conclusión de que la configuración de la banda de contacto es compatible con las predicciones del caso ideal.

- Se propone un mecanismo de estabilización térmica de la interfaz. Este mecanismo se basa en los resultados y la conclusión generales. Esto lleva concluir que los carburos metálicos preformados tienen un gran potencial en la estabilización térmica del comportamiento Schottky de los contactos.

Con el fin de dar una perspectiva futura a esta tesis, en primer lugar, me gustaría señalar que la incertidumbre sobre el origen de SCL en diamante H-terminado aún no se ha resuelto y es necesario continuar este camino hasta obtener un modelo que explique toda la evidencia científica relacionada con este complejo fenómeno. Esta comprensión es de gran interés en el diseño del dispositivo. Para trabajos futuros, los estudios XPS de presión cercana al ambiente o el Kelvin Probe AFM pueden evidenciar la dependencia de los cambios de flexión de la banda debido a la exposición al ambiente de gas diferente, e incluso en dispositivos operativos. Esto

podría brindar una nueva perspectiva directa sobre el efecto de la terminación superficial en el funcionamiento del dispositivo. Por otro lado, la generación de formas de flexión de la banda XPS propuesta debe motivar la reinterpretación de los resultados publicados, no solo en el campo de la electrónica del diamante sino con una aplicación general. Con respecto al diamante terminado en O, todavía hay nuevas preguntas, ya que podrían existir varias reconstrucciones compatibles con los resultados actuales de XPS. Los cálculos sobre la estabilidad y la configuración electrónica de estas nuevas reconstrucciones ayudarán a comprender mejor el papel del oxígeno en la superficie del diamante y su aplicación en los dispositivos. Aplicando este mismo método de análisis, también se podrían encontrar diferencias entre los distintos tratamientos de oxigenación que ayudarían a encontrar y comprender los más adecuados para controlar el comportamiento electrónico de los contactos. Una vez más, los estudios de superficie sobre los dispositivos operativos deben explorarse y ayudarán a aclarar estas diferencias entre los tratamientos a través de la información sobre el funcionamiento del dispositivo.

Con respecto a los estudios de WC, los carburos preformados son candidatos potenciales para la fabricación de contactos Schottky de diamante altamente estables. Estas deposiciones deben diferenciarse de las de los metales que forman carburos porque, para estos últimos, la formación del carburo requiere la reacción con la superficie del diamante que seguramente conlleva la ruptura de las condiciones de intercara iniciales. En las deposiciones de carburo preformadas, el contenido de carbono inicial actuaría como catalizador, deteniendo esta posible reacción y estabilizando térmicamente el comportamiento de contacto y la terminación del oxígeno. Un cierto nivel de reacción parece necesario para la reducción inicial de defectos de interfaz derivados de los procesos de fabricación de contactos. Por otro lado, el control de las propiedades de la superficie del diamante fuera de los contactos metálicos es clave para el funcionamiento del dispositivo dado que las superficies podrían significar un posible mecanismo de fuga. Experimentos como los ya propuestos en este texto ayudarían a avanzar en esta dirección.

Para concluir, los estudios realizados en esta tesis sirven para avanzar en el entendimiento de los fenómenos de superficies e intercaras de los contactos de diamante. Los asuntos aquí abordados son solo una muestra dentro del amplio y complejo abánico de aspectos y retos científicos-tecnológicos que definen el camino hacia el desarrollo de los dispositivos de potencia basados en el diamante. Con el tiempo, el estudio continuado de todos estos aspectos fundamentales proporcionará las respuestas necesarias para el control y desarrollo de esta deseable tecnología.

References

- Alba, G., Eon, D., Villar, M. P., Alcántara, R., Chicot, G., Cañas, J., et al. (2020). H-Terminated Diamond Surface Band Bending Characterization by Angle-Resolved XPS. *Surfaces*, 3(1), 61–71. <https://doi.org/10.3390/surfaces3010007>
- Alegre, M. P., Araújo, D., Fiori, A., Pinero, J. C., Lloret, F., Villar, M. P., et al. (2014). Critical boron-doping levels for generation of dislocations in synthetic diamond. *Applied Physics Letters*, 105(17), 1–6. <https://doi.org/10.1063/1.4900741>
- Alvarez, J., Houzé, F., Kleider, J. P., Liao, M. Y., & Koide, Y. (2006). Electrical characterization of Schottky diodes based on boron doped homoepitaxial diamond films by conducting probe atomic force microscopy. *Superlattices and Microstructures*, 40(4-6 SPEC. ISS.), 343–349. <https://doi.org/10.1016/j.spmi.2006.07.027>
- Ando, T., Yamamoto, K., Ishii, M., Kamo, M., & Sato, Y. (1993). Vapour-phase oxidation of diamond surfaces in O₂ studied by diffuse reflectance Fourier-transform infrared and temperature-programmed desorption spectroscopy. *Journal of the Chemical Society, Faraday Transactions*, 89(19), 3635–3640. <https://doi.org/10.1039/FT9938903635>
- Araujo, D., Bustarret, E., Tajani, A., Achatz, P., Gutierrez, M., Garcia, A. J., & Villar, M. P. (2010). Comparison of the crystalline quality of homoepitaxially grown CVD diamond layer on cleaved and polished substrates. *Physica Status Solidi A-Applications and Materials Science*, 207(9), 2023–2028. <https://doi.org/10.1002/pssa.201000141>
- Araujo, D., Alegre, M. P., Piñero, J. C., Fiori, A., & Bustarret, E. (2013). Boron concentration profiling by high angle annular dark field-scanning transmission electron microscopy in homoepitaxial d-doped diamond layers. *Applied Physics Letters*, 0–4.

- Barjon, J., Desfonds, P., Pinault, M. A., Kociniewski, T., Jomard, F., & Chevallier, J. (2007). Determination of the phosphorus content in diamond using cathodoluminescence spectroscopy. *Journal of Applied Physics*, *101*(11). <https://doi.org/10.1063/1.2735408>
- Baumann, P. K., & Nemanich, R. J. (1998a). Electron affinity and Schottky barrier height of metal-diamond (100), (111), and (110) interfaces. *Journal of Applied Physics*, *83*(4), 2072–2082. <https://doi.org/10.1063/1.366940>
- Baumann, P. K., & Nemanich, R. J. (1998b). Surface cleaning, electronic states and electron affinity of diamond (100), (111) and (110) surfaces. *Surface Science*, *409*(2), 320–335. [https://doi.org/10.1016/S0039-6028\(98\)00259-3](https://doi.org/10.1016/S0039-6028(98)00259-3)
- Baxter, R., Hastings, N., Law, A., & Glass, E. J. . (2008). ARPES - Theory and current applications. *Animal Genetics*, *39*(5), 561–563.
- Bergmaier, A., Dollinger, G., Aleksov, A., Gluche, P., & Kohn, E. (2001). Deuterium depth profiles at CVD diamond surfaces. *Surface Science*, *481*(1–3), 1–4. [https://doi.org/10.1016/S0039-6028\(01\)01030-5](https://doi.org/10.1016/S0039-6028(01)01030-5)
- Bernstein, R. W., & Grepstad, J. K. (1989). XPS intensity analysis for assessment of thickness and composition of thin overlayer films: application to chemically etched GaAs (100) Surfaces. *Surface and Interface Analysis*, *14*(March 1988), 109–114.
- Bobrov, K., Mayne, A., Comtet, G., Dujardin, G., Hellner, L., Comtet, G., et al. (2003). Atomic-scale visualization and surface electronic structure of the hydrogenated diamond C(100)-(2×1):H surface. *Physical Review B - Condensed Matter and Materials Physics*, *68*(19). <https://doi.org/10.1103/PhysRevB.68.195416>
- Boukherroub, R., Wallart, X., Szunerits, S., Marcus, B., Bouvier, P., & Mermoux, M. (2005). Photochemical oxidation of hydrogenated boron-doped diamond surfaces, *7*, 937–940. <https://doi.org/10.1016/j.elecom.2005.05.010>
- Brezeanu, M. (2007). *Diamond Schottky Barrier Diodes*. Cambridge University.
- Buhsmer, C. P., & Crayton, P. H. (1971). Carbon self-diffusion in tungsten carbide. *Journal of Materials Science*, *6*(7), 981–988. <https://doi.org/10.1007/BF00549949>
- Bundy, F. P., Hall, H. T., Strong, H. M., & Wentorf, R. H. (1955). Man-made diamonds. *Chemical and Engineering News*, *33*(8), 718. <https://doi.org/10.2493/jjspe1933.27.371>
- Burns, R. C., Chumakov, A. I., Connell, S. H., Dube, D., Godfried, H. P., Hansen, J. O., et al. (2009). HPHT growth and x-ray characterization of high-quality type IIa diamond. *Journal of Physics Condensed Matter*, *21*(36). <https://doi.org/10.1088/0953-8984/21/36/364224>

- Butenko, Y. V., Kuznetsov, V. L., Chuvilin, A. L., Kolomiichuk, V. N., Stankus, S. V., Khairulin, R. A., & Segall, B. (2000). Kinetics of the graphitization of dispersed diamonds at 'low' temperatures. *Journal of Applied Physics*, 88(7), 4380–4388. <https://doi.org/10.1063/1.1289791>
- Cañas, J., Alba, G., Leinen, D., Lloret, F., Gutierrez, M., Eon, D., et al. (2020). Diamond/ γ -alumina band offset determination by XPS. *Applied Surface Science*, 146301. <https://doi.org/10.1016/J.APSUSC.2020.146301>
- Chandran, M., Shasha, M., Michaelson, S., & Hoffman, A. (2015). Nitrogen termination of single crystal (100) diamond surface by radio frequency N₂ plasma process: An in-situ x-ray photoemission spectroscopy and secondary electron emission studies. *Applied Physics Letters*, 107(11), 111602. <https://doi.org/10.1063/1.4930945>
- Chen, C. T., & Sette, F. (1990). High Resolution Soft X-Ray Spectroscopies with the Dragon Beamline. *Physica Scripta*, 1990(T31), 119–126. <https://doi.org/10.1088/0031-8949/1990/T31/016>
- Chen, L. J., Liu, C. C., Tai, N. H., Lee, C. Y., Fang, W., & Lin, I. N. (2008). Effects of tungsten metal coatings on enhancing the characteristics of ultrananocrystalline diamond films. *Journal of Physical Chemistry C*, 112(10), 3759–3765. <https://doi.org/10.1021/jp709777g>
- Chen, W., Qi, D., Gao, X., & Wee, A. T. S. (2009). Surface transfer doping of semiconductors. *Progress in Surface Science*, 84(9–10), 279–321. <https://doi.org/10.1016/j.progsurf.2009.06.002>
- Chen, Y. G., Ogura, M., Yamasaki, S., & Okushi, H. (2005). Ohmic contacts on p-type homoepitaxial diamond and their thermal stability. *Semiconductor Science and Technology*, 20(8), 860–863. <https://doi.org/10.1088/0268-1242/20/8/041>
- Chevallier, J., Theys, B., Lusson, A., Grattapain, C., Deneuille, A., & Gheeraert, E. (1998). Hydrogen-boron interactions in-type diamond. *Physical Review B - Condensed Matter and Materials Physics*, 58(12), 7966–7969. <https://doi.org/10.1103/PhysRevB.58.7966>
- Chicot, G., Tran Thi, T. N., Fiori, A., Jomard, F., Gheeraert, E., Bustarret, E., & Pernot, J. (2012). Hole transport in boron delta-doped diamond structures. *Applied Physics Letters*, 101.
- Crawford, K. G., Tallaire, A., Li, X., Macdonald, D. A., Qi, D., & Moran, D. A. J. (2018). The role of hydrogen plasma power on surface roughness and carrier transport in transfer-doped H-diamond. *Diamond and Related Materials*, 84(2017), 48–54. <https://doi.org/10.1016/j.diamond.2018.03.005>
- Crist, B. V. (1992). Argon Implanted into Graphite, by XPS. *Surface Science Spectra*, 1(4), 376–

380. <https://doi.org/10.1116/1.1247636>
- Crist, B. V. (1999). Handbooks of Monochromatic XPS Spectra Volume 1 - The Elements and Native Oxides. *Handbook of The Elements and Native Oxides, 1*, 1–87. <https://doi.org/10.1002/pssb.2221980103>
- Dai-Yi, Q., & Zi, G. (1990). XPS study of tungsten carbide. *Chinese Journal of Chemistry*, 8(4), 301–305. <https://doi.org/10.1002/cjoc.19900080404>
- David, D. G. F., Pinault-Thaury, M. A., Ballutaud, D., & Godet, C. (2013). Sensitivity of photoelectron energy loss spectroscopy to surface reconstruction of microcrystalline diamond films. *Applied Surface Science*, 273, 607–612. <https://doi.org/10.1016/j.apsusc.2013.02.087>
- Davies, G., & Evans, T. (1972). Graphitization of diamond at zero pressure and at a high pressure. *Proceedings of the Royal Society of London. A. Mathematical and Physical Sciences*, 328(1574), 413–427. <https://doi.org/10.1098/rspa.1972.0086>
- Denisenko, A., Romanyuk, A., Pietzka, C., Scharpf, J., & Kohn, E. (2011). Electronic surface barrier properties of fluorine-terminated boron-doped diamond in electrolytes. *Surface Science*, 605(5–6), 632–637. <https://doi.org/10.1016/j.susc.2011.01.001>
- Diederich, L., Küttel, O. M., Schaller, E., & Schlapbach, L. (1996). Photoemission from the negative electron affinity (100) natural hydrogen terminated diamond surface. *Surface Science*, 349(2), 176–184. [https://doi.org/10.1016/0039-6028\(95\)01117-X](https://doi.org/10.1016/0039-6028(95)01117-X)
- Evans, T., & Phaal, C. (1961). The kinetics of the diamond-oxygen reaction. In *Proceedings of the Fifth Conference on Carbon* (pp. 147–153).
- Fadley, C. S. (1974). Instrumentation for surface studies: XPS angular distributions. *Journal of Electron Spectroscopy and Related Phenomena*, 5(1), 725–754. [https://doi.org/10.1016/0368-2048\(74\)85048-6](https://doi.org/10.1016/0368-2048(74)85048-6)
- Fadley, C. S. (1984). Angle-resolved x-ray photoelectron spectroscopy. *Progress in Surface Science*, 16(3), 275–388. [https://doi.org/10.1016/0079-6816\(84\)90001-7](https://doi.org/10.1016/0079-6816(84)90001-7)
- Fadley, C. S. (2010). X-ray photoelectron spectroscopy: Progress and perspectives. *Journal of Electron Spectroscopy and Related Phenomena*, 178–179(C), 2–32. <https://doi.org/10.1016/j.elspec.2010.01.006>
- Fan, Y., Fitzgerald, A. G., John, P., Troupe, C. E., & Wilson, J. I. B. (2002). X-ray photoelectron spectroscopy studies of CVD diamond films. *Surface and Interface Analysis*, 34(1), 703–707. <https://doi.org/10.1002/sia.1392>

-
- Feral, K. (2012). Detecting HPHT synthetic diamond using a handheld magnet. *Gems and Gemology*, 48(4), 262–272. <https://doi.org/10.5741/GEMS.48.4.262>
- Fernández-Lorenzo, C., Araújo, D., Martín, J., Alcántara, R., Navas, J., Villar, M. P., et al. (2010). Hydrogen passivation of boron acceptors in as-grown boron-doped CVD diamond epilayers. *Diamond and Related Materials*, 19(7–9), 904–907. <https://doi.org/10.1016/j.diamond.2010.02.030>
- Fiori, A. (2012). *New generations of boron-doped diamond structures by delta-doping technique for power electronics : CVD growth and characterization*.
- Fiori, A., Teraji, T., & Koide, Y. (2014a). Diamond Schottky diodes with ideality factors close to 1. *Applied Physics Letters*, 105(13), 1–5. <https://doi.org/10.1063/1.4897315>
- Fiori, A., Teraji, T., & Koide, Y. (2014b). Schottky-Barrier Inhomogeneities in WC / p -diamond at High Temperature. In *Extended Abstracts of the 2014 International Conference on Solid State Devices and Materials* (pp. 380–381).
- Fiori, A., Teraji, T., & Koide, Y. (2014c). Thermal stabilization and deterioration of the WC/p-type diamond (100) Schottky-barrier interface. *Physica Status Solidi (A) Applications and Materials Science*, 211(10), 2363–2366. <https://doi.org/10.1002/pssa.201431216>
- Foord, J. S., Hian, L. C., & Jackman, R. B. (2001). An investigation of the surface reactivity of diamond photocathodes with molecular and atomic oxygen species. *Diamond and Related Materials*, 10(3–7), 710–714. [https://doi.org/10.1016/S0925-9635\(00\)00605-1](https://doi.org/10.1016/S0925-9635(00)00605-1)
- Fujii, R., Gotoh, Y., Liao, M. Y., Tsuji, H., & Ishikawa, J. (2006). Work function measurement of transition metal nitride and carbide thin films. *Vacuum*, 80(7 SPEC. ISS.), 832–835. <https://doi.org/10.1016/j.vacuum.2005.11.030>
- Futera, Z., Watanabe, T., Einaga, Y., & Tateyama, Y. (2014). First principles calculation study on surfaces and water interfaces of boron-doped diamond. *Journal of Physical Chemistry C*, 118(38), 22040–22052. <https://doi.org/10.1021/jp506046m>
- Gao, X., Liu, L., Qi, D., Chen, S., Wee, A. T. S., Ouyang, T., et al. (2008). Water-induced negative electron affinity on diamond (100). *Journal of Physical Chemistry C*, 112(7), 2487–2491. <https://doi.org/10.1021/jp0726337>
- Gi, R. S., Mizumasa, T., Akiba, Y., Hirose, Y., Kurosu, T., & Iida, M. (1995). Formation mechanism of p-type surface conductive layer on deposited diamond films. *Japanese Journal of Applied Physics*, 34(10), 5550–5555. <https://doi.org/10.1143/JJAP.34.5550>
- Goldschmidt, J., & Brand, J. a. (1963). The tungsten-rich region of the system tungsten-carbon.
-

Journal of the Less-Common Metals, 5, 181–194.

- Goss, J. P., Jones, R., Heggie, M. I., Ewels, C. P., Briddon, P. R., & Öberg, S. (2002). Theory of hydrogen in diamond. *Physical Review B*, 65(11), 115207. <https://doi.org/10.1103/PhysRevB.65.115207>
- Goss, Jonathan P. (2003). Theory of hydrogen in diamond. *Journal of Physics: Condensed Matter*, 15(17), R551–R580. <https://doi.org/10.1088/0953-8984/15/17/201>
- Graupner, R., Maier, F., Ristein, J., Ley, L., & Jung, C. (1998). High-resolution surface-sensitive C core-level spectra of clean and hydrogen-terminated diamond (100) and (111) surfaces. *Physical Review B - Condensed Matter and Materials Physics*, 57(19), 12397–12409. <https://doi.org/10.1103/PhysRevB.57.12397>
- Hakansson, K. L., Johansson, H. I. P., & Johansson, L. I. (1994). High-resolution core-level study of hexagonal WC(0001). *Phys. Rev. B*, 49(3), 2035–2039.
- Hamza, A. V., Kubiak, G. D., & Stulen, R. H. (1990). Hydrogen chemisorption and the structure of the diamond C(100)-(2 × 1) surface. *Surface Science*, 237(1–3), 35–52. [https://doi.org/10.1016/0039-6028\(90\)90517-C](https://doi.org/10.1016/0039-6028(90)90517-C)
- Harris, S. J., & Goodwin, D. G. (1993). Growth on the reconstructed diamond (100) surface. *Journal of Physical Chemistry*, 97(1), 23–28. <https://doi.org/10.1021/j100103a007>
- Harris, S. J., & Weiner, A. M. (1990). Effects of Oxygen on Diamond Growth. In *Material research society symposium proceeding* (Vol. 162, pp. 103–107).
- Hasegawa, M., Takeuchi, D., Yamanaka, S., Ogura, M., Watanabe, H., Kobayashi, N., et al. (1999). N-Type Control By Sulfur Ion Implantation in Homoepitaxial Diamond Films Grown By Chemical Vapor Deposition. *Japanese Journal of Applied Physics, Part 2: Letters*, 38(12 B). <https://doi.org/10.1143/JJAP.38.L1519>
- Hayashi, K., Yamanaka, S., Okushi, H., & Kajimura, K. (1996). Study of the effect of hydrogen on transport properties in chemical vapor deposited diamond films by Hall measurements. *Applied Physics Letters*, 68(3), 376–378. <https://doi.org/10.1063/1.116690>
- Hong, S., & Chou, M. (1997). Theoretical study of hydrogen-covered diamond (100) surfaces: A chemical-potential analysis. *Physical Review B - Condensed Matter and Materials Physics*, 55(15), 9975–9982. <https://doi.org/10.1103/PhysRevB.55.9975>
- Ichikawa, K., Kodama, H., Suzuki, K., & Sawabe, A. (2016). Dislocation in heteroepitaxial diamond visualized by hydrogen plasma etching. *Thin Solid Films*, 600, 142–145. <https://doi.org/10.1016/j.tsf.2016.01.009>

- Isberg, J., Hammersberg, J., Johansson, E., Wikström, T., Twitchen, D. J., Whitehead, A. J., et al. (2002). High carrier mobility in single-crystal plasma-deposited diamond. *Science*, 297(5587), 1670–1672. <https://doi.org/10.1126/science.1074374>
- Ivanov, O. A., Muchnikov, A. B., Chernov, V. V., Bogdanov, S. A., Vikharev, A. L., & Butler, J. E. (2015). Experimental study of hydrogen plasma etching of (1 0 0) single crystal diamond in a MPACVD reactor. *Materials Letters*, 151, 115–118. <https://doi.org/10.1016/j.matlet.2015.03.073>
- John, P., & Stoikou, M. D. (2011). Hydrogen plasma interaction with (100) diamond surfaces. *Physical Chemistry Chemical Physics*, 13(24), 11503–11510. <https://doi.org/10.1039/c1cp20099b>
- John, P., Polwart, N., Troupe, C. E., & Wilson, J. I. B. (2003). The oxidation of diamond: The geometry and stretching frequency of carbonyl on the (100) surface. *Journal of the American Chemical Society*, 125(22), 6600–6601. <https://doi.org/10.1021/ja029586a>
- Joshi, A., Nimmagadda, R., & Herrington, J. (1990). Oxidation kinetics of diamond, graphite, and chemical vapor deposited diamond films by thermal gravimetry. *Journal of Vacuum Science & Technology A: Vacuum, Surfaces, and Films*, 8(3), 2137–2142. <https://doi.org/10.1116/1.577028>
- Kaibara, Y., Sugata, K., Tachiki, M., Umezawa, H., & Kawarada, H. (2003). Control wettability of the hydrogen-terminated diamond surface and the oxidized diamond surface using an atomic force microscope. *Diamond and Related Materials*, 12(3–7), 560–564. [https://doi.org/10.1016/s0925-9635\(02\)00373-4](https://doi.org/10.1016/s0925-9635(02)00373-4)
- Kajihara, S. A., Antonelli, A., & Bernhole, J. (1993). Impurity incorporation and doping of diamond. *Physica B*, 185, 144–149.
- Kamo, M., Sato, Y., Matsumoto, S., & Setaka, N. (1983). Diamond synthesis from gas phase in microwave plasma. *Journal of Crystal Growth*, 62(3), 642–644. [https://doi.org/10.1016/0022-0248\(83\)90411-6](https://doi.org/10.1016/0022-0248(83)90411-6)
- Kanai, C., Shichibu, Y., Watanabe, K., & Takakuwa, Y. (2002). Ab initio study on surface segregation of hydrogen from diamond C(100) surfaces, 65, 1–3. <https://doi.org/10.1103/PhysRevB.65.153312>
- Kanai, C., Watanabe, K., & Takakuwa, Y. (2003). Ab initio study on the electronic states of hydrogen defects in diamond subsurfaces. *Japanese Journal of Applied Physics, Part 1: Regular Papers and Short Notes and Review Papers*, 42(6 A), 3510–3513. <https://doi.org/10.1143/JJAP.42.3510>

- Kang, W. P., Wisitsora-at, A., Davidson, J. L., Li, Q., Kim, C. K., Xu, J. F., & Kerns, D. V. (1997). Effects of sp² content and surface treatment on the field emission of micropatterned pyramidal diamond tips. In *Proceedings of the IEEE International Vacuum Microelectronics Conference, IVMC* (Vol. 16, pp. 107–111). IEEE. <https://doi.org/10.1116/1.589881>
- Kawarada, H. (1996). Hydrogen-terminated diamond surfaces and interfaces. *Surface Science Reports*, 26(7), 205–259. [https://doi.org/10.1016/S0167-5729\(97\)80002-7](https://doi.org/10.1016/S0167-5729(97)80002-7)
- Kimura, K., Nakajima, K., Yamanaka, S., Hasegawa, M., & Okushi, H. (2001). Hydrogen depth-profiling in chemical-vapor-deposited diamond films by high-resolution elastic recoil detection. *Applied Physics Letters*, 78(12), 1679–1681. <https://doi.org/10.1063/1.1356452>
- Klauser, F., Ghodbane, S., Boukherroub, R., Szunerits, S., Steinmüller-nethl, D., Bertel, E., & Memmel, N. (2010). Comparison of different oxidation techniques on single-crystal and nanocrystalline diamond surfaces. *Diamond & Related Materials*, 19(5–6), 474–478. <https://doi.org/10.1016/j.diamond.2009.11.013>
- Koide, Y. (2008). Metal-diamond semiconductor interface and photodiode application. *Applied Surface Science*, 254(19), 6268–6272. <https://doi.org/10.1016/j.apsusc.2008.02.157>
- Koinkar, P. M., Patil, P. P., More, M. A., Tondare, V. N., & Joag, D. S. (2003). Field emission studies of CVD diamond thin films: Effect of acid treatment. *Vacuum*, 72(3), 321–326. <https://doi.org/10.1016/j.vacuum.2003.08.010>
- Koizumi, S., Kamo, M., Sato, Y., Ozaki, H., & Inuzuka, T. (1997). Growth and characterization of phosphorous doped {111} homoepitaxial diamond thin films. *Applied Physics Letters*, 71(8), 1065–1067. <https://doi.org/10.1063/1.119729>
- Koizumi, S., Watanabe, K., Hasegawa, M., & Kanda, H. (2001). Ultraviolet Emission from a Diamond pn Junction, 292(5523), 1899–1901. <https://doi.org/10.1126/science.1060258>
- Kono, S., Takano, T., Shimomura, M., Goto, T., Sato, K., Abukawa, T., et al. (2003). Electron-spectroscopy and -diffraction study of the conductivity of CVD diamond (2×1) surface. *Surface Science*. [https://doi.org/10.1016/S0039-6028\(03\)00241-3](https://doi.org/10.1016/S0039-6028(03)00241-3)
- Kono, S., Shiraishi, M., Goto, T., Abukawa, T., Tachiki, M., & Kawarada, H. (2005). An electron-spectroscopic view of CVD diamond surface conductivity. *Diamond and Related Materials*, 14(3–7), 459–465. <https://doi.org/10.1016/j.diamond.2004.11.011>
- Kono, S., Mizuochi, K., Takyō, G., Plusnin, N. I., Aoyama, T., Goto, T., et al. (2007). Surface Energy Band and Electron Affinity of Highly Phosphorous-doped Epitaxial CVD Diamond.

- E-Journal of Surface Science and Nanotechnology*, 5(July), 33–40.
<https://doi.org/10.1380/ejssnt.2007.33>
- Kono, S., Saitou, T., Kawata, H., Goto, T., Kakefuda, Y., & Komeda, T. (2009). Characteristic energy band values and electron attenuation length of a chemical-vapor-deposition diamond (001) surface. *Surface Science*, 603(6), 860–866.
<https://doi.org/10.1016/j.susc.2009.01.033>
- Kono, S., Saito, T., Kang, S. H., Jung, W. Y., Kim, B. Y., Kawata, H., et al. (2010). Band diagram for chemical vapor deposition diamond surface conductive layer: Presence of downward band bending due to shallow acceptors. *Surface Science*, 604(13–14), 1148–1165.
<https://doi.org/10.1016/j.susc.2010.03.031>
- Kono, S., Kodama, H., Ichikawa, K., Yoshikawa, T., Abukawa, T., & Sawabe, A. (2014). Electron spectro-microscopic determination of barrier height and spatial distribution of Au and Ag Schottky junctions on boron-doped diamond (001). *Japanese Journal of Applied Physics*, 53(5 SPEC. ISSUE 1). <https://doi.org/10.7567/JJAP.53.05FP03>
- Kono, S., Teraji, T., Kodama, H., Ichikawa, K., Ohnishi, S., & Sawabe, A. (2015). Direct determination of the barrier height of Au-based ohmic contact on p-type diamond (001). *Diamond and Related Materials*, 60, 117–122.
<https://doi.org/10.1016/j.diamond.2015.10.028>
- Kono, S., Sawabe, A., Kodama, H., Hayashi, Y., Kageura, T., Ogura, M., et al. (2019). Carbon 1s X-ray photoelectron spectra of realistic samples of hydrogen-terminated and oxygen-terminated CVD diamond (111) and (001). *Diamond and Related Materials*, 93(February), 105–130. <https://doi.org/10.1016/j.diamond.2019.01.017>
- Koslowski, B., Strobel, S., Wenig, M. J., Martschat, R., & Ziemann, P. (1998). On the roughness of hydrogen-plasma treated diamond (100) surfaces. *Diamond and Related Materials*, 7(97), 322–326.
- Koslowski, B., Strobel, S., & Ziemann, P. (2001). Are protons involved in the hydrogen-induced surface conductivity of diamond(001)? *Applied Physics A: Materials Science and Processing*, 72(3), 311–317. <https://doi.org/10.1007/s003390000694>
- Kozak, H., Kromka, A., Ukraintsev, E., Houdkova, J., Ledinsky, M., Vaněček, M., & Rezek, B. (2009). Detecting sp² phase on diamond surfaces by atomic force microscopy phase imaging and its effects on surface conductivity. *Diamond and Related Materials*, 18(5–8), 722–725. <https://doi.org/10.1016/j.diamond.2009.02.010>
- Krainy, I. L., & Asnin, V. M. (1998). Negative electron affinity mechanism for diamond

- surfaces. *Applied Physics Letters*, 72(20), 2574–2576. <https://doi.org/10.1063/1.121422>
- Kraut, E. A., Grant, R. W., Waldrop, J. R., & Kowalczyk, S. P. (1983). Semiconductor core-level to valence-band maximum binding-energy differences: Precise determination by x-ray photoelectron spectroscopy. *Physical Review B*, 28(4), 1965–1977. <https://doi.org/10.1103/PhysRevB.28.1965>
- Kubovic, M., & Kasu, M. (2010). Enhancement and stabilization of hole concentration of hydrogen-terminated diamond surface using ozone adsorbates. *Japanese Journal of Applied Physics*, 49(11), 11–14. <https://doi.org/10.1143/JJAP.49.110208>
- Kunz, C., Cowie, B. C. C., Drube, W., Lee, T. L., Thiess, S., Wild, C., & Zegenhagen, J. (2009). Relative electron inelastic mean free paths for diamond and graphite at 8 keV and intrinsic contributions to the energy-loss. *Journal of Electron Spectroscopy and Related Phenomena*, 173(1), 29–39. <https://doi.org/10.1016/j.elspec.2009.03.022>
- Kurlov, A. S., & Gusev, A. I. (2006). Tungsten carbides and W-C phase diagram. *Inorganic Materials*, 42(2), 121–127. <https://doi.org/10.1134/S0020168506020051>
- Kurlov, A. S., & Gusev, A. I. (2013). *Tungsten Carbides Structure*. https://doi.org/10.1007/978-3-319-00524-9_1
- Lagrange, J. P., Deneuve, A., & Gheeraert, E. (1998). Activation energy in low compensated homoepitaxial boron-doped diamond films. *Diamond and Related Materials*, 7(9), 1390–1393. [https://doi.org/10.1016/S0925-9635\(98\)00225-8](https://doi.org/10.1016/S0925-9635(98)00225-8)
- Laikhtman, A., Lafosse, A., Le Coat, Y., Azria, R., & Hoffman, A. (2003). Clarification of oxygen bonding on diamond surfaces by low energy electron stimulated desorption and high resolution electron energy loss spectroscopy. *Journal of Chemical Physics*, 119(3), 1794–1799. <https://doi.org/10.1063/1.1580097>
- Landstrass, M. I., & Ravi, K. V. (1989a). Hydrogen passivation of electrically active defects in diamond. *Applied Physics Letters*, 55(14), 1391–1393. <https://doi.org/10.1063/1.101604>
- Landstrass, M. I., & Ravi, K. V. (1989b). Resistivity of chemical vapor deposited diamond films. *Applied Physics Letters*, 55(10), 975–977. <https://doi.org/10.1063/1.101694>
- Lassner, E., & Schubert, W. D. (2005). *Tungsten: Properties, chemistry, technology of the element, alloys, and chemical compounds*.
- Lau, W. M., Huang, L. J., Bello, I., Yiu, Y. M., & Lee, S. T. (1994). Modification of surface band bending of diamond by low energy argon and carbon ion bombardment. *Journal of Applied Physics*, 75(7), 3385–3391. <https://doi.org/10.1063/1.357016>

- Lee, N., & Badzian, A. (1997). A study on surface morphologies of (001) homoepitaxial diamond films. *Diamond and Related Materials*, 6(1), 130–145. [https://doi.org/10.1016/S0925-9635\(96\)00698-X](https://doi.org/10.1016/S0925-9635(96)00698-X)
- Li, F., Zhang, J., Wang, X., Liu, Z., Wang, W., Li, S., & Wang, H. X. (2016). X-ray photoelectron spectroscopy study of Schottky junctions based on oxygen-/fluorine-terminated (100) diamond. *Diamond and Related Materials*, 63(100), 180–185. <https://doi.org/10.1016/j.diamond.2015.12.007>
- Li, F., Zhang, J., Wang, X., Zhang, M., & Wang, H. X. (2017). Barrier heights of Au on diamond with different terminations determined by X-ray photoelectron spectroscopy. *Coatings*, 7(7), 1–10. <https://doi.org/10.3390/coatings7070088>
- Li, F. N., Liu, J. W., Zhang, J. W., Wang, X. L., Wang, W., Liu, Z. C., & Wang, H. X. (2016). Measurement of barrier height of Pd on diamond (100) surface by X-ray photoelectron spectroscopy. *Applied Surface Science*, 370, 496–500. <https://doi.org/10.1016/j.apsusc.2016.02.189>
- Li, F. N., Li, Y., Fan, D. Y., & Wang, H. X. (2018). Barrier heights of Au, Pt, Pd, Ir, Cu on nitrogen terminated (1 0 0) diamond determined by X-ray photoelectron spectroscopy. *Applied Surface Science*, 456(April), 532–537. <https://doi.org/10.1016/j.apsusc.2018.06.184>
- Liao, M., Alvarez, J., & Koide, Y. (2005). Thermal stability of diamond photodiodes using tungsten carbide as schottky contact. *Japanese Journal of Applied Physics, Part 1: Regular Papers and Short Notes and Review Papers*, 44(11), 7832–7838. <https://doi.org/10.1143/JJAP.44.7832>
- Liao, M., Koide, Y., & Alvarez, J. (2006). Crystallographic and electrical characterization of tungsten carbide thin films for Schottky contact of diamond photodiode. *Journal of Vacuum Science and Technology B: Microelectronics and Nanometer Structures*, 24(1), 185–189. <https://doi.org/10.1116/1.2151909>
- Liu, A. Y., & Cohen, M. L. (1988). Theoretical study of the stability of cubic WC. *Solid State Communications*, 67(10), 907–910. [https://doi.org/10.1016/0038-1098\(88\)90454-1](https://doi.org/10.1016/0038-1098(88)90454-1)
- Lloret, F. (2017). *Croissance latérale MPCVD de diamant en homoépitaxie pour dispositifs électroniques de puissance*.
- Lloret, F., Eon, D., Bustarret, E., Donatini, F., & Araujo, D. (2021). Selectively boron doped homoepitaxial diamond growth for power device applications. *Applied Physics Letters*, 023504(118). <https://doi.org/10.1063/5.0031478>

- Loh, K. P., Xie, X. N., Lim, Y. H., Teo, E. J., Zheng, J. C., & Ando, T. (2002). Surface oxygenation studies on (1 0 0)-oriented diamond using an atom beam source and local anodic oxidation. *Surface Science*, *505*, 93–114. [https://doi.org/10.1016/S0039-6028\(02\)01103-2](https://doi.org/10.1016/S0039-6028(02)01103-2)
- Long, R., Dai, Y., & Guo, M. (2008). Characterization of diamond (100) surface with oxygen termination. *Applied Surface Science*, *254*(9), 2851–2855. <https://doi.org/10.1016/j.apsusc.2007.10.045>
- Lüth, H. (2010). *Solid Surfaces, Interfaces and Thin Films*. <https://doi.org/10.1007/978-3-642-13592-7>
- Maier, F., Graupner, R., Hollering, M., Hammer, L., Ristein, J., & Ley, L. (1999). Hydrogenated and bare diamond (110) surface: A combined LEED-, XPS-, and ARPES study. *Surface Science*, *443*(3), 177–185. [https://doi.org/10.1016/S0039-6028\(99\)01010-9](https://doi.org/10.1016/S0039-6028(99)01010-9)
- Maier, F., Riedel, M., Mantel, B., Ristein, J., & Ley, L. (2000). Origin of Surface Conductivity in Diamond. *Physical Review Letters*, *85*(16), 14–17. <https://doi.org/10.1103/PhysRevLett.85.3472>
- Maier, F., Ristein, J., & Ley, L. (2001). Electron affinity of plasma-hydrogenated and chemically oxidized diamond (100) surfaces. *Physical Review B - Condensed Matter and Materials Physics*, *64*(16), 1–7. <https://doi.org/10.1103/PhysRevB.64.165411>
- Maier, F., Riedel, M., Mantel, B., Ristein, J., & Ley, L. (2001). Maier et al. reply. *Physical Review Letters*, *87*(20), 209706–1. <https://doi.org/10.1103/PhysRevLett.87.209706>
- Maki, T., Shikama, S., Komori, M., Sakaguchi, Y., Sakuta, K., & Kobayashi, T. (1992). Hydrogenating effect of single-crystal diamond surface. *Japanese Journal of Applied Physics*, *31*(10), L1446–L1449. <https://doi.org/10.1143/JJAP.31.L1446>
- Makino, T., Kato, H., Ogura, M., Watanabe, H., Ri, S. G., Yamasaki, S., & Okushi, H. (2005). Strong excitonic emission from (001)-oriented diamond p-n junction. *Japanese Journal of Applied Physics, Part 2: Letters*, *44*(37–41), 1–4. <https://doi.org/10.1143/JJAP.44.L1190>
- Makino, T., Tanimoto, S., Hayashi, Y., Kato, H., Tokuda, N., Ogura, M., et al. (2009). Diamond Schottky- pn diode with high forward current density and fast switching operation. *Applied Physics Letters*, *94*(26), 1–4. <https://doi.org/10.1063/1.3159837>
- Maréchal, A., Kato, Y., Liao, M., & Koizumi, S. (2017). Interfacial energy barrier height of Al₂O₃/H-terminated (111) diamond heterointerface investigated by X-ray photoelectron spectroscopy. *Appl. Phys. Lett.*, *111*(111), 1–12. <https://doi.org/10.1063/1.5001070>

- Martineau, P., Gaukroger, M., Khan, R., & Evans, D. (2009). Effect of steps on dislocations in CVD diamond grown on {001} substrates. *Physica Status Solidi (C) Current Topics in Solid State Physics*, 6(8), 1953–1957. <https://doi.org/10.1002/pssc.200881465>
- Matsumoto, S., Sato, Y., Tsutsumi, M., & Setaka, N. (1982). Growth of diamond particles from methane-hydrogen gas. *Journal of Materials Science*, 17(11), 3106–3112. <https://doi.org/10.1007/BF01203472>
- Matsumoto, T., Mukose, T., Makino, T., Takeuchi, D., Yamasaki, S., Inokuma, T., & Tokuda, N. (2017). Diamond Schottky-pn diode using lightly nitrogen-doped layer. *Diamond and Related Materials*, 75, 152–154. <https://doi.org/10.1016/j.diamond.2017.03.018>
- May, P. W., Stone, J. C., Ashfold, M. N. R., Hallam, K. R., Wang, W. N., & Fox, N. A. (1998). The effect of diamond surface termination species upon field emission properties. *Diamond and Related Materials*, 7(2–5), 671–676. [https://doi.org/10.1016/s0925-9635\(97\)00181-7](https://doi.org/10.1016/s0925-9635(97)00181-7)
- Mcguire, G. E., Schweitzer, G. K., & Carlson, T. A. (1973). Study of Core Electron Binding Energies in Some Group IIIa, Vb, and VIb Compounds. *Inorganic Chemistry*, 12(10), 2450–2453. <https://doi.org/10.1021/ic50128a045>
- Mikhailov, S., Weber, J., Baer, Y., Hänni, W., & Tang, X.-M. (1995). Solid state reaction of Mo on H-terminated surface of diamond thin films. *Solid State Communications*, 93(11), 869–873. [https://doi.org/10.1016/0038-1098\(94\)00885-X](https://doi.org/10.1016/0038-1098(94)00885-X)
- Mikhailov, S. N., Ariosa, D., Weber, J., Baer, Y., Hänni, W., Tang, X.-M., & Alers, P. (1995). The behaviour of the molybdenum-CVD diamond interface at high temperature. *Diamond and Related Materials*, 4(9), 1137–1141. [https://doi.org/10.1016/0925-9635\(95\)00289-8](https://doi.org/10.1016/0925-9635(95)00289-8)
- Milat, O., Salamon, K., & Radić, N. (n.d.). Crystal structure and nanostructure of β -WC_{1-x}.
- Naamoun, M., Tallaire, A., Silva, F., Achard, J., Doppelt, P., & Gicquel, A. (2012). Etch-pit formation mechanism induced on HPHT and CVD diamond single crystals by H₂/O₂ plasma etching treatment: Part of topical section on fundamentals and applications of diamond. *Physica Status Solidi (A) Applications and Materials Science*, 209(9), 1715–1720. <https://doi.org/10.1002/pssa.201200069>
- Nakamura, J., & Ito, T. (2005). Oxidization process of CVD diamond (1 0 0):H₂ × 1 surfaces. *Applied Surface Science*, 244(1–4), 301–304. <https://doi.org/10.1016/j.apsusc.2004.12.005>
- Nakazawa, K., Tachiki, M., Kawarada, H., Kawamura, A., Horiuchi, K., & Ishikura, T. (2003). Cathodoluminescence and hall-effect measurements in sulfur-doped chemical-vapor-deposited diamond. *Applied Physics Letters*, 82(13), 2074–2076. <https://doi.org/10.1063/1.1563829>

- Navas, J., Araujo, D., Piñero, J. C., Sánchez-Coronilla, A., Blanco, E., Villar, P., et al. (2018). Oxygen termination of homoepitaxial diamond surface by ozone and chemical methods: An experimental and theoretical perspective. *Applied Surface Science*, *433*, 408–418. <https://doi.org/10.1016/j.apsusc.2017.10.065>
- Nečas, D., & Klapetek, P. (2012). Gwyddion: An open-source software for SPM data analysis. *Central European Journal of Physics*, *10*(1), 181–188. <https://doi.org/10.2478/s11534-011-0096-2>
- Nefedov, V. I., Firsov, M. N., & Shaplygin, I. S. (1982). Electronic structures of MRhO₂, MRh₂O₄, RhMO₄ and Rh₂MO₆ on the basis of X-ray spectroscopy and ESCA data. *Journal of Electron Spectroscopy and Related Phenomena*, *26*(1), 65–78. [https://doi.org/10.1016/0368-2048\(82\)87006-0](https://doi.org/10.1016/0368-2048(82)87006-0)
- Neto, M. A., Silva, E. L., Fernandes, A. J. S., Oliveira, F. J., & Silva, R. F. (2012). Diamond/WC bilayer formation mechanism by hot-filament CVD. *Surface and Coatings Technology*, *206*(13), 3055–3063. <https://doi.org/10.1016/j.surfcoat.2011.12.005>
- Nimmagadda, R. R., Joshi, A., & Hsu, W. L. (1990). Role of Microstructure on the Oxidation Behavior of Microwave Plasma Synthesized Diamond and Diamond-Like Carbon Films. *Journal of Materials Research*, *5*(11), 2445–2450. <https://doi.org/10.1557/JMR.1990.2445>
- Ogura, M., Kato, H., Makino, T., Okushi, H., & Yamasaki, S. (2011). Misorientation-angle dependence of boron incorporation into (0 0 1)-oriented chemical-vapor-deposited (CVD) diamond. *Journal of Crystal Growth*, *317*(1), 60–63. <https://doi.org/10.1016/j.jcrysgro.2011.01.010>
- Ohta, R., Saito, N., Inoue, Y., Sugimura, H., & Takai, O. (2004). Organosilane self-assembled monolayers directly linked to the diamond surfaces. *Journal of Vacuum Science & Technology A: Vacuum, Surfaces, and Films*, *22*(5), 2005–2009. <https://doi.org/10.1116/1.1776184>
- Omnès, F., Muret, P., Volpe, P. N., Wade, M., Pernot, J., & Jomard, F. (2011). Study of boron doping in MPCVD grown homoepitaxial diamond layers based on cathodoluminescence spectroscopy, secondary ion mass spectroscopy and capacitance-voltage measurements. *Diamond and Related Materials*, *20*(7), 912–916. <https://doi.org/10.1016/j.diamond.2011.05.010>
- Pehrsson, P. E., & Mercer, T. W. (2000). Oxidation of heated diamond C(100):H surfaces. *Surface Science*, *460*(1–3), 74–90. [https://doi.org/10.1016/S0039-6028\(00\)00495-7](https://doi.org/10.1016/S0039-6028(00)00495-7)
- Pehrsson, P. E., Mercer, T. W., & Chaney, J. A. (2002). Oxidation of the hydrogenated diamond

- (100) surface. *Surface Science*, 497(1–3), 13–28. [https://doi.org/10.1016/S0039-6028\(01\)01677-6](https://doi.org/10.1016/S0039-6028(01)01677-6)
- Petit, T., Arnault, J. C., Girard, H. A., Sennour, M., & Bergonzo, P. (2011). Early stages of surface graphitization on nanodiamond probed by x-ray photoelectron spectroscopy. *Physical Review B - Condensed Matter and Materials Physics*, 84(23), 1–5. <https://doi.org/10.1103/PhysRevB.84.233407>
- Pierson, H. O. (1996). Handbook of refractory carbides and nitrides : properties, characteristics, processing, and applications. *Handbook of Refractory Carbides and Nitrides*, 362. <https://doi.org/10.1016/B978-081551392-6.50005-2>
- Pietzka, C., Denisenko, A., Romanyuk, A., Schäfer, P. J., Kibler, L. A., Scharpf, J., & Kohn, E. (2010). Electronic surface barrier properties of boron-doped diamond oxidized by plasma treatment. *Diamond and Related Materials*, 19(2–3), 213–216. <https://doi.org/10.1016/j.diamond.2009.08.014>
- Piñero, J. C. (2016). *Role of interface configuration in diamond-related power devices*.
- Piñero, J. C., Araujo, D., Fiori, A., Traore, A., Villar, M. P., Eon, D., et al. (2017). Atomic composition of WC/ and Zr/O-terminated diamond Schottky interfaces close to ideality. *Applied Surface Science*, 395, 200–207. <https://doi.org/10.1016/j.apsusc.2016.04.166>
- Prins, J. F. (2000). N-type semiconducting diamond by means of oxygen-ion implantation. *Physical Review B - Condensed Matter and Materials Physics*, 61(11), 7191–7194. <https://doi.org/10.1103/PhysRevB.61.7191>
- Reinke, P., Francz, G., Oelhafen, P., & Ullmann, J. (1996). Structural changes in diamond and amorphous carbon induced by low-energy ion irradiation. *Physical Review B - Condensed Matter and Materials Physics*, 54(10), 7067–7073. <https://doi.org/10.1103/PhysRevB.54.7067>
- Ri, S.-G., Yoshida, H., Yamanaka, S., Watanabe, H., Takeuchi, D., & Okushi, H. (2002). Misorientation angle dependence of surface morphology in homoepitaxial diamond film growth at a low CH₄/H₂ ratio. *Journal of Crystal Growth*, 235(1–4), 300–306. [https://doi.org/10.1016/S0022-0248\(01\)01801-2](https://doi.org/10.1016/S0022-0248(01)01801-2)
- Ri, S.-G., Watanabe, H., Ogura, M., Takeuchi, D., Yamasaki, S., & Okushi, H. (2006). Hydrogen plasma etching mechanism on (0 0 1) diamond. *Journal of Crystal Growth*, 293(2), 311–317. <https://doi.org/10.1016/j.jcrysgro.2006.05.036>
- Riedel, M., Ristein, J., & Ley, L. (2004). Recovery of surface conductivity of H-terminated diamond after thermal annealing in vacuum. *Physical Review B - Condensed Matter and*

- Materials Physics*, 69(12), 1–8. <https://doi.org/10.1103/PhysRevB.69.125338>
- Ristein, J. (2006a). Surface science of diamond: Familiar and amazing. *Surface Science*, 600(18), 3677–3689. <https://doi.org/10.1016/j.susc.2006.01.087>
- Ristein, J. (2006b). Surface transfer doping of diamond. *Journal of Physics D: Applied Physics*, 39(4). <https://doi.org/10.1088/0022-3727/39/4/R01>
- Robins, L. H., Cook, L. P., Farabaugh, E. N., & Feldman, A. (1989). Cathodoluminescence of defects in diamond films and particles grown by hot-filament chemical-vapor deposition. *Physical Review B*, 39(18), 13367–13377. <https://doi.org/10.1103/PhysRevB.39.13367>
- Saada, D., Adler, J., & Kalish, R. (2000). Sulfur: A potential donor in diamond. *Applied Physics Letters*, 77(6), 878–879. <https://doi.org/10.1063/1.1306914>
- Sachtler, W. M. H., Dorgelo, G. J. H., & Holscher, A. A. (1966). THE WORK FUNCTION OF GOLD. *Surface Science*, 5, 221–229.
- Saguy, C., Cytermann, C., Fizgeer, B., Richter, V., Avigal, Y., Moriya, N., et al. (2003). Diffusion of hydrogen in undoped, p-type and n-type doped diamonds. *Diamond and Related Materials*, 12(3–7), 623–631. [https://doi.org/10.1016/S0925-9635\(02\)00403-X](https://doi.org/10.1016/S0925-9635(02)00403-X)
- Sarma, D. D., & Rao, C. N. R. (1980). XPS studies of oxides of second- and third-row transition metals including rare earths. *Journal of Electron Spectroscopy and Related Phenomena*, 20(1), 25–45. [https://doi.org/10.1016/0368-2048\(80\)85003-1](https://doi.org/10.1016/0368-2048(80)85003-1)
- Sato, H., & Kasu, M. (2013). Maximum hole concentration for Hydrogen-terminated diamond surfaces with various surface orientations obtained by exposure to highly concentrated NO₂. *Diamond and Related Materials*, 31(2), 47–49. <https://doi.org/10.1016/j.diamond.2012.10.007>
- Sawada, H., Ichinose, H., Watanabe, H., Takeuchi, D., & Okushi, H. (2001a). Cross-sectional TEM study of unepitaxial crystallites in a homoepitaxial diamond film. *Diamond and Related Materials*, 10(11), 2030–2034. [https://doi.org/10.1016/S0925-9635\(01\)00477-0](https://doi.org/10.1016/S0925-9635(01)00477-0)
- Sawada, H., Ichinose, H., Watanabe, H., Takeuchi, D., & Okushi, H. (2001b). Structure of unepitaxial crystallites in a homoepitaxial diamond film. *Diamond and Related Materials*, 10(11), 2096–2098. [https://doi.org/10.1016/S0925-9635\(01\)00485-X](https://doi.org/10.1016/S0925-9635(01)00485-X)
- Schreck, M., Hörmann, F., Roll, H., Lindner, J. K. N., & Stritzker, B. (2001). Diamond nucleation on iridium buffer layers and subsequent textured growth: A route for the realization of single-crystal diamond films. *Applied Physics Letters*, 78(2), 192–194. <https://doi.org/10.1063/1.1337648>

- Sette, F., Wertheim, G. K., Ma, Y., Meigs, G., Modesti, S., & Chen, C. T. (1990). Lifetime and screening of the C 1s photoemission in graphite. *Physical Review B*, *41*(14), 9766–9770. <https://doi.org/10.1103/PhysRevB.41.9766>
- Shinotsuka, H., Tanuma, S., Powell, C. J., & Penn, D. R. (2015). Calculations of electron inelastic mean free paths. X. Data for 41 elemental solids over the 50eV to 200keV range with the relativistic full Penn algorithm. *Surface and Interface Analysis*, *47*(9), 871–888. <https://doi.org/10.1002/sia.5789>
- Shiomi, H., Nishibayashi, Y., & Fujimori, N. (1991). Characterization of Boron-Doped diamond epitaxial films. *Japanese Journal of Applied Physics*, *30*(1363).
- Shirley, D. A. (1972). High-resolution x-ray photoemission spectrum of the valence bands of gold. *Physical Review B*, *5*(12), 4709–4714. <https://doi.org/10.1103/PhysRevB.5.4709>
- Shpilman, Z., Gouzman, I., Grossman, E., Akhvediani, R., & Hoffman, A. (2008). Chemical and morphological aspects of diamond film oxidation and regeneration. *Physica Status Solidi (A) Applications and Materials Science*, *205*(9), 2130–2135. <https://doi.org/10.1002/pssa.200879708>
- Shpilman, Z., Gouzman, I., Minton, T. K., Shen, L., Stacey, A., Orwa, J., et al. (2014). A near edge X-ray absorption fine structure study of oxidized single crystal and polycrystalline diamond surfaces. *Diamond and Related Materials*, *45*, 20–27. <https://doi.org/10.1016/j.diamond.2014.03.004>
- Skokov, S., Weiner, B., & Frenklach, M. (1994). Molecular-dynamics study of oxygenated (100) diamond surfaces. *Physical Review B*, *49*(16), 11374–11382. <https://doi.org/10.1103/PhysRevB.49.11374>
- Song, Y., & Larsson, K. (2015). A theoretical study of the effect of dopants on diamond (100) surface stabilization for different termination scenarios. *The Journal of Physical Chemistry C*, *119*(5), 2545–2556. <https://doi.org/10.1021/jp511077v>
- Speranza, G., Torrenzo, S., Filippi, M., Minati, L., Vittone, E., Pasquarelli, A., et al. (2010). In situ thermal treatment of UV-oxidized diamond hydrogenated surface. *Surface Science*, *604*(9–10), 753–761. <https://doi.org/10.1016/j.susc.2010.01.004>
- Speranza, G., Torrenzo, S., Miotello, A., Minati, L., Bernagozzi, I., Ferrari, M., et al. (2011). XPS and UPS in situ study of oxygen thermal desorption from nanocrystalline diamond surface oxidized by different process. *Diamond and Related Materials*, *20*(4), 560–563. <https://doi.org/10.1016/j.diamond.2011.03.001>
- Sque, S. J., Jones, R., & Briddon, P. R. (2006). Structure, electronics, and interaction of hydrogen

- and oxygen on diamond surfaces. *Physical Review B - Condensed Matter and Materials Physics*, 73(8), 1–15. <https://doi.org/10.1103/PhysRevB.73.085313>
- Stacey, A., Cowie, B. C. C., Orwa, J., Prawer, S., & Hoffman, A. (2010). Diamond C 1s core-level excitons: Surface sensitivity. *Physical Review B - Condensed Matter and Materials Physics*, 82(12), 1–7. <https://doi.org/10.1103/PhysRevB.82.125427>
- Stacey, A., O'Donnell, K. M., Chou, J. P., Schenk, A., Tadich, A., Dontschuk, N., et al. (2015). Nitrogen Terminated Diamond. *Advanced Materials Interfaces*, 2(10). <https://doi.org/10.1002/admi.201500079>
- Stacey, A., Dontschuk, N., Chou, J. P., Broadway, D. A., Schenk, A. K., Sear, M. J., et al. (2019). Evidence for Primal sp² Defects at the Diamond Surface: Candidates for Electron Trapping and Noise Sources. *Advanced Materials Interfaces*, 6(3), 1–8. <https://doi.org/10.1002/admi.201801449>
- Stallcup, R. E., & Perez, J. M. (2001). Scanning tunneling microscopy studies of temperature-dependent etching of diamond (100) by atomic hydrogen. *Physical Review Letters*, 86(15), 3368–3371. <https://doi.org/10.1103/PhysRevLett.86.3368>
- Stenger, I., Pinault-Thaury, M. A., Kociniowski, T., Lusson, A., Chikoidze, E., Jomard, F., et al. (2013). Impurity-to-band activation energy in phosphorus doped diamond. *Journal of Applied Physics*, 114(7). <https://doi.org/10.1063/1.4818946>
- Strobel, P., Ristein, J., & Ley, L. (2008). Controlled hydroxylation of diamond for covalent attachment of fullerene molecules. *Diamond and Related Materials*, 17(7–10), 1362–1366. <https://doi.org/10.1016/j.diamond.2008.03.013>
- Suda, Y., Yukimura, K., Nakamura, K., Takaki, K., & Sakai, Y. (2006). Deposition of tungsten carbide thin films by simultaneous RF sputtering. *Japanese Journal of Applied Physics, Part 1: Regular Papers and Short Notes and Review Papers*, 45(10 B), 8449–8452. <https://doi.org/10.1143/JJAP.45.8449>
- Sung, C. M., & Tai, M. F. (1997). Reactivities of Transition Metals with Carbon: Implications to the Mechanism of Diamond Synthesis Under High Pressure. *International Journal of Refractory Metals and Hard Materials*, 15(4), 237–256. [https://doi.org/10.1016/S0263-4368\(97\)00003-6](https://doi.org/10.1016/S0263-4368(97)00003-6)
- Tachibana, T., & Glass, J. T. (1993). Correlation of interface chemistry to electrical properties of metal contacts on diamond. *Diamond and Related Materials*, 2(5–7), 963–969. [https://doi.org/10.1016/0925-9635\(93\)90259-5](https://doi.org/10.1016/0925-9635(93)90259-5)

- Takeuchi, D., Yamanaka, S., Watanabe, H., Sawada, S., Ichinose, H., Okushi, H., & Kajimura, K. (1999). High quality homoepitaxial diamond thin film synthesis with high growth rate by a two-step growth method. *Diamond and Related Materials*, 8(6), 1046–1049. [https://doi.org/10.1016/S0925-9635\(99\)00002-3](https://doi.org/10.1016/S0925-9635(99)00002-3)
- Takeuchi, D., Ri, S.-G., Kato, H., Nebel, C. E., & Yamasaki, S. (2005). Negative electron affinity on hydrogen terminated diamond. *Physica Status Solidi (A)*, 202(11), 2098–2103. <https://doi.org/10.1002/pssa.200561927>
- Takeuchi, D., Ri, S. G., Tokuda, N., & Yamasaki, S. (2009). Recovery of negative electron affinity by annealing on (111) oxidized diamond surfaces. *Diamond and Related Materials*, 18(2–3), 206–209. <https://doi.org/10.1016/j.diamond.2008.10.007>
- Tallaire, A., Kasu, M., Ueda, K., & Makimoto, T. (2008). Origin of growth defects in CVD diamond epitaxial films. *Diamond and Related Materials*, 17(1), 60–65. <https://doi.org/10.1016/j.diamond.2007.10.003>
- Tavsanoglu, T., Begum, C., Alkan, M., & Yucel, O. (2013). Deposition and characterization of tungsten carbide thin films by DC magnetron sputtering for wear-resistant applications. *Jom*, 65(4), 562–566. <https://doi.org/10.1007/s11837-013-0571-x>
- Teraji, T., Koizumi, S., & Koide, Y. (2008). Ohmic contact for p -type diamond without postannealing. *Journal of Applied Physics*, 104(1), 10–13. <https://doi.org/10.1063/1.2936371>
- Teraji, T., Koide, Y., & Ito, T. (2009). High-temperature stability of Au/p-type diamond Schottky diode. *Physica Status Solidi - Rapid Research Letters*, 3(6), 211–213. <https://doi.org/10.1002/pssr.200903151>
- Teraji, T., Garino, Y., Koide, Y., & Ito, T. (2009). Low-leakage p-type diamond Schottky diodes prepared using vacuum ultraviolet light/ozone treatment. *Journal of Applied Physics*, 105(12), 20–23. <https://doi.org/10.1063/1.3153986>
- Teraji, T., Liao, M. Y., & Koide, Y. (2012). Localized mid-gap-states limited reverse current of diamond Schottky diodes. *Journal of Applied Physics*, 111(10). <https://doi.org/10.1063/1.4712437>
- Teraji, T., Koide, Y., & Ito, T. (2014). Schottky barrier height and thermal stability of p-diamond (100) Schottky interfaces. *Thin Solid Films*, 557, 241–248. <https://doi.org/10.1016/j.tsf.2013.11.132>
- de Theije, F. K., Reedijk, M. F., Arsic, J., van Enkevort, W. J. P., & Vlieg, E. (2001). Atomic structure of diamond (111) surfaces etched in oxygen water vapor. *Physical Review B* -

- Condensed Matter and Materials Physics*, 64(8), 1–7.
<https://doi.org/10.1103/PhysRevB.64.085403>
- Thomas, E. L. H., Mandal, S., Brousseau, E. B., & Williams, O. A. (2014). Silica based polishing of {100} and {111} single crystal diamond. *Science and Technology of Advanced Materials*, 15(3). <https://doi.org/10.1088/1468-6996/15/3/035013>
- Thomas, R. E., Rudder, R. A., & Markunas, R. J. (1992). Thermal desorption from hydrogenated and oxygenated diamond (100) surfaces. *Journal of Vacuum Science & Technology A: Vacuum, Surfaces, and Films*, 10(4), 2451–2457. <https://doi.org/10.1116/1.577983>
- Thoms, B. D., & Butler, J. E. (1995). HREELS and LEED of H/C(100): the 2 X 1 monohydride dimer row reconstruction. *Surface Science*, 328(3), 291–301. [https://doi.org/10.1016/0039-6028\(95\)00039-9](https://doi.org/10.1016/0039-6028(95)00039-9)
- Tian, Y. (1999). Study of field emission of acid treated diamond films. *Journal of Vacuum Science and Technology B: Microelectronics and Nanometer Structures*, 17(2), 688–689. <https://doi.org/10.1116/1.590619>
- Titantah, J. T., & Lamoen, D. (2005). Sp³/sp² characterization of carbon materials from first-principles calculations: X-ray photoelectron versus high energy electron energy-loss spectroscopy techniques. *Carbon*, 43(6), 1311–1316. <https://doi.org/10.1016/j.carbon.2005.01.002>
- Toros, A., Kiss, M., Graziosi, T., Mi, S., Berrazouane, R., Naamoun, M., et al. (2020). Reactive ion etching of single crystal diamond by inductively coupled plasma: State of the art and catalog of recipes. *Diamond and Related Materials*, 108(January). <https://doi.org/10.1016/j.diamond.2020.107839>
- Torrenço, S., Canteri, R., Dell'Anna, R., Minati, L., Pasquarelli, A., & Speranza, G. (2013). XPS and ToF-SIMS investigation of nanocrystalline diamond oxidized surfaces. *Applied Surface Science*, 276, 101–111. <https://doi.org/10.1016/j.apsusc.2013.03.041>
- Tougaard, S.; Simund, P. (1982). Elastic and inelastic scattering of electrons reflected from solids: Effects on energy spectra. *Physical Review B*, 25(7), 4452–4466. <https://doi.org/10.1103/PhysRevB.32.2808>
- Tranvouez, E., Boer-Duchemin, E., Mayne, A. J., Vanderbruggen, T., Scheele, M., Cartwright, R., et al. (2009). Influence of morphology on the conductance of single-crystal diamond surfaces measured by atomic force microscopy. *Journal of Applied Physics*, 106(5). <https://doi.org/10.1063/1.3211306>

- Traore, A. (2014). *High Power Diamond Schottky Diode*.
- Traoré, A., Muret, P., Fiori, A., Eon, D., Gheeraert, E., Pernot, J., et al. (2014). Zr / oxidized diamond interface for high power Schottky diodes, *052105*(2014). <https://doi.org/10.1063/1.4864060>
- Tsubouchi, N., Mokuno, Y., & Shikata, S. (2016). Characterizations of etch pits formed on single crystal diamond surface using oxygen/hydrogen plasma surface treatment. *Diamond and Related Materials*, *63*, 43–46. <https://doi.org/10.1016/j.diamond.2015.08.012>
- Ukhina, A. V., Yusuf, A. A., Dudina, D. V., Galashov, E. N., & Bokhonov, B. B. (2017). Surface modification of synthetic diamond with tungsten. *Proceedings - 2016 11th International Forum on Strategic Technology, IFOST 2016*, 95–98. <https://doi.org/10.1109/IFOST.2016.7884199>
- Umezawa, H. (2018). Recent advances in diamond power semiconductor devices. *Materials Science in Semiconductor Processing*, *78*(September 2017), 147–156. <https://doi.org/10.1016/j.mssp.2018.01.007>
- Umezawa, H., Kato, Y., & Shikata, S. (2013). 1 Ω On-Resistance Diamond Vertical-Schottky Barrier Diode Operated at 250 °C. *Applied Physics Express*, *6*(1), 011302. <https://doi.org/10.7567/APEX.6.011302>
- Verona, C., Ciccognani, W., Colangeli, S., Pietrantonio, F. D., Giovine, E., Limiti, E., et al. (2015). Gate-Source Distance Scaling Effects in H-Terminated Diamond MESFETs. *IEEE Transactions on Electron Devices*, *62*(4), 1150–1156. <https://doi.org/10.1109/TED.2015.2398891>
- Wade, T., Geis, M. W., Fedynyshyn, T. H., Vitale, S. A., Varghese, J. O., Lennon, D. M., et al. (2017). Effect of surface roughness and H-termination chemistry on diamond's semiconducting surface conductance. *Diamond and Related Materials*, *76*(April), 79–85. <https://doi.org/10.1016/j.diamond.2017.04.012>
- Wagner, C. D., Riggs, W. M., Davis, L. E., Moulder, J. F. F., Muilenberg, G. E., Stickle, W. F., et al. (1979). Handbook of X-Ray Photoelectron Spectroscopy. *Surface And Interface Analysis*. <https://doi.org/10.1002/sia.740030412>
- Wang, M., Simon, N., Decorse-pascanut, C., Bouttemy, M., Etcheberry, A., Li, M., et al. (2009). Comparison of the chemical composition of boron-doped diamond surfaces upon different oxidation processes. *Electrochimica Acta*, *54*(24), 5818–5824. <https://doi.org/10.1016/j.electacta.2009.05.037>
- Wang, M., Simon, N., Charrier, G., Bouttemy, M., Etcheberry, A., Li, M., et al. (2010).

- Distinction between surface hydroxyl and ether groups on boron-doped diamond electrodes using a chemical approach. *Electrochemistry Communications*, 12(3), 351–354. <https://doi.org/10.1016/j.elecom.2009.12.029>
- Wang, Y., & Yin, Z. (2014). Structural and electrical properties of sulfur-doped diamond thin films. *Plasma Science and Technology*, 16(3), 255–259. <https://doi.org/10.1088/1009-0630/16/3/15>
- Wang, Y. M., Wong, K. W., Lee, S. T., Nishitani-Gamo, M., Sakaguchi, I., Loh, K. P., & Ando, T. (2000). Recent studies on diamond surfaces. *Diamond and Related Materials*, 9(9), 1582–1590. [https://doi.org/10.1016/S0925-9635\(00\)00292-2](https://doi.org/10.1016/S0925-9635(00)00292-2)
- Warren, A., Nylund, A., & Olefjord, I. (1996). Oxidation of tungsten and tungsten carbide in dry and humid atmospheres. *International Journal of Refractory Metals and Hard Materials*, 14(5–6), 345–353. [https://doi.org/10.1016/s0263-4368\(96\)00027-3](https://doi.org/10.1016/s0263-4368(96)00027-3)
- Watanabe, J., Touge, M., & Sakamoto, T. (2013). Ultraviolet-irradiated precision polishing of diamond and its related materials. *Diamond and Related Materials*, 39, 14–19. <https://doi.org/10.1016/j.diamond.2013.07.001>
- Worrell, W. L. (1964). A thermodynamic analysis of the Cr-C-O, Mo-C-O, and W-C-O systems.
- Wort, C. J. H., & Balmer, R. S. (2008). Diamond as an electronic material. *Materials Today*, 11(1–2), 22–28. [https://doi.org/10.1016/S1369-7021\(07\)70349-8](https://doi.org/10.1016/S1369-7021(07)70349-8)
- Yeh, J. J., Pfeffer, R. L., Cole, M. W., Ohring, M., & Yehoda, J. E. (1996). Reactions between tungsten and molybdenum thin films and polycrystalline diamond substrates. *Diamond and Related Materials*, 5(10), 1195–1203. [https://doi.org/10.1016/0925-9635\(96\)00528-6](https://doi.org/10.1016/0925-9635(96)00528-6)
- Zaitsev, A. M. (2001). *Optical properties of Diamond: A data handbook*. Book. <https://doi.org/10.1007/978-3-642-56680-6>
- Zalar, A. (1985). Improved depth resolution by sample rotation during Auger electron spectroscopy depth profiling. *Thin Solid Films*, 124(3–4), 223–230. [https://doi.org/10.1016/0040-6090\(85\)90269-X](https://doi.org/10.1016/0040-6090(85)90269-X)
- Zheng, J. C., Xie, X. N., Wee, A. T. S., & Loh, K. P. (2001). Oxygen-induced surface state on diamond (100). *Diamond and Related Materials*, 10(3–7), 500–505. [https://doi.org/10.1016/S0925-9635\(00\)00439-8](https://doi.org/10.1016/S0925-9635(00)00439-8)




Gonzalo Alba Muñoz

Address: C/Bajo Guadalquivir, 59

11670, El Bosque (Cádiz)

Phone: +34 699212647

E-mail: gonzalo.alba@uca.es

 0000-0002-2360-7708

Date of birth: 10/08/1988

National ID: 15439083-B

Short Biography:

Gonzalo Alba is a native of the province of Cádiz (Andalusia, Spain). In 2014 he completed the Degree in Electronic Engineering (University of Cádiz) and in 2016 the Master's Degree in Electronics, Signal Processing and Communications (University of Seville). In 2017 he began his pre-doctoral stage in the Department of Materials Science (University of Cádiz) in the TEP-120 group. Since 2018 he is also a member of the Institute of Electron Microscopy and Materials (IMEYMAT). His studies focused on the characterization of diamond surfaces and metal / diamond contact interfaces combining TEM, FIB / SEM, XPS, AFM and electrical (I/V, C/V) characterization techniques in order to find relationships between the microstructure, chemistry and composition and the electrical behaviour of diamond-based power devices. As part of his internationalization, he has made stays at the Institut Néel (Grenoble, France) and at the National Institute for Materials Science (Tsukuba, Japan). In December 2020, he obtained a 3 years term “PTA 2019” grant (Ministry of Science, Innovation and Universities of Spain) and started to work as a research assistant at the University of Cádiz.

List of publications:

- **Alba, G., Leinen, D., Villar, M. P., Alcántara, R., Piñero, J. C., Fiori, A., et al.** (2020). *Comprehensive nanoscopic analysis of tungsten carbide/Oxygenated–diamond contacts for Schottky barrier diodes*. *Applied Surface Science*, 537(February 2020), 147874. <https://doi.org/10.1016/j.apsusc.2020.147874>
- **Alba, G., Pilar Villar, M., Alcántara, R., Navas, J., & Araujo, D.** (2020). *Surface states of (100) o-terminated diamond: Towards other 1 × 1:O reconstruction models*. *Nanomaterials*, 10(6), 1–15. <https://doi.org/10.3390/nano10061193>
- **Alba, G., Eon, D., Villar, M. P., Alcántara, R., Chicot, G., Cañas, J., et al.** (2020). *H-Terminated Diamond Surface Band Bending Characterization by Angle-Resolved XPS*. *Surfaces*, 3(1), 61–71. <https://doi.org/10.3390/surfaces3010007>
- **Cañas, J., Alba, G., Leinen, D., Lloret, F., Gutierrez, M., Eon, D., et al.** (2020). *Diamond/γ-alumina band offset determination by XPS*. *Applied Surface Science*, 146301. <https://doi.org/10.1016/J.APSUSC.2020.146301>
- **Araujo, D., Lloret, F., Alba, G., Alegre, M. P., & Villar, M. P.** (2021). *Dislocation generation mechanisms in heavily boron-doped diamond epilayers*. *Applied Physics Letters*, 052108(February). <https://doi.org/10.1063/5.0031476>
- **Piñero, J. C., de Vecchy, J., Fernández, D., Alba, G., Widiez, J., Di Cioccio, L., et al.** (2020). *Lattice performance during initial steps of the Smart-Cut™ process in semiconducting diamond: A STEM study*. *Applied Surface Science*, 528. <https://doi.org/10.1016/j.apsusc.2020.146998>
- **Araujo, D.; Suzuki, M.; Lloret, F.; Alba, G.; Villar, P.** (2021). *Diamond for Electronics: Materials, Processing and Devices*. *Materials*, 14, 7081. <https://doi.org/10.3390/ma14227081>

Congress contributions:

A total of 18 congress contribution in the 2017-2021 period. Among which it is highlighted:

- **Title:** *Diamond Surface Band Bending Estimation by ARXPS.*
Authors: G. Alba, R. Alcántara, M. P. Villar, A. Fiori, T. Teraji, D. Araujo.
Congress: 2019 MRS Fall Meeting
City: Boston, MA, USA
- **Title:** *TEM analysis on WC/diamond interfaces: towards degradation mechanism.*
Authors: G. Alba, R. Alcántara, M. P. Villar, A. Fiori, T. Teraji, D. Araujo.
Congress: 30th international conference on diamond and carbon materials 2019
City: Sevilla, Spain